Crystal Plasticity Simulation of in-grain Microstructural Evolution during Large Plastic Deformation

Sedighiani, K.

DOI
10.4233/uuid:38ca7b80-df99-4aae-b28d-70610229d3ed

Publication date
2022

Document Version
Final published version

Citation (APA)
Sedighiani, K. (2022). *Crystal Plasticity Simulation of in-grain Microstructural Evolution during Large Plastic Deformation*. [Dissertation (TU Delft), Delft University of Technology].
https://doi.org/10.4233/uuid:38ca7b80-df99-4aae-b28d-70610229d3ed

Important note
To cite this publication, please use the final published version (if applicable).
Please check the document version above.

Crystal Plasticity Simulation of in-grain Microstructural Evolution during Large Plastic Deformation

KARO SEDIGHIANI

Crystal Plasticity Simulation of in-grain Microstructural Evolution during Large Plastic Deformation

Dissertation

For the purpose of obtaining the degree of Doctor of Philosophy
at Delft University of Technology
by the authority of the Rector Magnificus, Prof.dr.ir. T.H.J.J. van der Hagen
chair of the Board of Doctorates
to be defended publicly on Monday 13 June 2022 at 17:30 o'clock

by

Karo SEDIGHIANI

Master of Science in Mechanical Engineering,
Eindhoven University of Technology, Eindhoven, The Netherlands,

Born in Saqqez, Kurdistan.

This dissertation has been approved by the promoters:

Prof. dr. ir. J. Sietsma
Prof. dr.-Ing. Habil. D. Raabe
Dr.-Ing. M. Diehl
Dr. rer. nat. F. Roters

Composition of the doctoral committee:

Rector Magnificus	chairperson
Prof. dr. ir. J. Sietsma	Delft University of Technology, promoter
Prof. dr.-Ing. Habil. D. Raabe	Max Planck Institute for Iron Research, promoter
Dr.-Ing. M. Diehl	KU Leuven, co-promoter
Dr. rer. nat. F. Roters	Max Planck Institute for Iron Research, co-promoter
Independent Members:	
Prof. dr. ir. L.A.I. Kestens	Delft University of Technology
Dr. ir. R.H.J. Peerlings	Eindhoven University of Technology
Prof. dr.-Ing. P. Eisenlohr	Michigan State University
Prof. S. Niezgoda	The Ohio State University
Reserved Member:	
Prof. dr. M.J. Santofimia Navarro	Delft University of Technology

Keywords: Crystal plasticity; Dislocation density; Parameter identification; Large deformation; Microstructure and microtexture evolution

Printed by: Proefschrijftmaken

ISBN 978-94-6423-858-7

An electronic version of this dissertation is available at
http://repository.tudelft.nl/.

Science may be described as the art of systematic over-simplification.

Karl Popper

SUMMARY

Plastic deformation of polycrystalline materials is significantly heterogeneous in terms of strain, stress, and crystal reorientation. The characterization of such localized deformation and microstructures formed during plastic deformation is vital in developing a thorough physics-based understanding of the underlying mechanisms behind localization phenomena such as fracture, shear banding, and nucleation during recrystallization.

Deformation microstructures are mainly quantified using experimental techniques such as electron backscattered diffraction (EBSD) and transmission electron microscopy (TEM). Despite the extensive amount of knowledge that can be developed from experimental studies, experimental techniques suffer from several drawbacks: (i) The microstructure and microtexture can be characterized solely based on the specimen surface, and determining the variation of microstructure through the thickness is only possible using destructive or highly advanced, expensive approaches. (ii) The actual neighboring and boundary conditions of the material points cannot be precisely determined. (iii) It is difficult to track the material points, especially during large deformation. (iv) A large number of experiments are required to acquire complete knowledge of the deformation history, which is extremely time-consuming and economically inefficient. (v) The experimental procedures usually contain uncertainty due to sensitivity to sample contamination and random errors.

Crystal plasticity simulations are a powerful alternative for quantifying the deformation heterogeneities and the associated complex mechanical fields. These models are developed based on physical mechanisms such as glide of dislocations on preferred slip systems and the interaction of dislocations with various defects. A severe obstacle for the routine use of crystal plasticity models is, however, the effort associated with determining their constitutive parameters. Obtaining these parameters usually requires time-consuming micromechanical tests that allow probing of individual grains. As the first step of the present research, a novel, computationally efficient, and fully automated approach is introduced to identify constitutive parameters from macroscopic tests (see Chapter 3). The approach uses the response surface methodology together with a genetic algorithm. The merits of the methodology are demonstrated on the examples of a dislocation-density-based crystal plasticity model for bcc steel, a phenomenological crystal plasticity model for fcc copper, and a phenomenological crystal plasticity model incorporating twinning deformation for hcp magnesium.

The proposed optimization approach also provides a tool to quantitatively and thoroughly analyze the relative influence of the different constitutive parameters and their interactions. This tool is used to examine the ability of a widely used temperature-dependent dislocation-density-based crystal plasticity formulation (see Chapter 4). For this purpose, the model parameters are first identified from experimental macroscopic stress-strain curves. Next, the influence of the individual parameters

on the observed behavior is analyzed. Based on mutual interactions between various parameters, the ability to find a unique parameter set is discussed. Particular attention is directed toward identifying possibly redundant material parameters, narrowing the acceptable range of material parameters based on physical criteria, and modifying the crystal plasticity formulation numerically for high-temperature use.

After determining the material parameters, the next step is to conduct large-deformation simulations to predict the deformation behavior of polycrystals. However, problems involving the deformation of solid materials are usually formulated in a Lagrangian context, i.e. the mesh is attached to the deformable body and deforms with a change in the shape of the material. As a result, the simulation mesh becomes distorted during deformation due to the heterogeneity of plastic deformation in polycrystals. The mesh distortion deteriorates the accuracy of the results, and after large strain localization levels, it is no longer possible to continue the simulation. Two adaptive remeshing approaches are introduced to overcome the mesh distortion problem and simulate large deformation of three-dimensional polycrystals (see Chapter 5). In the first approach, the geometry is created with a new mesh, and then the simulation is restarted as a new simulation in which the initial state is set based on the deformation state that had been reached. In the second approach, the mesh is smoothened by removing the distortion part of the deformation, and then the simulation is continued after finding a new equilibrium state for the smoothed mesh and geometry. The first method is highly efficient for conducting high-resolution large-deformation simulations. On the other hand, the second method's primary advantage is that it can overcome periodicity issues related to shear loading, and it can be used in conjunction with complex loading conditions. The merits of the methodologies are demonstrated using full-field simulations performed using the dislocation-density-based crystal plasticity model. Particular emphasis is put on studying the effect of resolution and adaptive meshing.

Finally, high-resolution three-dimensional crystal plasticity simulation and electron backscatter diffraction (EBSD) analysis are used to investigate deformation heterogeneity and microstructural evolution during cold rolling of interstitial free (IF-) steel (see Chapter 6). The in-grain texture evolution and misorientation spread are consistent for simulation and experimental results. Crystal plasticity simulation shows that two types of strain localization occur during large deformation of IF-steel. The first type applies to areas with large strain accumulation that appear as river patterns extending across the specimen. This type of shear localization can be seen as a cluster of shear bands, which pass through several grains and extend across the specimen. In addition to these river-like patterns, a second type of strain localization with rather sharp and highly localized in-grain deformation bands is identified. These localized features are orientation dependent and extend within a single grain. In addition to the strain localization, the evolution of in-grain orientation gradient, dislocation density, kernel average misorientation (KAM), and stress in major texture components are discussed.

CONTENTS

List of Figures

LIST OF TABLES

1

INTRODUCTION

1.1. Microstructure evolution

Accurate determination of the material properties is not possible without understanding the evolution and mechanical response of microstructural features. Besides, the underlying mechanisms behind localization phenomena such as fracture and damage are related to the strain localization and microstructural evolution during deformation. Moreover, understanding the physics governing the underlying mechanisms behind many multi-disciplinary material science problems is incomplete without adequately understanding internal stresses developed in these heterogeneous microstructures. For instance, the relaxation of internal stresses depends on physical mechanisms, such as diffusion or dislocation motion. This implies that the final response of a material after, for example, recrystallization and phase transformation depends on the initial microstructural features and internal stresses.

1.2. Computational methods

Various microstructure-based modeling methods have been developed to predict nano- to micro-scale microstructural deformation mechanisms. A few examples of the computational methods used frequently in materials science are discussed in the following.

Molecular dynamics This simulation method aims to simulate the dynamic evolution of the system by calculating the movement of particles in a certain period of time [1]. The trajectories of particles are usually calculated by solving Newton's equations of motion at an atomistic scale, where the potential energy for atomistic interaction is approximated using force fields. Molecular dynamics is frequently used to examine the dynamics of atomistic scale phenomena, such as dislocation evolution, microcracks, and thin-film growth [2]. This method is computationally expensive, and its main limitations are the size of the system and the time scale.

Discrete dislocation dynamics This simulation method aims to simulate dislocation motion, multiplication, and their interaction to gain insight into the topology evolution of dislocation networks and the material's mechanical properties [3, 4]. Unlike molecular dynamics that deals with conservative systems in which the local forces are described as a negative gradient of the potential, the discrete dislocation dynamics deals with the highly dissipative and anisotropic process of dislocation motion.

Crystal plasticity At a larger length scale than discrete dislocation dynamics, crystal plasticity simulations aim to simulate the material's mechanical response at the single-crystal level. Crystal plasticity models are developed based on physical mechanisms such as glide of dislocations on preferred slip systems and the interaction of dislocations with various defects [5], see Chapter 2 for more information.

1.3. Objective and outline of thesis

This work aims to demonstrate the possibility of using high-resolution crystal plasticity simulations for modeling the evolution of in-grain deformation heterogeneity during the large deformation of polycrystalline materials. However, a severe obstacle for the routine use of crystal plasticity models is the effort associated with determining their constitutive parameters. Obtaining these parameters usually requires time-consuming micromechanical tests that allow probing of individual grains. Therefore, an important prerequisite for exploiting the full predictive capabilities of physics-based models lies in the identification of an adequate set of material parameters within well-based physical bounds. In the first step, this work aims to develop a computationally efficient and fully automated approach to identify constitutive parameters from macroscopic tests. After determining the material parameters, the next challenge is to conduct large deformation simulations to predict the deformation behavior of polycrystals. Problems involving the deformation of solid materials are usually formulated in a Lagrangian context, i.e. the mesh is attached to the deformable body and deforms with a change in the shape of the material. As a result, the simulation mesh gets distorted during deformation due to the heterogeneity of plastic deformation in polycrystals. The mesh distortion deteriorates the accuracy of the results, and after large strain localization levels, it is no longer possible to continue the simulation. In the next step, this work aims to develop remeshing approaches to overcome the mesh distortion problem and simulate large deformation of three-dimensional polycrystals. Finally, the developed approaches are employed to investigate the microstructure and microtexture evolution during large deformation of interstitial free (IF-) steel. This thesis is organized in eight chapters as follows:

Chapter 2 provides an overview of the kinematics and constitutive laws of the crystal plasticity models used in the thesis. The crystal plasticity constitutive laws include a phenomenological model, a phenomenological model incorporating deformation twinning, and a dislocation-density-based model. The spectral solver implemented in DAMASK [6] is also explained. This solver is used to conduct the crystal plasticity simulations.

Chapter 3 presents a novel, and computationally efficient approach which allows the identification of constitutive parameters from macroscopic tests. The optimization approach uses the response surface methodology together with a genetic algorithm to determine an optimal set of parameters. It is especially suited for complex models with a large number of parameters. The proposed approach also enables to develop a quantitative and thorough understanding of the relative influence of the different constitutive parameters and their interactions. Such general insight into parameter relations in complex models can be used to improve constitutive laws and reduce redundancy in parameter sets. The merits of the methodology are demonstrated on the examples of a dislocation-density-based crystal plasticity model for bcc steel, a phenomenological crystal plasticity model for fcc copper, and a phenomenological crystal plasticity model incorporating twinning deformation for hcp magnesium.

Chapter 4 presents an in-depth analysis of the constitutive parameters of temperature-dependent dislocation-density-based constitutive laws to reproduce experimental results. First, the material parameters are identified from experimental macroscopic stress-strain curves using the optimization methodology introduced in Chapter 3. For this purpose, a systematic set of compression tests on interstitial free (IF) steel samples is performed at various temperatures and strain rates. Next, the influence of the individual parameters on the observed behavior is analyzed. Based on mutual interactions between various parameters, the ability to find a single parameter set is discussed. Particular attention is directed toward identifying possibly redundant material parameters, narrowing the acceptable range of material parameters based on physical criteria, and modifying the crystal plasticity formulation numerically for high-temperature use.

Chapter 5 presents two adaptive remeshing approaches for simulating large deformation of 3D polycrystals with high resolution under periodic boundary conditions. In the first approach, the geometry is recreated with a new mesh, and then the simulation is restarted as a new simulation in which the initial state is based on the last deformation state that had been reached. In the second approach, the mesh is smoothened by removing the distortion part of the deformation, and then the simulation is continued after finding a new equilibrium state for the smoothed mesh and geometry. The first method is highly efficient for conducting high-resolution large-deformation simulations. On the other hand, the second method's primary advantage is that it can overcome periodicity issues related to shear loading, and it can be used in conjunction with complex loading conditions. The merits of the methodologies are demonstrated using full-field simulations performed using the dislocation-density-based crystal plasticity model. Particular emphasis is put on studying the effect of resolution and adaptive meshing.

Chapter 6 investigates deformation heterogeneity and microstructure evolution during cold rolling of interstitial free (IF) steel using high-resolution three-dimensional crystal plasticity simulation and electron backscatter diffraction (EBSD) analysis. It is shown that the in-grain texture evolution and misorientation spread are consistent for simulation and experimental results. Crystal plasticity simulation reveals that two types of strain localization form during the large deformation of IF-steel. The first type applies to areas with large strain accumulation that appear as river patterns extending

across the specimen. This type of shear localization can be seen as a cluster of shear bands. In addition to the river-like patterns, a second type of strain localization with rather sharp and highly localized in-grain deformation bands is identified. These localized features are dependent on the crystallographic orientation and extend inside a single grain. In addition to the strain localization, the evolution of in-grain orientation gradient, dislocation density, kernel average misorientation (KAM), and stress in major texture components are discussed.

Chapter 7 presents a further investigation of some recommendations introduced in the other chapters. First, incorporating cross-slip annihilation into the hardening model of the dislocation-density-based model is examined. Then, two sequentially coupled models are investigated for modeling static recrystallization and meta-dynamic recrystallization. The results of this chapter are an introductory guideline for future work.

Finally, **Chapter 8** presents conclusions and some recommendations.

References

[1] A. F. Voter, D. W. Brenner, S. M. Foiles, and P. D. Godwin, *Interatomic potentials for atomistic simulations,* MRS Bulletin **21**, 17 (1996).

[2] D. Raabe, *Computational Materials Science: The Simulation of Materials Microstructures and Properties,* Wiley-VCH , 402 (1998).

[3] D. Weygand, L. H. Friedman, E. Van Der Giessen, and A. Needleman, *Discrete dislocation modeling in three-dimensional confined volumes,* Materials Science and Engineering A **309-310** (2001), 10.1016/S0921-5093(00)01632-4.

[4] O. Politano and J. M. Salazar, *A 3D mesoscopic approach for discrete dislocation dynamics,* Materials Science and Engineering A **309-310** (2001), 10.1016/S0921-5093(00)01765-2.

[5] F. Roters, P. Eisenlohr, L. Hantcherli, D. D. Tjahjanto, T. R. Bieler, and D. Raabe, *Overview of constitutive laws, kinematics, homogenization and multiscale methods in crystal plasticity finite-element modeling: Theory, experiments, applications,* Acta Materialia **58**, 1152 (2010).

[6] F. Roters, M. Diehl, P. Shanthraj, P. Eisenlohr, C. Reuber, S. Wong, T. Maiti, A. Ebrahimi, T. Hochrainer, H. Fabritius, S. Nikolov, M. Friák, N. Fujita, N. Grilli, K. Janssens, N. Jia, P. Kok, D. Ma, F. Meier, E. Werner, M. Stricker, D. Weygand, and D. Raabe, *DAMASK – The Düsseldorf Advanced Material Simulation Kit for modeling multi-physics crystal plasticity, thermal, and damage phenomena from the single crystal up to the component scale,* Computational Materials Science **158**, 420 (2019).

2

CRYSTAL PLASTICITY

Abstract

This chapter provides an overview of the kinematics and the three crystal plasticity constitutive laws used later in the thesis. The three crystal plasticity constitutive laws include a phenomenological model, a phenomenological model incorporating deformation twinning, and a dislocation-density-based model. A spectral solver implemented in DAMASK is used to conduct the crystal plasticity simulations using these constitutive laws.

2.1. Introduction

Taylor and Elam [1, 2] proposed the first model that described the plastic deformation of single crystals resulting from crystallographic slip. This model was later extended to analyze the deformation behavior of polycrystalline materials [3]. Hill [4] implemented this theory in a small-strain continuum mechanics framework. Later, Rice [5], Hill and Rice [6] extended this idea to be used along with the finite deformation framework by multiplicative decomposition of the deformation gradient into elastic and plastic components. This framework has been the basis for most of the crystal plasticity models developed later, e.g. [7–18]. This chapter first presents the kinematics for crystal plasticity modeling in a 3D continuum mechanics framework. Then, three crystal plasticity constitutive laws used later in the thesis are explained: a phenomenological crystal plasticity model, a phenomenological crystal plasticity model incorporating twinning deformation, and a dislocation-density-based crystal plasticity model.

2.2. Kinematics

Let us consider a deformable continuum body with volume $\mathscr{B}_0$ at its initially unloaded state. A position vector $\mathbf{x_0}$ gives the location of each material point in $\mathscr{B}_0$ with respect to a fixed coordinate system. The configuration is supposedly subjected to a time-dependent deformation. The location of each material point in the deformed configuration $\mathscr{B}_t$ at an arbitrary time t is denoted by $\mathbf{x}$. In a Lagrangian context, the deformed configuration $\mathbf{x}$ is then related to the reference configuration $\mathbf{x_0}$ through deformation gradient tensor $\mathbf{F}$ as:

$$\mathbf{F} = \frac{\partial \mathbf{x}}{\partial \mathbf{x_0}} \tag{2.1}$$

The kinematics for elastoplastic behavior within the finite deformation framework is defined by decomposing the deformation gradient tensor $\mathbf{F}$ into elastic, $\mathbf{F}_\mathrm{e}$, and plastic, $\mathbf{F}_\mathrm{p}$, components:

$$\mathbf{F} = \mathbf{F}_\mathrm{e}\mathbf{F}_\mathrm{p} \tag{2.2}$$

where subscripts "e" and "p" indicate elastic (reversible shape change) and plastic (irreversible shape change) parts of deformation gradient, respectively. The multiplicative decomposition is based on the concept that $\mathbf{F}_\mathrm{p}$ brings the reference configuration to a stress-free intermediate configuration. Then, $\mathbf{F}_\mathrm{e}$ brings the intermediate configuration to the current configuration. As a result, $\mathbf{F}_\mathrm{p}$ keeps the crystal lattice undistorted and unrotated, and the rotation of the configuration is defined only using $\mathbf{F}_\mathrm{e}$.

The rate at which a material is deforming is measured using the velocity gradient, $\mathbf{L}$, which is defined as

$$\mathbf{L} = \frac{\partial \mathbf{v}}{\partial \mathbf{x}} \tag{2.3}$$

where $\mathbf{v}$ is the velocity vector of the material point. $\mathbf{L}$ can be decomposed using Equation (2.2) and expressed in terms of $\mathbf{F}$ as:

$$\mathbf{L} = \dot{\mathbf{F}}\mathbf{F}^{-1} = \dot{\mathbf{F}}_e\mathbf{F}_e^{-1} + \mathbf{F}_e\left(\dot{\mathbf{F}}_p\mathbf{F}_p^{-1}\right)\mathbf{F}_e^{-1} = \mathbf{L}_e + \mathbf{F}_e\mathbf{L}_p\mathbf{F}_e^{-1} \tag{2.4}$$

where $\mathbf{L}_e$ is the elastic velocity gradient, $\mathbf{L}_p$ is the plastic velocity gradient at the intermediate configuration, and $\mathbf{F}_e$ is used to map $\mathbf{L}_p$ to the current configuration.

The plastic velocity gradient is obtained additively from individual contributions, indexed by n, and is driven by their work conjugate stress measures, i.e. the Mandel stress $\mathbf{M}_p$:

$$\mathbf{L}_p = \sum_n f_n\left(\mathbf{M}_p, ...\right) \tag{2.5}$$

The Mandel stress $\mathbf{M}_p$ is calculated from the second Piola–Kirchhoff stress $\mathbf{S}$, i.e. $\mathbf{S} = f(\mathbf{E}, ...)$, which can be linearly related to the Green–Lagrange elastic strain as:

$$\mathbf{S} = \mathbb{C} : \mathbf{E} \tag{2.6}$$

where the Green–Lagrange strain $\mathbf{E}$ in the intermediate configuration is given by:

$$\mathbf{E} = \frac{1}{2}\left(\mathbf{F}_e^{\mathrm{T}}\mathbf{F}_e - \mathbf{I}\right) \tag{2.7}$$

Plasticity in crystals occurs on well-defined slip systems that are available for a given crystallographic lattice. Each slip system is represented by two orthogonal unit vectors, i.e. the slip-plane normal and the slip direction within this plane. For instance, slip occurs in FCC materials on 12 slip systems formed by the $\{1\,1\,1\}$ planes and the $\langle 1\,1\,0\rangle$ directions. The plastic velocity gradient $\mathbf{L}_p$ is calculated as the sum of the shear contributions from these slip systems.

$$\mathbf{L}_p = \sum_{\alpha=1}^{N_s} \dot{\gamma}^\alpha\left(\mathbf{s}^\alpha \otimes \mathbf{n}^\alpha\right) \tag{2.8}$$

where $\dot{\gamma}^\alpha$ is the shear rate on the active slip systems α, and N_s is the number of active slip systems.

2.2.1. Crystallographic orientation

The decomposition order in Equation (2.2) allows considering the anisotropy and dependency of a constitutive law on crystallographic orientation. For a polycrystal analysis, stiffness tensors, slip plane normals, and slip directions of each crystal must be specified in a global coordinate system. Such tensorial quantities are typically defined in the lattice coordinate system to avoid unnecessary rotations of tensorial quantities. For this purpose, following Ma *et al.* [15], the initial value of $\mathbf{F}_p$ is set as the initial crystal orientation $\mathbf{O}_0$:

$$\mathbf{F}_p(t=0) = \mathbf{O}_0. \tag{2.9}$$

Therefore, the initial reference configuration for all crystals is the cube orientation. Then, $\mathbf{F}_e^0 = \mathbf{F}_e(\text{t=0})$ is set as $\mathbf{O}_0^{\mathrm{T}}$ to achieve the desired identity tensor, $\mathbf{I}$, for the initial deformation gradient tensor:

$$\mathbf{F}^0 = \mathbf{F}_e^0 \mathbf{F}_p^0 = \mathbf{I}. \tag{2.10}$$

The current crystal orientation $\mathbf{O}$ can then be calculated by polar decomposition of the current elastic deformation:

$$\mathbf{F}_e = \mathbf{V}_e \mathbf{O}^T, \tag{2.11}$$

where $\mathbf{V}_e$ is the elastic left stretch tensor.

2.3. Constitutive laws

The constitutive laws in a crystal plasticity model relate the kinetics of the deformation to the physics of the material behavior. During the last few decades, various constitutive inelastic flow laws have been developed, e.g. empirical visco-plastic models [5, 19], phenomenological models [7–9, 20–22], and physics-based models [10–18, 23–26]. These constitutive laws rely on state variables that constitute and track the deformation history, e.g. the critical resolved shear stress for the case of a phenomenological constitutive law or dislocation densities for the case of a dislocation-density-based constitutive law.

In DAMASK [27], a variety of constitutive laws are implemented, and they can be used for different crystal structures and definitions of slip system families such as face-centered cubic (fcc), body-centered cubic (bcc), hexagonal (hex), and body-centered tetragonal (bct) lattice types. In the following, we briefly present the three constitutive laws that have been used later in this thesis: a phenomenological crystal plasticity model, a phenomenological crystal plasticity model incorporating twinning deformation, and a dislocation-density-based crystal plasticity model.

2.3.1. Phenomenological model

The phenomenological model was first introduced by Hutchinson for fcc crystals [21]. This model uses a critical resolved shear stress, τ_0^α, as the state variable on each slip system α. This CP model has been modified later to be used for other crystal structures [27, 28]. In this crystal plasticity model, shear on each slip system occurs according to

$$\dot{\gamma}^\alpha = \dot{\gamma}_0 \left| \frac{\tau^\alpha}{\tau_0^\alpha} \right|^n \operatorname{sgn}(\tau^\alpha) \tag{2.12}$$

where τ^α is the resolved shear stress, τ_0^α is the slip resistance, $\dot{\gamma}_0$ is the reference shear rate, and n determines the strain rate sensitivity of slip. The influence of any other slip system, α', on the hardening behavior of a slip system α is given by:

$$\dot{\tau}_0^\alpha = \sum_{\alpha'=1}^{N_s} h_{\alpha\alpha'} \left| \dot{\gamma}^{\alpha'} \right| \tag{2.13}$$

where $h_{\alpha\alpha'}$ is the hardening matrix. It empirically captures the micromechanical interaction among different slip systems:

$$h_{\alpha\alpha'} = q_{\alpha\alpha'} \left[h_0 \left(1 - \frac{\tau_0^\alpha}{\tau_\infty} \right)^a \right] \tag{2.14}$$

where h_0, a, and τ_∞ are slip hardening parameters, which are assumed to be the same for all 12 slip systems of the $\{1\,1\,1\}\langle 1\,1\,0\rangle$ type in fcc crystals. $q_{\alpha\alpha'}$ is a measure for latent hardening, and its value is taken as 1.0 for coplanar slip systems α and α', and 1.4 otherwise. This renders the hardening behavior anisotropic.

2.3.2. Phenomenological model including deformation twinning

The phenomenological crystal plasticity model outlined above is extended to incorporate deformation twinning. Here, twinning is modeled in a pseudo-shear approach [29]. The plastic component of the material's internal state is parametrized in terms of a set of shear resistances τ_0 on $N_{\text{s+tw}} = N_\text{s} + N_\text{tw}$ slip and twin systems. During the deformation, the resistances on the slip systems $\alpha = 1,...,N_\text{s}$ evolve from their initial value τ_0 asymptotically to a system-dependent saturation value depending on the shear on different slip and twin systems as:

$$\dot{\tau}_0^\alpha = h_0^{\text{s-s}} \sum_{\alpha'=1}^{N_\text{s}} \left|\dot{\gamma}^{\alpha'}\right| \left|1 - \frac{\tau_0^{\alpha'}}{\tau_\infty^{\alpha'}}\right|^a \operatorname{sgn}\left(1 - \frac{\tau_0^{\alpha'}}{\tau_\infty^{\alpha'}}\right) h^{\alpha\alpha'} + \sum_{\beta'=1}^{N_\text{tw}} \dot{\gamma}^{\beta'} h^{\alpha\beta'} \tag{2.15}$$

where $h^{\alpha\alpha'}$ and $h^{\alpha\beta'}$ are the slip-slip [142,143] and slip-twin interaction matrices respectively, $h_0^{\text{s-s}}$ is a slip-hardening fitting parameter, and $\tau_\infty^{\alpha'}$ is the set of saturation stresses, respectively.

In a similar way, the resistances on the twin systems $\beta = 1,...,N_\text{tw}$ evolve as:

$$\dot{\tau}_0^\beta = h_0^{\text{tw-s}} \sum_{\alpha'=1}^{N_\text{s}} \left|\dot{\gamma}^{\alpha'}\right| h^{\beta\alpha'} + h_0^{\text{tw-tw}} \sum_{\beta'=1}^{N_\text{tw}} \dot{\gamma}^{\beta'} h^{\beta\beta'} \tag{2.16}$$

where $h_0^{\text{tw-s}}$ and $h_0^{\text{tw-tw}}$ are twinning-slip and twinning-twinning hardening fitting parameters, respectively.

Given a set of current slip resistances, shear on each slip system occurs according to

$$\dot{\gamma}^\alpha = (1 - f_\text{tw}^\text{tot})\, \dot{\gamma}_0^\text{s} \left|\frac{\tau^\alpha}{\tau_0^\alpha}\right|^{n_\text{s}} \operatorname{sgn}(\tau^\alpha), \tag{2.17}$$

and shear due to mechanical twinning occurs according to

$$\dot{\gamma} = (1 - f_\text{tw}^\text{tot})\, \dot{\gamma}_0^\text{tw} \left|\frac{\tau}{\tau_0}\right|^{n_\text{tw}} \mathscr{H}(\tau) \tag{2.18}$$

where $\mathscr{H}$ is the Heaviside or unit step function. f_tw^tot is the total twin volume fraction, and it is given by

$$f_\text{tw}^\text{tot} = \max\left(\sum_{\beta=1}^{N_\text{tw}} \underbrace{\gamma^\beta/\gamma_\text{char}}_{=:f_\text{tw}^\beta}, 1.0\right) \tag{2.19}$$

where γ_char is the characteristic shear due to mechanical twinning, the value of which depends on the twin system.

2.3.3. Dislocation-density-based model

The shear rate on the slip system α, $\dot{\gamma}^{\alpha}$, is related to the (average) velocity of mobile dislocations, v^{α}, by the Orowan equation [30]:

$$\dot{\gamma}^{\alpha} = \rho^{\alpha} b v^{\alpha}, \tag{2.20}$$

where ρ^{α} is the mobile dislocation density of the slip system α, and b is the length of the Burgers vector for slip.

The dislocation velocity is mainly controlled by the distance between the short-range barriers, barriers that can be overcome by thermal activation, and the average activation energy to overcome these barriers [31, 32]. The dislocation velocity is given as:

$$v^{\alpha} = \frac{l}{t_w + t_r}, \tag{2.21}$$

where l represents the average distance between the short-range barriers, t_w is the waiting time required to overcome a barrier, and t_r is the running time for a dislocation to move from one barrier to the next one. Based on the assumption that t_r is much smaller than t_w, the latter is often neglected. Following Kocks *et al.* [33], the waiting time is estimated as:

$$t_w = \omega_0^{-1} \exp\left(\frac{\Delta G}{k_B T}\right), \tag{2.22}$$

where ΔG is the average activation energy to overcome the short-range barriers, ω_0 is the attempt frequency, T is the absolute temperature, and k_B is Boltzmann's constant. Using Equations (2.21) and (2.22), the dislocation glide velocity is calculated as:

$$v^{\alpha} = v_0 \exp\left(\frac{-\Delta G}{k_B T}\right), \tag{2.23}$$

where $v_0 = l\omega_0$ is the dislocation glide velocity pre-factor. Inserting Equation (2.23) into Equation (2.20), gives the shear rate of slip system α as:

$$\dot{\gamma}^{\alpha} = \rho^{\alpha} b v_0 \exp\left(\frac{-\Delta G}{k_B T}\right) \tag{2.24}$$

The stress dependence of $\dot{\gamma}^{\alpha}$ is due to the stress dependence of ΔG. ΔG can be formulated as:

$$\Delta G = \Delta F \left\{1 - \left[\frac{\tau_T^{*\alpha}}{\tau_0^*}\right]^p\right\}^q, \tag{2.25}$$

where ΔF is the total short-range barrier energy, i.e. the activation energy for glide in the absence of any applied stresses. p and q define the shape of the short-range barrier. For most barrier profiles, $0 < p \leq 1$ and $1 \leq q \leq 2$ [33] is assumed. $\tau_T^{*\alpha}$ is the thermal component of the stress, which is calculated as:

$$\tau_T^{*\alpha} = \begin{cases} |\tau^{\alpha}| - \tau_{\mu}^{\alpha} & \text{for } |\tau^{\alpha}| > \tau_{\mu}^{\alpha} \\ 0 & \text{for } |\tau^{\alpha}| \leq \tau_{\mu}^{\alpha} \end{cases} \tag{2.26}$$

where τ^α is the total resolved shear stress on the slip system α, and τ_μ^α is the athermal component of the resolved shear stress which is given as:

$$\tau_\mu^\alpha = \mu b \left(\sum_{\alpha'=1}^{N_s} \xi_{\alpha\alpha'} (\rho^{\alpha'} + \rho_d^{\alpha'}) \right)^{1/2}, \tag{2.27}$$

where ρ_d^α is the dipole dislocation density of the slip system α, $\xi_{\alpha\alpha'}$ is the interaction coefficient matrix between the different slip systems α and α', and μ is the shear modulus.

τ_0^* is the barrier strength, i.e. the stress needed to overcome short-range barriers without thermal assistance, and is defined as:

$$\tau_0^* = (|\tau^\alpha| - \tau_\mu^\alpha) \qquad \text{at} \quad T = 0\ \text{K}, \tag{2.28}$$

Combining Equations (2.24) and (2.25), the shear rate for slip system α is

$$\dot{\gamma}^\alpha = \rho^\alpha b v_0 \exp\left(\frac{-\Delta F}{k_\text{B} T} \left\{ 1 - \left[\frac{\tau_T^{*\alpha}}{\tau_0^*} \right]^p \right\}^q \right) \text{sign}(\tau^\alpha), \tag{2.29}$$

Dislocation Density Evolution

The evolution rates of the mobile dislocation density and the dipole dislocation density are given respectively as:

$$\dot{\rho^\alpha} = \frac{|\dot{\gamma}^\alpha|}{b \Lambda^\alpha} - \frac{2 d_\text{dipole}^\alpha}{b} \rho^\alpha |\dot{\gamma}^\alpha| \tag{2.30}$$

and

$$\dot{\rho_d^\alpha} = \frac{2(d_\text{dipole}^\alpha - d_\text{anni}^\alpha)}{b} \rho^\alpha |\dot{\gamma}^\alpha| - \frac{2 d_\text{anni}^\alpha}{b} \rho_d^\alpha |\dot{\gamma}^\alpha| - \rho_d^\alpha \frac{4 v_\text{climb}}{d_\text{dipole}^\alpha - d_\text{anni}^\alpha} \tag{2.31}$$

The first term in Eq. (2.30) is the dislocation multiplication rate. The multiplication rate is controlled by the dislocation mean free path Λ^α, which is given as:

$$\frac{1}{\Lambda^\alpha} = \frac{1}{d_\text{g}} + \frac{1}{\lambda^\alpha} \tag{2.32}$$

where d_g is the average grain size, and

$$\frac{1}{\lambda^\alpha} = \frac{1}{C_\lambda} \left(\sum_{\alpha'=1}^{N_s} g_{\alpha\alpha'} (\rho^{\alpha'} + \rho_d^{\alpha'}) \right)^{1/2} \tag{2.33}$$

where C_λ is a coefficient determining the number of dislocations that a dislocation passes before it is trapped by forest dislocations. $g_{\alpha\alpha'}$ are coefficients that account for the interaction between dislocations on different slip systems [14].

The second term in Eq. (2.30) represents the decrease in the mobile dislocation density due to annihilation and dipole formation. Dislocation annihilation happens if, during a time increment $\mathrm{d}t$, there is a mobile dislocation with opposite sign within the area

$2d^{\alpha}_{\text{anni}} v^{\alpha} \mathrm{d}t$. d^{α}_{anni} is a critical distance for two mobile dislocations with opposite sign to annihilate. It is preferable to express d^{α}_{anni} as multiples of the Burgers vector length b:

$$d^{\alpha}_{\text{anni}} = C_{\text{anni}} b \tag{2.34}$$

where C_{anni} is the dislocation annihilation coefficient. The annihilation term in Eq. (2.30) is estimated based on the assumption of the same density of positive and negative dislocations.

The mobile dislocation density also decreases due to dipole formation. A dipole is formed when two mobile dislocations have a distance larger than d^{α}_{anni} but smaller than the critical distance for dipole formation, $d^{\alpha}_{\text{dipole}}$, see also the first and second terms in Eq. (2.31). The critical distance for dipole formation is given by

$$d^{\alpha}_{\text{dipole}} = \frac{\mu}{16\pi|\tau^{\alpha}|} b \tag{2.35}$$

The third term in Eq. (2.31) represents the decrease in the dipole dislocation density due to the thermal annihilation of edge dislocations by climb. Thermal annihilation plays a dominant role at high temperatures [34, 35]. The dislocation climb velocity, v_{climb}, is given as:

$$v_{\text{climb}} = \frac{3\mu D_0 \Omega}{2\pi k_{\text{B}} T} \left(\frac{1}{d^{\alpha}_{\text{dipole}} + d^{\alpha}_{\text{anni}}} \right) \exp(-\frac{Q_c}{k_{\text{B}} T}) \tag{2.36}$$

where D_0 is the self-diffusion coefficient, Ω is the activation volume for climb, and Q_c is the activation energy for climb.

2.4. Spectral method

The spectral method using Fast Fourier Transform (FFT) has been introduced in recent years as a promising alternative to the finite element method (FEM). This method was introduced initially to material mechanics by Moulinec and Suquet [36]. Since then, it has been improved and extended widely [37–40]. The spectral method has been successfully employed to model the mechanical behavior of polycrystalline materials [40–43]. The efficiency of the spectral method has been demonstrated systematically in comparison with FEM in [39, 44, 45]. The spectral solver implemented in DAMASK is based on the methods outlined in [39, 40].

References

[1] G. I. Taylor and C. F. Elam, *Bakerian Lecture: The distortion of an aluminium crystal during a tensile test,* Proceedings of the Royal Society of London. Series A, Containing Papers of a Mathematical and Physical Character **102**, 643 (1923).

[2] G. I. Taylor and C. F. Elam, *The plastic extension and fracture of aluminium crystals,* Proceedings of the Royal Society of London. Series A, Containing Papers of a Mathematical and Physical Character **108**, 28 (1925).

[3] G. I. Taylor, *Plastic strain in metals,* (1938).

[4] R. Hill, *Generalized constitutive relations for incremental deformation of metal crystals by multislip,* Journal of the Mechanics and Physics of Solids **14**, 95 (1966).

[5] J. Rice, *Inelastic constitutive relations for solids: An internal-variable theory and its application to metal plasticity,* Journal of the Mechanics and Physics of Solids **19**, 433 (1971).

[6] R. Hill and J. R. Rice, *Constitutive analysis of elastic-plastic crystals at arbitrary strain,* Journal of the Mechanics and Physics of Solids **20** (1972), 10.1016/0022-5096(72)90017-8.

[7] D. Peirce, R. Asaro, and A. Needleman, *An analysis of nonuniform and localized deformation in ductile single crystals,* Acta Metallurgica **30**, 1087 (1982).

[8] D. Peirce, R. Asaro, and A. Needleman, *Material rate dependence and localized deformation in crystalline solids,* Acta Metallurgica **31**, 1951 (1983).

[9] R. Becker, *Analysis of texture evolution in channel die compression—I. Effects of grain interaction,* Acta Metallurgica et Materialia **39**, 1211 (1991).

[10] A. Arsenlis and D. Parks, *Crystallographic aspects of geometrically-necessary and statistically-stored dislocation density,* Acta Materialia **47**, 1597 (1999).

[11] A. Arsenlis and D. Parks, *Modeling the evolution of crystallographic dislocation density in crystal plasticity,* Journal of the Mechanics and Physics of Solids **50**, 1979 (2002).

[12] L. Evers, D. Parks, W. Brekelmans, and M. Geers, *Crystal plasticity model with enhanced hardening by geometrically necessary dislocation accumulation,* Journal of the Mechanics and Physics of Solids **50**, 2403 (2002).

[13] K. Cheong and E. Busso, *Discrete dislocation density modelling of single phase FCC polycrystal aggregates,* Acta Materialia **52**, 5665 (2004).

[14] A. Ma and F. Roters, *A constitutive model for fcc single crystals based on dislocation densities and its application to uniaxial compression of aluminium single crystals,* Acta Materialia **52**, 3603 (2004).

[15] A. Ma, F. Roters, and D. Raabe, *A dislocation density based constitutive model for crystal plasticity FEM including geometrically necessary dislocations,* Acta Materialia **54**, 2169 (2006).

[16] H. Gao and Y. Huang, *Geometrically necessary dislocation and size-dependent plasticity,* Scripta Materialia **48**, 113 (2003).

[17] S. Wong, M. Madivala, U. Prahl, F. Roters, and D. Raabe, *Acta Materialia A crystal plasticity model for twinning- and transformation-induced plasticity,* Acta Materialia **118**, 140 (2016).

[18] D. Cereceda, M. Diehl, F. Roters, D. Raabe, J. Perlado, and J. Marian, *Unraveling the temperature dependence of the yield strength in single-crystal tungsten using atomistically-informed crystal plasticity calculations,* International Journal of Plasticity **78**, 242 (2016), arXiv:1506.02224 .

[19] R. Asaro and J. Rice, *Strain localization in ductile single crystals,* Journal of the Mechanics and Physics of Solids **25**, 309 (1977).

[20] E. Voce, *The relationship between stress and strain for homogeneous deformations,* Journal of the Institute of Metals **74**, 537 (1948).

[21] J. Hutchinson, *Bounds and Self-Consistent Estimates for Creep of Polycrystalline Materials,* Proceedings of the Royal Society A: Mathematical, Physical and Engineering Sciences **348**, 101 (1976).

[22] U. Kocks, *Laws for Work-Hardening and Low-Temperature Creep,* Journal of Engineering Materials and Technology **98**, 76 (1976).

[23] A. Arsenlis, D. Parks, R. Becker, and V. Bulatov, *On the evolution of crystallographic dislocation density in non-homogeneously deforming crystals,* Journal of the Mechanics and Physics of Solids **52**, 1213 (2004).

[24] L. Evers, W. Brekelmans, and M. Geers, *Scale dependent crystal plasticity framework with dislocation density and grain boundary effects,* International Journal of Solids and Structures **41**, 5209 (2004).

[25] L. Evers, W. Brekelmans, and M. Geers, *Non-local crystal plasticity model with intrinsic SSD and GND effects,* Journal of the Mechanics and Physics of Solids **52**, 2379 (2004).

[26] A. Ma, F. Roters, and D. Raabe, *On the consideration of interactions between dislocations and grain boundaries in crystal plasticity finite element modeling – Theory, experiments, and simulations,* Acta Materialia **54**, 2181 (2006).

[27] F. Roters, M. Diehl, P. Shanthraj, P. Eisenlohr, C. Reuber, S. Wong, T. Maiti, A. Ebrahimi, T. Hochrainer, H. Fabritius, S. Nikolov, M. Friák, N. Fujita, N. Grilli, K. Janssens, N. Jia, P. Kok, D. Ma, F. Meier, E. Werner, M. Stricker, D. Weygand, and D. Raabe, *DAMASK – The Düsseldorf Advanced Material Simulation Kit for modeling multi-physics crystal plasticity, thermal, and damage phenomena from the single crystal up to the component scale,* Computational Materials Science **158**, 420 (2019).

[28] F. Roters, P. Eisenlohr, L. Hantcherli, D. Tjahjanto, T. Bieler, and D. Raabe, *Overview of constitutive laws, kinematics, homogenization and multiscale methods in crystal plasticity finite-element modeling: Theory, experiments, applications,* Acta Materialia **58**, 1152 (2010).

[29] S. Kalidindi, *Incorporation of deformation twinning in crystal plasticity models,* Journal of the Mechanics and Physics of Solids **46**, 267 (1998).

[30] E. Orowan, *Zur Kristallplastizität. III - Über den Mechanismus des Gleitvorganges,* Zeitschrift für Physik **89**, 634 (1934).

[31] S. Nemat-Nasser, T. Okinaka, and L. Ni, *A physically-based constitutive model for BCC crystals with application to polycrystalline tantalum,* Journal of the Mechanics and Physics of Solids **46**, 1009 (1998).

[32] A. Amirkhizi and S. Nemat-Nasser, *A framework for numerical integration of crystal elasto-plastic constitutive equations compatible with explicit finite element codes,* International Journal of Plasticity **23**, 1918 (2007).

[33] U. Kocks, A. Argon, and M. Ashby, *Thermodynamics and kinetics of slip* (Pergamon Press, 1975).

[34] W. Nix, J. Gibeling, and D. Hughes, *Time-dependent deformation of metals,* Metallurgical Transactions A **16**, 2215 (1985).

[35] H. Zhang, X. Dong, D. Du, and Q. Wang, *A unified physically based crystal plasticity model for FCC metals over a wide range of temperatures and strain rates,* Materials Science and Engineering A **564**, 431 (2013).

[36] H. Moulinec and P. Suquet, *A fast numerical method for computing the linear and nonlinear mechanical properties of composites,* Comptes rendus de l'Académie des sciences. Série II, Mécanique, physique, chimie, astronomie **318** (1994).

[37] R. A. Lebensohn, *N-site modeling of a 3D viscoplastic polycrystal using Fast Fourier Transform,* Acta Materialia **49** (2001), 10.1016/S1359-6454(01)00172-0.

[38] R. A. Lebensohn, A. K. Kanjarla, and P. Eisenlohr, *An elasto-viscoplastic formulation based on fast Fourier transforms for the prediction of micromechanical fields in polycrystalline materials,* International Journal of Plasticity **32-33** (2012), 10.1016/j.ijplas.2011.12.005.

[39] P. Eisenlohr, M. Diehl, R. Lebensohn, and F. Roters, *A spectral method solution to crystal elasto-viscoplasticity at finite strains,* International Journal of Plasticity **46**, 37 (2013).

[40] P. Shanthraj, P. Eisenlohr, M. Diehl, and F. Roters, *Numerically robust spectral methods for crystal plasticity simulations of heterogeneous materials,* International Journal of Plasticity **66**, 31 (2015).

[41] F. Grennerat, M. Montagnat, O. Castelnau, P. Vacher, H. Moulinec, P. Suquet, and P. Duval, *Experimental characterization of the intragranular strain field in columnar ice during transient creep,* Acta Materialia **60** (2012), 10.1016/j.actamat.2012.03.025.

[42] R. A. Lebensohn, R. Brenner, O. Castelnau, and A. D. Rollett, *Orientation image-based micromechanical modelling of subgrain texture evolution in polycrystalline copper,* Acta Materialia **56** (2008), 10.1016/j.actamat.2008.04.016.

[43] R. A. Lebensohn, J. P. Escobedo, E. K. Cerreta, D. Dennis-Koller, C. A. Bronkhorst, and J. F. Bingert, *Modeling void growth in polycrystalline materials,* Acta Materialia **61** (2013), 10.1016/j.actamat.2013.08.004.

[44] A. Prakash and R. A. Lebensohn, *Simulation of micromechanical behavior of polycrystals: Finite elements versus fast Fourier transforms,* Modelling and Simulation in Materials Science and Engineering **17** (2009), 10.1088/0965-0393/17/6/064010.

[45] B. Liu, D. Raabe, F. Roters, P. Eisenlohr, and R. A. Lebensohn, *Comparison of finite element and fast Fourier transform crystal plasticity solvers for texture prediction,* Modelling and Simulation in Materials Science and Engineering **18** (2010), 10.1088/0965-0393/18/8/085005.

3

MATERIAL PARAMETERS IDENTIFICATION: METHODOLOGY

Abstract

A severe obstacle for the routine use of crystal plasticity models is the effort associated with determining their constitutive parameters. Obtaining these parameters usually requires time-consuming micromechanical tests that allow probing of individual grains. In this chapter, a novel, computationally efficient, and fully automated approach is introduced which allows the identification of constitutive parameters from macroscopic tests. The approach presented here uses the response surface methodology together with a genetic algorithm to determine an optimal set of parameters. It is especially suited for complex models with a large number of parameters. The proposed approach also helps to develop a quantitative and thorough understanding of the relative influence of the different constitutive parameters and their interactions. Such general insights into parameter relations in complex models can be used to improve constitutive laws and reduce redundancy in parameter sets. The merits of the methodology are demonstrated on the examples of a dislocation-density-based crystal plasticity model for bcc steel, a phenomenological crystal plasticity model for fcc copper, and a phenomenological crystal plasticity model incorporating twinning deformation for hcp magnesium. The approach proposed is, however, model-independent and can be also used to identify parameters of, for instance, fatigue, creep and damage models. The method has been implemented into the Düsseldorf Advanced Material Simulation Kit (DAMASK) and is available as free and open-source software.

Parts of this chapter have been published in Sedighiani *et al.* [1].

3.1. Introduction

Crystal plasticity (CP) models cast the extensive knowledge gained from experimental and theoretical studies of single crystal deformation and dislocation physics into anisotropic elastic-plastic mean-field continuum approximations applicable to a wide range of scenarios from small-scale micromechanical up to engineering time and length scales [2]. These models provide well-validated tools for predicting the evolution of crystallographic texture, dislocation density, stored mechanical energy, damage evolution, deformation-driven athermal transformations (such as twinning and martensite formation), in-grain lattice curvature as well as the associated mechanical behavior of polycrystalline materials subjected to coupled thermo-mechanical loads.

The constitutive laws in a CP model relate the kinetics of the deformation to the physics of the material behavior and depend on a number of adjustable parameters, yet, obeying physics-based upper and lower bounds. During the last few decades, various constitutive inelastic flow laws have been developed, e.g. empirical visco-plastic models [3, 4], phenomenological models [5–10], and physics-based models [11–23].

CP laws that are able to accurately predict the deformation behavior over a wide range of loading conditions are fairly complex and comprehensive. This complexity is partly due to the introduction of physics-based parameters, e.g. different classes of dislocation populations [24], non-Schmid stress projections [23], and precipitate morphology [2] to accurately describe the dislocation behavior and partly due to the introduction of multiple deformation mechanisms that interact and compete with dislocation slip such as martensite formation [25, 26], shear band formation [27, 28], and mechanical twinning [22, 29–33]. An unwanted side-effect of such advanced CP models is the increased number of adjustable constitutive parameters.

The capability of a constitutive model to accurately predict the deformation behavior of a specific material strongly depends on the values selected for the adjustable material parameters. Therefore, an important prerequisite for exploiting the full predictive capabilities of physics-based models lies in the identification of an adequate set of material parameters within well-based physical bounds. Theoretically, most of the constitutive parameters for a CP model can be measured directly from single crystal, single slip experiments [34, 35]. Practically, this is rarely done as typical engineering materials are often available only as polycrystals. One approach to determine the mechanical behavior of individual grains in polycrystalline samples is the use of nanoindentation experiments to probe individual grains [36–38]. A different approach was presented by Bertin *et al.* [34], who used a coupled experimental-numerical procedure to obtain CP parameters from the micro-mechanical behavior of a micro-beam made of two grains cut out of a polycrystalline sample. Because of the substantial experimental efforts associated with such "virtual single crystal" experiments, it is instead preferable to identify CP constitutive parameters from macroscopic stress–strain data obtained from standard tensile or compression testing. Such procedures would also catalyze wider use of advanced CP models in the industrial practice where access to small scale experiments for parameter identification is limited and/or too costly. In that context Herrera-Solaz *et al.* [39] developed an inverse optimization method to determine the single crystal parameters from experimental results of the mechanical behavior of polycrystals. Mandal *et al.* [40] used a canonical

correlation analysis to understand the effect of constitutive model parameters on the flow stress behavior for the case of a mechanical threshold stress model [41].

Identification of constitutive parameters requires to solve an inverse problem, i.e. adjusting material parameters until the simulation results match the experimental or reference data. For simple models with a small number of parameters, it is often possible to calibrate the parameters simply using a trial-and-error or a regression approach. However, this is impracticable for complex constitutive models with a large number of material parameters and non-linear interactions between them. In many cases, identifying the right set of parameters is even a limiting factor in introducing new micro-structural parameters or additional physics-based deformation mechanisms into CP models simply because experimental validation is unfeasible or the selection of the values for the material parameters involved is too arbitrary. The same applies to the introduction of new materials. Nowadays, in the advanced manufacturing practice, it is required that any material that is used in demanding parts and products must be amenable to established performance, manufacturing and crash simulations. Such a seamless knowledge transfer between basic materials science (in terms of the underlying deformation mechanisms and the microstructure evolution) and applied engineering (in terms of the targeted design and loading scenarios) marks an essential step in the industrial digitalization workflow. In other words, in the context of the rapidly progressing industry digitalization, any advanced product and process requires its digital twin, with as much materials physics input as required to arrive at reliable engineering predictions. Thus, when new or improved engineering materials are considered for products and processes they must be mapped first into their digital counterparts prior to feeding them into downstream manufacturing and releasing them into service. Therefore, developing an appropriate optimization methodology to determine the constitutive parameters is crucial for both, using existing and developing new constitutive laws.

Gradient-based optimization methods, such as the steepest descent method and Newton's methods, have been frequently utilized for this purpose, e.g. [39, 42–45]. Mahnken and Stein [42] and Saleeb *et al.* [43] used a gradient-based method to identify the material parameters for viscoplastic material models. Yang and Elgamal [44] employed a gradient-based method to determine the material parameters for a multi-surface-plasticity sand model. However, one of the main drawbacks of the gradient-based methods is their sensitivity to the choice of the initial guess [45]. In other words, the converged solution and the convergence rate strongly dependent on the starting point. This is especially problematic for complex constitutive laws with strong nonlinear response, such as typically encountered in the micromechanics of complex engineering materials with multiple deformation mechanisms. It is worth mentioning that due to the uncertainty and noise in the experimental data, there might be uncertainty or noise in the magnitude of the objective functions too. This also deteriorates the convergence behavior of gradient based methods. In summary, their limited robustness calls for alternatives to gradient-based methods for the identification of material parameters.

Direct search methods [46], such as genetic algorithms (GA), are a promising class of algorithms that do not have the mentioned drawbacks of gradient-based methods.

Unlike gradient-based methods, direct search methods do not require any information about the gradient of the objective function. In these methods, first a set of potential solutions for the optimization problem is randomly generated. Then, the next generation of potential solutions and the possible solutions for the optimization problem are determined only by the evaluation of the objective functions at the pre-existing points. Direct search methods are generally proven to be robust and reliable [45, 47]. However, the robustness is achieved at the cost of efficiency [48].

For direct search methods, a substantial number of evaluations of the objective functions to determine the quality of the potential solutions is needed. Therefore, the efficiency of these methods depends directly on the computational costs of the evaluated functions. In the case of fitting constitutive parameters, each evaluation requires to perform at least one if not several simulations, extract the outputs, and compare them with the experimental data. The computational costs of CP simulations are in general too high to repeat this procedure frequently. Therefore, despite the robustness of these optimization methods, they are inefficient in determining the material parameters for complex and computationally expensive CP laws. Direct search methods have been, however, used for numerically less demanding models, cf. [49].

For the routine use of genetic algorithms to identify the parameters of complex material laws, the computational costs of evaluating the constitutive response need to be reduced. Therefore, we introduce here an approach to identify CP constitutive parameters efficiently by approximating the constitutive response with the help of the response surface methodology (RSM) [50, 51]. More precisely, the stress response at different loading conditions is approximated using relationships defined between the adjustable material parameters and the stress response. This allows to perform more than 10^6 evaluations of the constitutive response in approximately the same time as needed for one CP simulation with a fairly complex dislocation-density-based constitutive model used in this study. It should be noted that in this study a Fast Fourier Transform (FFT) based spectral method is used to solve the partial differential equations for static equilibrium, which is a fast and time efficient alternative to the finite element method, see Section 2.4.

The usage of the RSM comes at the cost of performing a series of simulations using the original CP model to build an off-line database. The computational cost to build the database depends on the number of parameters used in the optimization. However, this number is still significantly lower than the number of simulations needed for a GA. The methodology developed in this study is demonstrated by determining the constitutive parameters of three widely used crystal plasticity models as explained in Chapter 2: a phenomenological model (see Section 2.3.1), a dislocation-density-based model (see Section 2.3.3) and a phenomenological model incorporating deformation twinning (see Section 2.3.2), all implemented in the DAMASK package [52].

3.2. Methodology

In the following, a novel approach is introduced to determine constitutive parameters of CP laws from macroscopic stress–strain curves using a genetic algorithm (GA, see Section 3.2.1). For identifying a valid set of material parameters, stress–strain curves obtained under different loading conditions, such as strain rate, temperature, and

loading direction, are required. When using a GA, for each loading condition hundreds of thousands of CP simulations are required. Since this is unfeasible, the response surface methodology (RSM, see Section 3.2.2) is employed to replace the CP simulations required to calculate a stress–strain curve.

3.2.1. Optimization: Genetic algorithm

Genetic algorithms are powerful optimization methods that usually converge to a global minimum of the objective function rather than getting stuck in a local minimum [53]. They are based on a randomized search technique which is motivated by the principles of natural selection and evolution processes [53, 54]. The terminology of GAs is therefore related to genetics, i.e.:

- A *gene* is an adjustable parameter of the objective function, i.e. in the current case a constitutive parameter.
- A *chromosome* is a full set of genes that are required to evaluate the objective function, i.e. in the current case a complete set of adjustable constitutive parameters for a specific CP law.
- A *population* is a set of chromosomes which are processed and compared to each other, i.e. translating in the current case to a collection of parameter sets for the CP law.

A GA is composed of different steps and processes. In the first step, a number of chromosomes are randomly selected to produce the initial population. In the next step, the chromosomes are manipulated to generate a new generation. This step involves the evaluation and selection of chromosomes inspired by biological processes such as crossover and mutation. The details of these processes are outlined in the following, and Fig. 3.1 summarizes the employed algorithm graphically.

3.2.1.1. Initial population

The first step in the GA is to define an initial population. The initial population of N_p chromosomes is randomly generated, where N_p is the size of the initial population. A chromosome, $\boldsymbol{\Theta}$, is made up of a number of genes, Θ_i,

$$\boldsymbol{\Theta} = (\Theta_1, \Theta_2, ..., \Theta_k)$$

The length of a chromosome, k, is equal to the number of adjustable (unknown) parameters in the optimization procedure. Each gene in the initial population is selected randomly from numbers spaced evenly in its specified range. The range for each parameter is selected based on known or reasonable physical bounds of the parameter. If the range of a parameter is larger than one order of magnitude, the parameter value is selected from numbers spaced evenly on a logarithmic scale.

It should be mentioned that defining ranges for the optimization is an advantage of the presented approach. All gradient-based optimization algorithms, such as the steepest descent algorithm, require an initial guess to be defined before starting the optimization process. The proper determination of such an initial guess is difficult and

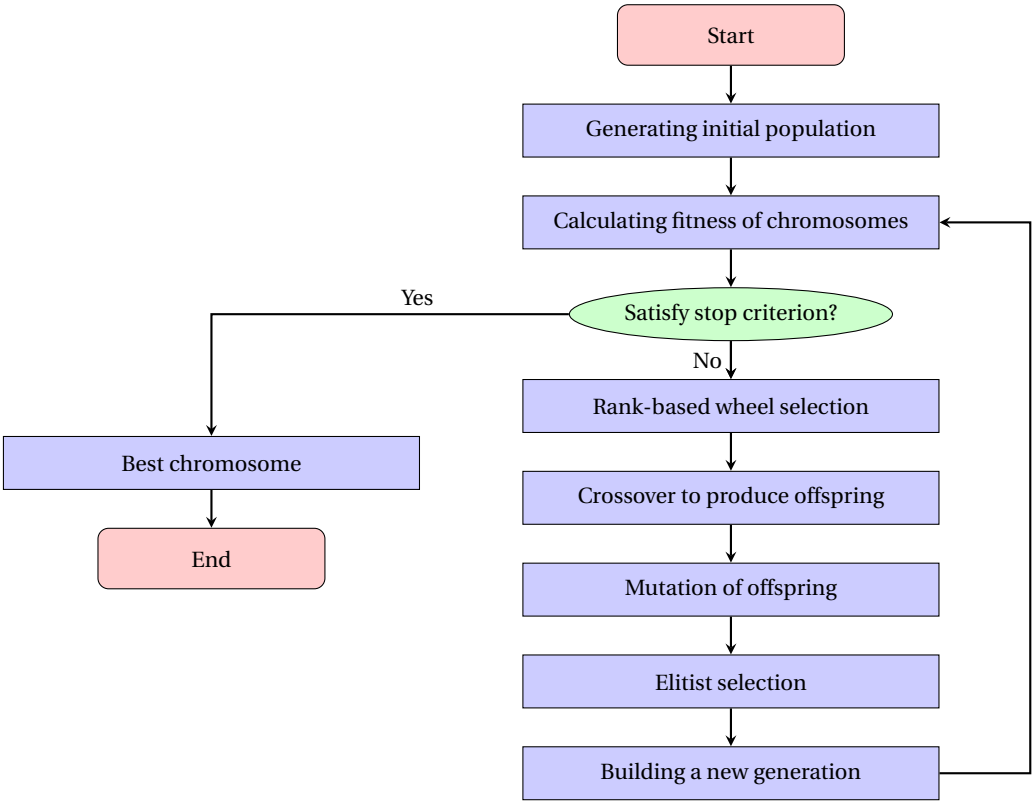

Fig. 3.1: Flowchart of the genetic algorithm: The algorithm starts from an initial, randomly generated population. Then, in an iterative process, the population is evolved toward better solutions. In each generation, the fitness of the chromosomes is evaluated, and the chromosomes with better fitness are selected to produce a new generation using biological processes such as crossover and mutation. The algorithm terminates when the stop criterion is satisfied.

vital since the optimization result is highly sensitive to this initial choice. Usually, the optimal solutions are located in very close vicinity of the initial guess. Although these algorithms are theoretically not constrained with ranges, in practice, they only search between two local maxima. In the presented methodology, a range for the parameters needs to be presented instead of the specific initial guess. Typically, selecting a range is more convenient than selecting a strictly defined initial guess. It should be noted that the optimization result is not sensitive to the selected ranges as long as the optimal solution is located inside of these ranges.

3.2.1.2. Objective functions and fitness

For chromosomes in the population a fitness value is determined which signifies its capability of reproducing the target response, i.e. the set of all measured stress–strain curves. To this end, one or more objective functions are introduced to measure the

agreement between target function and the result obtained with a specific chromosome.

Objective functions

The first objective function used here is the difference between the experimentally determined stress and the simulated stress at selected strain values. In this study, the commonly used L_2-norm, also called the Euclidean norm [55], is used to measure the distance, d_1, between both curves under loading condition m:

$$d_1^m(\boldsymbol{\Theta}, T, \dot{\varepsilon}) = \sqrt{\frac{\sum_{i=0}^{N} (\hat{\sigma}_i(\boldsymbol{\Theta}, T, \dot{\varepsilon}) - \sigma_i(T, \dot{\varepsilon}))^2}{\sum_{i=0}^{N} \sigma_i(T, \dot{\varepsilon})^2}} \tag{3.1}$$

where σ_i is the experimentally measured stress at strain level ε_i, and N is the total number of all strain levels considered. $\hat{\sigma}_i$ is the predicted stress response for the set of parameters $\boldsymbol{\Theta}$.

The distance function defined in Eq. (3.1) is used frequently as the sole objective function for optimization, e.g. [39, 56, 57]. However, this objective function captures only the absolute distance between two curves and fails in capturing the sign of deviation. In other words, a positive or negative distance between the simulation result and the experimental data cannot be distinguished using Eq. (3.1). Therefore, response stress–strain curves which are lower than, higher than, or crossing the experimental data may result in the same value for the error. To penalize a difference in the slope of the curves, a second type of objective function, d_2, is defined which measures the difference of the average slope between the response and experimental stress.

$$d_2^m(\boldsymbol{\Theta}, T, \dot{\varepsilon}) = \left| \frac{(\hat{\sigma}_N(\boldsymbol{\Theta}, T, \dot{\varepsilon}) - \hat{\sigma}_0(\boldsymbol{\Theta}, T, \dot{\varepsilon})) - (\sigma_N(T, \dot{\varepsilon}) - \sigma_0(T, \dot{\varepsilon}))}{\sigma_N(T, \dot{\varepsilon}) - \sigma_0(T, \dot{\varepsilon})} \right| \tag{3.2}$$

where indexes 0 and N represent the yield strain and the maximum evaluated strain, respectively. This objective function can give zero error for a stress–strain curve parallel to the experimental data and becomes non-zero for a crossing or non-parallel stress–strain curve. This value is added to the fitness value as a penalty for the deviation from the experimentally measured average hardening.

Both objective functions mentioned above cannot capture explicitly the temperature and strain rate sensitivity. In other words, they fail to capture the directional sensitivity of the stress–strain curves to a change in temperature or strain rate. Therefore, two additional types of objective functions are defined in this study, one evaluating the strain rate sensitivity:

$$d_3^m(\boldsymbol{\Theta}, T, \dot{\varepsilon}_k, \dot{\varepsilon}_l) = \sqrt{\frac{\sum_{i=0}^{N} [(\hat{\sigma}_i(\boldsymbol{\Theta}, T, \dot{\varepsilon}_l) - \hat{\sigma}_i(\boldsymbol{\Theta}, T, \dot{\varepsilon}_k)) - (\sigma_i(T, \dot{\varepsilon}_l) - \sigma_i(T, \dot{\varepsilon}_k))]^2}{\sum_{i=0}^{N} (\sigma_i(T, \dot{\varepsilon}_l) - \sigma_i(T, \dot{\varepsilon}_k))^2}} \tag{3.3}$$

and one evaluating the temperature sensitivity:

$$d_4^m(\boldsymbol{\Theta}, T_l, T_k, \dot{\varepsilon}) = \sqrt{\frac{\sum_{i=0}^{N} [(\hat{\sigma}_i(\boldsymbol{\Theta}, T_k, \dot{\varepsilon}) - \hat{\sigma}_i(\boldsymbol{\Theta}, T_l, \dot{\varepsilon})) - (\sigma_i(T_k, \dot{\varepsilon}) - \sigma_i(T_l, \dot{\varepsilon}))]^2}{\sum_{i=0}^{N} (\sigma_i(T_k, \dot{\varepsilon}) - \sigma_i(T_l, \dot{\varepsilon}))^2}} \tag{3.4}$$

where $(\dot{\varepsilon}_k, \dot{\varepsilon}_l)$ and (T_l, T_k) represent different combinations of strain rates and temperatures, respectively.

Fitness

The objective functions defined in Eq. (3.1) to Eq. (3.4) estimate the distance between the simulated stress and experimental data for one loading condition. The total normalized distance under all M considered loading conditions for each type of objective function is calculated as:

$$D_j(\boldsymbol{\Theta}) = \sum_{m=1}^{M} d_j^m(\boldsymbol{\Theta}, T, \dot{\varepsilon}), \qquad j = 1, 2, 3, 4 \tag{3.5}$$

Finally the fitness of a chromosome is calculated by combining the four types of objective functions as:

$$F(\boldsymbol{\Theta}) = \sum_{j=1}^{4} w_j D_j(\boldsymbol{\Theta}) \tag{3.6}$$

where w_j are weights for each type of objective functions.

3.2.1.3. Genetic algorithm processes

Selection

A chromosome with a better fitness value has a higher chance of being a parent which mates and recombines to create offspring for the next generation. In this study, the rank-based wheel approach [58] is used for selecting pairs of parents. According to this method, the chromosomes are first ranked based on their fitness values. Then, each chromosome gets a weight solely based on its relative ranking in the population, e.g. N_p (number of chromosomes in the population) for the best chromosome and one for the worse chromosome.

Crossover

Crossover is an operation in which a pair of chromosomes swap their genes to generate a new pair of offspring. Several approaches for crossover have been proposed [54, 59]. For this study, the single-point and reduced surrogate methods [59] are considered. In the single-point crossover, the chromosomes of both parents are divided into two parts. The division is applied at the same position for both parents which is selected randomly under the condition that each part contains at least one gene. The genes up to the division point for each parent are then combined with the remaining genes of the other parent to generate a pair of offspring. In the reduced surrogate crossover, single-point crossover is used for recombination of the genes from parents. However, in this method,

the division is limited to those positions which result in offsprings with different genes. If the parents are similar, and there are no possible crossover points, no action is taken. This crossover method reduces unwanted recombination in case parents have similar genes, and it prevents generating duplicate offspring. The effect of the crossover method on the robustness and efficiency of the GA is discussed in Section 3.3.2.7.

Mutation

Mutation randomly changes one or more genes in a chromosome with a probability equal to the mutation rate [60]. Mutation is used to maintain diversity during evolution of the population. Diversity helps to avoid local minima by preventing the generations from becoming very similar. High mutation rates render a GA into a random search algorithm. In this study, the mutation only changes one gene. In addition, the mutation rate is 0.01, which means the mutation changes approximately 1 out of 100 chromosomes.

Elitist selection

By means of elitist selection a small proportion of the best chromosomes from the current generation is preserved and passed without any changes to the next generation. Elitist selection increases the performance as it ensures that the achievement is not lost from one generation to the next. The elite chromosomes are not allowed to be crossed over or subjected to mutation. However, the elite chromosomes are eligible for selection as parents.

For this purpose, the population is first ranked according to the fitness value calculated using Eq. (3.6). Then, the best chromosomes are passed to the next generation. It is expected that the effect of the parameters is different for the different types of objective functions defined in Eq. (3.1) to Eq. (3.4). This implies that a chromosome with a high fitness value for one type of objective functions may contain a few high-quality genes. Therefore, the elitist selection is performed independently for each type of objective function using Eq. (3.5). In this study, the elitist operation preserves 1% of the chromosomes for each type of objective functions.

3.2.1.4. New generation

Finally, a new generation consists of chromosomes obtained by the following processes:

- Elite chromosomes ($\leq 5\%$)
- Offspring with mutation ($\approx 1\%$)
- Offspring without mutation (rest)

3.2.1.5. Stop criterion

The genetic algorithm stops when one of the following conditions is met:

- A large number of the chromosomes in a generation become equal (70% of the population in this study).
- There has been no improvement in the best solution for a number of generations (50 generations in this study).

- The maximal number of generations is reached (500 generations in this study).

Solutions are accepted only if one of the first two criteria are responsible for the termination of the GA. Terminating the GA by the third stop criterion shows that the optimization process has been unsuccessful, and the result from the optimization procedure is not acceptable.

3.2.2. Response surface methodology

A straightforward and simple way of estimating the fitness of a chromosome is to perform a simulation and compare the outputs with experimental results with the help of above defined objective functions. However, a GA involves a substantial number of evaluations. This makes the use of GAs time-consuming, if not even impossible when the evaluation function, i.e. here the CP simulation, is computationally expensive. Here, a cost-effective approximate evaluation function based on the response surface methodology (RSM) is used to evaluate the fitness of the chromosomes.

The response surface methodology is a statistical technique that gives the relationship between explanatory variables with one or more response variables [50, 51]. Based on this approach, a polynomial is fitted to approximate the response variables. This method is especially useful when the effects of an explanatory variable are dependent on the level of the other explanatory variables. In this study, the response variable is the stress and the explanatory variables are the adjustable constitutive parameters. Applied strain, temperature, and strain rate are independent (conditional) input variables.

The response surface methodology requires a series of designed experiments in the domain being studied to estimate the response. A factorial experiment or a fractional factorial design can be used to estimate a first-degree polynomial model [50, 51]. To build up a second-order (quadratic) polynomial model, which considers curvature in the response, more complex experimental designs such as three-level factorial, Box-Behnken, central composite, or Doehlert designs are needed [50, 51]. Design of experiments (DOE) helps to select a set of experiments (i.e. CP simulations) to efficiently fit the response surface.

3.2.2.1. Design of experiments

Design of experiments (DOE) is an efficient and systematic procedure of planning and conducting a set of experiments to analyze and interpret a group of explanatory (input) variables (factors) that controls a desired response (output variable). The term experiment refers to this systematic procedure of conducting the experiments. This method allows to determine the effect and interaction effect of different explanatory variables on the response variable, and what the target level of these explanatory variables should be to achieve a desired response. DOE involves selecting the variables, a range for each variable, and a design strategy.

Factorial design

There are different approaches available for a multi-factor DOE. One approach is called a full factorial experiment, in which all possible combinations of the variables are considered for all variable levels.

Two-level factorial design In a two-level factorial experimental design, each variable has two levels. The variables are normalized as:

$$\theta_i = \frac{\Theta_i - \Theta_i^m}{\Theta_i^s} \tag{3.7}$$

where θ_i is the normalized value for variable (i.e. gene) Θ_i. Θ_i^m and Θ_i^s are respectively the center point and the span of the range for Θ_i. Hence, -1 and 1 correspond to the lower and upper limits of an explanatory variable, respectively.

For a two-level full factorial design, the number of runs is 2^k, where k is the number of variables. Here, k corresponds to the length of the chromosomes in the GA optimization procedure. Fractional factorial design can be used to prevent the number of runs from becoming too large. The number of runs for a fractional factorial design is $2^{k-k'}$, where k' describes the size of the fraction of the full factorial used. Since the two-level factorial design is efficient and economical, it has been extensively used. However, it is only possible to build up a first-degree polynomial model when using a two-level factorial design.

Central composite design In order to include the curvature of the response surface, at least a three-level factorial design is needed. However, a three-level full factorial design requires 3^k experiments, making it unfeasible even for a moderate number of variables. Therefore, the three-level factorial design has been rarely used. Alternatively, the central composite design (CCD) [61], also known as Box-Wilson Central Composite Design, can be used to include curvature without needing to use the full three-level factorial design. A CCD consists of a two-level factorial or fractional factorial design with center points and a group of star points. The star points are defined at a distance of η from the center point, and they allow considering curvature in the response function. In this study, the face-centered (CCF) composite design is used in which the star points are at the center of each face of the factorial space, i.e. $\eta = 1$. Using this method the physical lower and upper limits are maintained. The number of the runs required for a central composite design is $k^2 + 2k + c_p$, where c_p is the number of center points.

3.2.2.2. Polynomial approximation

A polynomial is fitted to the values obtained at the support points to describe the response variable, here stress, as a function of the explanatory variables, here the adjustable material parameters. In this study, a second-order polynomial including up to four-way interaction effects is used:

$$\hat{\sigma} = \beta_0 + \sum_{i=1}^{k} \beta_i \theta_i + \sum_{i=1}^{k} \beta_{ii} \theta_i^2 + \sum_{1 \le i < j}^{k} \beta_{ij} \theta_i \theta_j + \sum_{1 \le i < j < l}^{k} \beta_{ijl} \theta_i \theta_j \theta_l + \sum_{1 \le i < j < l < m}^{k} \beta_{ijlm} \theta_i \theta_j \theta_l \theta_m + e \quad i \neq j \neq l \tag{3.8}$$

where θ_i and $\hat{\sigma}$ are the explanatory variables and response variables, respectively. e represents the error, the difference between the observed results and the predicted

values. β_0 is the constant effect. β_i is the main effect of parameter θ_i which determines the significance of the variable. β_{ij}, β_{ijl} and β_{ijlm} are two-way, three-way, and four-way interaction effects. β_{ii} are curvilinear (or quadratic) effects which represent the curvature in the response. The main effects and the interaction effects can be estimated from a two-level design. β_{ii} can be calculated only when a three- (or higher) level design such as CCD is used. Eq. (3.8) can be rewritten in matrix notation as:

$$\mathbf{Y}_{\hat{\sigma}} = \mathbf{X}_{\theta}\boldsymbol{\beta} + \mathbf{E} \tag{3.9}$$

where $\mathbf{Y}_{\hat{\sigma}}$ is the response matrix, $\mathbf{X}_{\theta}$ is the full experimental design matrix, $\boldsymbol{\beta}$ is the full parameter matrix, and $\mathbf{E}$ is the error matrix. $\boldsymbol{\beta}$ can be approximated using the method of least squares [51], which is a multiple regression technique to minimize the residual:

$$\boldsymbol{\beta} = (\mathbf{X}_{\theta}^{T}\mathbf{X}_{\theta})^{-1}(\mathbf{X}_{\theta}^{T}\mathbf{Y}_{\hat{\sigma}}) \tag{3.10}$$

It should be noted that the predicted polynomial is not a physical model, it is only a statistical approximation developed using regression analysis to predict the physical response.

The response stress $\hat{\sigma}$ is impacted by both explanatory variables and independent variables. The explanatory variables, θ, are the unknown constitutive material parameters which are needed to be identified. The independent variables are those variables at which a CP model should be able to predict the deformation behavior correctly. In other words, for a properly identified set of parameters $\boldsymbol{\Theta}$, a CP model should predict the deformation behavior correctly for all loading conditions considered. Then, the response stress for different loading conditions can be approximated as:

$$\hat{\sigma}_i(\boldsymbol{\Theta}, T, \dot{\varepsilon}) = \boldsymbol{\theta}\,\boldsymbol{\beta}_i(T, \dot{\varepsilon}) \tag{3.11}$$

where $\hat{\sigma}_i(\boldsymbol{\Theta}, T, \dot{\varepsilon})$ is the approximate response stress for explanatory variables $\boldsymbol{\Theta}$ at a discrete strain point i, temperature T, and strain rate $\dot{\varepsilon}$. $\boldsymbol{\beta}_i(T, \dot{\varepsilon})$ is the effects vector predicted at discrete strain point i, temperature T, and strain rate $\dot{\varepsilon}$. $\boldsymbol{\theta}$ is the full normalized experimental design vector. In this study, the independent variables are the applied strains, temperatures, and strain rates.

3.2.3. Approximate evaluation function correction

The polynomial used to predict the response stress is an approximation for the CP simulation, and it includes some statistical error. To compensate for this error and to improve the results, CP simulations are performed at the best solution determined through the use of GA and RSM. In the next step, when using the CP simulations, the constant effect in the off-line database is corrected such that the RSM matches the simulation result for this set of parameters. The updated database is then used to obtain the next best solution. This process is continued until the results are converged and no more improvement is observed.

3.2.4. Sensitivity analysis

As mentioned earlier, the number of experimental runs grows exponentially with an increase in the number of variables. A CP model, especially a physics-based one, has a

large number of variables. However, depending on the domain of interest (the applied strain, deformation temperature, and strain rate), some parameters may have a negligible effect on the response stress. Therefore, considering these ineffective parameters in the RSM is not efficient and practical. One way to increase the time efficiency of the methodology is the identification of these ineffective parameters using a sensitivity study. A sensitivity study is a technique to efficiently investigate how an explanatory variable impacts the response variable in the domain of interest. For conducting such a study, a low-resolution fractional factorial design is used, for more information see Section 3.2.2.1. The statistical significance of each parameter can be evaluated using the analysis of variance (ANOVA) [62]. The results from the sensitivity study serve as a tool to select proper constitutive parameters in the optimization procedure. Here it is used as an optional step before the actual optimization procedure.

3.2.5. Summary

The methodology presented in this section is summarized in the flowchart presented in Fig. 3.2.

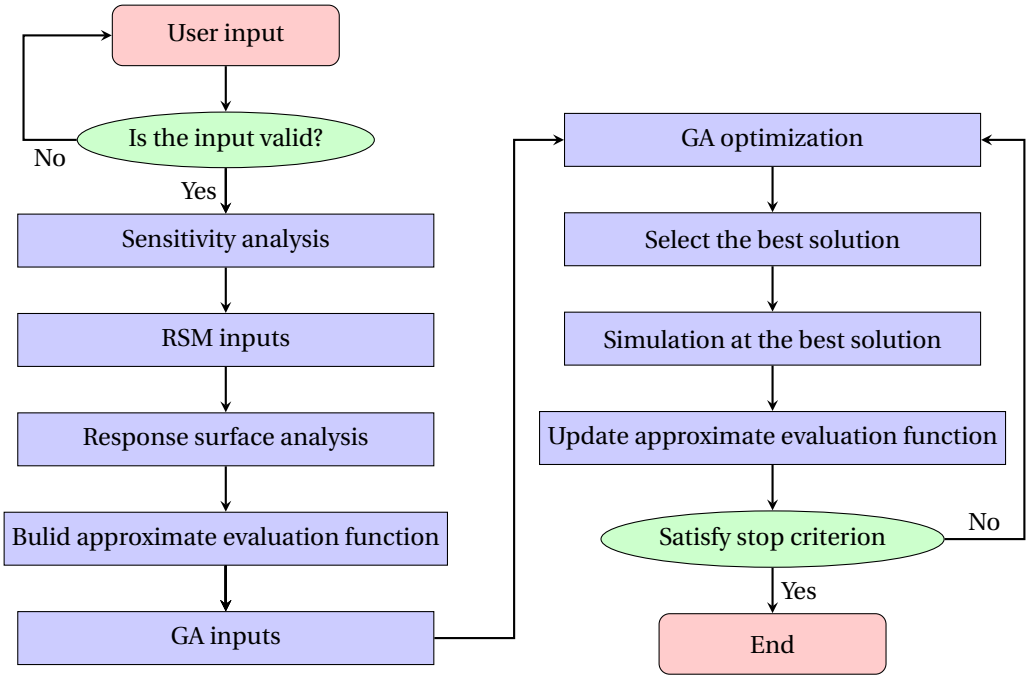

Fig. 3.2: Flowchart of the optimization procedure.

3.3. Results and discussion

In this section, the application of the methodology for a phenomenological CP model, see Section 2.3.1, a dislocation-density-based CP model, see Section 2.3.3, and a

phenomenological CP model incorporating deformation twinning, see Section 2.3.2, is discussed. The spectral solver implemented in DAMASK, see Section 2.4, is used to conduct the CP simulations using these three constitutive laws. The representative volume element (RVE) is made out of 512 grains. One grid point is used per grain which results in a grid of $8 \times 8 \times 8$ points. Periodic boundary conditions were applied to this RVE.

The robustness of the optimization approach is demonstrated using three sets of reference stress–strain curves computed with the employed CP models. The performance of the optimization methodology is accessed by comparing the optimization outputs with the original values of the parameters. In addition, two other main advantages of using such synthetic reference data are: Firstly, the reproduced stress–strain curves can be considered as a perfect set of reference data. Therefore, it can be best used to investigate the capabilities of the methodology without disturbance from experimental inaccuracies. Secondly, this data set follows the physics of the CP model. Therefore, the shortcomings and physical limitations of the CP model do not deteriorate the performance of the optimization methodology.

3.3.1. Phenomenological model

In this section, the novel optimization methodology is applied to determine the material parameters for the phenomenological model introduced in Section 2.3.1. In addition, the methodology is used to quantify the effects and interactions of the individual parameters.

3.3.1.1. Numerical inputs

Reference data sets

The material parameters listed in Table 3.1 are used to calculate reference stress–strain curves using the phenomenological constitutive model for a strain rate range from $10^{-5}\,\mathrm{s}^{-1}$ to $10^{3}\,\mathrm{s}^{-1}$. These material parameters are according to those reported for fcc copper [52]. In this example, a random orientation distribution was used. Periodic boundary conditions were applied to this RVE which was loaded in uniaxial compression up to 40 % strain.

Table 3.1: Material parameters used to produce reference stress–strain data for the phenomenological model.

variable	description	units	reference value
$C11$	elastic constant	MPa	100
$C12$	elastic constant	MPa	60
$C44$	elastic constant	MPa	30
$\dot{\gamma}_0$	reference shear rate	s^{-1}	0.001
τ_0	slip resistance	MPa	30
τ_∞	saturation stress	MPa	60
h_0	slip hardening parameter	MPa	80
n	strain rate sensitivity parameter	–	20
a	slip hardening parameter	–	2

Adjustable parameters and their ranges

Table 3.2 lists the ranges selected for the adjustable parameters of the phenomenological model. These ranges are used to build the off-line databases. The ranges of the parameters are selected in a way to be according to the values reported in the literature for fcc copper and to include the original set of data.

Table 3.2: Ranges of the adjustable parameters for the phenomenological CP model.

variable	units	range
τ_0	MPa	[15, 40]
τ_∞	MPa	[40, 70]
h_0	MPa	[60, 100]
n	–	[10, 30]
a	–	[1, 3]

3.3.1.2. Parameter effects and their interaction

The fitting methodology presented here does not only provide a set of parameters in a "black box" style, but it also enables to quantify the effects and interactions of the individual parameters. Such insights help to develop a quantitative and thorough understanding of the role of the underlying single crystal parameters in predicting the deformation behavior of a polycrystalline aggregate. This knowledge can be used to explore the shortcomings and possibly redundant parameters of a constitutive law towards improving existing or developing new constitutive laws.

This subsection provides a discussion on the effect of each parameter and interaction effect among different parameters in a polycrystalline aggregate. A main effect shows how the response variable is affected with a change in one of the independent variables, ignoring the effects of all other independent variables. An interaction effect implies how the effect of one independent variable may depend on the level of the other independent variables. It should be noted that the magnitude of the effects depends on the range selected for the parameters, a larger range for a variable results in a larger effect. The magnitudes of the effects are calculated using Eq. (3.10) and Eq. (3.11). In this study, only effects with an absolute magnitude larger than 30 % of the absolute magnitude of the largest effect will be shown. However, it should be noted that based on the output from ANOVA, there are many more significant effects than those shown in the figures.

Fig. 3.3(a) shows the main effects and the interaction effects for the stress at the yield point. The only significant parameters at the yield point are slip resistance, τ_0, and strain rate sensitivity parameter, n, with positive and negative effects, respectively. A positive main effect indicates that an increase in the variable increases the stress at the considered plastic strain level, whereas a negative main effect indicates that an increase in the variable decreases the resulting stress. For example, the main effect for τ_0 has a value of 58 for the case of $\dot{\varepsilon}_p = 10\ s^{-1}$ and $\varepsilon_p = 0$. This reveals that a change from 15 MPa (-1 level) to 40 MPa (+1 level), when all other parameters are at base level 0, results in approximately 2×58 MPa increase in the yield stress.

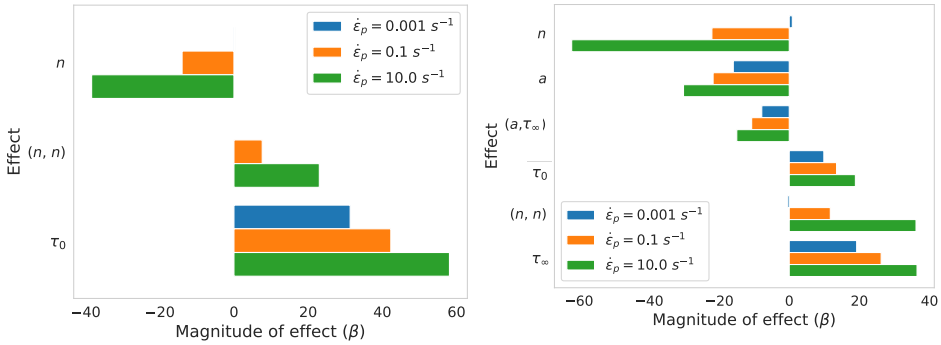

(a) $\varepsilon_p = 0$ (b) $\varepsilon_p = 0.36$

Fig. 3.3: The main effects and interactions effects for the stress at (a) $\varepsilon_p = 0$, (b) $\varepsilon_p = 0.36$. The magnitudes of the effects are calculated using Eq. (3.10) and Eq. (3.11), and they are in MPa. The material parameters are defined in Table 3.1.

Fig. 3.3 (b) shows the dominating main effects and the interaction effects for the stress at a plastic strain of $\varepsilon_p = 0.36$. At this plastic strain, the effect of other parameters becomes significant. The main effect of the strain rate sensitivity parameter, n, and the slip hardening parameter, a, is negative, while the main effect of slip resistance, τ_0, and saturation stress, τ_∞, is positive. The main effect of the slip hardening parameter, h_0, is positive but much smaller than the main effect for other parameters.

The interaction between some of the parameters is significant. For example, the interaction effect between a and τ_∞ is significant and negative. A negative two-way interaction means the main effect of one variable decreases as the level of the other variable increases. Therefore, the main effect of τ_∞ is lower at a higher level of a. A positive two-way interaction effect between two variables shows the opposite, the main effect of one variable increases if the level of other variable increases. In addition, the noticeable quadratic effect for n and a is an evidence for curvature in the stress response.

The effect of all parameters increases with an increase in strain rate. However, the increase is noticeably larger for the strain rate sensitivity parameter n in comparison to the other parameters. This confirms that the rate sensitivity is mainly controlled by n.

Fig. 3.4(a) shows the effects plot for the stress at different applied strain levels. It can be seen that the magnitude of the effect for different parameters is highly dependent on the applied strain. For all parameters, the magnitude of the effect is larger at higher applied strains except for τ_0, for which the magnitude of the main effect decreases with an increase in applied strain. Fig. 3.4(b) shows the effects plot for the average strain hardening rate. Obviously, the main effect for all parameters is significant. The main effect of τ_0, n and a is negative, while the main effect of τ_∞ is positive. Again, the effects are stronger at higher strain rates.

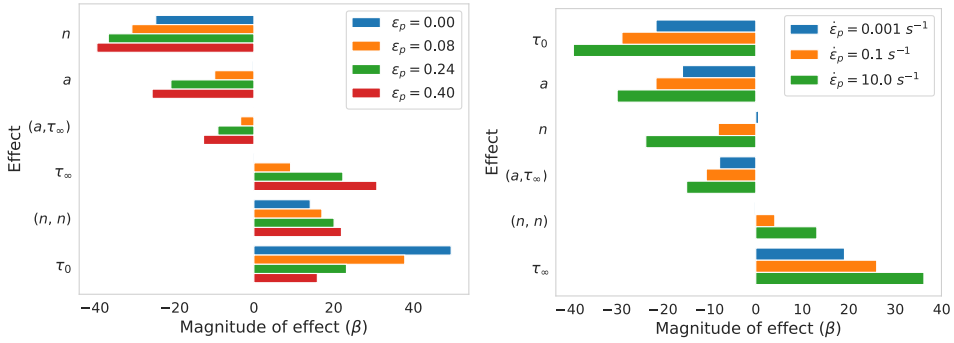

(a) (b)

Fig. 3.4: (a) The effects plot for the stress at different applied strains for $\dot{\varepsilon} = 1\ s^{-1}$, (b) the effects plot for the average strain hardening rate. The magnitudes of the effects are calculated using Eq. (3.10) and Eq. (3.11), and they are in MPa. The material parameters are defined in Table 3.1.

3.3.1.3. Determined parameter set

Fig. 3.5 shows the results from 20 independent optimization runs. The error analysis shows that the maximum error in the predicted stress–strain curves for all 20 optimization runs is around 0.5 MPa for the load case of $\dot{\varepsilon} = 1000\ s^{-1}$ at $\varepsilon_p = 0.4$. Therefore, all the solutions can be considered as a good solution to predict the deformation behavior.

The optimized values for τ_0 and n are exactly the same as the original values up to two significant digits. This reveals that these parameters have a unique contribution to the CP model, and the optimization methodology is able to capture this uniqueness.

The optimized solutions for the other parameters are located in a distribution around the original values. The optimization results for τ_∞ are distributed between 57.4 MPa to 63.1 MPa. This is around 19% of the optimization range, which is in general acceptable. Therefore, this parameter can be predicted properly, however, with some deviation from the original value. The main reason for this error can be attributed to the boundary conditions used in the optimization. τ_∞ determines the steady-state stress at high applied strains. However, the reference data used for the optimization are limited to a maximum strain of 0.4. Therefore, no unique solution can be achieved for τ_∞.

The optimization results for a are distributed between 1.77 to 2.28, which is around 26% of the optimization range. This distribution is relatively wide but around the original reference data. This parameter mainly affects the hardening behavior. As it was observed, there is a strong interaction between a and τ_∞ and both parameters can compensate each other to a high degree. Therefore, with no unique solution for τ_∞, it is not possible to reach a unique solution for a.

The optimization results for h_0 are distributed between 73.6 MPa to 87.6 MPa, which is around 35% of the optimization range. This distribution is relatively wide but again it is essentially accumulated around the original reference data. The main effect for h_0 is considerably smaller than those of the other parameters. Therefore, the scatter in the optimized values for this parameter has a negligible effect on the stress–strain curves. In general, it is difficult to reach a unique solution for parameters with a small effect.

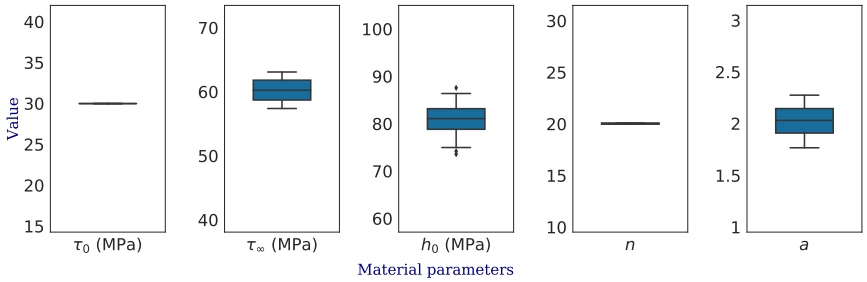

Fig. 3.5: The box plot of the optimized solutions from 20 optimization runs for the phenomenological model.

3.3.2. Dislocation-density-based model

As a second application example, the methodology's performance is investigated for a temperature- and strain rate-dependent crystal plasticity model. For this purpose, the methodology is applied to determine the material parameters for the dislocation-density-based model, see Section 2.3.3, using stress-strain curves obtained at a wide range of temperature and strain rate. Additionally, this example is used to examine the robustness of the methodology and the performance of the genetic algorithm.

3.3.2.1. Numerical inputs

Reference data set

The material parameters listed in Tables 3.3 and 3.4 are used together with temperature-dependent elastic constants from [63, 64] to compute stress–strain curves for a temperature range from 30 K to 900 K and a strain rate range from 0.01 s^{-1} to 10 s^{-1}. As the model is strain rate and temperature sensitive, the respective objective functions are used. The orientation distribution was chosen to match the weak texture commonly observed for hot-rolled IF steel as shown in Fig. 4.1. Periodic boundary conditions were applied to this RVE which was loaded in uniaxial compression up to 40 % strain.

Adjustable parameters and their ranges

Table 3.5 list the ranges selected for the adjustable parameters for the dislocation-density-based model. These ranges are used to build the off-line databases. The ranges of the parameters are selected relatively wide and include the original set of data. It should be noted that the optimization result is not sensitive to the selected ranges as long as the RSM can statistically describe the CP model.

Recovery parameters

The parameters defining recovery due to dislocation climb, see Eq. (2.36), have a significant effect on the strain hardening behavior. However, the recovery term in the investigated constitutive law is not able to describe recovery over the range of temperatures considered in this study. More precisely, the model predicts a very rapid increase of climb velocity even for a small increase in the temperature and, hence, the

Table 3.3: Material parameters used to produce reference stress–strain data for the dislocation-density-based CP model.

variable	description	units	reference value
ρ^{α}	initial dislocation density	m/m^3	6.85×10^{10}
v_0	dislocation glide velocity pre-factor	m/s	4.8×10^{4}
ΔF	activation energy for dislocation glide	J	1.87×10^{-19}
p	p-exponent in glide velocity	–	0.32
q	q-exponent in glide velocity	–	1.46
τ_0^*	short-range barriers strength at 0 K	MPa	395
B	drag coefficient	Pa s	10^{-4}
d_g	average grain size	µm	50
C_λ	parameter controlling dislocation mean free path	–	48.2
C_{anni}	Coefficient for dislocation annihilation	–	8.7
b	Burgers vector	nm	0.248

Table 3.4: Coefficients of interaction between different slip systems for iron from [65].

self	coplanar	collinear	orthogonal	glissile	sessile
0.1	0.1	0.72	0.053	0.137	0.073

Table 3.5: Ranges of the adjustable parameters for the dislocation-density-based CP model.

variable	units	range
ρ^{α}	m/m^3	$[10^{10}, 10^{12}]$
v_0	m/s	$[10^{4}, 10^{6}]$
ΔF	J	$[1.5, 2.5] \times 10^{-19}$
p	–	[0.25, 0.7]
q	–	[1.2, 1.8]
τ_0^*	MPa	[250, 500]
B	Pa s	$[10^{-2}, 10^{-5}]$
d_g	µm	[30, 100]
C_λ	–	[20, 60]
C_{anni}	–	[5, 25]

formulation becomes unstable after a temperature rise of around 200 K to 300 K. Due to resulting convergence issues, it was not possible to identify values for the recovery parameters in a systematic way for a large temperature range. Therefore, the climb based dynamic recovery is neglected in this study. Although the effect of recovery may be negligible at low temperatures, it has a considerable effect on the strain hardening behavior at high temperatures.

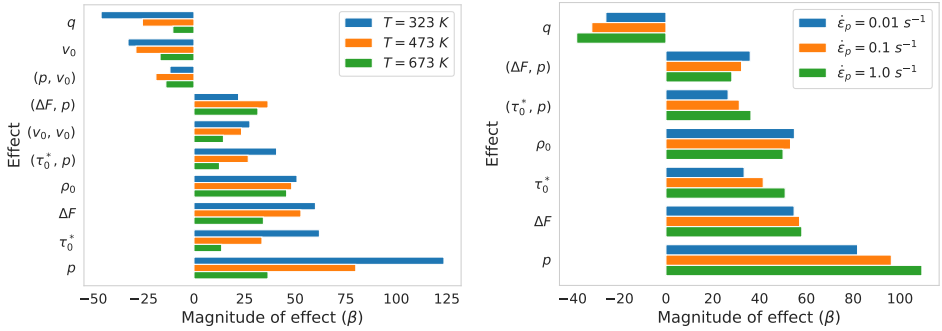

(a) $\dot{\varepsilon}_p = 1s^{-1}$ (b) $T = 373K$

Fig. 3.6: The main effects and interactions effects for the stress at the yield point (a) for $\dot{\varepsilon} = 1.0s^{-1}$ at varying temperatures, (b) for $T = 373\ K$ at varying strain rates. The magnitudes of the effects are calculated using Eq. (3.10) and Eq. (3.11), and they are in MPa. The material parameters are defined in Table 3.3.

3.3.2.2. Sensitivity analysis

A sensitivity study was performed to determine the statistically significant material parameters for the ranges presented in Table 3.5. The significance of each parameter was evaluated using the ANOVA test. It was observed that, despite the relatively large ranges selected for d_g and B, their effects are not statistically significant for any loading condition. Therefore, they have been removed from the optimization process, and their values have been fixed at 50 µm and 10^{-4} Pa s, respectively, to save computational time.

3.3.2.3. Parameter effects and their interaction

Yield stress

Fig. 3.6 shows the effects plot of the different parameters at the yield point for the resulting stress. It can be seen that the main effect for p, τ_0^*, ΔF, and ρ_0^α is positive. Therefore, the resulting yield stress increases with an increase in these variables. The main effect for q and v_0 is negative, and an increase in the magnitude of these variables decreases the resulting yield stress.

Obviously, there are significant interactions between some of the parameters. For example, the interaction between p and τ_0^* is noticeably strong and positive. Therefore, the main effect of p is higher at a higher level of τ_0^*. The negative two-way interaction effect between p and v_0 shows the opposite, the main effect of p decreases if the level of v_0 increases.

The ANOVA also shows that some of the three-way and four-way interaction effects are statistically significant. This is especially the case at high temperatures and for interaction effects between p, q, τ_0^*, ΔF, and v_0. Including the high-order interaction terms in the polynomial approximation therefore results in a better prediction of the response stress. Hence, in this study, up to four-way interaction effects are used, see Eq. (3.8).

Temperature sensitivity

Fig. 3.7(a) shows the influence of the dominant parameters on the temperature sensitivity, $(\hat{\sigma}_{T_1} - \hat{\sigma}_{T_2})|_{\dot{\varepsilon}_p = const}$, at the yield point. The results show that the temperature

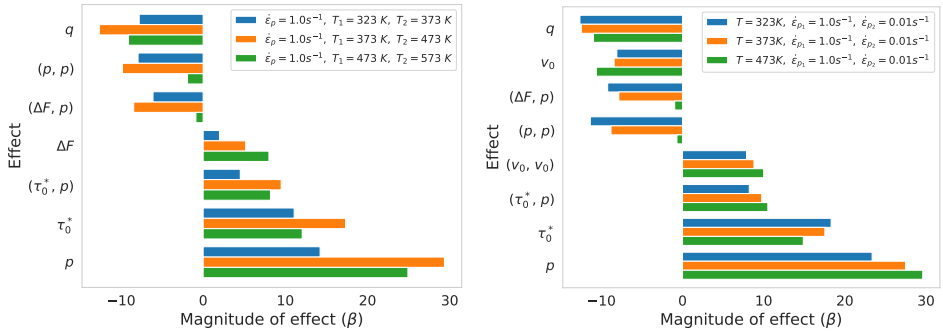

(a) $\dot{\varepsilon} = 1s^{-1}$ (b) $T = 373K$

Fig. 3.7: The main effects and interactions effects for stress at the yield point for (a) temperature sensitivity, (b) strain rate sensitivity. The magnitudes of the effects are calculated using Eq. (3.10) and Eq. (3.11), and they are in MPa. The material parameters are defined in Table 3.3.

sensitivity is mainly controlled by the parameters which define the barrier, i.e. τ_0^*, ΔF, p, and q. The main effect for p, τ_0^*, and ΔF is positive, while the main effect for q is negative. There are also significant interactions between these parameters.

Strain rate sensitivity

Fig. 3.7(b) shows the influence of the dominant parameters on the strain rate sensitivity, $(\hat{\sigma}_{\dot{\varepsilon}_{p_1}} - \hat{\sigma}_{\dot{\varepsilon}_{p_2}})|_{T=const}$, at the yield point. Similar to the temperature sensitivity, the strain rate sensitivity is mainly controlled by the barrier's parameters. However, the influence of v_0 is more pronounced than for the temperature dependency. The main effect for p and τ_0^* is positive, while the main effect for q and v_0 is negative. As for the temperature sensitivity, there are some significant two-way interaction effects.

Hardening-rate sensitivity

Fig. 3.8 shows the effects plot for the average strain hardening rate. The most significant parameters are C_{anni} and C_λ. The main effect for both parameters are negative while their interaction effect is positive. Therefore, the effect of each of these two parameters is stronger when the other parameter is at its lowest level. The noticeable quadratic effect for C_λ is an evidence for curvature in the stress response. It can be seen that the magnitude of the main effect is strongly dependent on the applied strain. Moreover, the effect of C_{anni} is stronger than C_λ at higher strains. Therefore, a higher value for C_{anni} results in an earlier steady-state condition in the stress–strain curve. This result shows that, despite the strong interaction between these two parameters, there is a relevant difference between their roles.

3.3.2.4. Grouping the parameters

It is important to notice that there is no significant interaction between C_{anni} and C_λ with the other parameters, i.e. p, τ_0^*, ΔF, ρ_0^α, q, and v_0. This indicates the possibility of grouping the parameters into two blocks in the RSM study. The main advantage of

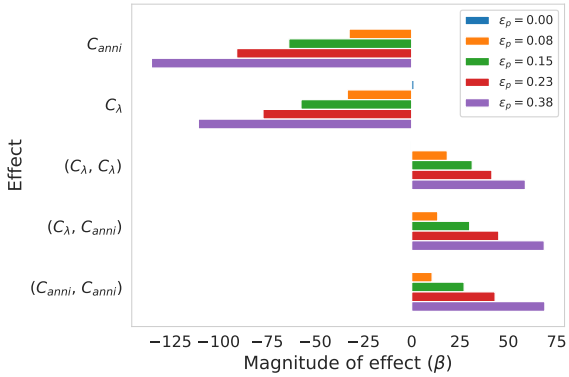

Fig. 3.8: The main effects and interactions effects for stress at varying applied strains. The magnitudes of the effects are calculated using Eq. (3.10) and Eq. (3.11), and they are in MPa. The material parameters are defined in Table 3.3.

grouping the parameters is the substantial decrease in the number of simulations required to build the off-line database. This reduction is especially significant when a model requires a large number of parameters and when these parameters can be split into independent groups. For the considered case of the dislocation-density-based model, $2^8 = 256$ simulations are needed per loading conditions to build a full-fractional database. By grouping the parameters in two blocks of six and two parameters, only $2^6 + 2^2 = 68$ simulations are needed. In addition, grouping results in a lower error in the response estimated by the RSM. Therefore, a better convergence for the optimization procedure can be achieved.

A closer look on the physical effect of the parameters reveals that the yield stress is determined mainly by p, τ_0^*, ΔF, ρ_0^α, q, and ν_0, while C_{anni} and C_λ are dominating the hardening behavior. Therefore, the two groups of the parameters can be determined independently from each other. For example, using the experimental data for yield strength and in the absence of hardening data, one can still accurately identify p, τ_0^*, ΔF, ρ_0^α, q, and ν_0. This is of practical relevance since for many materials the yield strength is well characterized at different deformation temperatures and strain rates.

The results in the following are obtained by separating the parameters into two groups based on their interactions and their effects. The first group includes p, τ_0^*, ΔF, ρ^α, q, and ν_0, and the second group includes C_{anni} and C_λ.

3.3.2.5. Determined parameter set

Fig. 3.9 shows the results from 20 independent optimization runs, and the complete set of optimized parameters for five optimization runs is listed in Table 3.6. Except for one optimization (run 11, see the outliers in Fig. 3.9), the optimization methodology recovers the original parameters with good accuracy. Even for run 11 the relative error in yield stress is below 1%. The optimized values for ρ^α, C_{anni}, and C_λ are exactly the same as the original values up to two significant figures. This reveals that these parameters have

Table 3.6: The complete set of optimized parameters for five different optimization runs.

optimization run	ρ^{α} (m/m^3)	ΔF (J)	p	q	τ_0^* (MPa)	v_0 (m/s)	C_λ	C_{anni}
2	6.85×10^{11}	1.84×10^{-19}	0.338	1.52	402	5.01×10^4	48	8.82
7	6.85×10^{11}	1.79×10^{-19}	0.353	1.57	410	4.37×10^4	48	8.82
11	6.85×10^{11}	2.00×10^{-19}	0.277	1.28	359	5.37×10^4	48	8.82
14	6.85×10^{11}	1.86×10^{-19}	0.318	1.43	388	3.72×10^4	48	8.82
19	6.85×10^{11}	1.85×10^{-19}	0.331	1.47	395	5.25×10^4	48	8.82

a unique contribution to the CP model, and the optimization methodology is, therefore, able to recover the original values.

For v_0, the optimization outputs are located in a relatively narrow distribution around the original value between 2.29×10^4 ms^{-1} to 7.94×10^4 ms^{-1}, which is around 5.7% of the optimization range. The main effect for v_0 is relatively small in comparison to the other parameters. Therefore, it is in general difficult to reach the original value for this parameter, and the obtained values scatter around the original value.

For p, q, ΔF, and τ_0^* the optimization outputs are located in a wider distribution around the original values. For p the optimization results are distributed between 0.32 to 0.36, which is around 9.6% of the optimization range. The distribution for q is between 1.43 to 1.58, which is around 25% of the optimization range. The optimization results for ΔF are distributed between 1.73×10^{-19} J to 1.92×10^{-19} J, which is around 19% of the optimization range. The distribution for τ_0^* is between 388 MPa to 412 MPa, which is around 9.6% of the optimization range.

p, q, ΔF, and τ_0^* have a strong interaction with each other, and the stress–strain curves from the CP model are underdetermined for a large range of temperatures and strain rates. As a result, the difference between the error from different sets of solutions is very subtle and reaching the exact original set of values for these parameters is not possible. This topic will be discussed in more detail in Chapter 4 which is focused on the numerics of the dislocation-density-based model.

Fig. 3.10 shows the error in the yield stress prediction for 20 optimization runs. It can be clearly seen that the error for the different sets of the optimized solutions is considerably small, even for optimization run 11. The maximum error mostly occurs at the lowest temperature loading condition, i.e. T = 30 K, where the stress magnitude is in the order of 1 GPa. Here, the maximum relative error is approximately 1 % for the optimization run 11.

3.3.2.6. Robustness

Here we used simulated data as reference, however, the experimental data usually used as input contains non-systematic errors. These errors may affect the robustness and performance of an optimization algorithm in reaching a solution. To investigate the effects of imperfection on the robustness of the optimization methodology introduced in this study, an imperfect set of reference data was created by introducing a random error (noise) between ±2.5% of the yield stress into the reference stress–strain curves.

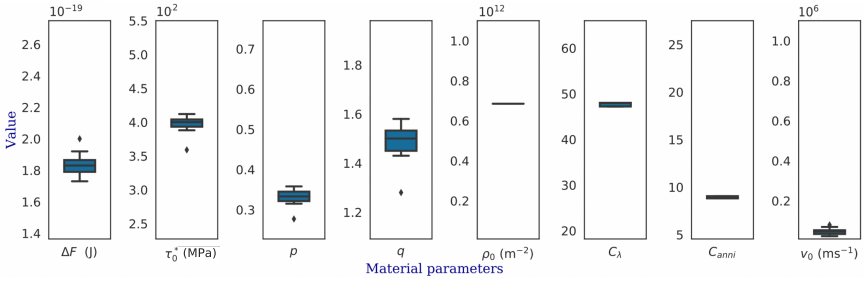

Fig. 3.9: The box plot of the optimized solutions from 20 optimization runs for the dislocation-density-based model.

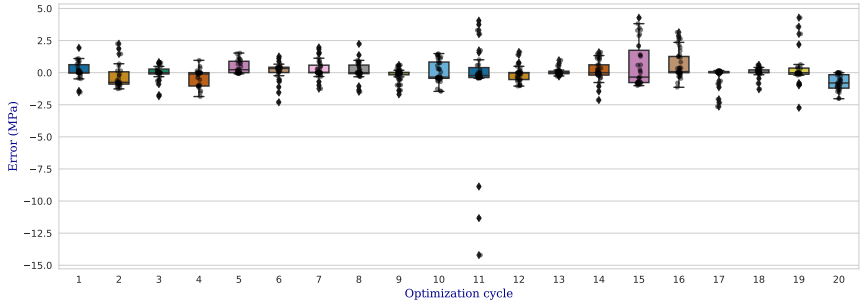

Fig. 3.10: The error in the yield stress prediction using the optimized solutions from different optimization runs. The errors corresponds to the different loading conditions, *i.e.* different loading temperatures and strain rates.

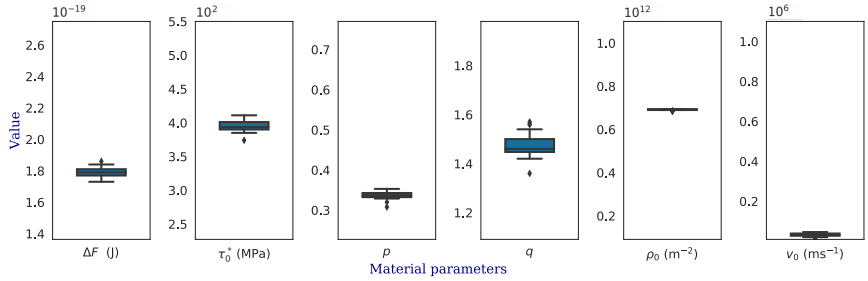

Fig. 3.11: The optimized solution from 20 optimization runs for the dislocation-density-based model in the case of imperfect set of reference data.

Although the error in an experimental set of data can exceed ±2.5%, these errors are normally systematic, e.g. creating a shift in the experimental data. Such a shift in the reference data set does not affect the robustness of the methodology. However, it results in a different set of optimized parameters compared to the original reference data set. Unlike the systematic errors, random non-systematic errors can deteriorate the performance of an optimization methodology. Therefore, in this study, a random non-systematic error of ±2.5% has been introduced into the perfect synthetic reference data set. The value of ±2.5% is selected to keep the correct trend in the strain rate and temperature sensitivity, e.g. to avoid a lower yield point at higher strain rates. As in the case of experimental results, the employed model is not able to reproduce these deteriorated curves exactly.

Fig. 3.11 shows the optimization outputs for 20 independent optimization runs. It can be seen that the random error does not affect the values of the obtained parameters noticeably. The converged values for ρ_0^α, C_λ, and d_{anni}^α are almost the same as the original values with less than 1% deviation from the original data. The optimization results for v_0 are distributed between $1.2 \times 10^4\,\text{ms}^{-1}$ to $4.6 \times 10^4\,\text{ms}^{-1}$, which is around 1% of the optimization range. The distribution for ΔF is between 1.73×10^{-19} J to 1.84×10^{-19} J, which is around 11% of the optimization range. For τ_0^* the distribution is between 385 MPa to 411 MPa, which is around 10.4% of the optimization range; For p it is between 0.32 to 0.35, which is around 6.7% of the optimization range. The distribution for q is between 1.42 to 1.54, which is around 20% of the optimization range.

Interestingly, the distribution for v_0, p, q, ΔF, and τ_0^* is narrower for the case of imperfect reference data than for the case of perfect reference data. This can be explained as follows: For the case of the perfect set of reference data, the ideal solution results in a fitness value of zero. A small deviation from the ideal case leads to a small error in the reproduced stress–strain curves. According to the equations presented in Section 3.2.1.2, the individual objective functions are calculated by the sum of the square of the errors. Consequently, the fitness values is less affected by small errors. While for the case of the imperfect set of reference data, the error for an imaginary best solution is already large. Therefore, a deviation from the best solution results in a relatively larger error and the convergence to the optimal solution is easier.

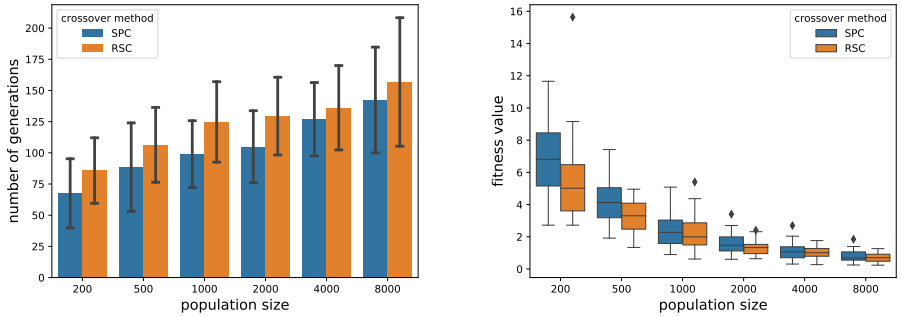

Fig. 3.12: Efficiency and robustness of the GA for different population sizes and two types of crossover. SPC and RSC stand for single-point crossover and reduced surrogate crossover, respectively. (a) Number of generations needed for a GA to be completed. The error bar shows the standard deviation of the observations. (b) Distribution of the fitness value of the converged solutions for different population sizes and crossover techniques.

3.3.2.7. Performance analysis for the genetic algorithm

As mentioned in Section 3.2.1, a genetic algorithm consists of several steps and operations. In this section, the effect of two important features of the GA, namely, population size and type of crossover, on the robustness and efficiency of the GA are studied using the perfect reference data introduced above in Section 3.3.2.1. Two types of crossover, namely single-point crossover (SPC) and reduced surrogate crossover (SRC), are investigated for different population sizes ranging from 200 to 8000 chromosomes. For each case study, 25 GA runs are performed, and the resulting data is statistically analyzed.

Efficiency of the GA

Fig. 3.12(a) shows the number of generations required for the GA to converge to a solution. It can be seen that the number of generations needed for the GA to converge is dependent on the type of the crossover used. The number of generations to convergence is higher for the reduced surrogate crossover than for the single-point crossover. This is because the reduced surrogate crossover avoids producing parent clones. Therefore, for this crossover technique, the second stop criterion, i.e. no improvement in the best solution for 50 generations, is usually responsible for terminating the GA. The population size also has a noticeable effect on the number of generations required to convergence. For both crossover methods, the number of generations needed for convergence increases with an increase in the population size.

Robustness of the GA

Fig. 3.12(b) shows the distribution of the fitness value of the converged solutions for different population sizes and types of crossover. The population size has a significant effect on the mean and the range of the distribution. For a comparably small population size of 200, the range of the distribution is wide, and most of the optimization processes do not converge to the optimal solution. The distribution range of the fitness

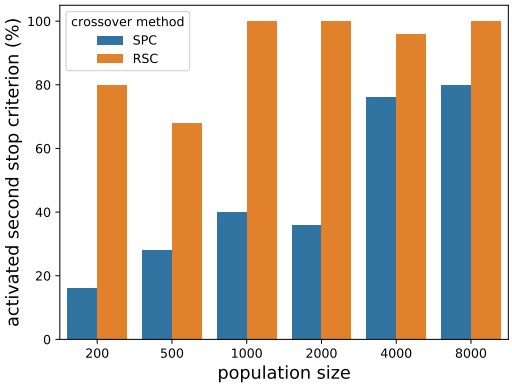

Fig. 3.13: Percentage of GA runs terminated by the second stop criterion, i.e. no improvement in the best solution for 50 generations. The rest of the GA runs were terminated by the first stop criterion, i.e. 70% of the chromosomes in a generation become equal, and none of the GA runs was terminated by the third stop criterion, i.e. reaching 500 generations. The results are shown for different population sizes and two types of crossover. SPC and RSC stand for single-point crossover and reduced surrogate crossover, respectively.

values for the population size of 500 is almost two times smaller than the distribution of the fitness values for the population size of 200. The rate of improvement in the quality of the optimal solution, the fitness value, decreases for large population sizes.

A comparison between the results from the two types of crossover reveals that the reduced surrogate crossover results in a narrower distribution of the fitness values and a higher quality of the solution. However, this distinction becomes insignificant at high population sizes. Since single-point crossover needs a smaller number of generations to convergence, and the time efficiency of the GA has a strong relationship with the number of generations, it can be concluded that the single-point crossover has better efficiency.

Stop criterion

The results show that in the case of using the single-point crossover and small population sizes most of the optimization runs are terminated by the first criterion, i.e. 70% of the chromosomes in a generation become equal. Hence, only for a few limited cases the second criterion, i.e. no improvement in the best solution for 50 generations, is responsible for the termination. However, at large population sizes, i.e. 4000 and 8000, the second criterion is responsible for the termination of most of GA runs. For the reduced surrogate crossover, the second criterion is responsible for the termination of most of the GA runs independently of the population size. None of the optimization cases was terminated by the third stop criterion, i.e. reaching 500 generations.

3.3.3. Phenomenological model including deformation twinning

As a third and final application example, the methodology's performance is investigated when numerous deformation mechanisms are available. For this purpose, the presented parameter identification procedure has been used to identify the constitutive

parameters of a CP model for a Magnesium alloy with a hexagonal close-packed crystal (hcp) structure. The availability of multiple slip and twin systems makes the plastic deformation of Mg alloys strongly anisotropic and non-linear. The CP model used here is described in Section 2.3.2.

3.3.3.1. Numerical inputs

Reference data sets

The material parameters listed in Table 3.7 have been used to calculate reference stress–strain curves using the phenomenological constitutive model incorporating deformation twinning. These material parameters have been chosen according to those reported for magnesium alloys in [52]. It should be noted that n_{tw} has a significant effect on the convergence and the numerical costs of the simulations. Zhang and Joshi [66] and Herrera-Solaz *et al.* [39] observed that for a large n_{tw}, the convergence becomes significantly difficult and time-consuming. In this study, we also observed that the convergence time increases significantly when n_{tw} exceeds 10. Furthermore, it was observed for some combinations of the material parameters that no convergence is achieved when n_{tw} is larger than 10. Therefore, here, a smaller value for n_{tw} has been used compared to what was reported in [52].

The crystallographic orientation distribution used here is a strong basal texture with the c-axis parallel to the normal direction (ND), a typical crystallographic texture observed for rolled Mg alloys. The pole figures of the crystallographic orientation distribution are plotted in Fig. 3.14. For such a strong texture, the plastic deformation behavior is highly anisotropic, especially for an hcp crystal structure. This indicates that for different loading directions different slip and/or twin systems are activated. If a slip or twinning family is not activated for any of the imposed loading conditions, it will not be possible to identify the values of the underlying material parameters. To enable the identification of all material parameters, it is necessary to use reference data for different strain modes. For this purpose, the simulations have been performed under both compression and tension for seven different loading conditions, as shown in Fig. 3.15. In the figure, the arrow indicates the loading orientation (loading angle) for tension/compression, and the dark gray face indicates the constraint direction for plane-strain loading conditions. All simulations have been performed at different strain rates ranging from $10^{-5}\,\text{s}^{-1}$ to $1\,\text{s}^{-1}$.

Adjustable parameters and their ranges

Table 3.8 lists the ranges selected for the adjustable parameters of the CP model. These ranges have been selected according to those experimentally reported in the literature for single crystal Mg alloys, see Zhang and Joshi [66] for more detailed information. The spread of the reported data in the literature for $\tau_{0,\text{pyr}\langle\text{c+a}\rangle}$ and $\tau_{0,\text{C2}}$ is larger in comparison with the rest of the parameters. Therefore wide ranges for these two parameters have been considered.

3.3.3.2. Sensitivity and effect analysis

A sensitivity analysis is performed to determine the statistically significant material parameters for the ranges presented in Table 3.8. Fig. 3.16 and Fig. 3.17 show the effects plot for the resulting stress, respectively, at $\varepsilon_p = 0$ and $\varepsilon_p = 0.3$ under different loading

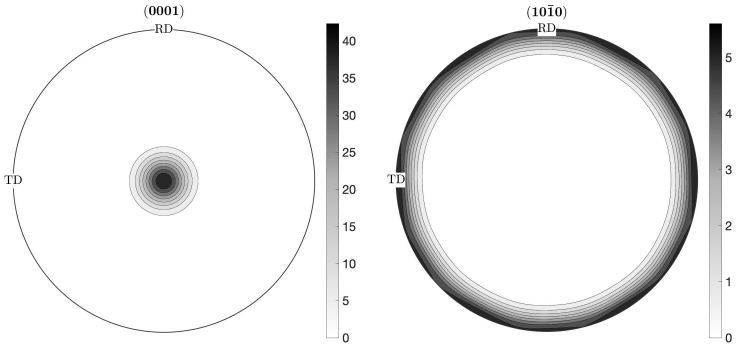

Fig. 3.14: Pole figures of the initial texture of the Mg alloy used as input to create the RVE for the simulations. The intensities in the legend are given in units of multiples of a random distribution, whereby a random texture would give a value of unity.

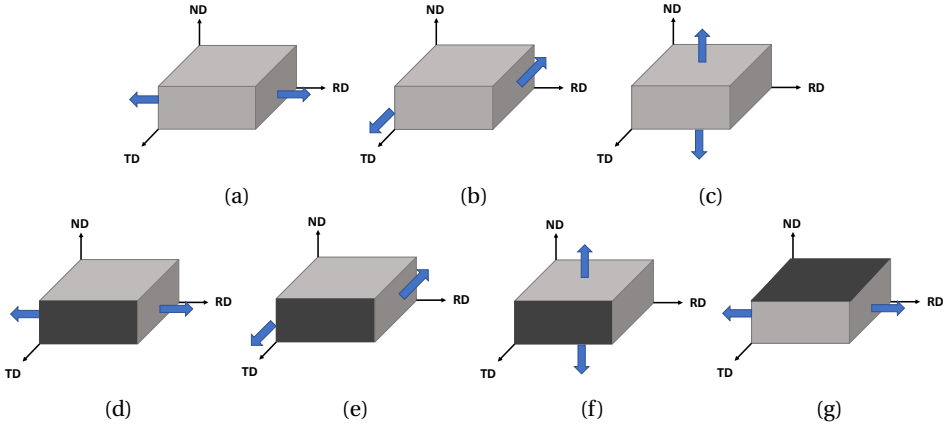

Fig. 3.15: Schematic of the loading conditions used for the simulations. The arrows indicate the loading orientation for the loading direction (tension/compression), and the dark gray faces indicate the constraint direction for the plane-strain loading conditions. (a) uniaxial compression/tension along RD, (b) uniaxial compression/tension in the RD-ND plane at 45° from both RD and ND, (c) uniaxial compression/tension along ND, (d) plane-strain compression/tension along RD with TD as the constraint direction, (e) plane-strain compression/tension in the RD-ND plane at 45° from both RD and ND with TD as the constraint direction, (f) plane-strain compression/tension along ND with TD as the constraint direction, (g) plane-strain compression/tension along RD with ND as the constraint direction.

Table 3.7: Material parameters used to produce reference stress–strain data for the phenomenological model incorporating deformation twinning.

variable	description	units	reference value
c/a	lattice parameter ratio	–	1.6235
C_{11}	elastic constant	MPa	59.3
$C33$	elastic constant	MPa	61.5
$C44$	elastic constant	MPa	16.4
$C12$	elastic constant	MPa	25.7
$C13$	elastic constant	MPa	21.4
$\dot{\gamma}_0^{\mathrm{s}}$	twinning reference shear rate	s^{-1}	0.001
$\dot{\gamma}_0^{\mathrm{tw}}$	slip reference shear rate	s^{-1}	0.001
$\tau_{0,\mathrm{basal}}$	basal slip resistance	MPa	10
$\tau_{0,\mathrm{pris}}$	prismatic slip resistance	MPa	55
$\tau_{0,\mathrm{pyr\langle a\rangle}}$	pyramidal ⟨a⟩ slip resistance	MPa	60
$\tau_{0,\mathrm{T1}}$	tensile twin resistance	MPa	45
$\tau_{0,\mathrm{C2}}$	compressive twin resistance	MPa	80
$\tau_{\infty,\mathrm{basal}}$	basal saturation stress	MPa	45
$\tau_{\infty,\mathrm{pris}}$	prismatic saturation stress	MPa	135
$h_0^{\mathrm{tw\text{-}tw}}$	twin-twin hardening parameter	MPa	50
$h_0^{\mathrm{s\text{-}s}}$	slip-slip hardening parameter	MPa	500
$h_0^{\mathrm{tw\text{-}s}}$	twin-slip hardening parameter	MPa	150
n_{s}	slip strain rate sensitivity parameter	–	10
n_{tw}	twinning strain rate sensitivity parameter	–	5
a	slip hardening parameter	–	2.5

conditions. It should be noted that based on the output from ANOVA, there are many more statistically significant effects than those shown in the figures, however, only the most pronounced effects are shown here.

The anisotropic plastic behavior is fully reflected in the effect analysis. We find that the effects and interaction effects of different parameters strongly depend on the loading conditions (loading orientation, loading direction, and loading mode). For example, a compressive loading along the c-axis (load case c) can be accommodated by pyramidal ⟨c+a⟩ slip and compression twin modes. As expected, the effect analysis shows that under this loading condition the main effects and interaction effects for the pyramidal ⟨c+a⟩ slip and compression twin modes are high, while the effects of the other slip and twinning modes are relatively small or even insignificant.

We observed from the effect analysis that some of the loading conditions used in this study are mutually dependent, i.e. loading condition a (uniaxial compression/tension along RD) with loading condition g (plane-strain compression/tension along RD with ND as the constraint direction), loading condition b (uniaxial compression/tension in the RD-ND plane at 45° from both RD and ND) with loading

Table 3.8: Ranges of the adjustable parameters for the phenomenological CP model incorporating deformation twinning.

variable	units	range
$\tau_{0,\text{basal}}$	MPa	[5, 30]
$\tau_{0,\text{pris}}$	MPa	[30, 60]
$\tau_{0,\text{pyr}\langle\text{a}\rangle}$	MPa	[50, 90]
$\tau_{0,\text{pyr}\langle\text{c+a}\rangle}$	MPa	[50, 110]
$\tau_{0,\text{T1}}$	MPa	[35, 70]
$\tau_{0,\text{C2}}$	MPa	[60, 120]
$\tau_{\infty,\text{basal}}$	MPa	[30, 60]
$\tau_{\infty,\text{pris}}$	MPa	[100, 160]
$\tau_{\infty,\text{pyr}\langle\text{a}\rangle}$	MPa	[120, 180]
$\tau_{\infty,\text{pyr}\langle\text{c+a}\rangle}$	MPa	[120, 180]
$h_0^{\text{tw-tw}}$	MPa	[30, 80]
$h_0^{\text{tw-s}}$	MPa	[100, 200]
$h_0^{\text{s-s}}$	MPa	[400, 600]
n_s	–	[15, 35]
n_tw	–	[3, 8]
a	–	[2, 4]

condition e (plane-strain compression/tension in the RD-ND plane at 45° from both RD and ND with TD as the constraint direction), and loading condition c (uniaxial compression/tension along ND) with loading condition f (plane-strain compression/tension along ND with TD as the constraint direction). Therefore, the results for the effect analysis for loading conditions e, f, and g are not presented here. It should be noted that, although these loading conditions have been considered in the optimization procedure, their effects on the optimized solutions are negligible.

The accuracy of the optimization output for each parameter is dependent on how significant the effects of that parameter are. It is obvious that if a slip or twinning family is not activated in any of the imposed loading conditions, the effect for the related parameters will be negligible, and it will be impossible to identify those parameters accurately. According to the effect analysis, for all parameters, except $h_0^{\text{tw-s}}$, there is at least one loading condition where the effect of the parameter is significant. Therefore, theoretically, the loading conditions used in this study suffice to determine all the parameters except for $h_0^{\text{tw-s}}$.

3.3.3.3. Grouping the parameters

The only statistically significant parameters at the yield stress are $\tau_{0,\text{basal}}$, $\tau_{0,\text{pris}}$, $\tau_{0,\text{pyr}\langle\text{a}\rangle}$, $\tau_{0,\text{pyr}\langle\text{c+a}\rangle}$, $\tau_{0,\text{T1}}$, $\tau_{0,\text{C2}}$, n_s, and n_tw. As mentioned earlier, splitting the parameters into different groups results in a substantial decrease in the number of simulations required to build the off-line database. Therefore, in this application example, the parameters have been divided into two different groups. The first group includes $\tau_{0,\text{basal}}$, $\tau_{0,\text{pris}}$,

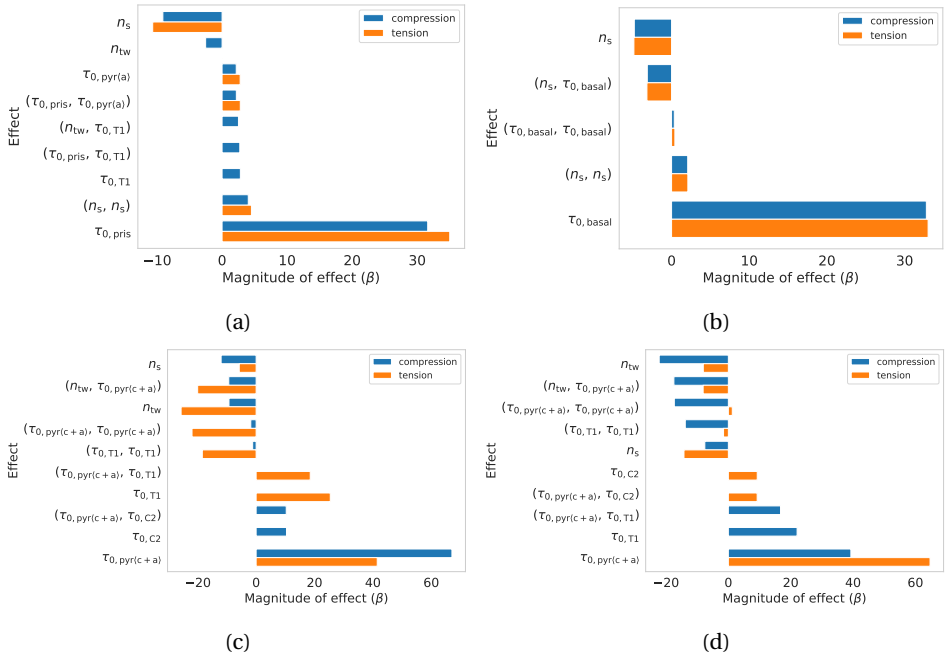

Fig. 3.16: The main effects and interaction effects for the stress at the yield point under the different loading conditions shown in Fig. 3.15, (a) loading condition a – uniaxial compression/tension along RD, (b) loading condition b – uniaxial compression/tension in the RD-ND plane at 45° from both RD and ND, (c), loading conditions c – uniaxial compression/tension along ND, and (d) loading condition d – plane-strain compression/tension along RD with TD as the constraint direction. The results are shown for $\dot{\varepsilon}$= 0.1 s^{-1} under compression and tension. The magnitudes of the effects are calculated using Eq. (3.10) and Eq. (3.11), and they are in MPa. The material parameters are defined in Table 3.7.

$\tau_{0,\text{pyr}\langle a\rangle}$, $\tau_{0,\text{pyr}\langle c+a\rangle}$, $\tau_{0,\text{T1}}$, $\tau_{0,\text{C2}}$, n_s, and n_{tw}. These parameters will be determined using the yield stress data. The second group includes $\tau_{0,\text{pyr}\langle a\rangle}$, $\tau_{\infty,\text{basal}}$, $\tau_{\infty,\text{pris}}$, $\tau_{\infty,\text{pyr}\langle a\rangle}$, $\tau_{\infty,\text{pyr}\langle c+a\rangle}$, $h_0^{\text{s-s}}$, $h_0^{\text{tw-tw}}$, and a. These parameters will be determined using the data at higher strains and the strain hardening behavior.

It should be noted that $\tau_{0,\text{pyr}\langle a\rangle}$ has been considered in both groups. Although the effect of $\tau_{0,\text{pyr}\langle a\rangle}$ is statistically significant for loading condition a, uniaxial compression/tension along RD, its magnitude is much smaller than the rest of the parameters. Besides, there is a strong interaction between this parameter and $\tau_{0,\text{pris}}$. As a result, uniquely identifying $\tau_{0,\text{pyr}\langle a\rangle}$ using only the yield stress data is difficult. To overcome this problem, this parameter was considered in both groups. Despite the relatively large range selected for $h_0^{\text{tw-s}}$, its effect is not significant at any loading conditions. Therefore, it has been removed from the optimization procedure and its value has been fixed as 150 MPa to save computation time.

3.3.3.4. Determined parameter set

Fig. 3.18 shows the results from 20 independent optimization runs. It can be seen that the optimization methodology recovers the original parameters for the first group of

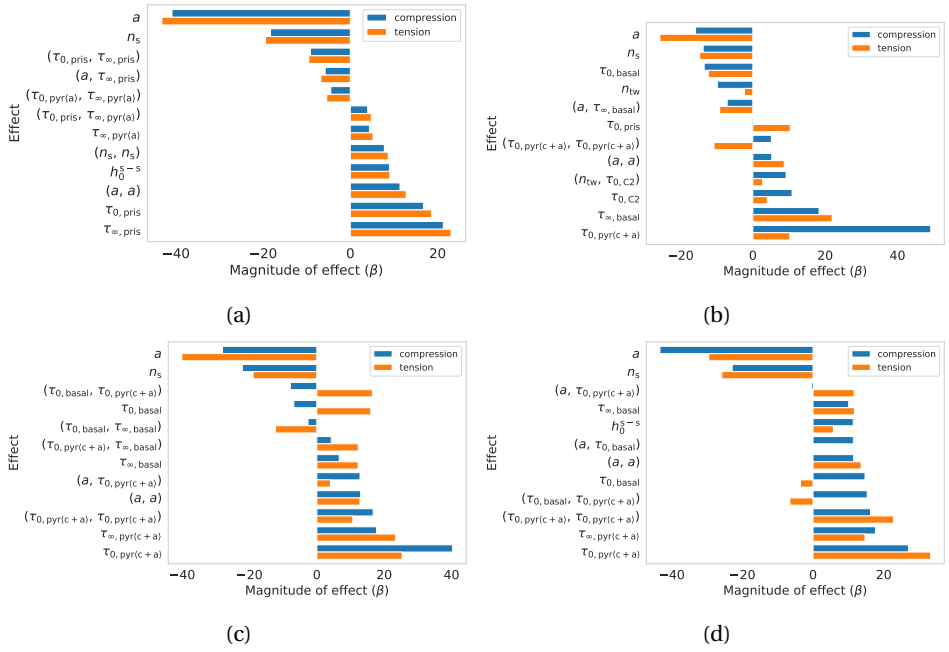

Fig. 3.17: The main effects and interaction effects for the stress at ε_p=0.3 under the different loading conditions shown in Fig. 3.15, (a) loading condition a – uniaxial compression/tension along RD, (b) loading condition b – uniaxial compression/tension in the RD-ND plane at 45° from both RD and ND, (c), loading conditions c – uniaxial compression/tension along ND, and (d) loading condition d – plane-strain compression/tension along RD with TD as the constraint direction. The results are shown for $\dot{\varepsilon}$= 0.1 s^{-1} under compression and tension. The magnitudes of the effects are calculated using Eq. (3.10) and Eq. (3.11), and they are in MPa. The material parameters are defined in Table 3.7.

parameters, namely $\tau_{0,\text{basal}}$, $\tau_{0,\text{pris}}$, $\tau_{0,\text{pyr}\langle a\rangle}$, $\tau_{0,\text{pyr}\langle c+a\rangle}$, $\tau_{0,\text{T1}}$, $\tau_{0,\text{C2}}$, n_s, and n_{tw}, with an accuracy of ±1%. This reveals that all these parameters have a unique contribution to the CP model, and the optimization methodology is able to capture this uniqueness.

Unlike the first group of parameters, a distribution is achieved for the optimized solutions of the second group of parameters, namely $\tau_{\infty,\text{basal}}$, $\tau_{\infty,\text{pris}}$, $\tau_{\infty,\text{pyr}\langle a\rangle}$, $\tau_{\infty,\text{pyr}\langle c+a\rangle}$, $h_0^{\text{s-s}}$, and a. It should be noted that the error in the predicted stress–strain curves is less than 0.6 MPa for all 20 optimization runs despite the distribution achieved for these parameters. As mentioned in Section 2.3.1, a and τ_∞ are strongly correlated and mutually dependent. Considering both parameters in the optimization leads to an underdetermined system that has multiple feasible solutions. Therefore, no unique solution can be achieved when both a and τ_∞ are considered in the optimization procedure.

The mutually dependent parameters in CP models are, in general, a serious obstacle when aiming to identify a unique solution for the associated optimization problems. This issue is often not noticed (or maybe not reported) since the optimization methodologies are usually performed using experimental data. In this case, there is no reference set of parameters to evaluate the quality of the solution, and a parameter set is considered as good if the experimental data can be reproduced. One way to

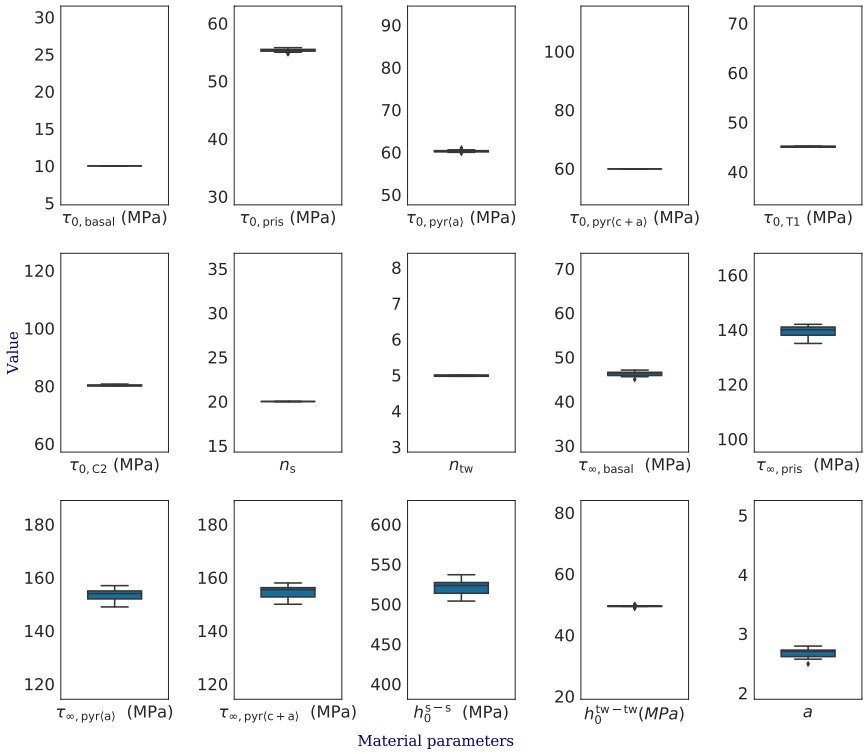

Fig. 3.18: The box plot of the optimized solutions from 20 optimization runs for the phenomenological CP model incorporating deformation twinning.

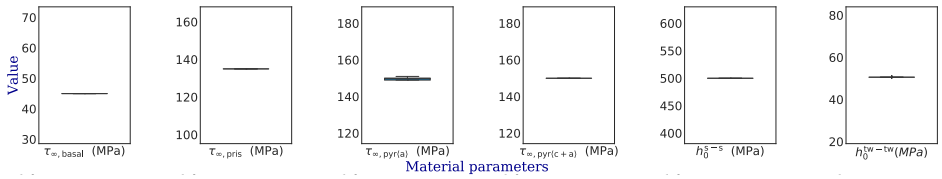

Fig. 3.19: The box plot of the optimized solutions from 20 optimization runs for the phenomenological CP model incorporating deformation twinning when a is removed from the optimization procedure and fixed at a value of 2.5.

overcome such a problem is to identify these parameters and to remove them from the optimization process. Fig. 3.19 shows the results from 20 independent optimization runs when a is removed from the optimization procedure and fixed at a value of 2.5. It can be seen that now all the parameters can be determined uniquely, and the optimization methodology can recover the original values for the parameters. On the long run, it is desirable to develop constitutive models without such redundant parameters.

3.4. Conclusions

In this study, a novel and computationally efficient approach was developed for identifying constitutive parameters from macroscopic stress–strain data. The power of this methodology was demonstrated on the examples of a phenomenological, a dislocation-density-based CP model, and a phenomenological model incorporating deformation twinning. It was shown that the methodology reliably reproduces the known parameters of simulated reference compression/tension tests. Moreover, the outcome of the identification procedure helps to quantitatively and systematically study the role of the underlying single crystal parameters in predicting the deformation behavior of a polycrystalline aggregate.

The main observations for the phenomenological model are:

- The only significant parameters at the yield point are τ_0 and n with positive and negative effects, respectively.
- At higher strains, all parameters, except h_0, have a significant effect with negative effect for n and a and positive effect for τ_0 and τ_∞.
- The main effect for h_0 is much smaller than for all other parameters.
- The optimization methodology can reach a unique solution for τ_0 and n, while it predicts a (small) distribution for the other parameters.

The main observations for the dislocation-density-based model are:

- The main effect for p, τ_0^*, ΔF, and ρ_0^α is positive, i.e. the resulting stress increases with an increase in these parameters.
- The main effect for q and v_0 is negative, i.e. the resulting stress decreases with an increase in these parameters.

- p, q, ΔF, and τ_0^* have a strong interaction with each other, and the CP model is underdetermined for a large range of temperature and strain rates.
- There is no significant interaction between d^{α}_{anni} and C_λ and the other parameters, *i.e.* p, τ_0^*, ΔF, ρ_0^{α}, q, and υ_0. Therefore, the parameters can be grouped into two independent blocks.
- p, τ_0^*, ΔF, ρ_0^{α}, q, and υ_0 can be determined from the yield stress data, while d^{α}_{anni} and C_λ can be determined from the hardening behavior.
- The optimization methodology can reach a unique solution for ρ^{α}, d^{α}_{anni}, and C_λ, while it predicts a narrow distribution for τ_0^*, ΔF, p, q, and υ_0.

The main observations for the phenomenological model incorporating deformation twinning are:

- The significant parameters at the yield point are $\tau_{0,\text{basal}}$, $\tau_{0,\text{pris}}$, $\tau_{0,\text{pyr}\langle\text{a}\rangle}$, $\tau_{0,\text{pyr}\langle\text{c+a}\rangle}$, $\tau_{0,\text{T1}}$, $\tau_{0,\text{C2}}$, n_{s}, and n_{tw}. These parameters can be uniquely determined if a sufficiently variable set of loading conditions is used in the optimization procedure to capture the strong anisotropic plastic deformation behavior of hcp materials.
- There is a strong correlation between a and $\tau_{\infty,\text{basal}}$, $\tau_{\infty,\text{pris}}$, $\tau_{\infty,\text{pyr}\langle\text{a}\rangle}$, $\tau_{\infty,\text{pyr}\langle\text{c+a}\rangle}$, $h_0^{\text{s-s}}$, which prevents determining these parameters in an unambiguous and unique manner.
- One way to overcome the problem of correlated parameters is to identify these parameters with the help of the current methodology and to remove them from the optimization process. The results show that a unique solution for $\tau_{\infty,\text{basal}}$, $\tau_{\infty,\text{pris}}$, $\tau_{\infty,\text{pyr}\langle\text{a}\rangle}$, $\tau_{\infty,\text{pyr}\langle\text{c+a}\rangle}$, $h_0^{\text{s-s}}$ can be achieved, if a is removed from the optimization procedure.

References

[1] K. Sedighiani, M. Diehl, K. Traka, F. Roters, J. Sietsma, and D. Raabe, *An efficient and robust approach to determine material parameters of crystal plasticity constitutive laws from macro-scale stress–strain curves,* International Journal of Plasticity **134**, 102779 (2020).

[2] F. Roters, P. Eisenlohr, L. Hantcherli, D. Tjahjanto, T. Bieler, and D. Raabe, *Overview of constitutive laws, kinematics, homogenization and multiscale methods in crystal plasticity finite-element modeling: Theory, experiments, applications,* Acta Materialia **58**, 1152 (2010).

[3] J. Rice, *Inelastic constitutive relations for solids: An internal-variable theory and its application to metal plasticity,* Journal of the Mechanics and Physics of Solids **19**, 433 (1971).

[4] R. Asaro and J. Rice, *Strain localization in ductile single crystals,* Journal of the Mechanics and Physics of Solids **25**, 309 (1977).

[5] E. Voce, *The relationship between stress and strain for homogeneous deformations,* Journal of the Institute of Metals **74**, 537 (1948).

[6] J. Hutchinson, *Bounds and Self-Consistent Estimates for Creep of Polycrystalline Materials,* Proceedings of the Royal Society A: Mathematical, Physical and Engineering Sciences **348**, 101 (1976).

[7] U. Kocks, *Laws for Work-Hardening and Low-Temperature Creep,* Journal of Engineering Materials and Technology **98**, 76 (1976).

[8] D. Peirce, R. Asaro, and A. Needleman, *An analysis of nonuniform and localized deformation in ductile single crystals,* Acta Metallurgica **30**, 1087 (1982).

[9] D. Peirce, R. Asaro, and A. Needleman, *Material rate dependence and localized deformation in crystalline solids,* Acta Metallurgica **31**, 1951 (1983).

[10] R. Becker, *Analysis of texture evolution in channel die compression—I. Effects of grain interaction,* Acta Metallurgica et Materialia **39**, 1211 (1991).

[11] A. Arsenlis and D. Parks, *Crystallographic aspects of geometrically-necessary and statistically-stored dislocation density,* Acta Materialia **47**, 1597 (1999).

[12] A. Arsenlis and D. Parks, *Modeling the evolution of crystallographic dislocation density in crystal plasticity,* Journal of the Mechanics and Physics of Solids **50**, 1979 (2002).

[13] A. Arsenlis, D. Parks, R. Becker, and V. Bulatov, *On the evolution of crystallographic dislocation density in non-homogeneously deforming crystals,* Journal of the Mechanics and Physics of Solids **52**, 1213 (2004).

[14] L. Evers, D. Parks, W. Brekelmans, and M. Geers, *Crystal plasticity model with enhanced hardening by geometrically necessary dislocation accumulation,* Journal of the Mechanics and Physics of Solids **50**, 2403 (2002).

[15] L. Evers, W. Brekelmans, and M. Geers, *Scale dependent crystal plasticity framework with dislocation density and grain boundary effects,* International Journal of Solids and Structures **41**, 5209 (2004).

[16] L. Evers, W. Brekelmans, and M. Geers, *Non-local crystal plasticity model with intrinsic SSD and GND effects,* Journal of the Mechanics and Physics of Solids **52**, 2379 (2004).

[17] K. Cheong and E. Busso, *Discrete dislocation density modelling of single phase FCC polycrystal aggregates,* Acta Materialia **52**, 5665 (2004).

[18] A. Ma and F. Roters, *A constitutive model for fcc single crystals based on dislocation densities and its application to uniaxial compression of aluminium single crystals,* Acta Materialia **52**, 3603 (2004).

[19] A. Ma, F. Roters, and D. Raabe, *A dislocation density based constitutive model for crystal plasticity FEM including geometrically necessary dislocations,* Acta Materialia **54**, 2169 (2006).

[20] A. Ma, F. Roters, and D. Raabe, *On the consideration of interactions between dislocations and grain boundaries in crystal plasticity finite element modeling – Theory, experiments, and simulations,* Acta Materialia **54**, 2181 (2006).

[21] H. Gao and Y. Huang, *Geometrically necessary dislocation and size-dependent plasticity,* Scripta Materialia **48**, 113 (2003).

[22] S. Wong, M. Madivala, U. Prahl, F. Roters, and D. Raabe, *Acta Materialia A crystal plasticity model for twinning- and transformation-induced plasticity,* Acta Materialia **118**, 140 (2016).

[23] D. Cereceda, M. Diehl, F. Roters, D. Raabe, J. Perlado, and J. Marian, *Unraveling the temperature dependence of the yield strength in single-crystal tungsten using atomistically-informed crystal plasticity calculations,* International Journal of Plasticity **78**, 242 (2016), arXiv:1506.02224 .

[24] C. Reuber, P. Eisenlohr, F. Roters, and D. Raabe, *Dislocation density distribution around an indent in single-crystalline nickel : Comparing nonlocal crystal plasticity finite-element predictions with experiments,* Acta Materialia **71**, 333 (2014).

[25] P. Thamburaja and L. Anand, *Polycrystalline shape-memory materials: effect of crystallographic texture,* Journal of the Mechanics and Physics of Solids **49**, 709 (2001).

[26] Y. Lan, N. Xiao, D. Li, and Y. Li, *Mesoscale simulation of deformed austenite decomposition into ferrite by coupling a cellular automaton method with a crystal plasticity finite element model,* Acta Materialia **53**, 991 (2005).

[27] L. Anand and C. Su, *A theory for amorphous viscoplastic materials undergoing finite deformations, with application to metallic glasses,* Journal of the Mechanics and Physics of Solids **53**, 1362 (2005).

[28] L. Anand and C. Su, *A constitutive theory for metallic glasses at high homologous temperatures,* Acta Materialia **55**, 3735 (2007).

[29] S. Kalidindi, *Incorporation of deformation twinning in crystal plasticity models,* Journal of the Mechanics and Physics of Solids **46**, 267 (1998).

[30] A. Staroselsky and L. Anand, *Inelastic deformation of polycrystalline face centered cubic materials by slip and twinning,* Journal of the Mechanics and Physics of Solids **46**, 671 (1998).

[31] W. Marketz, F. Fischer, F. Kauffmann, G. Dehm, T. Bidlingmaier, A. Wanner, and H. Clemens, *On the role of twinning during room temperature deformation of γ-TiAl based alloys,* Materials Science and Engineering: A **329-331**, 177 (2002).

[32] A. Salem, S. Kalidindi, and S. Semiatin, *Strain hardening due to deformation twinning in α-titanium: Constitutive relations and crystal-plasticity modeling,* Acta Materialia **53**, 3495 (2005).

[33] C. Liu, P. Shanthraj, M. Diehl, F. Roters, S. Dong, J. Dong, W. Ding, and D. Raabe, *An integrated crystal plasticity–phase field model for spatially resolved twin nucleation, propagation, and growth in hexagonal materials,* International Journal of Plasticity **106**, 203 (2018).

[34] M. Bertin, C. Du, J. Hoefnagels, and F. Hild, *Crystal plasticity parameter identification with 3D measurements and Integrated Digital Image Correlation,* Acta Materialia **116**, 321 (2016).

[35] D. Raabe, M. Sachtleber, Z. Zhao, F. Roters, and S. Zaefferer, *Micromechanical and macromechanical effects in grain scale polycrystal plasticity experimentation and simulation,* Acta Materialia **49**, 3433 (2001).

[36] C. Zambaldi, Y. Yang, T. Bieler, and D. Raabe, *Orientation informed nanoindentation of α-titanium: Indentation pileup in hexagonal metals deforming by prismatic slip,* Journal of Materials Research **27**, 356 (2012).

[37] C. C. Tasan, M. Diehl, D. Yan, C. Zambaldi, P. Shanthraj, F. Roters, and D. Raabe, *Integrated experimental-simulation analysis of stress and strain partitioning in multiphase alloys,* Acta Materialia **81**, 386 (2014).

[38] A. Chakraborty and P. Eisenlohr, *Evaluation of an inverse methodology for estimating constitutive parameters in face-centered cubic materials from single crystal indentations,* European Journal of Mechanics, A/Solids **66**, 114 (2017).

[39] V. Herrera-Solaz, J. LLorca, E. Dogan, I. Karaman, and J. Segurado, *An inverse optimization strategy to determine single crystal mechanical behavior from polycrystal tests: Application to AZ31 Mg alloy,* International Journal of Plasticity **57**, 1 (2014).

[40] S. Mandal, B. T. Gockel, and A. Rollett, *Application of canonical correlation analysis to a sensitivity study of constitutive model parameter fitting,* Materials and Design **132**, 30 (2017).

[41] R. Lebensohn and C. Tomé, *A self-consistent anisotropic approach for the simulation of plastic deformation and texture development of polycrystals: Application to zirconium alloys,* Acta Metallurgica et Materialia **41**, 2611 (1993).

[42] R. Mahnken and E. Stein, *A unified approach for parameter identification of inelastic material models in the frame of the finite element method,* Computer Methods in Applied Mechanics and Engineering **136**, 225 (1996).

[43] A. Saleeb, A. Gendy, and T. Wilt, *Parameter-estimation algorithms for characterizing a class of isotropic and anisotropic viscoplastic material models,* Mechanics Time-Dependent Materials **6**, 323 (2002).

[44] Z. Yang and A. Elgamal, *Application of unconstrained optimization and sensitivity analysis to calibration of a soil constitutive model,* International Journal for Numerical and Analytical Methods in Geomechanics **27**, 1277 (2003).

[45] A. Andrade-Campos, S. Thuillier, P. Pilvin, and F. Teixeira-Dias, *On the determination of material parameters for internal variable thermoelastic-viscoplastic constitutive models,* International Journal of Plasticity **23**, 1349 (2007).

[46] T. Kolda, R. Lewis, and V. Torczon, *Optimization by Direct Search: New Perspectives on Some Classical and Modern Methods,* SIAM Review **45**, 385 (2003).

[47] J. Qu, Q. Jin, and B. Xu, *Parameter identification for improved viscoplastic model considering dynamic recrystallization,* International Journal of Plasticity **21**, 1267 (2005).

[48] T. Furukawa, T. Sugata, S. Yoshimura, and M. Hoffman, *An automated system for simulation and parameter identification of inelastic constitutive models,* Computer Methods in Applied Mechanics and Engineering **191**, 2235 (2002).

[49] D. Agius, M. Kajtaz, K. Kourousis, C. Wallbrink, C. Wang, W. Hu, and J. Silva, *Sensitivity and optimisation of the Chaboche plasticity model parameters in strain-life fatigue predictions,* Materials and Design **118**, 107 (2017).

[50] L. Moran, L. Hanlon, A. Von Kienlin, B. McBreen, S. McBreen, S. McGlynn, J. French, R. Preece, Y. Kaneko, O. Williams, K. Bennett, and R. Kippen, *European Space Agency, (Special Publication) ESA SP*, 552 (2004) pp. 653–656, arXiv:0404126 [astro-ph] .

[51] M. Bezerra, R. Santelli, E. Oliveira, L. Villar, and L. Escaleira, *Response surface methodology (RSM) as a tool for optimization in analytical chemistry,* Talanta **76**, 965 (2008).

[52] F. Roters, M. Diehl, P. Shanthraj, P. Eisenlohr, C. Reuber, S. Wong, T. Maiti, A. Ebrahimi, T. Hochrainer, H. Fabritius, S. Nikolov, M. Friák, N. Fujita, N. Grilli, K. Janssens, N. Jia, P. Kok, D. Ma, F. Meier, E. Werner, M. Stricker, D. Weygand, and D. Raabe, *DAMASK – The Düsseldorf Advanced Material Simulation Kit for modeling multi-physics crystal plasticity, thermal, and damage phenomena from the single crystal up to the component scale,* Computational Materials Science **158**, 420 (2019).

[53] D. Goldberg, *Genetic Algorithms in Search, Optimization and Machine Learning*, 1st ed. (Addison-Wesley Longman Publishing Co., Inc., 1989).

[54] A. Beg and M. Islam, *Advantages and limitations of genetic algorithms for clustering records,* Proceedings of the 2016 IEEE 11th Conference on Industrial Electronics and Applications, ICIEA 2016 , 2478 (2016).

[55] T. Harth, S. Schwan, J. Lehn, and F. Kollmann, *International Journal of Plasticity*, Vol. 20 (2004) pp. 1403–1440.

[56] T. Furukawa and G. Yagawa, *Inelastic constitutive parameter identification using an evolutionary algorithm with continuous individuals,* International Journal for Numerical Methods in Engineering (1997), 10.1002/(SICI)1097-0207(19970330)40:6<1071::AID-NME99>3.0.CO;2-8.

[57] R. De-Carvalho, R. Valente, and A. Andrade-Campos, *Optimization strategies for non-linear material parameters identification in metal forming problems,* Computers and Structures **89**, 246 (2011).

[58] C. Ahn and R. Ramakrishna, *A genetic algorithm for shortest path routing problem and the sizing of populations,* IEEE Transactions on Evolutionary Computation **6**, 566 (2002).

[59] A. Umbarkar and P. Sheth, *Crossover operators in genetic algorithms: a review,* ICTACT Journal on Soft Computing **06**, 1083 (2015).

[60] N. Soni and T. Kumar, *Study of Various Mutation Operators in Genetic Algorithms,* International Journal of Computer Science and Information Technologies (IJCSIT) (2014).

[61] G. Box and K. Wilson, *On the Experimental Attainment of Optimum Conditions,* Journal of the Royal Statistical Society: Series B (Methodological) (1951), 10.1111/j.2517-6161.1951.tb00067.x.

[62] C. Doncaster and A. Davey, *Analysis of Variance and Covariance: How to Choose and Construct Models for the Life Sciences* (2007).

[63] D. Dever, *Temperature dependence of the elastic constants in α-iron single crystals: Relationship to spin order and diffusion anomalies,* Journal of Applied Physics **43**, 3293 (1972).

[64] J. Adams, D. Agosta, R. Leisure, and H. Ledbetter, *Elastic constants of monocrystal iron from 3 to 500 K,* Journal of Applied Physics **100** (2006), 10.1063/1.2365714.

[65] R. Madec and L. Kubin, *Dislocation strengthening in FCC metals and in BCC metals at high temperatures,* Acta Materialia **126**, 166 (2017).

[66] J. Zhang and S. Joshi, *Phenomenological crystal plasticity modeling and detailed micromechanical investigations of pure magnesium,* Journal of the Mechanics and Physics of Solids **60**, 945 (2012).

4

ANALYSIS OF THE DISLOCATION DENSITY-BASED MODEL

Abstract

Physics-based crystal plasticity models rely on certain statistical assumptions for the collective behavior of dislocation populations on one slip system and their interactions with the dislocations on the other slip systems. One main advantage of using such physics-based constitutive dislocation models in crystal plasticity kinematic frameworks is their suitability for predicting the mechanical behavior of polycrystals over a wide range of deformation temperatures and strain rates with the same physics-based parameter set. In this study, the ability of a widely used temperature-dependent dislocation-density-based crystal plasticity formulation to reproduce experimental results, with a main focus on the yield stress behavior, is investigated. First, the material parameters are identified from experimental macroscopic stress-strain curves using the optimization methodology introduced in Chapter 3. For this purpose, a systematic set of compression tests on interstitial free (IF) steel samples is performed at various temperatures and strain rates. Next, the influence of the individual parameters on the observed behavior is analyzed. Based on mutual interactions between various parameters, the ability to find a single parameter set is discussed. This allows identifying shortcomings of the constitutive law and sketch ideas for possible improvements. Particular attention is directed toward identifying possibly redundant material parameters, narrowing the acceptable range of material parameters based on physical criteria, and modifying the crystal plasticity formulation numerically for high-temperature use.

Parts of this chapter have been published in Sedighiani *et al.* [1].

4.1. Introduction

Crystal plasticity (CP) models are powerful and indispensable tools for modeling and understanding the relationship between the microstructure and the mechanical behavior of crystalline materials [2]. In CP modeling, the deformation's kinetics is related to the physics of the material behavior through the constitutive law. Such constitutive law relies on internal state variables that constitute and track the deformation history. Various constitutive flow laws have been developed during the last few decades, e.g. phenomenological constitutive models [3–6] and physics-based constitutive models [7–11].

Phenomenological models use laws with fitted variables and are numerically cost-effective. While they incorporate the relevant features of plastic slip in metals via kinematic and kinetic assumptions, phenomenological models suffer from the drawback that they consider very limited physical information to define slip rates and the evolution of the internal variables. In other words, the internal variables are not directly related to physical quantities and, hence, their evolution laws are not related to physical processes, such as dislocation production, annihilation, interaction with other defects or thermal activation of specific dislocation processes. Therefore, any value of the constitutive parameters is deemed valid as long as the behavior of interest, such as the stress-strain curve, is predicted correctly, under the exact boundary and starting conditions where the parameters were fitted. This means, however, that there is no guarantee that the model correctly predicts the behavior for other loading conditions, e.g. strain rate and temperature, than the ones that have been used for fitting [12].

In contrast to phenomenological models, physics-based constitutive laws rely on physically-defined internal variables, e.g. typically dislocation densities, twin volume fractions, etc. [2]. Dislocations are the most crucial internal variable type in the case of plasticity of materials with medium and high stacking fault energy as they are the carriers of the plastic deformation. In a physics-based crystal plasticity model, the plastic deformation is defined by the dislocation motion, and the hardening behavior is expressed in terms of generation, interaction, and annihilation of dislocations on different slip systems. Orowan [13] related the plastic slip rate on a given slip system to the motion of dislocations through an average dislocation velocity. This dislocation motion is impeded by short-range and long-range barriers. The short-range barriers are those that can be overcome by thermal activation, while the long-range barriers are those which are too strong for thermal activation to be significant, such as the interaction between dislocations. At a finite temperature, thermal energy helps a dislocation to overcome short-range barriers by thermal activation, and the average dislocation velocity is determined by the probability of a successful jump from one obstacle to the next [7, 14, 15]. Therefore, the average dislocation velocity is temperature-dependent. Kocks *et al.* [7] decomposed the stress required for dislocation glide into an athermal component and a thermal component, and they related the probability of the successful jumps and the average dislocation velocity to the thermal stress.

The ideas of Orowan [13] and Kocks *et al.* [7] form the basis for most temperature-dependent physics-based crystal plasticity models: Nemat-Nasser *et al.* [8] suggested a dislocation-density-based model for face-centered cubic (fcc) and body-centered cubic (bcc) crystals which considers the effect of short-range and

long-range barriers on the motion of dislocations. Voyiadjis and Abed [16] proposed a constitutive model based on thermally activated dislocation glides, which takes into account the effect of the evolution of mobile and forest dislocation densities on the thermal and athermal parts of flow stress. Arsenlis and Parks [9] implemented thermally activated dislocation-based constitutive laws into a crystal plasticity finite element (CPFE) simulation framework. Cheong and Busso [17] developed a model in which the dislocations are discretized into edge and screw components with intrinsically different relative mobilities and dynamic recovery processes. Ma and Roters [10] and Ma *et al.* [18, 19] developed a dislocation-density-based constitutive model for fcc and bcc crystals in which the geometrically necessary dislocation density is used in addition to the statistically stored dislocations in order to consider strain gradients and the microstructural size sensitivity. Evers *et al.* [20, 21] developed a non-local crystal plasticity model that incorporates the interactions of various types of dislocation densities. Reuber *et al.* [22] developed a model that explicitly accounts for the spatial redistribution of sign-polarized dislocation populations due to their motion. Monnet *et al.* [23] proposed a dislocation-density-based crystal plasticity law for predicting the deformation behavior of bcc crystal at low- and high-temperature regimes. Alankar *et al.* [24] presented a model for bcc crystals in which they considered the individual behavior of screw and edge dislocations. Cereceda *et al.* [25] formulated and parametrized a velocity law for screw dislocations in bcc Tungsten based on atomistic simulations. Yuan *et al.* [26, 27] developed a model for single crystal plasticity which considers both dislocation glide and climb. Later, Yuan *et al.* [28] incorporated the dislocation line energy into the dislocation-density-based crystal plasticity model. Castelluccio and McDowell [29] presented a cyclic crystal plasticity model by introducing a back stress formulation related to the mesoscale dislocation substructure. Luscher *et al.* [30], Addessio *et al.* [31] developed a dislocation-density-based model to investigate the deformation of metals under dynamic and shock-loading conditions. Keshavarz and Ghosh [32, 33], Ghosh *et al.* [34], Keshavarz *et al.* [35] proposed crystal plasticity constitutive models for modeling Ni-based superalloys in which the grain-scale response is obtained from the homogenization of the dislocation-density-based subgrain model. Alankar *et al.* [36] proposed a constitutive plasticity model for the prismatic slip in hexagonal α-titanium. Wong *et al.* [37] incorporated both, transformation-induced plasticity and twinning-induced plasticity in a thermally activated dislocation-density-based crystal plasticity model. Patra and McDowell [38, 39], Li *et al.* [40], Chakraborty and Bulent Biner [41] developed crystal plasticity models for the inelastic deformation of irradiated bcc metals. Patra and McDowell [42] presented a coupled continuum damage framework with a dislocation density-based crystal plasticity model to simulate failure initiation in irradiated bcc materials. Zhao *et al.* [43, 44] developed a coupled full-field model between fast Fourier transform-based crystal plasticity model and a phase-field recrystallization model to investigate the evolution of microstructural and micromechanical fields in polycrystals during dynamic recrystallization. Ha *et al.* [45] developed a new time-integration algorithm for the dislocation-density-based CP model in which stresses and dislocation densities are solved simultaneously. Furthermore, constitutive laws developed based on such thermally activated dislocation slip formulation is extensively used to investigate different deformation behavior such as the impact of hydrogen on the

plastic deformation of metal under monotonic and cyclic loading [46], the contribution of non-Schmid effects on the deformation behavior of Fe single crystal [47], the development of residual phase stresses due to processing in additively manufactured two-phase steel [48], the impact of crystallographic orientations on the evolution of misorientations and residual strains in Zircaloy [49], the deformation behavior of irradiated metals [50–52], the single crystal behavior of nanostructured pure Ti [53]. These are only a few examples of the diverse models developed in the last few decades based on the temperature-dependent physics-based concept introduced by Kocks *et al.* [7].

All such physics-based CP models have a large number of adjustable material parameters [54]. Most of these constitutive parameters have a physical meaning, and the order of magnitude for them and most of their physics-defined upper and lower bounds are known [10, 54, 55]. Physics-based models are, therefore, only correctly parametrized for a specific material under the two conditions that they predict the correct behavior (e.g. flow curves) *and* their parameters (e.g. the stacking fault energy) have the appropriate values. The advantage of a physically parameterized model is its *predictive* capability over a broad range of loading conditions using a single set of material parameters, i.e. all loading conditions for which the underlying physical processes do not change.

However, even though in physics-based CP models the order of magnitude for most of the parameters is known, a remaining obstacle for the routine use is posed by the complexity of calibrating its parameters for a desired material. In this chapter, the presented methodology in Chapter 3 is employed to determine the constitutive parameters of the dislocation-density-based CP model introduced in Section 2.3.3. A systematic series of compression tests were conducted at different deformation temperatures and strain rates on interstitial-free (IF) steel samples. The stress–strain curves from these experiments are used to determine the constitutive parameters. Furthermore, the uniqueness of the identified parameters is investigated. For this purpose, it is necessary first to understand the impact of the single-crystal parameters on the deformation behavior of polycrystals and second, to analyze the complex and non-linear interactions among the variables. The methodology introduced in Chapter 3 is also used for this task as it allows to quantitatively analyze the effect of different constitutive parameters and their interactions. Based on this analysis, the relevance and impact of the individual material parameters and their interactions are discussed. Moreover, the shortcomings of the constitutive law are addressed, and tighter bounds than those found in the literature are presented for selected parameters. The temperature-dependent motion of dislocations in the constitutive law used in this chapter has the same basis as the one proposed by Kocks *et al.* [7]. Therefore, most of the conclusions made in this study are applicable also to many other models that use the same concept, and this knowledge can help improve existing or newly developed constitutive laws.

This chapter is organized as follows. Section 4.2 presents the experimental procedure and results of the compression tests conducted on IF steel at different temperatures and strain rates. This section is followed by a description of the simulation procedure and setup in Section 4.3. The identified material parameters and their effects are presented in Section 4.4. The results are discussed in Section 4.5, which includes a discussion on the high-temperature instability of the CP model, acceptable

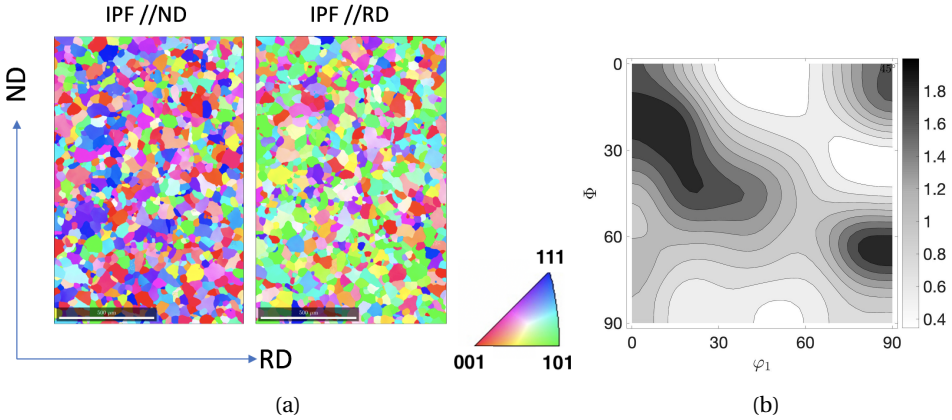

(a) (b)

Fig. 4.1: (a) Electron backscatter diffraction inverse pole figure map of the hot rolled IF-steel measured across the thickness (ND) perpendicular to the rolling direction (RD), and (b) $\varphi_2 = 45^\circ$ ODF section of the as-received hot-rolled IF steel.

physical ranges for some parameters, and the uniqueness of the identified material parameters. The main conclusions of this work are summarized in Section 4.6.

4.2. Experiments

4.2.1. Material

The material used in the present study is an IF steel with chemical composition as given in Table 6.1. The initial microstructure and crystallographic texture of the material were measured across the thickness (ND) perpendicular to the rolling direction (RD) using electron backscatter diffraction (EBSD). Standard metallographic techniques were used to prepare the specimens for characterization. Analysis of the EBSD data was performed using the TSL OIM software. The grain structure is almost completely equiaxed, and the material exhibits a mild texture, see Fig. 4.1.

Table 4.1: The chemical composition of the IF steel considered in this study.

element	C	Mn	S	Ti	N	Al	Cr	Fe
wt. (%)	0.002	0.095	0.006	0.045	0.002	0.05	0.02	balance

4.2.2. Compression testing

The uniaxial compression tests were performed in a Bähr DIL 805A/D deformation dilatometer. Cylindrical specimens with a diameter of 3 mm and a height of 6 mm were extracted by wire electrical discharge machining from the as-delivered hot-rolled sheet along the rolling direction. The temperature of the specimens was measured during the heating and deformation by means of a thermocouple attached to the surface of the specimen. The specimens were heated to the deformation temperatures with a heating

rate of 50 K s^{-1} and then held at the deformation temperature for 2 s before applying the deformation.

Specimens were deformed to a logarithmic strain of about 0.65. However, for a few cases of low temperatures and high strain rates, the applied strain was limited to 0.4 or 0.5 to prevent exceeding the load limit of the machine. Nine different deformation temperatures, namely 323, 373, 473, 573, 673, 773, 873, 973, and 1073 K, and three different strain rates, namely 0.01, 0.1, and 1.0 s^{-1}, were used in compression tests. All tests were performed at isothermal loading conditions. However, for low temperature and high strain rate cases of (T, $\dot{\varepsilon}$) = (323 K, 1.0 s^{-1}), (373 K, 1.0 s^{-1}), and (473 K, 1.0 s^{-1}), a temperature rise of 31, 26, and 11 K, respectively, was observed. For all other experiments, the temperature rise during deformation was negligible.

The equivalent true stress–logarithmic strain curves obtained from the compression tests at different temperatures and strain rates are shown in Fig. 4.2. Generally, it can be seen that the hardening rate decreases with an increase in deformation temperature for a given strain rate, and it increases with an increase in strain rate for a fixed deformation temperature. In this work, all comparisons between simulated and the experimental data are performed using the equivalent true stress and equivalent logarithmic strain. For the sake of brevity, they will be referred to as stress and strain, respectively, in the remainder of this study.

Figure 4.3 shows the variation of yield stress with deformation temperature at different strain rates. It is obvious that the influence of deformation temperature and strain rate on the yield stress is significant for the tested conditions. For a given strain rate, a decrease in yield stress can be seen with an increase in temperature. In contrast, the yield stress increases with an increase in strain rate for a given deformation temperature. However, the rate of change in the yield stress is considerably dependent on the deformation temperature and strain rate. At low temperatures, the yield stress is highly temperature and strain rate sensitive. The sensitivity to a change in deformation temperature or strain rate decreases by increasing the deformation temperature. An intermediate regime is observed at which the sensitivity to a change in deformation temperature or strain rate is minimal. After this transition regime, the dependency of the yield stress to temperature and strain rates increases again.

4.3. Simulations

The Fast Fourier Transform (FFT)-based spectral solver [56–58] implemented in DAMASK, see Section 2.4, is used to conduct CP simulations using the dislocation-density-based constitutive law outlined in Section 2.3.3. It is assumed that the slip occurs on 24 slip systems: 12 slip systems of $\langle 1\,1\,1\rangle\{1\,1\,0\}$ and 12 slip systems of $\langle 1\,1\,1\rangle\{1\,1\,2\}$. The representative volume element (RVE) is made of 512 grains, as shown in Fig. 4.4(a). A grid with dimension $8 \times 8 \times 8$ was used, i.e. each grain is represented by one voxel. The texture and the crystallographic orientations of the grains were assigned according to the EBSD map of the undeformed sample using the approach presented in [59]. Fig. 4.4(b) shows the $\varphi_2 = 45°$ ODF section of the RVE. Periodic boundary conditions hold on this RVE which was subjected to uniaxial compression up to around 0.4 strain.

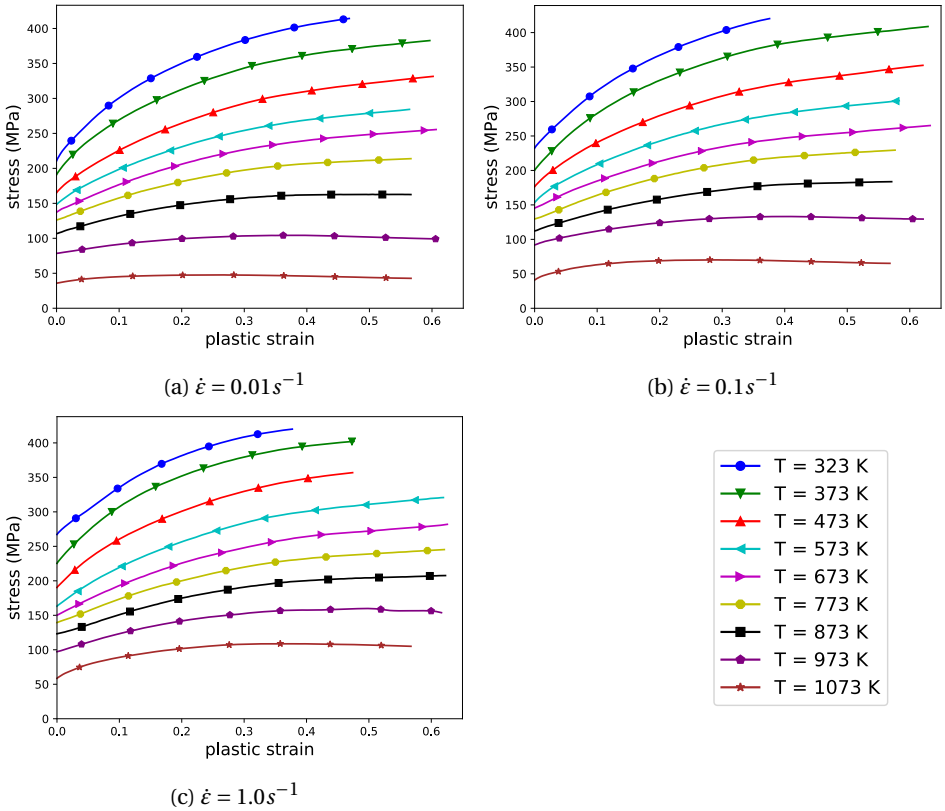

(a) $\dot{\varepsilon} = 0.01s^{-1}$

(b) $\dot{\varepsilon} = 0.1s^{-1}$

(c) $\dot{\varepsilon} = 1.0s^{-1}$

Fig. 4.2: Equivalent true stress-logarithmic strain curves for IF steel deformed by compression at various temperatures at strain rates of (a) $0.01s^{-1}$, (b) $0.1s^{-1}$, and (c) $1.0s^{-1}$.

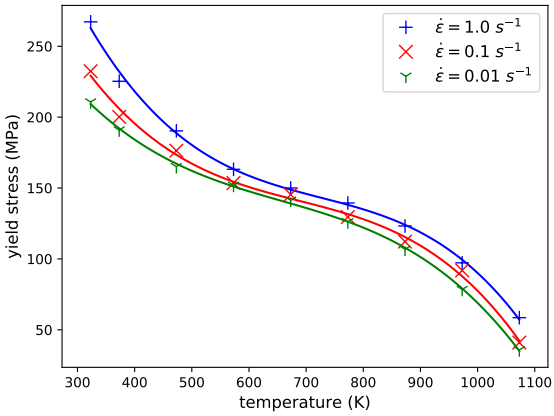

Fig. 4.3: Variation of yield stress with temperature for different strain rates. The solid lines are third-order regression lines.

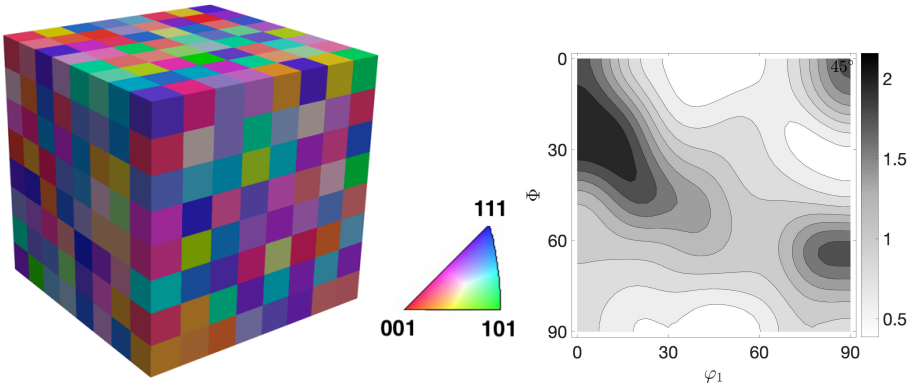

(a) (b)

Fig. 4.4: (a) Voxel representation of the RVE used in the CP simulations. The RVE is made of 512 grains and each grains is represented by one voxel. The coloring displays the Inverse Pole Figure (IPF) color map parallel to the loading (vertical) direction. (b) $\varphi_2 = 45^\circ$ ODF section of the RVE.

4.3.1. Adjustable model parameters

Table 4.2 lists the ranges of the adjustable model parameters used to build the off-line database for the response surface methodology, see Chapter 3 for more information. These ranges are selected based on the physical interpretation of the parameters and the values reported in the literature. However, the ranges provided in the literature for p and q are considered as too wide. Therefore, new ranges are introduced for them as elaborated in more detail later (Section 4.5.2).

Table 4.2: Ranges of the adjustable model parameters used in the optimization.

variable	description	units	range
ρ_0^α	initial dislocation density	m/m^3	$[10^{11}, 10^{13}]$
$v_0 = l\omega_0$	dislocation glide velocity pre-factor	m/s	$[10^2, 10^4]$
ΔF	activation energy for dislocation glide	J	$[1.3, 2.5] \times 10^{-19}$
p	p-exponent in glide velocity	–	[0.25, 0.7]
q	q-exponent in glide velocity	–	[1.2, 1.85]
τ_0^*	short-range barriers strength at 0 K	MPa	[300, 600]
C_λ	parameter controlling dislocation mean free path	–	[10, 50]
C_{anni}	Coefficient for dislocation annihilation	–	[2, 15]

4.3.2. Fixed model parameters

In this study, some of the parameters are considered to be known and fixed. These parameters will not be studied in the optimization procedure. The elastic coefficients are considered to be temperature-dependent, and they are taken from [60, 61]. The dislocation interaction coefficients are also taken as an average value for iron from [62], see Table 4.3. The Burgers vector is also a known material constant and equals 0.248 nm.

Table 4.3: Coefficients of interaction between different slip systems.

self	coplanar	collinear	orthogonal	glissile	sessile
0.1	0.1	0.72	0.053	0.137	0.073

4.4. Results

The values selected for material parameters strongly influence a crystal plasticity model's ability to correctly predict a specific material's deformation behavior. Therefore, a prerequisite for utilizing any constitutive models is determining a proper set of material parameters. Theoretically, most of the material parameters for a physics-based crystal plasticity model can be determined directly from single-crystal experiments [63, 64]. However, since engineering materials are usually only available as

polycrystals after synthesis, homogenization, and processing, it is more convenient to identify the material parameters from experimental macroscopic tests such as stress–strain data. This methodology introduced in Chapter 3 is used here to identify the material parameters from macroscopic stress–strain curves for IF steel. The methodology is also employed to quantitatively and systematically analyze the relatively complex dislocation-density-based CP model.

4.4.1. Optimized parameters

Grouping the parameters

It was shown in Chapter 3 that the yield stress is controlled mainly by p, τ_0^*, ΔF, ρ_0^α, q, and ν_0, while the hardening behavior depends mainly on C_{anni} and C_λ. In addition, there is no significant interaction between C_{anni} and C_λ on the one hand and p, τ_0^*, ΔF, ρ_0^α, q, and ν_0 on the other hand. This opens the possibility of splitting the material parameters into two groups for the RSM analysis and determining parameters in these groups independently. For instance, using experimental data for yield stress alone is sufficient for accurate identification of p, τ_0^*, ΔF, ρ_0^α, q, and ν_0. In the following, the material parameters are identified based on the grouping approach described in the previous section. The first group includes p, τ_0^*, ΔF, ρ^α, q, and ν_0, and the second group includes C_{anni} and C_λ, see Section 3.3.2.4 for more details on grouping the parameters.

Identified material parameters

Table 4.4 lists the optimized constitutive parameters obtained for IF steel. This set of parameters can be used to capture the temperature and strain rate sensitivity of the plastic deformation for a wide range of temperatures and strain rates. CP simulations are performed using this single set of parameters, and the results obtained for yield stress and hardening behavior are discussed in Section 4.4.1.1 and Section 4.4.1.2, respectively. In addition, the uniqueness and dependency of these parameters are discussed in Section 4.5.3.

Table 4.4: Optimized constitutive parameters for IF steel.

ρ_0^α (m^{-2})	ν_0 (ms^{-1})	ΔF (J)	τ_0^* (MPa)	p	q	C_λ	C_{anni}
2.81×10^{12}	1.4×10^{3}	1.57×10^{-19}	454	0.325	1.55	23.3	7.4

4.4.1.1. Yield stress prediction

The yield stress in dependence of temperature predicted with the optimized parameters is shown in Fig. 4.5. The experimental data is given for comparison. It can be seen that the crystal plasticity model is capable of predicting the yield stress over a wide range of temperatures and strain rates. Moreover, the model is able to capture the rate sensitivity at different temperatures and vice versa. The maximum error observed for temperatures lower than 773 K is approximately 5.7 MPa, which is for the loading condition of $T = 373$ K and $\dot{\varepsilon}_p = 1.0\ \text{s}^{-1}$. However, the model fails to correctly predict the material response at temperatures above 800 K. Around this point, there is a second pronounced drop in the experimental data, while the simulations predict only a much smaller decrease.

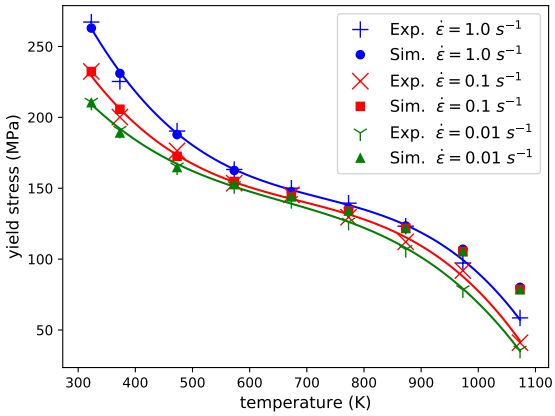

Fig. 4.5: Predicted yield stress versus temperature for optimized parameters as compared with experimental data. The solid lines are third-order regression lines for the experimental data. The crystal plasticity model is capable of predicting the yield stress over a wide range of temperatures and strain rates using a single set of material parameters. However, the model fails to correctly predict the material response at temperatures above 800 K. This indicates that the CP model does not include some physical effects occurring at elevated temperatures.

To investigate the observed discrepancy between the simulation results and the experimental data, Eq. (2.29) is rewritten for the resolved shear stress as a function of shear rate and temperature:

$$\tau^\alpha = \tau_\mu^\alpha + \tau_T^{*\alpha} = \tau_\mu^\alpha + \tau_0^* \left[1 - \left(- \frac{k_\mathrm{B} T \ln(\frac{|\dot{\gamma}^\alpha|}{\rho^\alpha b v_0 \omega_0})}{\Delta F} \right)^{\frac{1}{q}} \right]^{\frac{1}{p}}, \tag{4.1}$$

The derivative with respect to temperature of Eq. (4.1) can be calculated as:

$$\frac{\mathrm{d}\tau^\alpha}{\mathrm{d}T} = - \frac{\tau_0^* \left(- \frac{k_\mathrm{B} T \ln(\frac{|\dot{\gamma}^\alpha|}{\rho^\alpha b v_0 \omega_0})}{\Delta F} \right)^{\frac{1}{q}} \left[1 - \left(- \frac{k_\mathrm{B} T \ln(\frac{|\dot{\gamma}^\alpha|}{\rho^\alpha b v_0 \omega_0})}{\Delta F} \right)^{\frac{1}{q}} \right]^{-1+\frac{1}{p}}}{p\, q\, T}, \tag{4.2}$$

These equations indicate that the thermal stress smoothly decreases for an increase in temperature, see also Fig. 4.7. However, based on Eq. (4.2), the rate of decrease in thermal stress decreases with an increase in temperature until it becomes zero at a critical temperature, T_c. After this point, the thermal stress component vanishes, and the athermal component solely determines the resolved shear stress, see Section 4.5.1. Therefore, the CP model predicts a smooth decrease of the flow stress until a plateau at T_c is reached. Consequently, the second drop in the yield stress cannot be predicted using this type of thermally activated constitutive law. It should be noted that the ongoing decrease of the yield stress seen in the simulation results is only due to the dependency

of the athermal stress on temperature through the temperature dependency of the shear modulus. Consequently, this decrease is independent of the applied strain rate.

The experimentally observed drop of the yield stress for higher temperatures suggests the activation of a new mechanism at high temperatures. One possible explanation for this second drop is climb-based recovery during the heating period prior to deformation. The reduced initial dislocation densities to match the experimental data are listed in Table 4.5 for three exemplar loading conditions. The data show that a considerable amount of recovery is required before the onset of the plastic deformation to reproduce the experimental data. However, the specimens were machined from an as-delivered hot-rolled sheet and consequently, the EBSD data shows no in-grain misorientation patterns. Moreover, the high heating rate, $50\,\mathrm{K\,s^{-1}}$, used to heat up the samples prior to deformation kept the time at elevated temperatures short. Therefore, significant recovery does not seem a plausible explanation for the decrease of the yield stress for testing temperatures above approximately 800 K.

Table 4.5: The initial dislocation density needed to reproduce the experiential data for three exemplar loading conditions.

Loading conditions	(973 K, 0.1 s^{-1})	(1073 K, 0.01 s^{-1})	(1073 K, 1.0 s^{-1})
ρ_0^α (m/m^3)	2.14×10^{12}	5.85×10^{11}	1.50×10^{12}

A second possibility to explain the second drop is a dependency of the dislocation interaction coefficients, $\xi_{\alpha\alpha'}$, on the temperature. However, these interactions are typically considered as too strong for thermal activation to be significant. Nevertheless, Table 4.6 lists the required reduction in the dislocation interaction coefficients to reproduce the experimental data under the assumption of a constant ratio for all interactions. It can be seen that a significant reduction in the dislocation interaction coefficients is required. Therefore, the temperature dependency of the dislocation interaction coefficient would be too high to be physically plausible.

Table 4.6: The required reduction in the dislocation interaction coefficients to reproduce the experimental data for three exemplar loading conditions.

Loading conditions	(973 K, 0.1 s^{-1})	(1073 K, 0.01 s^{-1})	(1073 K, 1.0 s^{-1})
reduction (%)	25%	79%	47%

A third possibility to explain the second drop can be attributed to the way Eq. (2.29) is derived. In this form of thermally activated constitutive law, the short-range barriers are defined in an average sense using an average barrier's strength τ_0^* and average activation energy for glide ΔF. The average shape of the barriers is defined by p and q. However, short-range barriers may have different characteristics and physical meaning, and it may not be possible to present all types of barriers collectively as one average set. Therefore, one suggestion to solve this issue is to estimate the dislocation velocity using two or more different classes of short range obstacles. A promising approach for novel CP constitutive models targeting deformations at high temperature, therefore, is the consideration of a temperature dependence of obstacles. However, evaluating such new and more complex approach is beyond the scope of this study.

Finally, as a fourth possibility, the second drop of the yield stress observed at high temperatures can be attributed to the use of an isotropic effective shear modulus when calculating the effect of dislocation interactions in Eq. (2.27). Voigt's [65] and Reuss's [66] assumptions are the two approaches for calculating the equivalent shear modulus which predict the upper and lower bounds of the effective shear modulus [67], respectively. In this study, the former assumption is used. However, since for ferritic steels the anisotropy ratio $2C_{44}/(C_{11} - C_{12})$ rises from approximately 2.4 at 300 K to approximately 7.4 at 1173 K, the assumption of an isotropic equivalent shear modulus might be inappropriate for elevated temperatures. At least at the level of individual dislocations, it is well-established that the elastic anisotropy has strong effects on the yield behavior [68–70] and high elastic anisotropy may result in a pronounced softening irrespective of the mean shear modulus [69]. It remains an open question how this knowledge from small scale investigations can be used to improve the mean field approximations used in continuum scale CP formulations.

4.4.1.2. Hardening behavior

Fig. 4.6 shows the stress-strain curves for different loading conditions. Despite some discrepancies at high strains, there is an acceptable agreement between the simulation results and the experimental data at low temperatures. These discrepancies are mainly due to neglecting the cross-slip annihilation in the crystal plasticity formulations. Therefore, contrary to the experimental data, the simulated stress-strain curves do not tend to reach a steady-state condition. However, the deviation from the experimental results is noticeable at high temperatures. This difference is likely due to neglecting climb based dynamic recovery, which can significantly affect the strain hardening response. While the description for climb based recovery currently implemented in DAMASK is based on physical arguments [18, 37], it cannot be applied over a broad range of deformation temperatures, see Section 3.3.2.1. The model predicts a sharp increase in the climb velocity even for a small temperature rise. Consequently, the formulation becomes unstable after an increase of around 200 K to 300 K in the temperature. Because of the convergence issues, it was impossible to determine a unique set of recovery parameters applicable to a wide range of deformation temperature. Hence, here dynamic recovery due to the dislocation climb is neglected.

4.5. Discussion

4.5.1. Modifying the CP model for high-temperature applications

The optimization methodology introduced in Chapter 3 explores different combinations of material parameters at different loading conditions to find a set of parameters that reproduces all experimental results. Consequently, its success depends on the stability of the CP model within the whole parameter space. However, no converge was observed for certain parameter combinations at elevated temperatures. In this subsection, the reason for this instability and an approach to overcome this issue are discussed.

The constitutive law is based on the assumption that dislocation motion is impeded by short-range and long-range barriers. The short-range barriers are those barriers that can be overcome by thermal activation, while the long-range barriers are essentially independent of temperature since they are too strong for thermal activation to be

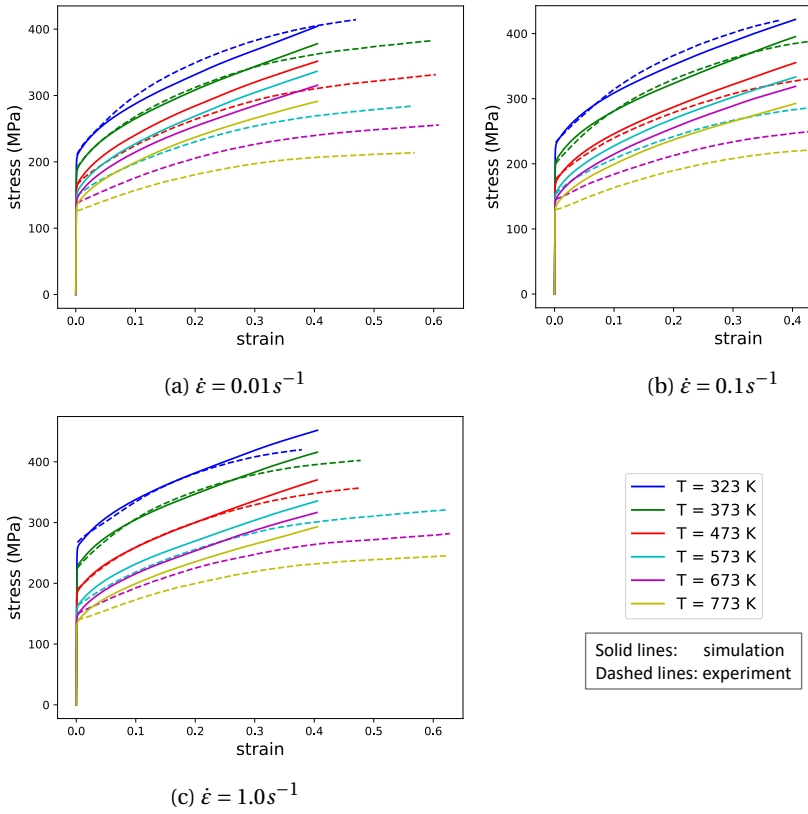

(a) $\dot{\varepsilon} = 0.01s^{-1}$

(b) $\dot{\varepsilon} = 0.1s^{-1}$

(c) $\dot{\varepsilon} = 1.0s^{-1}$

Fig. 4.6: Comparison between the model prediction and the experimental data for equivalent true stress-logarithmic strain curves deformed at various temperatures and at strain rates of (a) $0.01s^{-1}$, (b) $0.1s^{-1}$, and (c) $1.0s^{-1}$. The solid lines show the model prediction, and the dashed lines show the experimental data.

significant. Therefore, the resolved shear stress consists of a thermal component, $\tau_T^{*\alpha}$, and an athermal component, τ_μ^α. The thermal component is the main reason for the temperature and strain rate sensitivity of the flow stress. The athermal component is temperature-dependent only through the temperature dependency of the shear modulus, see Eq. (2.27)

An increase in the deformation temperature or a decrease in the applied strain rate increases the probability of thermal activation, which results in a reduction in the flow stress. However, there is a critical temperature T_c, above which there is sufficient thermal energy to overcome the short-range barriers by thermal activation alone, i.e. $\tau_T^{*\alpha} = 0$. The critical temperature can be calculated as:

$$T_c = -\frac{\Delta F}{k_B \log[\frac{|\dot{\gamma}^\alpha|}{\rho^\alpha b v_0}]} \tag{4.3}$$

For temperatures above the critical temperature, the shear rate formulation reduces to:

$$\dot{\gamma}^\alpha = \rho^\alpha b v_0 \exp\left(\frac{-\Delta F}{k_B T}\right) \qquad \text{for} \quad T \geqslant T_c \tag{4.4}$$

At the starting point of the plastic deformation, ρ^α can be considered as a constant parameter and equal to ρ_0^α for all samples. Therefore, all parameters in this equation are constant except T. Hence, for $T \geqslant T_c$, the shear rate is related to temperature only and does not depend on the effective applied stress. This results in numerical instabilities and convergence cannot be achieved at temperatures close to and above the critical temperature. Clearly, this behavior does not only cause numerical issues but it is also unphysical.

To understand why the original formulation does not give reasonable results for high temperatures, it should be recalled that the the dislocation velocity is controlled by the waiting time and running time, see Eq. (2.21). However, it was assumed that the running time is much smaller than the waiting time, and, hence, its effect is negligible. At temperatures close to or above the critical temperature, this assumption is no longer valid and the running time is comparable to or even higher than the waiting time. Therefore, it cannot be neglected.

The running velocity of a dislocation can be calculated using the second law of Newton [71]. The balance of the forces acting on a unit length of dislocation line can be written as:

$$m\dot{v}_r^\alpha = F^\alpha - B v_r^\alpha, \tag{4.5}$$

where $B v_r^\alpha$ is the drag force on a unit length of dislocation on the slip plane α, and m is the effective dislocation line mass, a measure that is usually taken to quantify the defect's inertia. F^α is the effective force acting on the same length of dislocation:

$$F^\alpha = (\tau^\alpha - \tau_\mu^\alpha) b = \tau_T^{*\alpha} b, \tag{4.6}$$

For low and moderate strain rates, the inertia term can be neglected, and the running velocity follows a viscous flow law:

$$v_r^\alpha = \frac{\tau_T^{*\alpha} b}{B}, \tag{4.7}$$

This allows to calculate the effective velocity as:

$$v^\alpha = \frac{l}{t_w + t_r} = \frac{1}{\frac{t_w}{l} + \frac{t_r}{l}} = \frac{1}{\frac{1}{v_b^\alpha} + \frac{1}{v_r^\alpha}}, \tag{4.8}$$

where $v_b^\alpha = t_w / l$ is the same velocity as presented earlier in Eq. (2.23).

For temperatures much lower than the critical temperatures, $v_b^\alpha \ll v_r^\alpha$ holds, and the original formulation is approximately recovered. However, with increasing temperature the running time will become more important until it finally fully determines the velocity. Therefore, numerical instabilities described in Eq. (4.4) are avoided and a physically sound behavior is achieved even for higher temperatures. This allows to find suitable parameter combinations from the whole parameter space, which does not contain "forbidden regions" of numerical instabilities (cf. Sections 4.5.2 and 4.5.3.2).

4.5.2. Physics-based limit for material parameters p and q

The profile of the barrier is controlled via parameters p and q, which are usually seen as free parameters with $0 < p \leq 1$ and $1 \leq q \leq 2$ [7]. However, these limits present only the extreme cases for which Eq. (4.1) is mathematically valid. In this section, the effect of these two parameters on the thermal stress is discussed and an approach is presented for determining (more narrow) physical limits.

The parameters p, q, ΔF, and τ_0^* together define the relation between the activation energy for dislocation glide, ΔG, and the thermal component of the stress, $\tau_T^{*\alpha}$. However, the development of thermal stress with temperature is affected differently by these parameters. ΔF is a coefficient for the temperature-dependent ratio inside the exponential term, and it linearly affects this ratio. As a result, the critical temperature T_c is linearly dependent on ΔF, while it is independent of the other three barrier parameters, see Eq. (4.3). The stress needed to overcome the barrier at 0 K is solely defined by the barrier strength τ_0^*. The curvature between 0 K and T_c, is defined by p and q. Although both of the parameters have a significant effect on the curvature for all temperatures between these two points, the effect of p and q is more pronounced at high and low temperatures, respectively (Fig. 4.7).

The limits proposed in the literature for p and q are defined based on mathematical arguments, and they describe the experimental observations only qualitatively. For $p > 1.0$ or $q < 1.0$, the sign of the curvature in the thermal stress versus temperature curve is reversed in comparison to the experimentally observed behavior. For $p \leq 0$ the resolved shear stress becomes larger than the barrier strength. To our knowledge, there is no such argument why q should be strictly smaller than 2. One reason, however, can be the intense effect of a large q at very low temperatures, i.e. a large q results in a significant drop in the thermal stress with a small increase in temperature. To prevent such an extreme condition, having an upper bound for q seems physically reasonable.

As outlined, the advised limits for p and q except the upper bound for q only ensure that the general shape of the curve is qualitatively reasonable. However, unwanted behavior is already observed when choosing values in the vicinity of

the limits. For instance, a small p results in an almost constant τ^* over a vast range of temperatures, see the red dashed line in Fig. 4.7. Although a wide temperature-insensitive regime has been observed for some materials, modeling this phenomenon by setting p to small values results in an unphysical barrier profile: A small p requires a higher value for ΔF which in turn increases T_c beyond reasonable values. It is physically more meaningful to attribute the temperature insensitivity to the critical temperature and the energy needed to overcome the barrier. As mentioned earlier, the thermal stress vanishes for temperatures larger than the critical temperature, and the temperature-insensitive regime can be achieved again.

Now the question arises whether there is a physics-based limit for p and q. There may be no exact answer to this question because of two main reasons: Firstly, these two parameters are introduced into the equations in a phenomenological way, and they are not derived based on any obstacle profiles. Secondly, there is a strong correlation between these two parameters, which results in a dependency of the limiting bounds to the value of the other parameter. For example, a range for p may be reasonable at a specific q, while it is not reasonable for another q.

Although no strict physics-based limit can be provided for p and q, it is still possible to limit these two parameters based on physical criteria. Combining Eqs. (2.29) and (4.4) gives:

$$\left(\frac{\tau_T^{*\alpha}}{\tau_0^*}\right)^p = 1 - \left(\frac{T}{T_c}\right)^{\frac{1}{q}} \tag{4.9}$$

A lower bound for p can be determined by setting a limit for the degree of flatness of the thermal stress before T_c. In other words, by setting a reasonable minimum increase in the stress ratio at a specific temperature ratio, a lower bound for p can be estimated. For example, by assuming the minimum required stress ratio of $\tau_T^{*\alpha}/\tau_0^* = 0.001$ at $T/T_c = 0.8$, the lower limit for p is approximately 0.25 when $q = 1$. The choice of $p = 0.25$ already results in an extremely wide temperature-insensitive regime below the critical temperature.

A literature survey shows, however, that small values for p, such as 0.1, have been frequently identified to match experimental data, e.g. [9, 45, 54, 72]. The reason for the frequently reported small p could be related to the numerical difficulties at temperatures close to or above the critical temperature, see Section 4.5.1. A small p has been used to increase the critical temperature, and consequently to postpone the numerical instability. However, the numerical difficulties can be overcome using the alternative formulation presented for dislocation velocity in Section 4.5.1 which makes artificially high critical temperatures unnecessary.

Equation (4.9) can also be used to estimate an upper bound for q. For example, by assuming a maximum acceptable drop of 5 % in the stress ratio, i.e. $\tau_T^{*\alpha}/\tau_0^* = 0.95$, at $T/T_c = 0.001$, the upper limit of $q \approx 1.85$ is achieved when $p = 0.5$. Even $q = 1.85$ results in a relatively sharp drop in the thermal stress for a very small increase in temperature. Therefore, it seems physically reasonable to use $q < 1.85$ when p is close to 0.5. It should be noted that the upper bound of q is strongly dependent on p, and an higher bound for q can be reasonable for a large p.

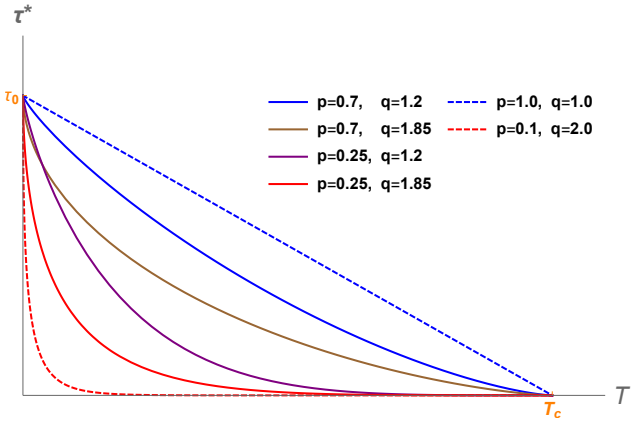

Fig. 4.7: Thermal stress versus temperature for different combinations of p and q. The usual limits for p and q are $0 < p \leq 1$ and $1 \leq q \leq 2$. Setting $p = 1$ and $q = 1$, the blue dashed line, results in a linear relationship between thermal stress and temperature, which corresponds to a physically unreasonable rectangular profile for the barrier and a non-smooth transition at the critical temperature. A small p, such as $p = 0.1$, results in a physically unacceptable flat curve for a vast range of temperatures below T_c, and it indirectly shifts the critical temperature, see the red dashed line. Although no strict physics-based limit can be provided for p and q, it is still possible to limit them in a physically measurable way using the slope of the curve at 0 K and T_c. The solid lines show the resulting curves for different combinations of p and $q$using the limits calculated in this study.

Setting $p = 1$ and $q = 1$ results in a linear relationship between thermal stress and temperature as shown in Fig. 4.7, which corresponds to a rectangular profile for the barrier. Such a barrier profile results in a non-smooth transition at the critical temperature. Therefore, one may consider an upper bound around 0.7–0.8 for p to have a smoother transition at the critical temperature. The same argument may be used for q, and one may consider a lower bound of 1.2 for q. Fig. 4.7 shows thermal stress versus temperature for the suggested bounds.

It should be noted that the mentioned ranges for p and q still include extreme combinations which may result in unphysical behaviors, see the red solid line in Fig. 4.7. This is especially true for regimes where p approaches the lower bound, and q approaches the upper bound.

4.5.3. Uniqueness of parameters

In this section, the uniqueness of the parameters obtained as the optimal solution by the RSM-GA approach is discussed. For the sake of convenience, the parameters are categorized into two groups: The first group includes v_0 and ρ_0^α. These two parameters characterize the most relevant features of the dislocation network for plastic deformation, i.e. the dislocation density and the distribution of dislocation segment lengths. They have a linear relationship with the shear rate, see Eq. (2.29). The second group includes those parameters that define the short-range barrier, i.e. p, q, τ_0^*, and ΔF. These parameters appear in the exponential part of the shear rate formulation.

4.5.3.1. Dislocation network parameters: v_0 and ρ_0^α

The velocity pre-factor v_0 has a linear relationship with the shear rate, which results in a relatively low influence of this parameter on the yield stress in comparison to the other parameters. This small effect of v_0 may lead to a misinterpretation of its importance. The initial mobile dislocation density ρ_0^α also has a linear relationship with the shear rate. However, due to its dominating influence on the athermal stress component, its effect is generally much higher than v_0 and comparable to the effect of other material parameters. Despite the significant effect of ρ_0^α on the yield stress, a survey of the pertinent literature reveals that its value is often assumed without any critical assessment. In this section, the distinctive role of these two parameters is discussed, and the possibility of finding a unique solution for both is elaborated.

Using Eq. (4.1) and by assuming τ_μ^α is temperature and strain rate independent, one can determine the relationship for temperature- over strain rate-sensitivity as

$$\frac{\frac{\mathrm{d}\tau^\alpha}{\mathrm{d}T}|_{\dot\gamma^\alpha=const}}{\frac{\mathrm{d}\tau^\alpha}{\mathrm{d}\dot\gamma^\alpha}|_{T=const}} = \frac{|\dot\gamma^\alpha|\log[\frac{|\dot\gamma^\alpha|}{\rho^\alpha b v_0}]}{T}. \tag{4.10}$$

It can be seen that the temperature- over strain rate-sensitivity ratio itself depends on the temperature and shear rate. This ratio decreases with an increase in temperature for a given shear rate and increases with an increase in the shear rate for a given temperature. However, the only way to alter the temperature- over strain rate-sensitivity ratio for a given temperature and strain rate is an adjustment of $\rho^\alpha b v_0$. In other words, to reach a particular combination of yield stresses at different temperatures and strain rates, this product needs to be adequately determined. Since the Burgers vector is a known parameter, the only open parameters are ρ^α and v_0.

The same conclusion can be derived from the RSM study. Fig. 4.8 shows the effects plot for temperature- over strain rate-sensitivity ratio at the yield point for two typical cases. Clearly, the most pronounced two parameters which affect the temperature- over strain rate-sensitivity ratio are v_0 and ρ_0^α. Other parameters influence the temperature-over strain rate-sensitivity ratio only through interaction with these two parameters.

These results reveal that it is possible to reach a unique solution for the product $\rho^\alpha v_0$ if the boundary conditions for the optimization are appropriately selected in a way that captures the temperature over strain rate sensitivity. On the other hand, ρ_0^α contributes also to the athermal component of the stress. Therefore, its effects can be distinguished from the effects of v_0. It can be concluded that the value for both parameters can be uniquely determined.

To test this hypothesis, 50 independent optimization runs have been performed. The results for the optimized solutions are shown in Fig. 4.9. It can be seen that there is a clear convergence for ρ_0^α, and the optimization methodology is able to determine this parameter uniquely. The distribution for ρ_0^α is around 0.2 % of the optimization range. The optimization outputs for v_0 are also located in a relatively narrow distribution, i.e. around 5 % of the optimization range. The main reason for the broader range of solutions for v_0 is its small main effect, which results in a negligible error in the stress–strain curves for a change in its value.

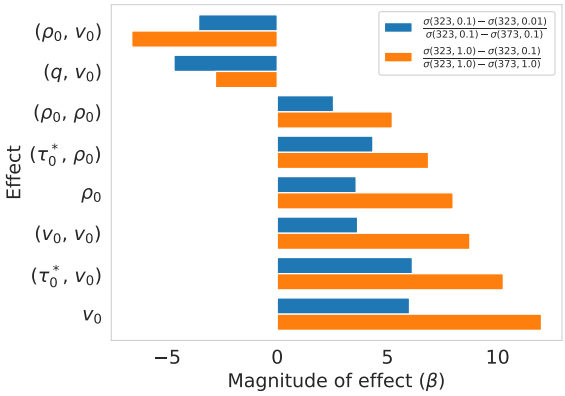

Fig. 4.8: Effects plot for temperature- over strain rate-sensitivity ratio. v_0 and ρ_0^α are the main two parameters which affect the temperature over strain rate sensitivity.

It should be noted that the discussion in this section does not mean that the other parameters have no effect on the temperature or strain rate sensitivity of the yield stress. In fact, the barrier parameters mainly determine the temperature and the strain rate sensitivity, while ρ_0^α and v_0 adjust the temperature- over strain rate-sensitivity ratio.

4.5.3.2. Barrier parameters: p, q, τ, and ΔF

The barrier parameters define the activation energy for dislocation glide, i.e. $\Delta G = \Delta F(1-(\tau^\alpha/\tau_0^*)^p)^q$. These parameters strongly influence the temperature and strain rate sensitivity and the overall stress level. In this section, the impact of these parameters on the constitutive behavior is outlined, and the possibility of reaching a unique solution for them is discussed.

Fig. 4.9 shows the optimized solution for these parameters from 50 independent optimization runs. The optimized solutions for τ_0^* and q are distributed in a very wide range, i.e. these parameters do not converge to a unique solution. Besides, p converges to the lower bound of the allowed range. Therefore, also p cannot be considered as a converged parameter despite its narrow distribution. Additional investigations show that, regardless of the selected bounds, p always converges to the lower bound. These additional investigations also show that the value for ΔF depends strongly on the value of p. Hence, also ΔF cannot be considered as a converged parameter despite its narrow distribution. Table 4.7 shows the values for four exemplar optimized solutions with almost the same fitness value. It is obvious that multiple solutions result in a similar constitutive behavior. It is even possible to find multiple suitable solutions for any other three parameters even when one of the parameters is set to a fixed value. For example, parameter sets 3 and 4 in Table 4.7 are obtained for a fixed value of $p = 0.25$.

Fig. 4.10 shows the thermal stress versus temperature for two different sets of parameters. The predicted thermal stresses almost overlap for a wide range of temperatures, and the observed difference is much smaller than the expected experimental errors. Although there is a clear disagreement between the two curves at low temperatures, it is impossible to make a differentiation between these two cases

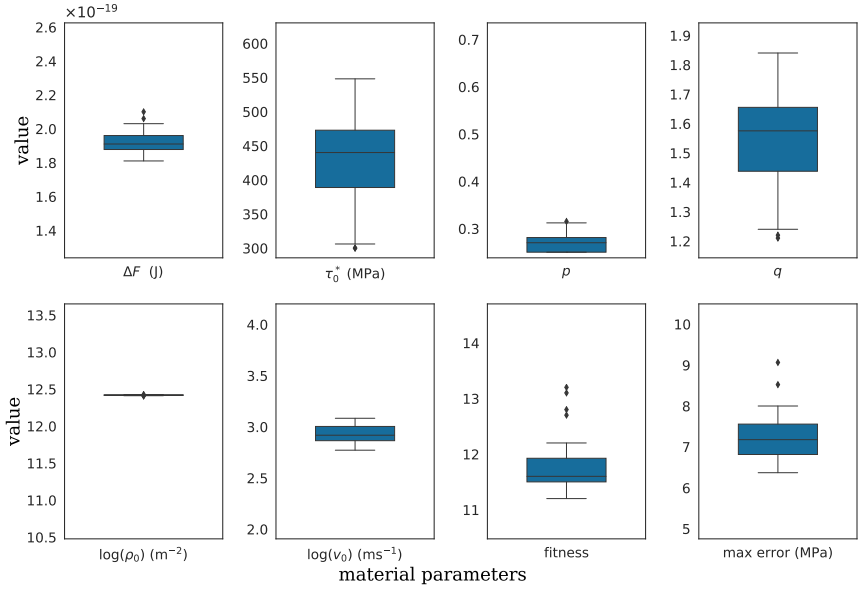

Fig. 4.9: The optimized solutions from 50 independent optimization runs. The distribution of the fitness value and the maximum observed error in the yield stress prediction shows that the optimized solution from different runs has nearly the same quality. It should be noted that a solution with a lower maximum observed error does not necessarily have a better fitness value, see Eq. (3.6) for how the fitness values are calculated. There is a very good convergence for both ρ_0^{α} and v_0. However, the optimized solutions for τ_0^* and q are distributed in a very wide range, and these two parameters are not converged to a unique solution. Besides, p converges to the lower bound of the optimization range, and it cannot be considered as a converged parameter despite its narrow distribution. The converged value for ΔF is strongly dependent on the converged value for p. Hence, ΔF also cannot be considered as a converged parameter despite its relatively narrow distribution.

Table 4.7: Four exemplar optimized solutions with almost similar fitness values. Examples 3 and 4 show the possibility of finding multiple suitable solutions even if one parameter is set to a constant value.

parameter set	ΔF (J)	τ_0^* (MPa)	p	q	fitness value
1	1.82×10^{-19}	548	0.30	1.82	11.5
2	1.88×10^{-19}	448	0.27	1.58	11.5
3	1.90×10^{-19}	334	0.25	1.30	11.5
4	2.00×10^{-19}	440	0.25	1.50	11.8

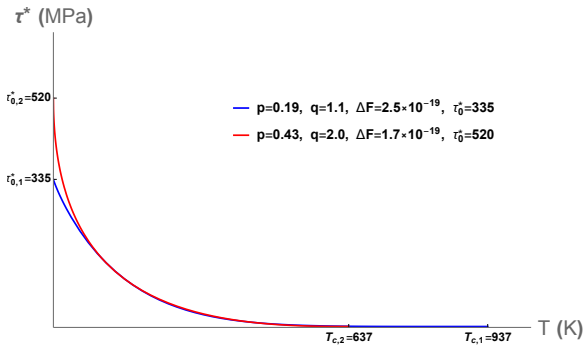

Fig. 4.10: Thermal stress versus temperature for two different sets of parameters. Although there is a clear disagreement between the two curves at very low temperatures and the estimated critical temperature, the predicted thermal stresses almost overlap for a wide range of temperatures.

during the optimization procedure due to the lack of experimental data for these temperatures. It can be concluded that no unique solution for the barrier parameters can be achieved using the current set of experimental data.

Even though the difference between the value of the predicted thermal stress is negligible at elevated temperatures, there is a significant difference between the predicted critical temperatures for the two cases given in Fig. 4.10. As discussed earlier in Section 4.5.1, ΔF is the only barrier parameter that affects the critical temperature. Therefore, the start of the temperature-insensitive regime is determined solely by ΔF. However, as discussed in Section 4.5.2, p has a significant effect on thermal stress's flatness when approaching the critical temperature. In other words, for a small p, there is a wide temperature range before the critical temperature where the thermal stress is almost zero. Although p theoretically does not affect the critical temperature, it practically creates a region that is hardly distinguishable from the region above the critical temperature. This allows to use a combination of a high ΔF and a small p without any notable change in the thermal stress response. However, both solutions will have a significantly different critical temperatures, see Fig. 4.10. It can be concluded that an infinite number of numerically equivalent solutions can be found if no assumption about the value of the critical temperature is made.

On the other hand, the decrease of the thermal stress in the low temperature regime depends strongly on q. For different values of τ_0^*, the parameters q and—to some extent—p can be selected in a way to compensate for the difference in the barrier strength for temperatures close to 0 K, see the solid red curve in Fig. 4.10. Based on this fact and the underdetermined system at high temperatures, different sets of parameters result in a very similar behavior over a vast range of temperatures. Therefore, it is not possible to find a unique set of parameters without any assumption about the values for either τ_0^* or ΔF.

This issue is mainly because p and q are introduced into the equations in a purely phenomenological way to relate ΔG to ΔF. Originally, Eq. (2.29) has been derived for a barrier with a rectangular profile, i.e. $p = 1.0$ and $q = 1.0$. Therefore, ΔF is related to τ_0^* as $\Delta F = \tau_0^* b l^2$. This results in a linear relationship between thermal stress and temperature,

which is physically not plausible. Introduction of p and q allows to add curvature to the thermal stress curve. As a result of how p and q are introduced into the equations, it is no longer possible to physically relate τ_0^* and ΔF. This results in a situation where the critical temperature is completely independent of τ_0^*. Therefore, the system becomes an underdetermined system for a vast range of temperatures, and the only way to uniquely determine all four parameters will be by knowing both the critical temperature and the barrier's strength.

Due to many uncertainties and complexities in the deformation behavior at high temperatures, the critical temperature cannot be determined with certainty. Moreover, experiments at temperatures close to 0 K are needed to determine τ_0^*, which is not an easy and routine experiment to perform. Therefore, neither T_c nor τ_0^* is easy to determine experimentally. Consequently, reaching a unique solution for the barrier parameters is very challenging.

One way to partially overcome this issue is by constraining the critical temperature. Although it is difficult to determine the critical temperature precisely, a range for the critical temperature can be estimated based on the rate of change in the yield stress with temperature. This estimated range can be used along with Eq. (4.3) to constrain the critical temperature.

As discussed earlier in Section 4.4.1.1, the inflection point in the yield stress versus deformation temperature curve may correspond to the activation of a new softening mechanism. However, before the inflection point, the rate of change in the yield stress with temperature is decreased considerably, and the experimental data show a tendency to reach a plateau. It can be expected that the critical temperature lies in the vicinity but higher than the inflection point. The inflection points determined in this study are 725, 688, and 656 K for the strain rates of 1.0, 0.1, and 0.01 s^{-1}, respectively. Hence, the critical temperature range is here selected to be between 600 to 900 K. The upper limit is selected high enough to prevent over constraining the critical temperature.

Fig. 4.11 shows the optimized solutions from 50 independent optimization runs when the critical temperature is constrained. It can be seen that the distribution for p is still relatively narrow, around 10% of the optimization range, and p is no longer converging to the lower bound. Consequently, the values achieved for ΔF also can be considered as adequately converged solutions. The optimization outputs for ΔF are distributed in a range around 5% of the optimization range. The width of the distribution for τ_0^* and q is noticeably smaller than for the unconstrained case. However, these distributions are still too wide to be considered as converged solutions. It can be concluded that constraining the critical temperature is partially solving the problem at high temperatures. It also improves the results for τ_0^* and q. However, it seems that the system is still underdetermined, especially at low temperatures. Therefore, to fully solve the issue, experimental data at much lower temperatures are required. Constraining the critical temperature does not noticeably affect the distribution for ρ_0^α and v_0.

The main reason for introducing p and q in the way outlined in this section is the simplicity of the equations. An alternative approach to fundamentally overcome the non-uniqueness issue is by using a mathematically reasonable profile for the barrier, such as a sinusoidal profile. In this case, ΔG can be estimated directly from the barrier's

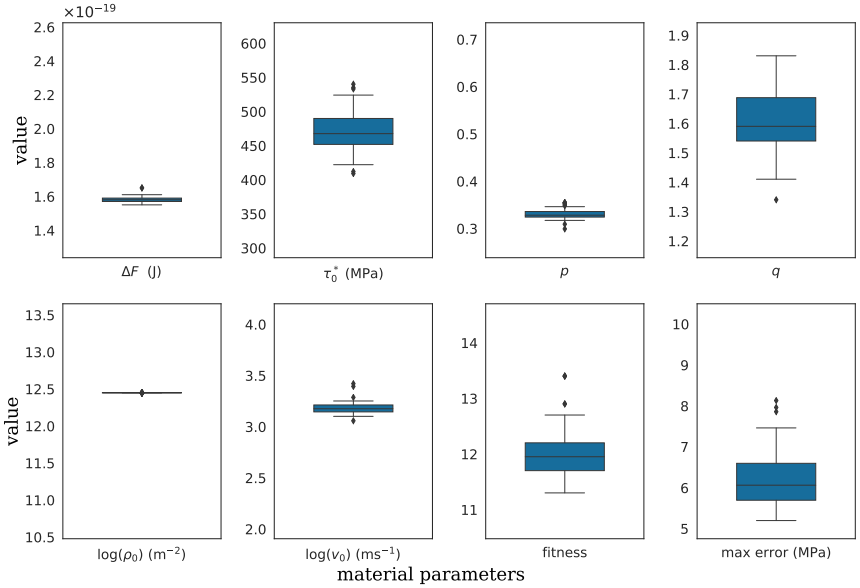

Fig. 4.11: The optimized solutions from 50 independent optimization runs for constrained critical temperature. Constraining the critical temperature is partially solving the issue of having an underdetermined system at high temperatures. Besides, it improves the results for τ_0^* and q. However, the system is still underdetermined, especially at low temperatures.

profile by calculating the activation volume for dislocation glide. This overcomes the need to introduce the curvature in thermal stress by phenomenological parameters like p and q. Although such a barrier profile results in more complex equations for the constitutive law, it reduces the number of *phenomenological* material parameters by one or two. This can be a significant advantage for physics-based models, which generally have a large number of material parameters. Evaluating such an approach is, however, beyond the scope of this manuscript.

4.6. Conclusions

The material parameters for a physics-based crystal plasticity model were identified using macroscopic stress–strain curve data experimentally obtained for IF steel. The uniqueness of the parameters was studied, and an in-depth analysis of the parameters was provided. Since the temperature-dependent motion of dislocations of the constitutive law used in this study has the same basis as the one proposed by Kocks *et al.* [7], most of the conclusions made here are expandable to many other models that use the same concept.

The following conclusions can be drawn:

- The dislocation-density-based constitutive law is capable of predicting the polycrystal yield stress behavior over a wide range of temperatures and strain

rates with a single set of material parameters. However, it fails to predict the material response at very high temperatures correctly.

- The temperature-dependent crystal plasticity model is not numerically stable at temperatures close to or above the critical temperature if only the waiting time is considered in the formulation of the dislocation velocity. The formulation can be modified and stabilized at high temperatures by adding the running time into the formulations.
- The ranges provided for p and q, parameters which determine the shape of the short-range barrier, in the literature are rather wide and include unphysical barrier profiles. New limits for these two parameters were provided.
- Initial dislocation density ρ_0^α and dislocation glide velocity pre-factor v_0 are determining the temperature- over strain rate-sensitivity ratio. Due to this distinct role of the two parameters, it is possible to determine them uniquely.
- The barrier parameters are the main variables in determining the stress response at the yield point. The temperature and strain rate sensitivity is also mainly controlled by them.
- The system is underdetermined for the barrier parameters. Prior knowledge about the barrier's strength and the critical temperature is necessary to uniquely determine these parameters.
- Although the critical temperature is theoretically independent of the shape of the barrier, it is practically altered by the material parameter p.

References

[1] K. Sedighiani, K. Traka, F. Roters, D. Raabe, J. Sietsma, and M. Diehl, *Determination and analysis of the constitutive parameters of temperature-dependent dislocation-density-based crystal plasticity models,* Mechanics of Materials (2021), 10.1016/j.mechmat.2021.104117.

[2] F. Roters, P. Eisenlohr, L. Hantcherli, D. Tjahjanto, T. Bieler, and D. Raabe, *Overview of constitutive laws, kinematics, homogenization and multiscale methods in crystal plasticity finite-element modeling: Theory, experiments, applications,* Acta Materialia **58**, 1152 (2010).

[3] E. Voce, *The relationship between stress and strain for homogeneous deformations,* Journal of the Institute of Metals **74**, 537 (1948).

[4] J. Hutchinson, *Bounds and Self-Consistent Estimates for Creep of Polycrystalline Materials,* Proceedings of the Royal Society A: Mathematical, Physical and Engineering Sciences **348**, 101 (1976).

[5] D. Peirce, R. Asaro, and A. Needleman, *An analysis of nonuniform and localized deformation in ductile single crystals,* Acta Metallurgica **30**, 1087 (1982).

[6] R. Becker, *Analysis of texture evolution in channel die compression—I. Effects of grain interaction,* Acta Metallurgica et Materialia **39**, 1211 (1991).

[7] U. Kocks, A. Argon, and M. Ashby, *Thermodynamics and kinetics of slip* (Pergamon Press, 1975).

[8] S. Nemat-Nasser, T. Okinaka, and L. Ni, *A physically-based constitutive model for BCC crystals with application to polycrystalline tantalum,* Journal of the Mechanics and Physics of Solids **46**, 1009 (1998).

[9] A. Arsenlis and D. Parks, *Modeling the evolution of crystallographic dislocation density in crystal plasticity,* Journal of the Mechanics and Physics of Solids **50**, 1979 (2002).

[10] A. Ma and F. Roters, *A constitutive model for fcc single crystals based on dislocation densities and its application to uniaxial compression of aluminium single crystals,* Acta Materialia **52**, 3603 (2004).

[11] L. Evers, D. Parks, W. Brekelmans, and M. Geers, *Crystal plasticity model with enhanced hardening by geometrically necessary dislocation accumulation,* Journal of the Mechanics and Physics of Solids **50**, 2403 (2002).

[12] S. Mandal, B. T. Gockel, and A. Rollett, *Application of canonical correlation analysis to a sensitivity study of constitutive model parameter fitting,* Materials and Design **132**, 30 (2017).

[13] E. Orowan, *Zur Kristallplastizität. III - Über den Mechanismus des Gleitvorganges,* Zeitschrift für Physik **89**, 634 (1934).

[14] K. Ono, *Temperature dependence of dispersed barrier hardening,* Journal of Applied Physics **39** (1968), 10.1063/1.1656434.

[15] G. Regazzoni, U. F. Kocks, and P. S. Follansbee, *Dislocation kinetics at high strain rates,* Acta Metallurgica **35** (1987), 10.1016/0001-6160(87)90285-9.

[16] G. Voyiadjis and F. Abed, *Effect of dislocation density evolution on the thermomechanical response of metals with different crystal structures at low and high strain rates and temperatures,* Archives of Mechanics **57**, 299 (2005).

[17] K. Cheong and E. Busso, *Discrete dislocation density modelling of single phase FCC polycrystal aggregates,* Acta Materialia **52**, 5665 (2004).

[18] A. Ma, F. Roters, and D. Raabe, *A dislocation density based constitutive model for crystal plasticity FEM including geometrically necessary dislocations,* Acta Materialia **54**, 2169 (2006).

[19] A. Ma, F. Roters, and D. Raabe, *On the consideration of interactions between dislocations and grain boundaries in crystal plasticity finite element modeling – Theory, experiments, and simulations,* Acta Materialia **54**, 2181 (2006).

[20] L. Evers, W. Brekelmans, and M. Geers, *Scale dependent crystal plasticity framework with dislocation density and grain boundary effects,* International Journal of Solids and Structures **41**, 5209 (2004).

[21] L. Evers, W. Brekelmans, and M. Geers, *Non-local crystal plasticity model with intrinsic SSD and GND effects,* Journal of the Mechanics and Physics of Solids **52**, 2379 (2004).

[22] C. Reuber, P. Eisenlohr, F. Roters, and D. Raabe, *Dislocation density distribution around an indent in single-crystalline nickel : Comparing nonlocal crystal plasticity finite-element predictions with experiments,* Acta Materialia **71**, 333 (2014).

[23] G. Monnet, L. Vincent, and B. Devincre, *Dislocation-dynamics based crystal plasticity law for the low- and high-temperature deformation regimes of bcc crystal,* Acta Materialia **61**, 6178 (2013).

[24] A. Alankar, D. Field, and D. Raabe, *Plastic anisotropy of electro-deposited pure α-iron with sharp crystallographic <1 1 1>// texture in normal direction: Analysis by an explicitly dislocation-based crystal plasticity model,* International Journal of Plasticity **52**, 18 (2014).

[25] D. Cereceda, M. Diehl, F. Roters, D. Raabe, J. Perlado, and J. Marian, *Unraveling the temperature dependence of the yield strength in single-crystal tungsten using atomistically-informed crystal plasticity calculations,* International Journal of Plasticity **78**, 242 (2016), arXiv:1506.02224 .

[26] S. Yuan, M. Huang, Y. Zhu, and Z. Li, *A dislocation climb/glide coupled crystal plasticity constitutive model and its finite element implementation,* Mechanics of Materials **118** (2018), 10.1016/j.mechmat.2017.12.009.

[27] S. Yuan, Y. Zhu, S. Liang, M. Huang, and Z. Li, *Dislocation-density based size-dependent crystal plasticity framework accounting for climb of piled up dislocations at elevated temperature,* Mechanics of Materials **134** (2019), 10.1016/j.mechmat.2019.04.015.

[28] S. Yuan, Y. Zhu, M. Huang, S. Liang, and Z. Li, *Dislocation-density based crystal plasticity model with hydrogen-enhanced localized plasticity in polycrystalline face-centered cubic metals,* Mechanics of Materials **148** (2020), 10.1016/j.mechmat.2020.103472.

[29] G. Castelluccio and D. McDowell, *Mesoscale cyclic crystal plasticity with dislocation substructures,* International Journal of Plasticity **98** (2017), 10.1016/j.ijplas.2017.06.002.

[30] D. Luscher, F. Addessio, M. Cawkwell, and K. Ramos, *A dislocation density-based continuum model of the anisotropic shock response of single crystal α-cyclotrimethylene trinitramine,* Journal of the Mechanics and Physics of Solids **98** (2017), 10.1016/j.jmps.2016.09.005.

[31] F. Addessio, D. Luscher, M. Cawkwell, and K. Ramos, *A single-crystal model for the high-strain rate deformation of cyclotrimethylene trinitramine including phase transformations and plastic slip,* Journal of Applied Physics **121** (2017), 10.1063/1.4983009.

[32] S. Keshavarz and S. Ghosh, *Multi-scale crystal plasticity finite element model approach to modeling nickel-based superalloys,* Acta Materialia **61** (2013), 10.1016/j.actamat.2013.07.038.

[33] S. Keshavarz and S. Ghosh, *Hierarchical crystal plasticity FE model for nickel-based superalloys: Sub-grain microstructures to polycrystalline aggregates,* International Journal of Solids and Structures **55** (2015), 10.1016/j.ijsolstr.2014.03.037.

[34] S. Ghosh, G. Weber, and S. Keshavarz, *Multiscale modeling of polycrystalline nickel-based superalloys accounting for subgrain microstructures,* Mechanics Research Communications **78** (2016), 10.1016/j.mechrescom.2015.12.001.

[35] S. Keshavarz, S. Ghosh, A. Reid, and S. Langer, *A non-Schmid crystal plasticity finite element approach to multi-scale modeling of nickel-based superalloys,* Acta Materialia **114** (2016), 10.1016/j.actamat.2016.05.016.

[36] A. Alankar, P. Eisenlohr, and D. Raabe, *A dislocation density-based crystal plasticity constitutive model for prismatic slip in α-titanium,* Acta Materialia **59**, 7003 (2011).

[37] S. Wong, M. Madivala, U. Prahl, F. Roters, and D. Raabe, *Acta Materialia A crystal plasticity model for twinning- and transformation-induced plasticity,* Acta Materialia **118**, 140 (2016).

[38] A. Patra and D. McDowell, *Crystal plasticity-based constitutive modelling of irradiated bcc structures,* Philosophical Magazine **92**, 861 (2012).

[39] A. Patra and D. McDowell, *Continuum modeling of localized deformation in irradiated bcc materials,* Journal of Nuclear Materials **432** (2013), 10.1016/j.jnucmat.2012.08.021.

[40] D. Li, H. Zbib, X. Sun, and M. Khaleel, *Predicting plastic flow and irradiation hardening of iron single crystal with mechanism-based continuum dislocation dynamics,* International Journal of Plasticity **52** (2014), 10.1016/j.ijplas.2013.01.015.

[41] P. Chakraborty and S. Bulent Biner, *Crystal plasticity modeling of irradiation effects on flow stress in pure-iron and iron-copper alloys,* Mechanics of Materials **101** (2016), 10.1016/j.mechmat.2016.07.013.

[42] A. Patra and D. McDowell, *A void nucleation and growth based damage framework to model failure initiation ahead of a sharp notch in irradiated bcc materials,* Journal of the Mechanics and Physics of Solids **74** (2015), 10.1016/j.jmps.2014.10.006.

[43] P. Zhao, T. Song En Low, Y. Wang, and S. Niezgoda, *An integrated full-field model of concurrent plastic deformation and microstructure evolution: Application to 3D simulation of dynamic recrystallization in polycrystalline copper,* International Journal of Plasticity **80** (2016), 10.1016/j.ijplas.2015.12.010.

[44] P. Zhao, Y. Wang, and S. Niezgoda, *Microstructural and micromechanical evolution during dynamic recrystallization,* International Journal of Plasticity **100** (2018), 10.1016/j.ijplas.2017.09.009.

[45] S. Ha, J. Jang, and K. Kim, *Finite element implementation of dislocation-density-based crystal plasticity model and its application to pure aluminum crystalline materials,* International Journal of Mechanical Sciences **120**, 249 (2017).

[46] G. Castelluccio, C. Geller, and D. McDowell, *A rationale for modeling hydrogen effects on plastic deformation across scales in FCC metals,* International Journal of Plasticity **111** (2018), 10.1016/j.ijplas.2018.07.009.

[47] A. Patra, T. Zhu, and D. McDowell, *Constitutive equations for modeling non-Schmid effects in single crystal bcc-Fe at low and ambient temperatures,* International Journal of Plasticity **59** (2014), 10.1016/j.ijplas.2014.03.016.

[48] R. Pokharel, A. Patra, D. Brown, B. Clausen, S. Vogel, and G. Gray, *An analysis of phase stresses in additively manufactured 304L stainless steel using neutron diffraction measurements and crystal plasticity finite element simulations,* International Journal of Plasticity **121** (2019), 10.1016/j.ijplas.2019.06.005.

[49] K. Thool, A. Patra, D. Fullwood, K. Krishna, D. Srivastava, and I. Samajdar, *The role of crystallographic orientations on heterogeneous deformation in a zirconium alloy: A combined experimental and modeling study,* International Journal of Plasticity **133** (2020), 10.1016/j.ijplas.2020.102785.

[50] A. Patra and D. McDowell, *Crystal plasticity investigation of the microstructural factors influencing dislocation channeling in a model irradiated bcc material,* Acta Materialia **110** (2016), 10.1016/j.actamat.2016.03.041.

[51] P. Lin, J. Nie, and M. Liu, *Study on irradiation effect in stress-strain response with CPFEM during nano-indentation,* Nuclear Materials and Energy **22** (2020), 10.1016/j.nme.2020.100737.

[52] Y. Liu, J. Nie, P. Lin, and M. Liu, *Irradiation tensile property and fracture toughness evaluation study of A508-3 steel based on multi-scale approach,* Annals of Nuclear Energy **138** (2020), 10.1016/j.anucene.2019.107157.

[53] D. Rodríguez-Galán, I. Sabirov, and J. Segurado, *Temperature and stain rate effect on the deformation of nanostructured pure titanium,* International Journal of Plasticity **70** (2015), 10.1016/j.ijplas.2015.04.002.

[54] A. Khan, J. Liu, J. Yoon, and R. Nambori, *Strain rate effect of high purity aluminum single crystals: Experiments and simulations,* International Journal of Plasticity **67**, 39 (2015).

[55] K. Sedighiani, M. Diehl, K. Traka, F. Roters, J. Sietsma, and D. Raabe, *An efficient and robust approach to determine material parameters of crystal plasticity constitutive laws from macro-scale stress–strain curves,* International Journal of Plasticity **134**, 102779 (2020).

[56] P. Eisenlohr, M. Diehl, R. Lebensohn, and F. Roters, *A spectral method solution to crystal elasto-viscoplasticity at finite strains,* International Journal of Plasticity **46**, 37 (2013).

[57] P. Shanthraj, P. Eisenlohr, M. Diehl, and F. Roters, *Numerically robust spectral methods for crystal plasticity simulations of heterogeneous materials,* International Journal of Plasticity **66**, 31 (2015).

[58] P. Shanthraj, M. Diehl, P. Eisenlohr, F. Roters, and D. Raabe, *Spectral Solvers for Crystal Plasticity and Multi-physics Simulations,* in *Handbook of Mechanics of Materials* (2019).

[59] P. Eisenlohr and F. Roters, *Selecting a set of discrete orientations for accurate texture reconstruction,* Computational Materials Science **42** (2008), 10.1016/j.commatsci.2007.09.015.

[60] D. Dever, *Temperature dependence of the elastic constants in α-iron single crystals: Relationship to spin order and diffusion anomalies,* Journal of Applied Physics **43**, 3293 (1972).

[61] J. Adams, D. Agosta, R. Leisure, and H. Ledbetter, *Elastic constants of monocrystal iron from 3 to 500 K,* Journal of Applied Physics **100** (2006), 10.1063/1.2365714.

[62] R. Madec and L. Kubin, *Dislocation strengthening in FCC metals and in BCC metals at high temperatures,* Acta Materialia **126**, 166 (2017).

[63] M. Bertin, C. Du, J. Hoefnagels, and F. Hild, *Crystal plasticity parameter identification with 3D measurements and Integrated Digital Image Correlation,* Acta Materialia **116**, 321 (2016).

[64] D. Raabe, M. Sachtleber, Z. Zhao, F. Roters, and S. Zaefferer, *Micromechanical and macromechanical effects in grain scale polycrystal plasticity experimentation and simulation,* Acta Materialia **49**, 3433 (2001).

[65] W. Voigt, *Ueber die Beziehung zwischen den beiden Elasticitätsconstanten isotroper Körper,* Annalen der Physik **274**, 573 (1889).

[66] A. Reuss, *Berechnung der Fließgrenze von Mischkristallen auf Grund der Plastizitätsbedingung für Einkristalle,* Zeitschrift für Angewandte Mathematik und Mechanik **9**, 49 (1929).

[67] R. Hill, *The elastic behaviour of a crystalline aggregate,* Proceedings of the Physical Society. Section A **65**, 349 (1952).

[68] S. Fitzgerald and S. Dudarev, *Dislocation pile-ups in Fe at high temperature,* Proceedings of the Royal Society A: Mathematical, Physical and Engineering Sciences **464** (2008), 10.1098/rspa.2008.0116.

[69] S. Fitzgerald, *Frank-Read sources and the yield of anisotropic cubic crystals,* Philosophical Magazine Letters **90** (2010), 10.1080/09500830903571392.

[70] S. Aubry, S. Fitzgerald, S. Dudarev, and W. Cai, *Equilibrium shape of dislocation shear loops in anisotropic α-Fe,* Modelling and Simulation in Materials Science and Engineering **19** (2011), 10.1088/0965-0393/19/6/065006.

[71] B. Hansen, I. Beyerlein, C. Bronkhorst, E. Cerreta, and D. Dennis-Koller, *A dislocation-based multi-rate single crystal plasticity model,* International Journal of Plasticity **44** (2013), 10.1016/j.ijplas.2012.12.006.

[72] A. Alankar, I. N. Mastorakos, and D. Field, *A dislocation-density-based 3D crystal plasticity model for pure aluminum,* Acta Materialia **57**, 5936 (2009).

5

LARGE-DEFORMATION MODELING

Abstract

The capability of high-resolution modeling of crystals subjected to large deformation is essential in predicting many important phenomena occurring in polycrystalline materials, such as microstructure and in-grain texture evolution. However, due to the heterogeneity of the plastic deformation in polycrystals, the simulation mesh is distorted during the deformation. This mesh distortion deteriorates the accuracy of the results, and after reaching high local strain levels, it is no longer possible to continue the simulation. In this chapter, two different adaptive remeshing approaches are introduced for simulating large deformation of 3D polycrystals with high resolution under periodic boundary conditions. In the first approach, a new geometry with a new mesh is created, and then the simulation is restarted as a new simulation in which the initial state is set based on the last deformation state that had been reached. In the second approach, the mesh is smoothened by removing the distortion part of the deformation, and then the simulation is continued after finding a new equilibrium state for the smoothed mesh and geometry. The first method is highly efficient for conducting high-resolution large-deformation simulations. On the other hand, the second method's primary advantage is that it can overcome periodicity issues related to shear loading, and it can be used in conjunction with complex loading conditions. The merits of the methodologies are demonstrated using full-field simulations performed using a dislocation-density-based crystal plasticity model. Particular emphasis is put on studying the effect of resolution and adaptive meshing. The algorithms presented have been implemented into the free and open-source software package, DAMASK (Düsseldorf Advanced Material Simulation Kit).

Parts of this chapter have been published in Sedighiani *et al.* [1].

5.1. Introduction

Metallic materials for structural applications are produced as polycrystals, i.e. they consist of many grains, each with a specific crystallographic orientation. As a result, the level of plastic deformation in a strained polycrystal varies from crystal to crystal, depending on its orientation, geometry, neighboring crystals, and loading conditions [2]. In addition to such intergranular deformation heterogeneity, significant intragranular heterogeniety, i.e. localized continuous or discontinuous orientation spread within a grain forms during plastic deformation [3–9].

The characterization of such localized deformations and microstructures formed during the deformation of polycrystalline materials is vital in developing a thorough physical understanding of the underlying mechanisms behind localization phenomena [10, 11] such as fracture [12, 13], shear banding [14–19] and nucleation during recrystallization [20–24]. Crystal plasticity simulations [25] have been proven to be powerful tools for modeling and predicting the evolution of such deformation heterogeneities and the associated complex mechanical fields [26–39]. These models are developed based on physical mechanisms such as glide of dislocations on preferred slip systems and the interaction of dislocations with various defects [25].

The amount of detail that can be observed using a crystal plasticity simulation strongly depends on the simulation resolution [40–43]. A low-resolution simulation with only one or a few elements per crystal is sufficient to predict macro-scale (global) data such as global crystallographic texture [14] or stress-strain response [40]. However, to achieve a more detailed description of meso-scale deformation localization effects, the simulation resolution needs to be increased significantly, even to hundreds of thousands of elements per crystal [40–43].

At the same time, many of these localization phenomena emerge at medium to large strains [44, 45]. For example, microstructures in pure nickel evolve from typical dense dislocation walls and microbands to lamellar boundaries in a strain range of 0.8 to 2.7 [46]. Therefore, the capability to perform high-resolution large-deformation simulations provides an indispensable means for predicting strain localization and analyzing microstructure evolution.

Typically, continuum mechanical problems involving the deformation of solid materials are formulated in a Lagrangian context, i.e. the mesh is attached to the deformable body and deforms with a change in the shape of the material. However, the relative position of the material points and the mesh (nodes) remains fixed. This means that the mesh gets distorted due to the strain localization. The mesh distortion initially introduces errors in the solution and delays convergence. Ultimately, the distortion becomes too large, and the simulation fails to converge. The maximum possible applied strain depends on many factors, such as the constitutive law, loading conditions, polycrystal morphology, and the simulation resolution [43]. A higher simulation resolution allows capturing more detailed localized deformation features, which results in earlier convergence issues.

In order to overcome the mesh distortion problem and reach larger strains, it is required to remove the mesh distortion and reconstruct a new undistorted mesh–a process that is called remeshing [47–52]. After building the new mesh, the simulation can be restarted on the reconstructed mesh. The most challenging step in any

remeshing algorithm is transferring the state variables from the distorted mesh to the newly reconstructed mesh. The hurdle is that reaching an exact identity between the deformed and the remeshed stage is impossible, and some information is always lost. However, the two stages must be sufficiently similar so that the two configurations reproduce almost identical responses.

In general, two different approaches are used for mapping the state variables between the two stages. According to the first mapping approach, the value of the state variables at each point in the newly generated undistorted mesh is determined directly from the closest corresponding point of the deformed mesh [47, 50]. The second mapping approach uses the interpolation of the state variables at adjacent elements to determine the values of the state variables at the new undistorted elements [52].

The interpolation of state variables is problematic in large strain crystal plasticity formulations. This is because some state variables, such as the crystallographic orientations, are not spatially continuous. In addition, there is no monotonic relation between mechanical behavior and orientation, i.e. interpolating between two crystals with the same behavior, but different orientations might result in an orientation with different behavior. This also holds if crystal symmetries are taken into account. Furthermore, the interpolation of some tensorial quantities is not straightforward. For example, interpolation of the deformation gradient tensor $\mathbf{F}$ might result in a non-compatible displacement field.

Prakash *et al.* [49] used a spherical linear interpolation developed by Shoemake [53] to interpolate the crystallographic orientations and the rotation tensor. They applied this approach to a mean-field visco-plastic self-consistent model. Kim *et al.* [50] compared the nearest neighbor mapping-based approach with an interpolation-based approach for full-field crystal plasticity simulations. They found that the nearest neighbor mapping-based method performs better than the interpolation-based approach. Frydrych *et al.* [52] developed two different interpolation-based methods that consider the spherical space of orientations. They performed a comprehensive comparison between these two methods and an approach based on the nearest neighbor mapping. Although they observed that all three methods provide almost identical macroscopic mechanical responses, they concluded that the nearest neighbor mapping-based approach predicts less reliable results for some state variables than the two interpolation-based methods. This is contrary to what Kim *et al.* [50] observed. It should be noted that Frydrych *et al.* [52] studied only low-resolution polycrystal examples with idealized grain geometry, which might be the reason for the interpolation-based methods' better performance.

Although the interpolation approach may reduce the jumps and provide a more continuous map of the state variables, this comes at the cost of smoothing away physically meaningful sharp localized deformation features. Therefore, the interpolation approach is less suited when aiming at the simulation of strain localization and in-grain orientation spread. This may not be a problem for low-resolution simulations, in which the main outputs are macroscopic crystallographic texture or stress-strain curve. However, this impacts the output of high-resolution simulations, where capturing deformation localization and microstructure evolution is the primary objective. One should note that the nearest

neighbor mapping-based approach is more sensitive to frequent early remeshing after small strains. Frequent remeshing can affect the remeshing accuracy by eliminating the difference between the volume fraction of different elements.

This chapter introduces two remeshing techniques to overcome the mesh distortion problem in high-resolution crystal plasticity simulations. Both approaches use a nearest-neighbor mapping algorithm to transfer the state variables from the distorted mesh to a new undistorted mesh. This study focuses specifically on designing remeshing methodologies that are efficient and applicable for high-resolution 3D crystal plasticity simulations of representative volume elements (RVEs) under periodic boundary conditions. With this in mind, a global adaptive scheme is implemented in both approaches, allowing the free adjustment of the number of elements in the three coordinate directions at each remeshing step. The adaptivity scheme provides a tool to increase the resolution based on the problem and the deformation heterogeneity to efficiently and adequately model the microstructure evolution. In this work, a Fast Fourier Transform (FFT) based spectral method is used to solve the partial differential equations for static equilibrium, see Section 2.4. Accordingly, the elements (voxels) used in the simulations are rectangular cuboids, i.e. right angles hexahedron. These elements are conceptually similar to reduced-integration, linear brick elements used in finite element analysis, i.e. cuboid elements with just a single integration point located at the element's centroid.

This chapter thoroughly examines and elaborates on the remeshing methodologies' capability in predicting the deformation heterogeneity and microstructure evolution at large strains. For this purpose, the crystal plasticity framework is first explained in Section 5.2. Then, the two remeshing approaches are explained in Section 5.3. In Section 5.4, various high-resolution examples are used to examine and validate the methodologies by answering the following questions: How accurate are the two introduced methodologies (Section 5.4.1)? What is the effect of adaptivity on the accuracy and simulation outputs (Section 5.4.2)? What are the advantages and disadvantages of the two remeshing approaches (Section 5.4.3)? How to overcome challenges related to remeshing for problems involving shear loading (Section 5.4.4)? How does simplifying a 3D simulation to a quasi-3D simulation affect the results (Section 5.4.5)? Finally, the methodologies are used to predict the deformation behavior and microstructure evolution during the large deformation of a 3D polycrystal with high resolution (Section 5.4.6).

5.2. Crystal plasticity framework

We use DAMASK [54] to conduct the crystal plasticity simulations. In DAMASK, a variety of constitutive laws are available, see Chapter 2 for more detail. These constitutive laws rely on state variables that constitute and track the deformation history [55, 56], e.g. the critical resolved shear stress for the case of the phenomenological constitutive law or the dislocation density for the case of the dislocation-density-based constitutive law. For the case studies presented in this study, the simulations are conducted using the dislocation-density-based constitutive law as outlined in Section 2.3.3. However, the remeshing approaches, introduced in Section 5.3, are independent of the constitutive law and they can be used with any crystal plasticity model. The material

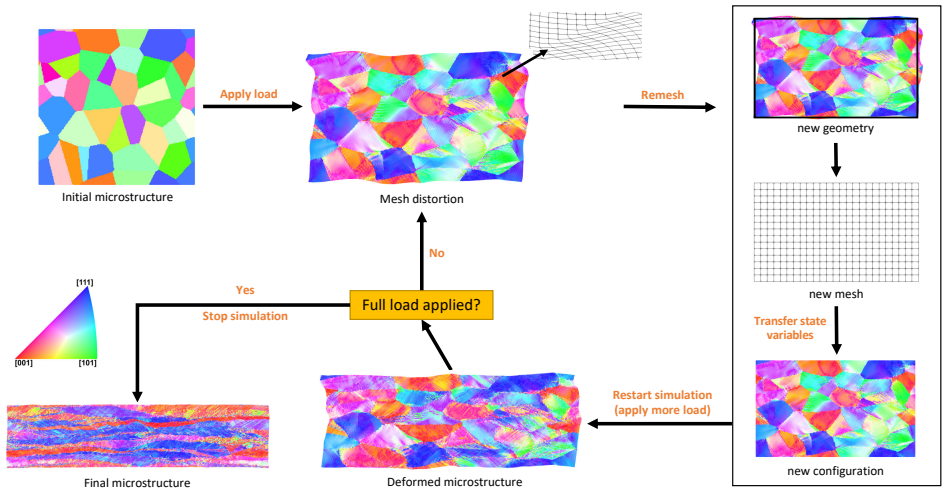

Fig. 5.1: The schematic shows the mesh replacement method workflow. The deformed configuration with the distorted mesh is replaced by a new configuration with an undistorted mesh. Then, the state variables from the deformed mesh are mapped onto the new mesh using a nearest-neighbor mapping algorithm. This remeshing algorithm allows assigning a new mesh resolution to the new configuration. Finally, the new configuration is used to restart and continue the simulation as a new simulation.

parameters are chosen to be according to those identified for Interstitial Free (IF) steel in Chapter 4.

5.3. Methodology

5.3.1. Remeshing techniques

This section explains two remeshing techniques developed in this work to overcome the mesh distortion problem. Besides, the differences between the approaches are elaborated.

5.3.1.1. Mesh replacement method

The mesh replacement method is based on replacing the distorted mesh with a newly created undistorted mesh, see Fig. 5.1. According to this remeshing technique, a new (cuboid) geometry is first created, which matches the average outer dimensions of the deformed geometry considering the periodicity of the configuration. Then, the original mesh is replaced by a new mesh assigned to this new geometry. Finally, the simulation is restarted using the new configuration as a new simulation without any mesh distortion. This is physically equivalent to replacing the deformation gradient tensor with the identity tensor and the full relaxation of the elastic deformation; see Section 5.3.2.1 for more information. The selection of the resolution for the new mesh is following an adaptive scheme, which allows updating the resolution during the deformation at each remeshing step. The adaptivity is described and studied in more detail in Section 5.3.3.

Once the new geometry and the new mesh are available, the state variables from the deformed stage are mapped onto the newly created mesh. The mapping is performed

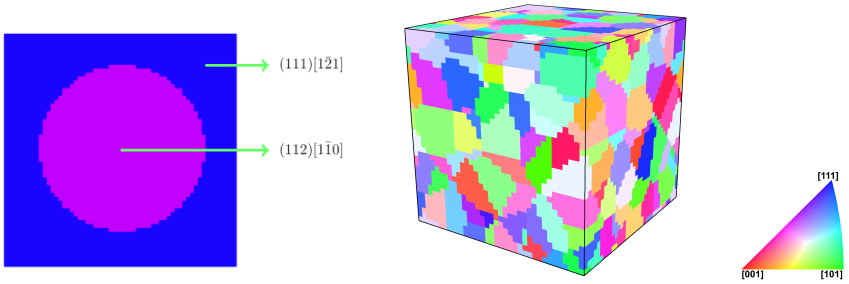

(a) Example 1 (b) Example 2

Fig. 5.2: Voxel representation of the RVEs used in the crystal plasticity simulations to show the capabilities of the remeshing approaches. The coloring follows the IPF color map parallel to the loading (vertical) direction. (a) Example 1: a quasi-3D RVE made of 2 grains with an initial mesh of 60 × 60 elements. (b) Example 2: a 3D polycrystal RVE made of 216 grains with an initial mesh of 36 × 36 × 36 elements.

5

using a nearest-neighbor mapping algorithm to transfer the state variables from the deformed state to the points in the new mesh. The transferred state variables and the mapping procedure are discussed in more detail in Section 5.3.2.

The similitude between the deformed configuration and the remeshed configuration for the mesh replacement method is tested using the two examples shown in Fig. 5.2. Fig. 5.2(a) illustrates a high-resolution quasi-3D, i.e. one element in the transverse direction, bicrystal RVE with a mesh of 60 × 60 elements. This example is selected because its deformation is heterogeneous, and, at the same time, its deformation results in a non-random distribution of the state variables, e.g. a bimodal distribution of the Euler angles. As a result, it is straightforward to trace any changes and evaluate the accuracy of the remeshing approach. Fig. 5.3 shows the deformed configuration before and after remeshing for this example. It is clear that most of the main features are captured and transferred to the remeshed RVE. The Kolmogorov-Smirnov test [57] is used to assess the accuracy of the remeshing and the similitude between the two stages. The Kolmogorov-Smirnov test quantifies the maximum difference between the cumulative distribution function of two distributions. The Kolmogorov-Smirnov values for both the total dislocation density and the rotation angle are 0.007. It is clear that such difference between the two cumulative distributions is negligible.

The rotation angle, $|\Delta\theta|$, is the absolute amount of rotation (re-orientation) a simulation point undergoes during the entire deformation history. It is calculated as:

$$|\Delta\theta| = \arccos\{([\mathrm{tr}(\mathbf{O}\mathbf{O}_0^{\mathrm{T}}) - 1]/2\}, \tag{5.1}$$

where $\mathbf{O}$ and $\mathbf{O}_0$ are the current and the initial orientation matrixes. The symbol "tr()" stands for the trace of a matrix.

The second example to study the accuracy of the mesh replacement method is a 3D polycrystal RVE, as shown in Fig. 5.2(b). The deformed configuration before remeshing and the remeshed configuration are shown in Fig. 5.4. Unlike the first example, the state variables' distribution for this example is close to a normal distribution. The Kolmogorov-Smirnov values for the total dislocation density and the rotation angle are

0.003 and 0.002, respectively. Again, the difference between the two cumulative distributions is negligible.

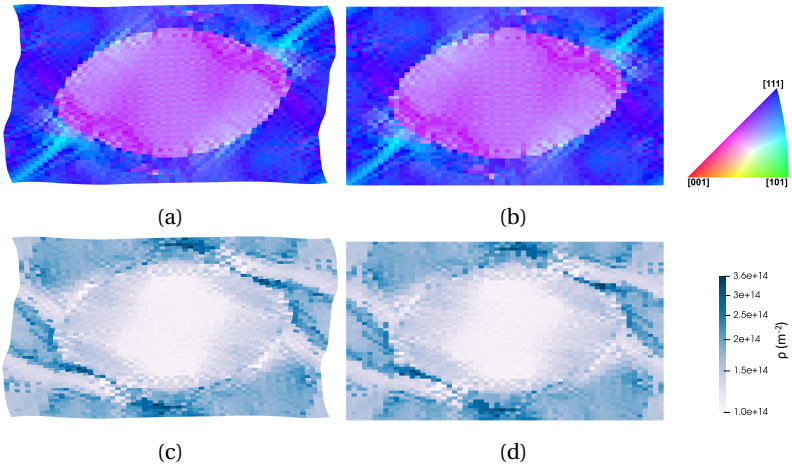

Fig. 5.3: The data mapping step for the mesh replacement method is examined by comparing the outputs before and after remeshing for the bicrystal RVE presented in Fig. 5.2(a) subjected to 25% thickness reduction. IPF color map parallel to the loading (vertical) direction before (a) and after (b) remeshing; mobile dislocation density map before (c) and after (d) remeshing.

5.3.1.2. Mesh distortion control method

In the case of FFT-based spectral solvers, which always operate on a cubic domain that is infinitely repeated, the mesh replacement method can be used only with loading conditions that preserve the periodicity of the configuration, e.g. tensile, compression, or biaxial loading conditions. For this reason, this approach cannot be employed to simulate cases where the RVE is under loading conditions that involve a shear deformation. However, shear deformation is present in many industrial applications, and it is essential to be able to include such type of loading condition during large deformation of polycrystals. Therefore, a second approach, the mesh distortion control method, is developed to enable remeshing under shear loading. In Section 5.4.4, information about shear loading and the related challenges is given.

The mesh distortion control method is working based on smoothing the distorted mesh to continue the simulation in its current state, see Fig. 5.5. The new undistorted mesh is achieved by modifying the deformation map and removing the locally fluctuating part of the deformation, see Section 5.3.2.1. Since the average deformation is maintained, this remeshing technique can be used along with periodic configurations subjected to an arbitrary loading condition, such as those loading conditions involving a shear deformation, see Section 5.4.4 for more detail. This remeshing procedure also allows using the adaptivity scheme introduced in Section 5.3.3 for updating the simulation resolution at each remeshing step.

The similitude between the deformed and the remeshed configurations for the mesh distortion control method is tested using two examples, as shown in Fig. 5.6.

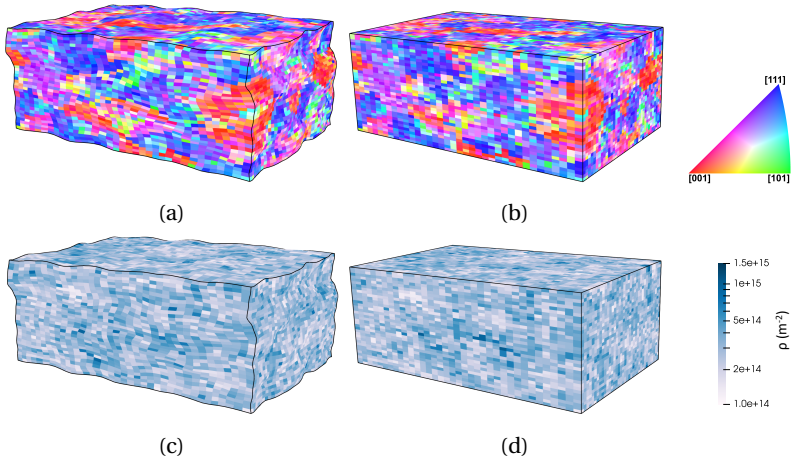

Fig. 5.4: The data mapping step for the mesh replacement method is examined by comparing the outputs before and after remeshing for the 3D polycrystal RVE presented in Fig. 5.2(b) subjected to 40% thickness reduction. IPF color map parallel to the loading (vertical) direction before (a) and after (b) remeshing; mobile dislocation density map before (c) and after (d) remeshing.

Fig. 5.6(a) represents a quasi-3D bicrystal RVE similar to the one used in the previous section. However, here the orientations of the two grains are exchanged. Fig. 5.7 shows the deformed bicrystal RVE before remeshing and the configuration after remeshing for this RVE. Obviously, the main features are captured and transferred to the remeshed configuration. The Kolmogorov-Smirnov values for the total dislocation density and the rotation angle distributions are 0.005 and 0.003, respectively. It is evident that the difference between the two distributions is negligible.

The second example to study the accuracy of the mesh distortion control method is a 3D polycrystal RVE, as presented in Fig. 5.6(b). The deformed and the remeshed configurations are shown in Fig. 5.8. The Kolmogorov-Smirnov values for the total dislocation density and the rotation angle are 0.001 and 0.003, respectively. Again, the difference between the two distributions is negligible.

5.3.2. Mapping variables

Mapping the microstructural and mechanical variables from the deformed state onto the new mesh is performed using a nearest-neighbor mapping algorithm that identifies the nearest point[1] in the original deformed mesh for each point in the newly created mesh [58]. The nearest neighbor is determined using the Euclidean distances measured between points in the deformed and the remeshed configurations. It should be noted that more than one point in the remeshed state might acquire their state variables from the same point during mapping. This is especially the case when the number of elements is increased using the adaptive meshing scheme introduced in Section 5.3.3. After assigning a corresponding point in the old configuration to each point in the new configuration, the microstructural and mechanical variables are transferred to the new

[1] Fourier points in the case of a spectral solver and integration points in the case of a finite element solver.

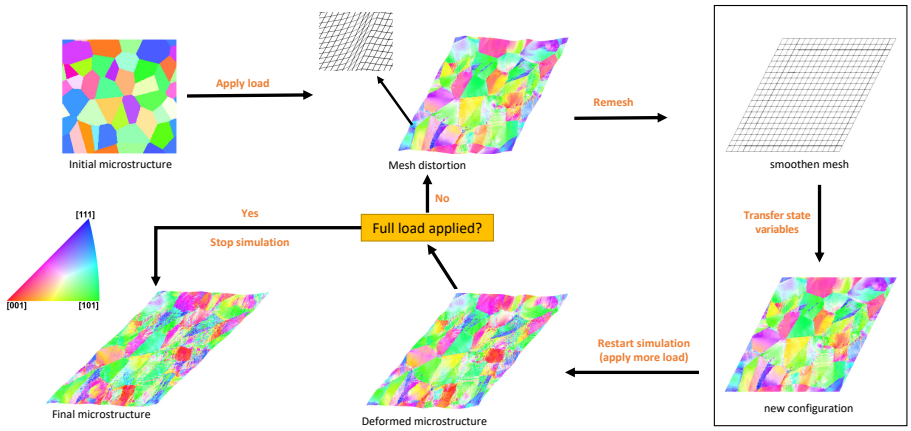

Fig. 5.5: The schematic shows the mesh distortion control method workflow. The undistorted mesh is achieved by removing the fluctuating part of the deformation and only keeping the homogeneous part of the deformation. Then, the state variables from the deformed state are mapped onto the smoothed mesh using a nearest-neighbor mapping algorithm. This remeshing algorithm allows assigning a new mesh resolution to the new configuration. The new configuration is used to restart and continue the simulation.

configuration. Different processes are used here for different variables. In general, the variables are handled in three different ways, as explained in the following.

5.3.2.1. Deformation gradient tensor

Mesh replacement method

The deformation gradient tensor is handled differently for the two remeshing methods. For the mesh replacement method, the deformation gradient tensor is replaced by the identity tensor, and the elastic deformation during the remeshing procedure is fully relaxed. Since the elastic strains during large deformation are usually significantly smaller than the plastic strains, approximately two orders of magnitude, the relaxation of the elastic deformation has a negligible effect on the resulting mechanical fields at large plastic strains [48]. Because of the full relaxation of the elastic deformation, the new configuration is in mechanical equilibrium.

Mesh distortion control method

In the mesh distortion method, the locally fluctuating part of the deformation map is calculated for each element, and then it is removed from the deformation. In other words, only the spatially homogeneous part of the deformation is maintained, i.e. the average deformation gradient tensor, which is also equal to the deformation gradient applied as a boundary condition. For this purpose, the deformation gradient tensor, $\mathbf{F}$, is split into the sum of a spatially homogeneous part, $\overline{\mathbf{F}}$, and a locally fluctuating part $\widetilde{\mathbf{F}}$:

$$\mathbf{F} = \overline{\mathbf{F}} + \widetilde{\mathbf{F}}. \tag{5.2}$$

Now the new undistorted mesh is generated using the modified deformation map, $\chi^{\mathrm{r}}(\mathbf{x})$, as:

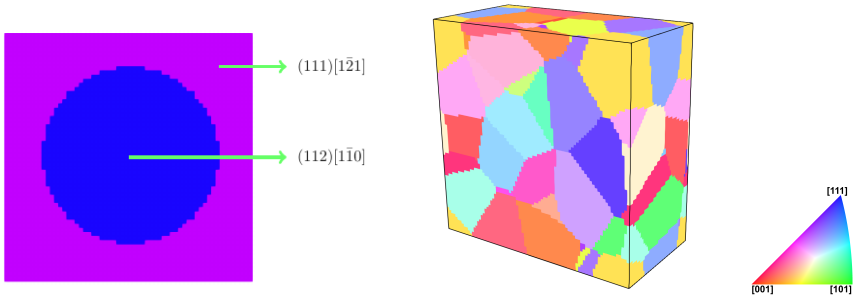

(a) Example 3 (b) Example 4

Fig. 5.6: Voxel representation of the RVEs used in the crystal plasticity simulations to show capabilities of the mesh distortion control remeshing method. The coloring follows the Inverse Pole Figure (IPF) color map parallel to the vertical direction. (a) Example 3: a quasi-3D RVE made of 2 grains with an initial mesh of 60×60 elements. (b) Example 2: a 3D polycrystal RVE made of 32 grains with an initial mesh of $80 \times 40 \times 80$ elements.

5

$$\chi^{r}(\mathbf{x}) = \chi(\mathbf{x_0}) - \tilde{\mathbf{F}}\mathbf{x} = \bar{\mathbf{F}}\mathbf{x}. \tag{5.3}$$

Here, a new mechanical equilibrium state for the undistorted mesh needs to be calculated. i.e. a state where zero net forces are acting on the material volume. Mathematically, for static equilibrium, this is expressed as [54]:

$$\text{Div}\,\mathbf{P} = 0 \quad in\ \mathscr{B}_0. \tag{5.4}$$

5.3.2.2. Crystal orientations

As mentioned in Section 2.2.1, the initial crystal orientation of each simulation point is introduced via $\mathbf{F}_p^0$, and the initial $\mathbf{F}_e^0$ is set as the inverse of $\mathbf{F}_p^0$ to achieve the desired identity deformation gradient tensor at the beginning of the simulation. During the deformation, the orientation of the simulation points evolves according to the loading, orientation, and neighboring points. The current orientation of each simulation point can be calculated using the rotational part of the elastic deformation gradient tensor; see Eq. (2.11). With this in mind, during the remeshing step, the deformation gradient tensor is modified and updated to achieve an undistorted mesh. This adjustment in the deformation gradient tensor must be reflected in the plastic deformation tensor to achieve a correct initial state for the simulation points' current orientation. Since the mesh distortion is handled differently for the two remeshing methods, the plastic deformation gradient tensor must also be adjusted accordingly.

Mesh replacement method

In the mesh replacement method, the restart of the remeshing analysis is handled similarly to a new simulation in which the initial state variables are modified according to the latest state of the deformation before remeshing. Moreover, according to this approach, the deformation gradient tensor is fully relaxed to the identity tensor. Therefore, to accommodate the current orientation of the crystal points, the plastic deformation tensor is replaced with current orientation of the simulation points, i.e.

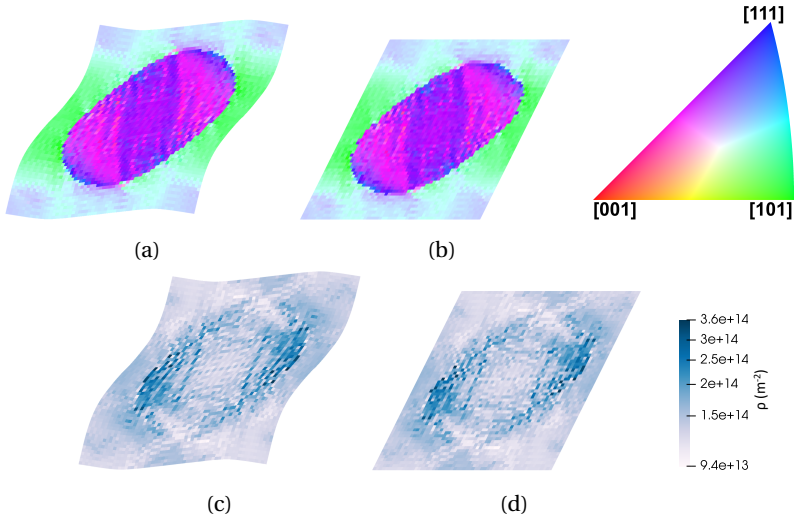

Fig. 5.7: The data mapping step for the mesh distortion control method is examined by comparing the outputs before and after remeshing for the bicrystal RVE presented in Fig. 5.6(a) subjected to 0.5 simple shear loading. IPF color map parallel to the vertical direction before (a) and after (b) remeshing; mobile dislocation density map before (c) and after (d) remeshing.

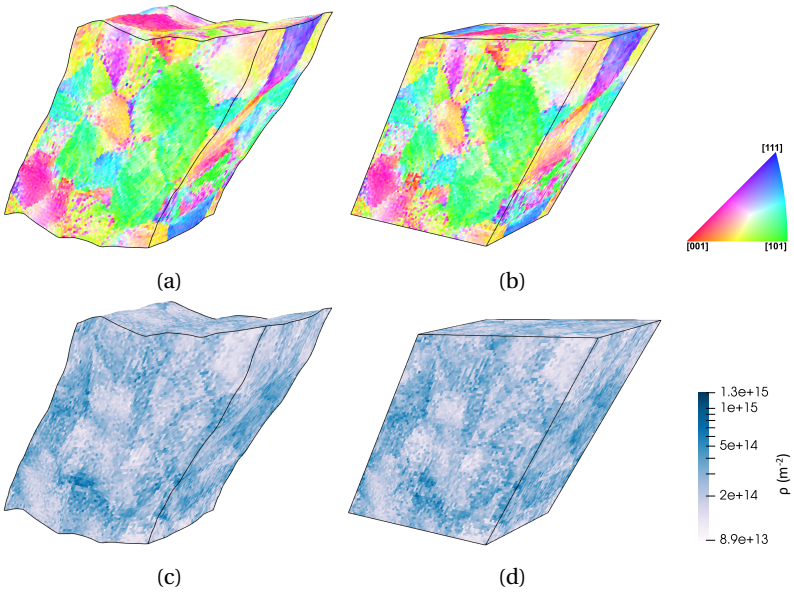

Fig. 5.8: The data mapping step for the mesh distortion control method is examined by comparing the outputs before and after remeshing for the bicrystal RVE presented in Fig. 5.6(b) subjected to 0.5 simple shear loading. IPF color map parallel to the vertical direction before (a) and after (b) remeshing; mobile dislocation density map before (c) and after (d) remeshing.

$\mathbf{F}_p^r = \mathbf{O}$. At the same time, the elastic deformation gradient tensor is set to the inverse of $\mathbf{F}_p^r$. The superscript "r" stands for the initial condition of the remeshed configuration before restarting the simulation.

Mesh distortion control method

According to the mesh distortion control method, the fluctuating part of the deformation is removed to overcome the distortion problem, and the deformation gradient tensor is adjusted to the average gradient deformation tensor. The deformation gradient tensor before restarting the simulation, i.e. after the remeshing step, can be written as:

$$\mathbf{F}^r = \overline{\mathbf{F}} = \mathbf{F}_e^r \mathbf{F}_p^r = \mathbf{F}_e \mathbf{F}_p^r. \tag{5.5}$$

Since the plastic deformation is much larger than the elastic deformation, it is assumed here that the fluctuating part belongs fully to the plastic deformation, and therefore $\mathbf{F}_e^r = \mathbf{F}_e$. The adjusted remeshed plastic deformation tensor, $\mathbf{F}_p^r$, can now be calculated as:

$$\mathbf{F}_p^r = \mathbf{F}_e^{-1} \overline{\mathbf{F}} = (\mathbf{F}_p \mathbf{F}^{-1}) \overline{\mathbf{F}}. \tag{5.6}$$

This newly calculated plastic deformation tensor includes the current orientation and the average plastic strain.

5.3.2.3. All other state variables

All other state variables, such as dislocation density or accumulated shear strain on each slip system, are directly mapped from the old simulation to the new simulation. This procedure follows an adaptable framework, and it allows mapping different state variables based on the constitutive law in use. As a result, the remeshing methodologies are flexible to be used with any crystal plasticity model.

5.3.3. An adaptive scheme for updating resolution: adaptivity

During large deformation, the elements' aspect ratio, i.e. the ratio of the element size in the stretching direction to the element size in the compression direction, can become very large. Extensively elongated elements introduce errors in the simulation and, more importantly, can prevent strain localization. To overcome this problem, we have implemented a global adaptive scheme for both remeshing approaches. This adaptive scheme is flexible and allows selecting any desired number of elements in the three coordinate directions independently at any remeshing step. Such ability to adapt the resolution according to the problem is crucial for large deformation simulations.

Fig. 5.9(a) shows the IPF color map parallel to the loading direction for the deformed configuration. The remeshed configurations achieved using three different resolutions are shown in Fig. 5.9(b-d). Here, the remeshing is performed using the mesh replacement method, and the initial microstructure is according to the bicrystal example shown in Fig. 5.2(a). Fig. 5.10 shows the total dislocation density and the rotation angle distributions for these cases. It is clear from both figures that all the remeshing resolution cases selected here properly represent the deformed state. Although some improvement in the remeshing state can be observed for higher mesh resolutions, this improvement is subtle according to the Kolmogorov-Smirnov values

presented in Table 5.1. The effect of remeshing resolution and adaptivity on the microstructure evolution is discussed in 5.4.2.

Table 5.1: The Kolmogorov-Smirnov values obtained for cases remeshed with different resolutions.

Resolution		60 × 60	107 × 60	214 × 120	428 × 240
Kolmogorov-Smirnov value	ρ^{α}	0.007	0.005	0.004	0.002
	$\lvert\Delta\theta\rvert$	0.007	0.005	0.003	0.001

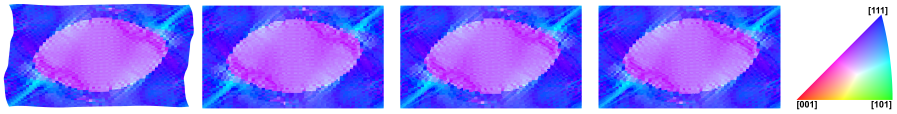

(a) (b) (c) (d)

Fig. 5.9: Effect of remeshing resolution on the similitude of the configurations before and after remeshing. The figures show the IPF color map parallel to the loading (vertical) direction for the example presented in Fig. 5.2(a) subjected to 25% thickness reduction: (a) before remeshing with initial mesh of 60 × 60 elements, (b) remeshed to a new mesh of 107 × 60 elements, (c) remeshed to a new mesh of 214 × 120 elements, (d) remeshed to a new mesh of 428 × 240 elements.

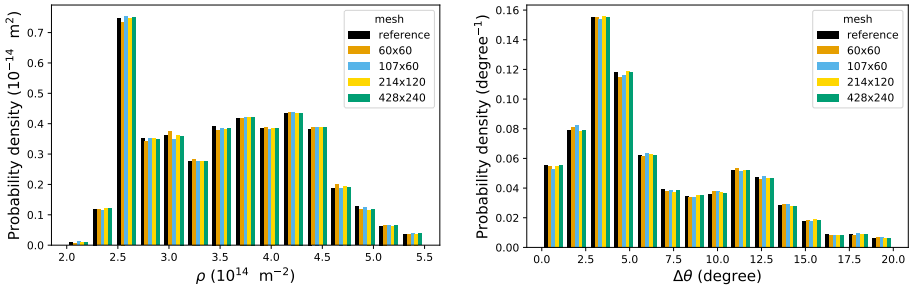

(a) (b)

Fig. 5.10: Influence of the remeshing resolution on the distribution of (a) total dislocation density, (b) rotation angle. The initial number of elements for the reference configuration is 60 × 60. The results are shown for the cases presented in Fig. 5.9.

5.4. Results and discussion

5.4.1. Remeshing accuracy

In this study, two different remeshing approaches were introduced to solve the mesh distortion problem. It was shown that the deformed and the remeshed configurations are almost equivalent, and the mapping procedure can transfer the state variables accurately. Now the question arises, how does the remeshing procedure affect the microstructure and the mechanical fields developed during the simulation? To answer this question, we deform the RVEs to the largest achievable strain without remeshing.

This simulated state is used as the reference state, and it is compared to the results obtained using different remeshing strategies. This comparison is used to analyze and discuss the accuracy of the remeshing approaches.

5.4.1.1. Mesh replacement method

For the mesh replacement method, the bicrystal example presented in Fig. 5.2(a) is used for evaluating the remeshing approach. This RVE is subjected to a plane-strain compression up to 25% thickness reduction using different remeshing strategies:

- 1 step of 25% without remeshing (strategy *A*)
- 5 steps of 5% (strategy *B*)
- 3 steps of 10% + 10% + 5% (strategy *C*)
- 2 steps of 15% + 10% (strategy *D*)

Strategy *A*, the case without remeshing, is used as a reference case to evaluate the accuracy of the remeshing method. The stress-strain curves obtained using different remeshing strategies are compared to the reference case in Fig. 5.11. After a very small recovery strain, the remeshed configuration reaches the same stress level as the case without remeshing, and the effect of the remeshing process on the stress-strain curves becomes negligible. Generally, for the minimal impact of the remeshing on the results, the remeshing strain should be selected large enough relative to this recovery strain.

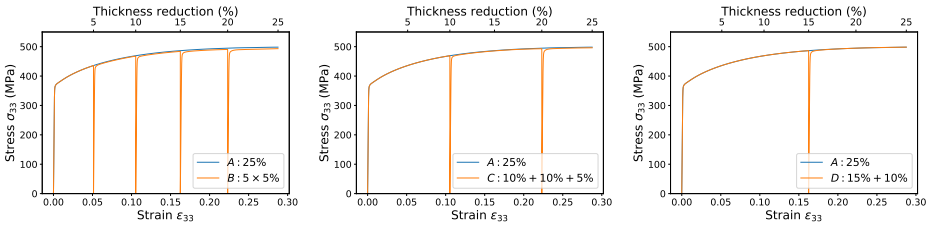

(a) remeshing strategy B (b) remeshing strategy C (c) remeshing strategy D

Fig. 5.11: Influence of the remeshing strategy on the stress-strain curves. The y-axis and x-axis show respectively the stress and the logarithmic strain in the compression direction. The blue curve shows the stress-strain curve for reference case A.

The IPF color map parallel to the loading (vertical) direction, the mobile dislocation density maps, and orientation distribution functions (ODFs) for the different remeshing strategies are shown in Fig. 5.12. Fig. 5.13 illustrates the distributions of the total dislocation density and the rotation angle for the different remeshing strategies. There is a very good agreement between results obtained using remeshing strategies *C* and *D* with reference case *A*. However, a comparison between results obtained using remeshing strategy *B* and reference case *A* reveals some small differences in the predicted shape of the central grain. The stress-strain curve for strategy *B* also shows a little deviation from the reference case. The fluctuation part of deformation, which is directly related to the deformation localization, is not fully developed at small strains.

Therefore, when small remeshing strains are used, the localized deformation may not be fully captured during the remeshing process. As a result, frequent remeshing after a small strain attenuates strain localization. However, when the remeshing procedure is applied in larger strain steps, i.e. remeshing strategies *C* and *D*, the deviation between the remeshed simulations and the reference simulation becomes small and negligible. The Kolmogorov-Smirnov values for all cases are listed in Table 5.2.

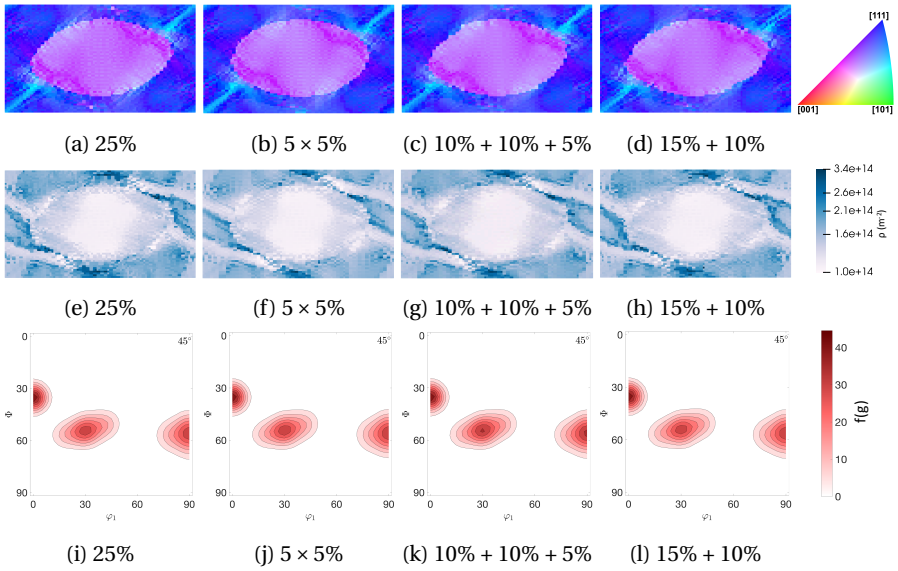

Fig. 5.12: Influence of the remeshing strategy on the simulation outputs. (a-d) IPF color maps parallel to the loading (vertical) direction, (e-h) mobile dislocation density maps, and (i-l) orientation density f(g) maps obtained from the ODFs. The results are for the example presented in Fig. 5.2(a).

Although early remeshing can smoothen the localized deformation and affect the outputs' accuracy, remeshing after a large strain, late remeshing, can also deteriorate the accuracy and the computational efficiency. Large distortion in the mesh introduces numerical errors in the simulation. Therefore, as the first drawback, when the remeshing procedure is applied late after the distortions become too large, the state variables will include errors. These numerical errors would be transferred during the remeshing process. The mesh distortion and numerical errors also can affect the simulations' convergence and computational cost. We observed that the number of iterations needed for reaching convergence is directly related to the level of mesh distortion.

Table 5.2: The Kolmogorov-Smirnov values obtained from different remeshing strategies.

	mesh replacement method			mesh distortion control method		
strategy	$5\times5\%$	$10\%+10\%+5\%$	$15\%+10\%$	$0.2+0.2+0.1$	$0.25+0.25$	$0.4+0.1$
ρ^{α}	0.072	0.046	0.017	0.025	0.022	0.019
$\lvert\Delta\theta\rvert$	0.038	0.029	0.025	0.028	0.036	0.028

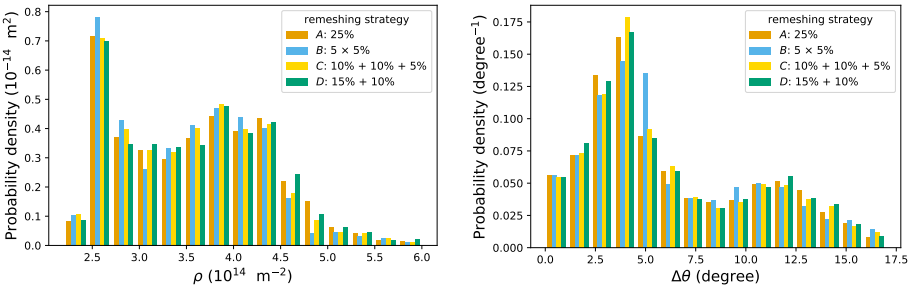

(a) (b)

Fig. 5.13: The influence of the remeshing strategy on the distribution of (a) total dislocation density, (b) rotation angle. strategy *A* show the outputs for the case without remeshing. The results are for the example presented in Fig. 5.2(a) subjected to 25% thickness reduction.

5.4.1.2. Mesh distortion control method

For the mesh distortion control method, the bicrystal example presented in Fig. 5.6(a) is used for evaluating the remeshing approach. The RVE is subjected to a simple shear of 0.5 using different remeshing strategies:

- 1 step of 0.5 without remeshing (strategy *E*)
- 3 steps of 0.2 + 0.2 + 0.1 (strategy *F*)
- 2 steps of 0.25 + 0.25 (strategy *G*)
- 2 steps of 0.4 + 0.1 (strategy *H*)

Strategy *E*, the case without remeshing, is used as a reference case to evaluate the accuracy of the remeshing method. The stress-strain curves obtained using different remeshing strategies are compared to the reference case in Fig. 5.14. The recovery strain for the mesh distortion control method is much smaller than for the mesh replacement method, and the remeshed configuration immediately reaches the same stress level as the case without remeshing.

The IPF color map parallel to the vertical direction, the mobile dislocation density maps, and orientation distribution functions (ODFs) for the different remeshing strategies are shown in Fig. 5.15. Fig. 5.16 illustrates the distributions of the total dislocation density and the rotation angle for different remeshing strategies. There is a very good agreement between results obtained using different remeshing strategies and

the reference case *E*. The Kolmogorov-Smirnov values for all the remeshing strategies are listed in Table 5.2.

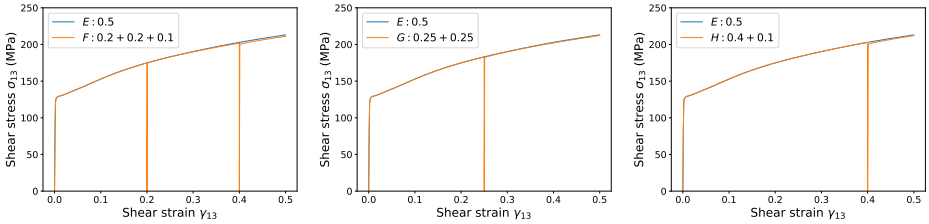

(a) remeshing strategy F (b) remeshing strategy G (c) remeshing strategy H

Fig. 5.14: Influence of the remeshing strategy on the stress-strain curves. The y-axis and x-axis show respectively the stress and the logarithmic strain in the compression direction. The blue curve shows the stress-strain curve for reference case E.

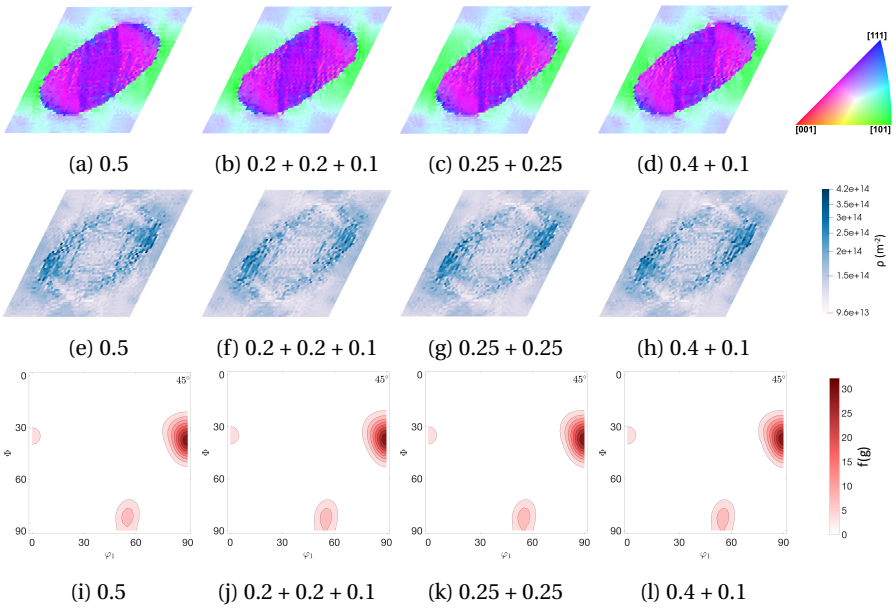

(a) 0.5 (b) 0.2 + 0.2 + 0.1 (c) 0.25 + 0.25 (d) 0.4 + 0.1

(e) 0.5 (f) 0.2 + 0.2 + 0.1 (g) 0.25 + 0.25 (h) 0.4 + 0.1

(i) 0.5 (j) 0.2 + 0.2 + 0.1 (k) 0.25 + 0.25 (l) 0.4 + 0.1

Fig. 5.15: Influence of the remeshing strategy on the simulation outputs. (a-d) IPF color maps parallel to the vertical direction, (e-h) mobile dislocation density maps, and (i-l) orientation density f(g) maps obtained from the ODFs. The results are for the example presented in Fig. 5.2(c).

5.4.2. Adaptivity and mesh refinement effects

The global adaptive scheme implemented in both remeshing approaches allows adjusting the number of elements in the three coordinate directions at any remeshing step. This ability to adjust the resolution is essential for accurate and efficient simulation of large deformations. This section explains the importance and the primary

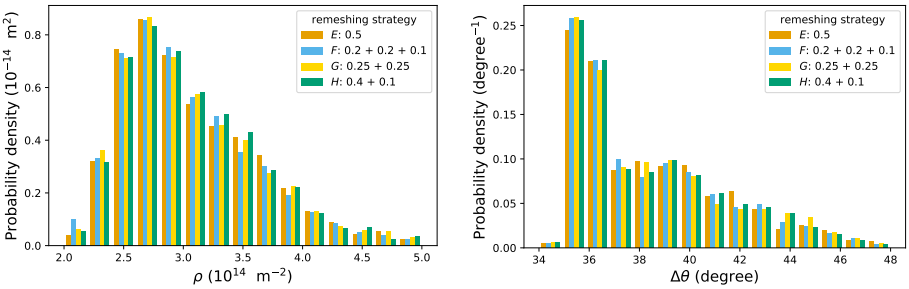

(a) (b)

Fig. 5.16: The influence of the remeshing strategy on the distribution of (a) total dislocation density, (b) rotation angle. Strategy *E* show the outputs for the case without remeshing. The results are for the example presented in Fig. 5.6(a) subjected to 0.5 shear strain.

5

capabilities of the adaptivity scheme and discusses its influence on the level of detail captured in a large deformation crystal plasticity simulation.

Fig. 5.17(a) shows the RVE presented in Fig. 5.2(a) after 75% thickness reduction. For this case, the mesh replacement method is used without the adaptive scheme, i.e. the mesh density is kept constant as 60×60. The element size in the loading direction decreases with increasing the deformation, while the element is elongated in the stretching direction. Therefore, the element becomes rectangular, and the element aspect ratio, the ratio of the element size in the stretching direction to the element size in the compression direction, considerably increases. Although a small aspect ratio at small strain is not an issue, this can introduce inaccuracies at large deformations when the aspect ratio becomes too large. For example, for the RVE subjected to 75% thickness reduction, the elements aspect ratio is around 16. Similarly, the aspect ratio increases to 45 for an RVE subjected to 85% thickness reduction. Such extensively elongated elements introduce errors in the simulation. In addition, an element represents the average response of a section in the discretized space. Therefore, if the element size is larger than the localized features, such as shear bands, it will capture only the homogenized behavior and not the morphology of the localized deformation. As a result, highly elongated elements can prevent strain localization from occurring. Hence, the ability to adjust the resolution according to the problem is crucial for large deformation simulations. In the following, we present two different strategies for adjusting the resolution during deformation.

Constant element size approach

The first approach, which we call the constant element size approach, is based on keeping the element size in all directions constant by adaptively changing the number of elements in different directions during the simulation. This implies decreasing the number of elements in the compression direction and increasing the number of elements in the stretching direction. Using this adaptive meshing method, the number of elements remains approximately constant throughout the simulation. This approach's success requires an initial high mesh density since it results in a significant

decrease in the number of elements in the compression direction. However, once the starting mesh density is adequately selected, one can reach the desired mesh density at the end of the simulation.

Fig. 5.17(b) and Fig. 5.17(e) show the results obtained using the constant element size approach. The initial number of elements are 240 × 240, which are adjusted adaptively to 873 × 66 after 75% thickness reduction. It can be seen that the adaptivity helps to adjust the resolution and to prevent the elements from becoming extensively elongated. More importantly, comparing Fig. 5.17(a) and Fig. 5.17(b) or Fig. 5.17(d) and Fig. 5.17(e) reveals that the amount of detail and deformation heterogeneity captured using the adaptive simulation is considerably higher than the non-adaptive simulation. The elongated elements in the non-adaptive simulation prevent the formation of sharply localized features during the deformation.

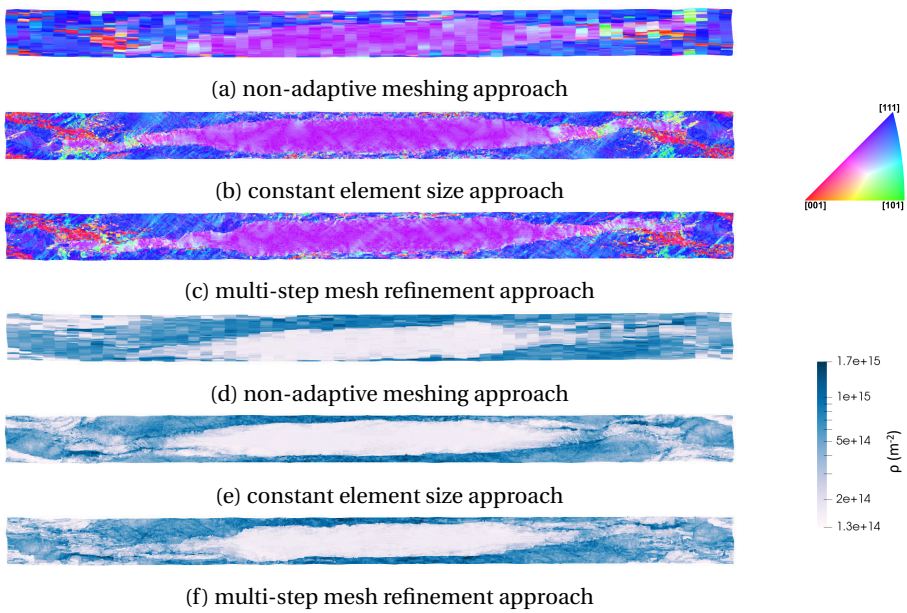

Fig. 5.17: Effect of adaptive remeshing and mesh refinement on the simulation outputs; (a–c) IPF color maps parallel to the loading (vertical) direction, (d–f) mobile dislocation density maps. For the non-adaptive simulation, the initial mesh density of 60 × 60 is kept constant during the deformation, which results in highly elongated elements at large deformations. For the multi-step mesh refinement the number of elements is gradually increased during the deformation to 777 × 60, while for the case of the constant element size approach, the initial number of elements is 240 × 240, which is adjusted gradually to 873 × 66. The results are shown for the example presented in Fig. 5.2 subjected to 75% thickness reduction.

Fig. 5.18 shows the distribution of the total dislocation density, rotation angle, Euler angle Φ, and average misorientation. For calculating the average misorientation of a simulation point, first, the disorientations, i.e. the misorientation considering the cubic symmetry of the material, between the point and all neighboring points are calculated. Then, the average misorientation is calculated. Despite the apparent differences between the amount of localized detail captured using the adaptive and non-adaptive

simulations, there are some large-scale similarities between the distributions of outputs. This similarity is pronounced for variables such as dislocation density, rotation angle, and Euler angle Φ with the Kolmogorov-Smirnov values of 0.072, 0.046, and 0.061, respectively. However, the similarity lessens for the average misorientation, with a Kolmogorov-Smirnov value of 0.131. The average misorientation is a measure of local misorientation, and its value depends on the local variation of the orientation of a point and its neighboring points. Therefore, as is expected, its distribution is affected more strongly by the resolution of the simulation.

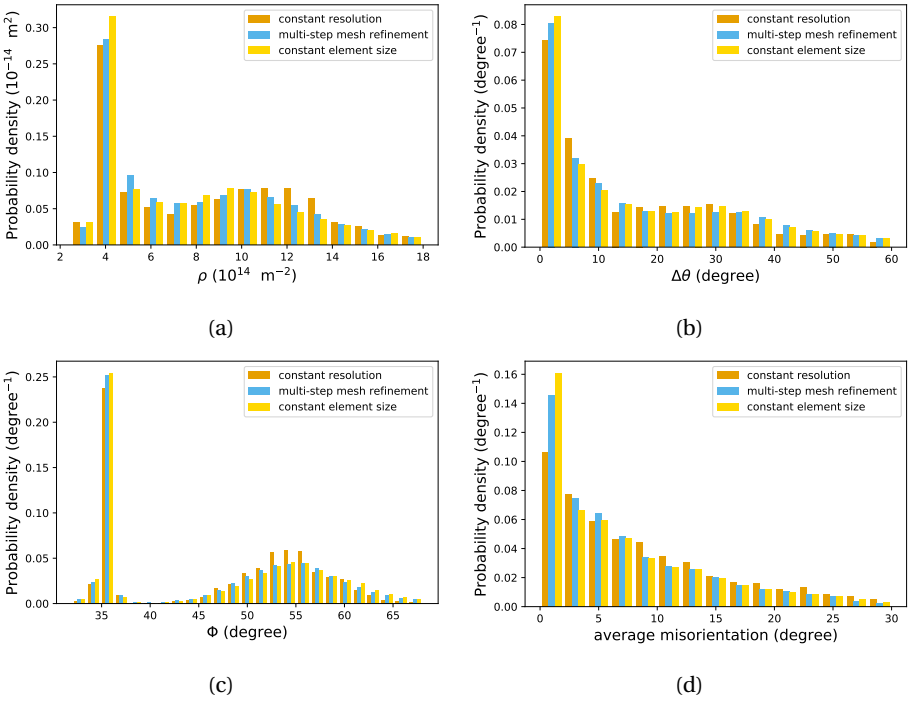

Fig. 5.18: Effect of adaptive remeshing and mesh refinement on the distribution of (a) total dislocation density, (b) rotation angle, (c) Euler angle Φ, (d) Kernel average misorientation. The results are shown for the cases presented in Fig. 5.17.

Multi-step mesh refinement method

The constant element size approach results in a significant decrease in the number of elements in the compression direction, and its success requires an initially high mesh resolution. As a result, it is not computationally efficient for high-resolution crystal plasticity problems. Here, we introduce a second adaptivity approach, which is named the multi-step mesh refinement method. The idea behind this approach is to keep the number of elements in the compression direction constant, i.e. 60 elements for the current example. The number of elements in the stretching direction is then adjusted accordingly to keep the elements close to cube-shaped. Accordingly, the multi-step

mesh refinement approach leads to a gradual rise in the number of points and the simulation resolution during the deformation. We recommend keeping the element number in the most compressed direction constant to ensure a minimum information loss during mapping with a minimal increase in the simulation points. It should be noted that using extra elements in the most compressed direction may improve the mapping, but it also inefficiently increases the simulation resolution. Fig. 5.17(c) and Fig. 5.17(f) show the results when this adaptive scheme is used, and the number of elements in different directions are gradually increased to 777×60.

The results from the two adaptive strategies are very similar. However, for the mentioned example, the computational cost of the multi-step refinement approach is around 18 times less than the constant element size approach. Using the multi-step refinement approach, one can start the simulation with a low but reasonable resolution and gradually increase the resolution to the desired one at the end of the simulation. As a result, a significant portion of the simulation will be done with a lower resolution, which substantially reduces the computational cost and boosts the simulation speed. This is essentially important for high-resolution crystal plasticity simulations, which are, in general, time-consuming simulations.

5.4.3. Comparing mesh replacement method and mesh distortion control method

The two remeshing algorithms proposed in this study are compared in Fig. 5.19. The results are for the RVE in Fig. 5.2(a) subjected to 50% thickness reduction. The results obtained from the two approaches are in good agreement. The Kolmogorov-Smirnov values for the distribution of the total dislocation density, rotation angle, Euler angle Φ, and average misorientation are 0.052, 0.064, 0.059, and 0.038, respectively. The distributions of these variables are shown in Fig. 5.20. It can be seen that the differences belong mainly to the lower tail of the distributions. Besides, there is a good agreement between the distributions for the average misorientation.

We observed that the mesh distortion control method's computational cost, especially at higher strains, is significantly higher than the mesh replacement method. For example, the total number of iterations required to reach 50% thickness reduction for the mesh distortion control method is around two times higher than for the mesh replacement method. This ratio is four times higher to reach 70% thickness reduction. Since the difference between outputs is subtle, for cases where both approaches are applicable, e.g. compression and tension loading, one can save a substantial amount of computational cost using the mesh replacement method. The mesh distortion control method's main advantage is for cases where the mesh replacement method is not applicable, as explained in the next section.

5.4.4. Shear deformation

Shear deformation takes place in many industrial processes, e.g. during the rolling near the surface [59], asymmetric rolling [60], or extrusion and reversible rolling [61]. However, performing remeshing when the configuration is subjected to a loading condition that involves shearing is challenging. This is because it is difficult for such loading conditions to preserve the periodicity requirements, see Fig. 5.21(a). Frydrych

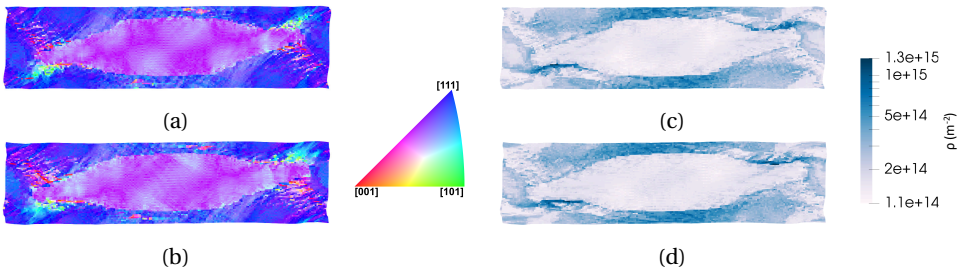

Fig. 5.19: Effect of remeshing approach on the simulation outputs. The results are shown for the bicrystal example presented in Fig. 5.2(a) subjected to 50% thickness reduction. (a,b) IPF color maps parallel to the loading (vertical) direction, (c,d) mobile dislocation density maps.

et al. [52] performed the remeshing for an RVE under simple shear according to an approach based on the structure periodicity, as shown in Fig. 5.21(b). This approach requires the remeshing to be performed at a particular strain point at which the corners of the generated cube-shape configurations coincide precisely with the corners of the deformed configuration.

Although this approach can be used for simulating large shear deformation under periodic boundary conditions, it has two main drawbacks: Firstly, the application of this approach is limited to structures under simple shear. In other words, this approach cannot be used to simulate mixed loading conditions, where the shear load is applied simultaneously with another type of load, such as compression or tension. Secondly, the remeshing approach needs to be performed at a particular strain point. Therefore, if the mesh distortion becomes too large and the simulation fails before this specific strain point, the remeshing cannot be applied.

The mesh distortion control method, see Section 5.3.1.2 for detail, can overcome the challenges related to loading conditions involving shearing. According to this approach, the undistorted mesh is achieved by maintaining the spatially homogeneous part of the deformation and only removing the fluctuating part of the deformation. This means that the applied boundary conditions for the restart analysis are defined according to the initial geometry and similar to when there is no remeshing. As a result, independent of the remeshing strain and the loading type, the periodicity is always preserved, and this approach can be used for any desired loading conditions. Fig. 5.22 shows an RVE subjected to a mixed loading condition, i.e. compression and shear deformation. Here, the RVE presented in Fig. 5.2(a) is subjected to 75% thickness reduction and 20% shearing.

5.4.5. High-resolution 3D simulations: grain shape effect

While the influence of crystallographic orientation/texture is extensively discussed in the literature, less attention has been paid to the effect of the grain shape and its neighboring conditions on the plastic deformation heterogeneity. One reason for this might be the computational/experimental efforts that are required for systematic investigations in this enlarged parameter space. From the computational point of view, studying the grain shape requires a high-resolution crystal plasticity simulation. The

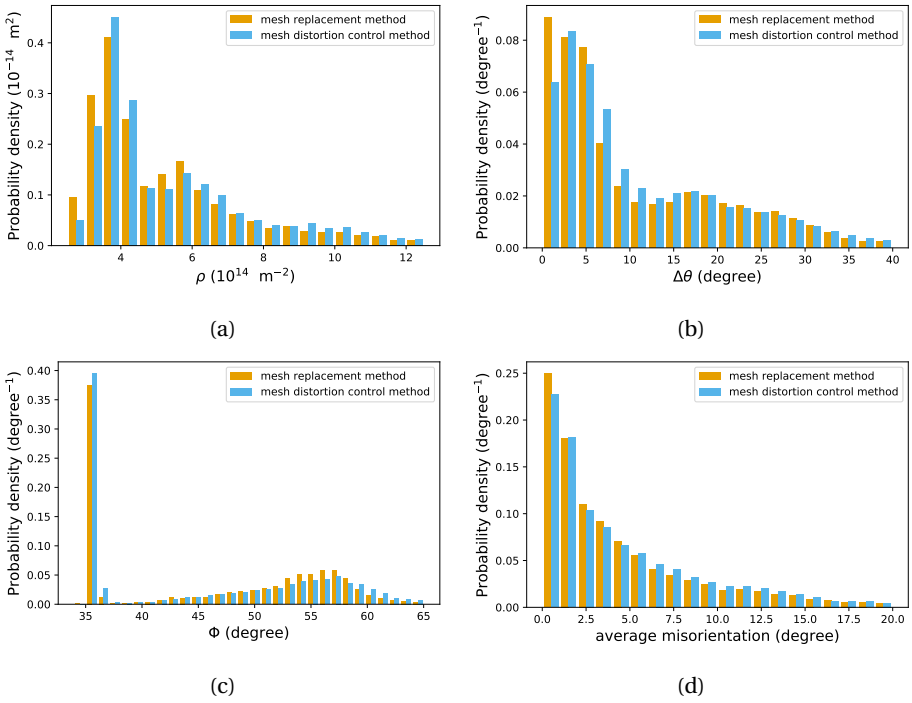

Fig. 5.20: Effect of remeshing approach on the distribution of (a) total dislocation density, (b) rotation angle, (c) Euler angle Φ, (d) average misorientation. The results are shown for the cases presented in Fig. 5.19.

first hurdle of high-resolution crystal plasticity simulations is the significant increase in the computational cost with an increase in the simulation resolution. This is a limiting factor in the number of elements per grain and the number of grains used in a polycrystal simulation. The second problem is that since a higher resolution simulation allows capturing more detailed localized deformation features, as discussed earlier, it is prone to earlier convergence issues.

The remeshing approaches introduced in this study allow us to overcome the convergence issues. Furthermore, the multi-step mesh refinement approach suggested in Section 5.4.2 provides a computationally efficient strategy to simulate large-deformation high-resolution problems. In this section, the merits of this combined modeling strategy in investigating the grain shape effect are shown using a high-resolution bicrystal example. For this purpose, we use an RVE similar to the one presented in Fig. 5.2(a). However, for the current investigation, the diameter of the central grain is reduced to 60% of the configuration's thickness. Fig. 5.23(a) and Fig. 5.23(d) show respectively the IPF color map parallel to the loading direction and the mobile dislocation density map for this RVE. Here, only one element is used in the transverse direction.

In the next step, the RVE is converted to a full 3D model by extruding the quasi-3D RVE in the transverse direction to generate a cubic RVE. In this case, the central grain

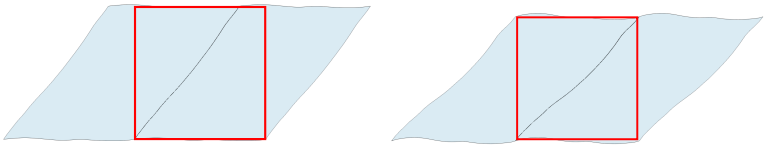

(a) (b)

Fig. 5.21: A schematic plot showing the challenges of preserving the periodicity requirements of the configuration during the remeshing for a configuration subjected to simple shear. The deformed RVE and a copy of it are shown in light blue. The red square shows the newly generated RVE after remeshing. (a) The periodicity requirements are violated during remeshing when the RVE is subjected to a shear strain of 0.8. (b) To preserve the periodicity requirements, the remeshing needs to be performed at a particular strain point, i.e. a shear strain of 1 for the depicted example. As a result, this approach is limited to structures under simple shear. The mesh distortion control method, see Section 5.3.1.2, can overcome the challenges related to loading conditions involving shearing. Using this remeshing approach, independent of the remeshing strain and the loading type, the periodicity is always preserved, and therefore, this remeshing approach can be used to simulate any desired loading conditions.

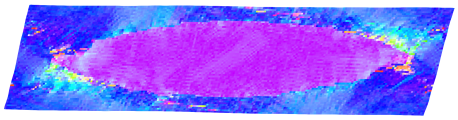

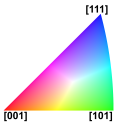

(a) 50% thickness reduction and 13.3% shearing

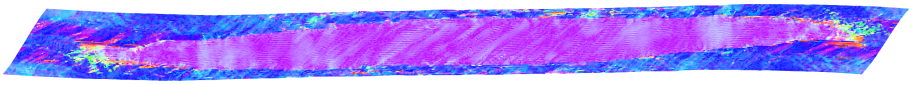

(b) 75% thickness reduction and 20% shearing

Fig. 5.22: The mesh distortion control method is employed to simulate a structure subjected to mixed compression and shear loading. The figures show IPF color maps parallel to the vertical direction for the example presented in Fig. 5.2(a).

has a cylindrical shape. Fig. 5.23(b) shows the results for the mid-surface obtained using this 3D simulation after 75% thickness reduction. The initial number of elements for this simulation are $60 \times 30 \times 60$, and were increased gradually to $777 \times 109 \times 60$ during the 75% thickness reduction. In general, both simulations give the same response. The main difference between the two simulations is the slightly sharper localized deformation in the 2D simulation. Moreover, we observed that the difference between the results at the surface of the 3D simulation and the quasi-3D simulation is more pronounced.

In the final step, the effect of substituting the cylindrical grain with a spherical grain with the same diameter is investigated. Fig. 5.23(c) and Fig. 5.23(e) show respectively the IPF color map parallel to the loading direction and the mobile dislocation density map after 75% thickness reduction. The results are shown at the mid-surface in the transverse direction. The texture and microstructures developed during the deformation are visibly altered by the change in the grain shape. Therefore, though the quasi-3D simulation is able to reproduce the 3D results for the exactly equivalent microstructure, it is unable to incorporate the actual effect of grain morphology. The

distributions of the total dislocation density and rotation angle for the three discussed cases are shown in Fig. 5.24.

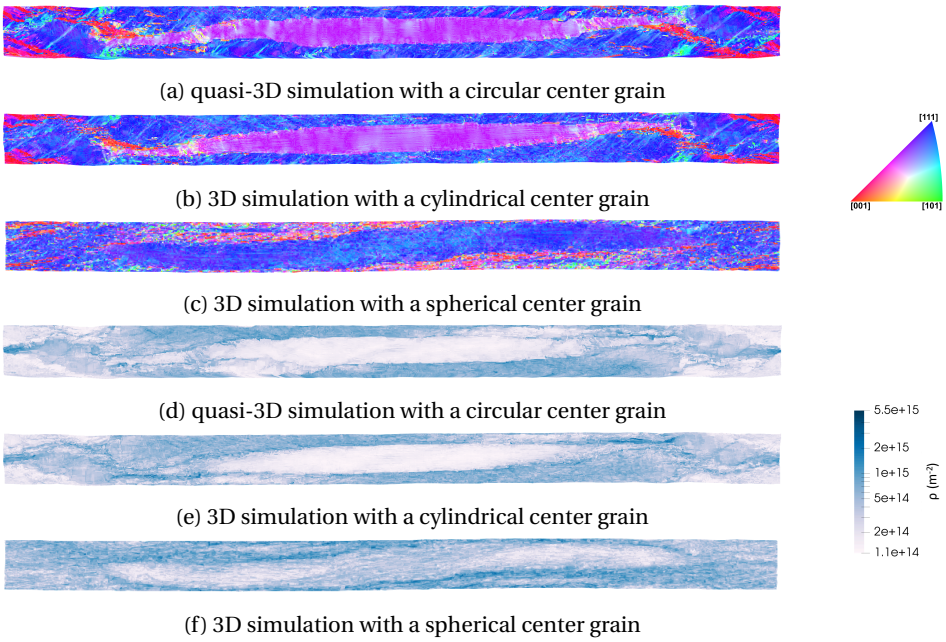

Fig. 5.23: The effect of grain shape on the microstructure evolution. The results are shown for a bicrystal example similar to the one presented in Fig. 5.2(a), but with a slightly smaller center grain. The RVE is subjected to 75% thickness reduction. (a-c) IPF color maps parallel to the loading (vertical) direction, (d-f) mobile dislocation density maps.

5.4.6. High-resolution 3D simulations: application to polycrystals

In this section, the remeshing methodology is applied to perform a high-resolution large-deformation crystal plasticity simulation on a 3D polycrystal example. For this purpose, the simulation is carried out on a polycrystal configuration made of 38 randomly oriented grains, as illustrated in Fig. 5.25. The properties used in the crystal plasticity simulations are similar to those proposed for IF steel in Chapter 4. The RVE is subjected to plane-strain compression up to a thickness reduction of 80%. The initial number of elements at the beginning of the deformation is $80 \times 48 \times 320$. The mesh density is gradually increased to $1314 \times 48 \times 320$ during the deformation, i.e. the number of elements is increased by a factor of 16. The remeshing steps are performed after approximately 0.1 logarithmic strain.

Fig. 5.25 shows the IPF color maps parallel to the loading (vertical) and stretching (horizontal) directions after 20, 40, 60, and 80% thickness reduction. It can be seen how the plastic deformation leads to changes in the grains' orientation and, consequently, to the development of deformation textures. As the load increases, a strong α-fiber texture

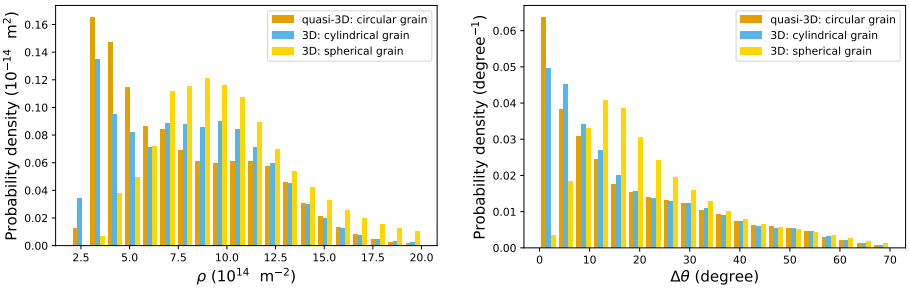

(a) (b)

Fig. 5.24: Effect of grain shape on the distribution of (a) total dislocation density, (b) rotation angle. The results are shown for the cases presented in Fig. 5.23.

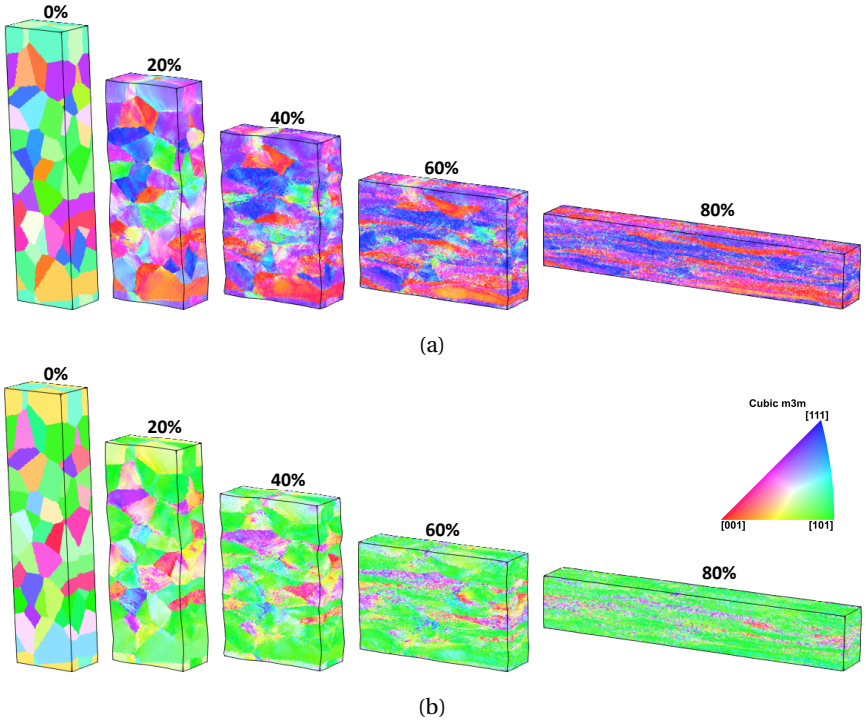

(a)

(b)

Fig. 5.25: IPF color maps parallel to the (a) loading (vertical) direction (b) stretching (horizontal) direction at different thickness reductions for a 3D high-resolution polycrystal made of 38 randomly oriented grains.

(RD//⟨1 1 0⟩) and a comparably weaker γ-fiber (ND//⟨1 1 1⟩) texture are developed, typical for IF steel [62, 63].

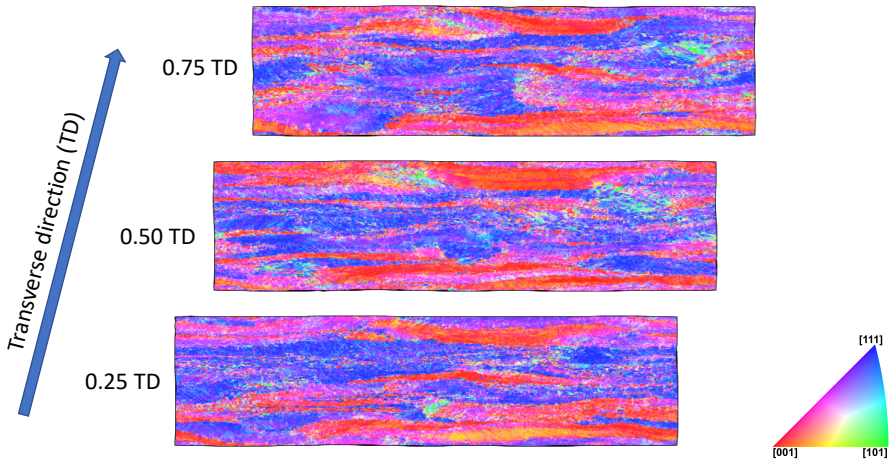

Fig. 5.26: IPF color maps parallel to the loading (vertical) direction at different transverse positions for the same RVE presented in Fig. 5.25 subjected to 75% thickness reduction.

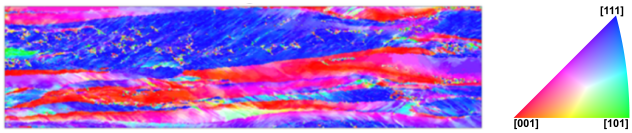

Fig. 5.27: Electron backscattered diffraction (EBSD) measurements of a cold rolled IF steel sample after 75% thickness reduction. The figure shows the IPF color map parallel to the normal (loading) direction for a section of $60 \times 230\ \mu m^2$.

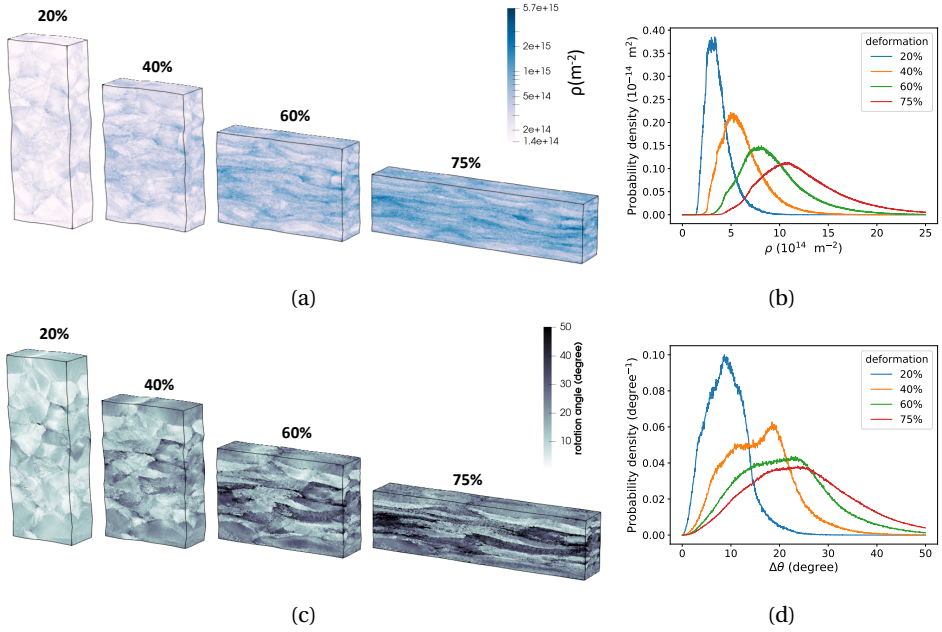

Fig. 5.28: Deformation heterogeneity in a 3D high-resolution polycrystal made of 38 randomly oriented grains at different thickness reductions, (a) evolution of the dislocation density, (b) the corresponding distributions. (c) evolution of the rotation angle, see Eq. (5.1), (d) the corresponding distributions.

The IPF color maps parallel to the loading (vertical) direction for three different sections in the transverse direction are shown in Fig. 5.26. The results are for 75% thickness reduction. It can be seen from this figure and Fig. 5.25 how the originally uniformly orientated crystals are subdivided and rotated into portions with different orientations. In other words, the heterogeneous deformations within individual grains result in the grain fragmentation and the development of smaller grains separated by high-angle misorientation boundaries. The plastic heterogeneity of the deformation depends on many factors, such as the orientation distribution, grain shape, or grain size. However, in general, the heterogeneity of the deformation is more pronounced in the γ-fiber grains. The qualitative resemblance of these results with experimentally observed Electron backscattered diffraction (EBSD) maps is striking. As an example, an EBSD measurement for a cold-rolled IF-steel sample after 75% thickness reduction is shown in Fig. 5.27. It should be noted that the experimental data provided here does not represent the same sample as the simulated one. A detailed comparison between the simulation results and the EBSD data is provided in Chapter 6, which is focused on microstructure evolution in IF-steel.

Fig. 5.28 shows the development of the dislocation density and the rotation angle at different thickness reduction levels. The results reveal that the development of dislocation density and rotation angle is different based on the crystals' orientation, and their distributions are inhomogeneous at all strain levels.

5.5. Conclusions

Problems involving the deformation of solid materials are usually formulated in a way that the mesh is attached to the deformable body and deforms with a change in the shape of the material. This means that the mesh gets distorted due to the heterogeneity of the deformation. In this study, two different approaches to overcome the mesh distortion problem at large strains were proposed, i.e. the mesh replacement method and the mesh distortion control method. The accuracy of the two methods was examined using different test cases designed to evaluate the various steps involved. It was shown that both approaches enable conducting high-resolution large-deformation crystal plasticity simulations and overcoming the associated mesh distortion problem due to the strain localization.

In the mesh replacement method, the deformed configuration with the distorted mesh is replaced by a new configuration with an undistorted mesh. Therefore, it can be stated that the mesh replacement method is like starting a new analysis in which the initial state of the model is obtained from a different analysis. In the mesh distortion control method, the undistorted mesh is achieved by removing the fluctuating part of the deformation and keeping the homogeneous part of the deformation. Hence, contrary to the mesh replacement method, this approach requires finding a new equilibrium state for the smoothed mesh. This leads to a higher computational cost for the mesh distortion control method, especially at large strains. Since no significant difference between the results from the two remeshing approaches was observed, a substantial amount of computational cost can be saved using the mesh replacement method. However, in the case of using periodic boundary conditions, it is challenging to preserve the periodicity requirements for some loading conditions, e.g. loadings involving shear. For such complex loading conditions, the mesh distortion method was proposed. Since the homogeneous part of the deformation is retained during the undistorted mesh generation for the mesh distortion control method, the periodicity requirements are always conserved regardless of the loading condition. Therefore, the mesh distortion control method's main advantage is that it enables remeshing in situations where the periodicity of the geometry would be broken by the mesh replacement method.

A global adaptive scheme was implemented for both remeshing approaches, allowing to update the number of elements in the three coordinate directions at any remeshing steps. This adaptive scheme is important to prevent the elements' aspect ratio from becoming too large. Besides, a multi-step mesh refinement approach was suggested for efficient simulation of large-deformation high-resolution crystal plasticity problems. It was shown that this adaptive meshing strategy can be used, for example, to capture the effect of grain shape on the plastic deformation heterogeneity.

Finally, the mesh replacement method was employed to carry out a 3D high-resolution large-deformation crystal plasticity simulation. It was observed that the remeshing approaches allow capturing the development of deformation heterogeneity and strain localization in polycrystals, e.g. in-grain orientation spread. Such detailed high-resolution large-deformation simulations can be used to thoroughly analyze how, for example, deformation heterogeneity or in-grain orientation spread depends on the crystal orientation, neighbor grains, or any other relevant factors. Moreover,

capturing such localized details enables modeling subsequent processes, such as recrystallization, which are dependent on the formation of these localized deformation features.

References

[1] K. Sedighiani, V. Shah, K. Traka, M. Diehl, F. Roters, J. Sietsma, and D. Raabe, *Large-deformation crystal plasticity simulation of microstructure and microtexture evolution through adaptive remeshing,* International Journal of Plasticity **146**, 103078 (2021).

[2] S. Choi, *Simulation of stored energy and orientation gradients in cold-rolled interstitial free steels,* Acta Materialia **51**, 1775 (2003).

[3] A. J. Beaudoin, H. Mecking, and U. F. Kocks, *Development of localized orientation gradients in fcc polycrystals,* Philosophical Magazine A: Physics of Condensed Matter, Structure, Defects and Mechanical Properties **73** (1996), 10.1080/01418619608242998.

[4] M. Sachtleber, Z. Zhao, and D. Raabe, *Experimental investigation of plastic grain interaction,* Materials Science and Engineering A **336**, 81 (2002).

[5] D. Raabe, Z. Zhao, and F. Roters, *Study on the orientational stability of cube-oriented FCC crystals under plane strain by use of a texture component crystal plasticity finite element method,* Scripta Materialia **50** (2004), 10.1016/j.scriptamat.2003.11.061.

[6] C. Zhang, H. Li, P. Eisenlohr, W. Liu, C. J. Boehlert, M. A. Crimp, and T. R. Bieler, *Effect of realistic 3D microstructure in crystal plasticity finite element analysis of polycrystalline Ti-5Al-2.5Sn,* International Journal of Plasticity **69** (2015), 10.1016/j.ijplas.2015.01.003.

[7] J. Oddershede, J. P. Wright, A. Beaudoin, and G. Winther, *Deformation-induced orientation spread in individual bulk grains of an interstitial-free steel,* Acta Materialia **85** (2015), 10.1016/j.actamat.2014.11.038.

[8] D. Wang, M. Diehl, F. Roters, and D. Raabe, *On the role of the collinear dislocation interaction in deformation patterning and laminate formation in single crystal plasticity,* Mechanics of Materials **125** (2018), 10.1016/j.mechmat.2018.06.007.

[9] J. Cappola, J. C. Stinville, M. Charpagne, P. G. Callahan, M. P. Echlin, T. M. Pollock, A. Pilchak, and M. Kasemer, *On the Localization of Plastic Strain in Microtextured Regions of Ti-6Al-4V,* Acta Materialia **204**, 116492 (2021).

[10] M. Dao and M. Lit, *A micromechanics study on strain-localization-induced fracture initiation in bending using crystal plasticity models,* Philosophical Magazine A: Physics of Condensed Matter, Structure, Defects and Mechanical Properties **81** (2001), 10.1080/01418610108216649.

[11] C. C. Tasan, J. P. M. Hoefnagels, M. Diehl, D. Yan, F. Roters, and D. Raabe, *Strain localization and damage in dual phase steels investigated by coupled in-situ deformation experiments and crystal plasticity simulations,* International Journal of Plasticity **63**, 198 (2014).

[12] H. Proudhon, J. Li, F. Wang, A. Roos, V. Chiaruttini, and S. Forest, *3D simulation of short fatigue crack propagation by finite element crystal plasticity and remeshing,* in *International Journal of Fatigue*, Vol. 82 (Elsevier Ltd, 2016) pp. 238–246.

[13] M. Diehl, M. Wicke, P. Shanthraj, F. Roters, A. Brueckner-Foit, and D. Raabe, *Coupled Crystal Plasticity–Phase Field Fracture Simulation Study on Damage Evolution Around a Void: Pore Shape Versus Crystallographic Orientation,* Jom **69**, 872 (2017).

[14] G. Sarma and P. Dawson, *Effects of interactions among crystals on the inhomogeneous deformations of polycrystals,* Acta Materialia **44**, 1937 (1996).

[15] S. Forest, *Modeling slip, kink and shear banding in classical and generalized single crystal plasticity,* Acta Materialia **46** (1998), 10.1016/S1359-6454(98)00012-3.

[16] P. Bate, *Modelling deformation microstructure with the crystal plasticity finite-element method,* Philosophical Transactions of the Royal Society A: Mathematical, Physical and Engineering Sciences **357** (1999), 10.1098/rsta.1999.0391.

[17] A. K. Kanjarla, P. Van Houtte, and L. Delannay, *Assessment of plastic heterogeneity in grain interaction models using crystal plasticity finite element method,* International Journal of Plasticity **26** (2010), 10.1016/j.ijplas.2009.05.005.

[18] N. Jia, F. Roters, P. Eisenlohr, C. Kords, and D. Raabe, *Non-crystallographic shear banding in crystal plasticity FEM simulations: Example of texture evolution in α-brass,* Acta Materialia **60** (2012), 10.1016/j.actamat.2011.10.047.

[19] M. Kasemer and P. Dawson, *A finite element methodology to incorporate kinematic activation of discrete deformation twins in a crystal plasticity framework,* Computer Methods in Applied Mechanics and Engineering **358** (2020), 10.1016/j.cma.2019.112653.

[20] L. Chen, J. Chen, R. A. Lebensohn, Y. Z. Ji, T. W. Heo, S. Bhattacharyya, K. Chang, S. Mathaudhu, Z. K. Liu, and L. Q. Chen, *An integrated fast Fourier transform-based phase-field and crystal plasticity approach to model recrystallization of three dimensional polycrystals,* Computer Methods in Applied Mechanics and Engineering **285**, 829 (2015).

[21] P. Zhao, T. Song En Low, Y. Wang, and S. Niezgoda, *An integrated full-field model of concurrent plastic deformation and microstructure evolution: Application to 3D simulation of dynamic recrystallization in polycrystalline copper,* International Journal of Plasticity **80** (2016), 10.1016/j.ijplas.2015.12.010.

[22] D. Kim, W. Woo, W. Park, Y. Im, and A. Rollett, *Mesoscopic coupled modeling of texture formation during recrystallization considering stored energy decomposition,* Computational Materials Science **129** (2017), 10.1016/j.commatsci.2016.11.048.

[23] K. K. Alaneme and E. A. Okotete, *Recrystallization mechanisms and microstructure development in emerging metallic materials: A review,* (2019).

[24] M. Diehl and M. Kühbach, *Coupled experimental-computational analysis of primary static recrystallization in low carbon steel,* Modelling and Simulation in Materials Science and Engineering **28** (2020), 10.1088/1361-651X/ab51bd.

[25] F. Roters, P. Eisenlohr, L. Hantcherli, D. Tjahjanto, T. Bieler, and D. Raabe, *Overview of constitutive laws, kinematics, homogenization and multiscale methods in crystal plasticity finite-element modeling: Theory, experiments, applications,* Acta Materialia **58**, 1152 (2010).

[26] C. C. Tasan, M. Diehl, D. Yan, C. Zambaldi, P. Shanthraj, F. Roters, and D. Raabe, *Integrated experimental-simulation analysis of stress and strain partitioning in multiphase alloys,* Acta Materialia **81**, 386 (2014).

[27] M. Khadyko, S. Dumoulin, and O. S. Hopperstad, *Texture gradients and strain localisation in extruded aluminium profile,* International Journal of Solids and Structures **97_98**, 239 (2016).

[28] M. Diehl, D. An, P. Shanthraj, S. Zaefferer, F. Roters, and D. Raabe, *Crystal plasticity study on stress and strain partitioning in a measured 3D dual phase steel microstructure,* Physical Mesomechanics **20** (2017), 10.1134/S1029959917030079.

[29] M. Diehl, M. Groeber, C. Haase, D. A. Molodov, F. Roters, and D. Raabe, *Identifying Structure–Property Relationships Through DREAM.3D Representative Volume Elements and DAMASK Crystal Plasticity Simulations: An Integrated Computational Materials Engineering Approach,* JOM **69** (2017), 10.1007/s11837-017-2303-0.

[30] A. Vidyasagar, A. Tutcuoglu, and D. Kochmann, *Deformation patterning in finite-strain crystal plasticity by spectral homogenization with application to magnesium,* Computer Methods in Applied Mechanics and Engineering **335**, 584 (2018).

[31] H. Zhang, J. Liu, D. Sui, Z. Cui, and M. W. Fu, *Study of microstructural grain and geometric size effects on plastic heterogeneities at grain-level by using crystal plasticity modeling with high-fidelity representative microstructures,* International Journal of Plasticity **100** (2018), 10.1016/j.ijplas.2017.09.011.

[32] L. Chen, T. E. James Edwards, F. Di Gioacchino, W. J. Clegg, F. P. E. Dunne, and M. S. Pham, *Crystal plasticity analysis of deformation anisotropy of lamellar TiAl alloy: 3D microstructure-based modelling and in-situ microcompression,* International Journal of Plasticity **119** (2019), 10.1016/j.ijplas.2019.04.012.

[33] M. Diehl, J. Niehuesbernd, and E. Bruder, *Quantifying the contribution of crystallographic texture and grain morphology on the elastic and plastic anisotropy of bcc steel,* Metals **9** (2019), 10.3390/met9121252.

[34] D. S. Connolly, C. P. Kohar, W. Muhammad, L. G. Hector, R. K. Mishra, and K. Inal, *A coupled thermomechanical crystal plasticity model applied to Quenched and Partitioned steel,* International Journal of Plasticity **133**, 102757 (2020).

[35] Y. Liang, Q. He, S. Jiang, and C. Zhao, *Investigation on Texture Evolution Mechanism of NiTiFe Shape Memory Alloy Under Plane Strain Compression,* Metals and Materials International (2020), 10.1007/s12540-020-00741-6.

[36] M. Jalili and B. Soltani, *Investigation the micromechanisms of strain localization formation in AZ31 Mg alloy: A mesoscale 3D full-field crystal plasticity computational homogenization study,* European Journal of Mechanics, A/Solids **80**, 103903 (2020).

[37] C. Gierden, J. Kochmann, J. Waimann, T. Kinner-Becker, J. Sölter, B. Svendsen, and S. Reese, *Efficient two-scale FE-FFT-based mechanical process simulation of elasto-viscoplastic polycrystals at finite strains,* Computer Methods in Applied Mechanics and Engineering **374**, 113566 (2021).

[38] T. F. van Nuland, J. A. van Dommelen, and M. G. Geers, *Microstructural modeling of anisotropic plasticity in large scale additively manufactured 316L stainless steel,* Mechanics of Materials **153** (2021), 10.1016/j.mechmat.2020.103664.

[39] J. L. Dequiedt and C. Denoual, *Localization of plastic deformation in stretching sheets with a crystal plasticity approach: Competition between weakest link and instable mode controlled process,* International Journal of Solids and Structures **210-211** (2021), 10.1016/j.ijsolstr.2020.11.021.

[40] O. Diard, S. Leclercq, G. Rousselier, and G. Cailletaud, *Evaluation of finite element based analysis of 3D multicrystalline aggregates plasticity Application to crystal plasticity model identification and the study of stress and strain fields near grain boundaries,* International Journal of Plasticity **21**, 691 (2005).

[41] Z. Zhao, S. Kuchnicki, R. Radovitzky, and A. Cuitiño, *Influence of in-grain mesh resolution on the prediction of deformation textures in fcc polycrystals by crystal plasticity FEM,* Acta Materialia **55**, 2361 (2007).

[42] H. Ritz and P. Dawson, *Sensitivity to grain discretization of the simulated crystal stress distributions in FCC polycrystals,* Modelling and Simulation in Materials Science and Engineering **17** (2009), 10.1088/0965-0393/17/1/015001.

[43] H. Lim, C. C. Battaile, J. E. Bishop, and J. W. Foulk, *Investigating mesh sensitivity and polycrystalline RVEs in crystal plasticity finite element simulations,* International Journal of Plasticity **121**, 101 (2019).

[44] S. Kweon and D. S. Raja, *Comparison of anisotropy evolution in BCC and FCC metals using crystal plasticity and texture analysis,* European Journal of Mechanics, A/Solids **62**, 22 (2017).

[45] D. Savage, I. Beyerlein, N. Mara, S. Vogel, R. McCabe, and M. Knezevic, *Microstructure and texture evolution in Mg/Nb layered materials made by accumulative roll bonding,* International Journal of Plasticity **125**, 1 (2020).

[46] D. A. Hughes and N. Hansen, *Microstructure and strength of nickel at large strains,* Acta Materialia **48**, 2985 (2000).

[47] H. Resk, L. Delannay, M. Bernacki, T. Coupez, and R. Logé, *Adaptive mesh refinement and automatic remeshing in crystal plasticity finite element simulations,* Modelling and Simulation in Materials Science and Engineering **17** (2009), 10.1088/0965-0393/17/7/075012.

[48] R. Quey, P. R. Dawson, and F. Barbe, *Large-scale 3D random polycrystals for the finite element method: Generation, meshing and remeshing,* Computer Methods in Applied Mechanics and Engineering **200**, 1729 (2011).

[49] A. Prakash, W. G. Nöhring, R. A. Lebensohn, H. W. Höppel, and E. Bitzek, *A multiscale simulation framework of the accumulative roll bonding process accounting for texture evolution,* Materials Science and Engineering A **631**, 104 (2015).

[50] D. K. Kim, J. M. Kim, W. W. Park, H. Lee, Y. T. Im, and Y. S. Lee, *Three-dimensional crystal plasticity finite element analysis of microstructure and texture evolution during channel die compression of if steel,* Computational Materials Science **100**, 52 (2015).

[51] H. Proudhon, J. Li, F. Wang, A. Roos, V. Chiaruttini, and S. Forest, *3D simulation of short fatigue crack propagation by finite element crystal plasticity and remeshing,* in *International Journal of Fatigue*, Vol. 82 (Elsevier Ltd, 2016) pp. 238–246.

[52] K. Frydrych, K. Kowalczyk-Gajewska, and A. Prakash, *On solution mapping and remeshing in crystal plasticity finite element simulations: application to equal channel angular pressing,* Modelling and Simulation in Materials Science and Engineering **27** (2019), 10.1088/1361-651X/ab28e3.

[53] K. Shoemake, *Animating rotation with quaternion curves,* Computer Graphics (ACM) **19** (1985), 10.1145/325165.325242.

[54] F. Roters, M. Diehl, P. Shanthraj, P. Eisenlohr, C. Reuber, S. Wong, T. Maiti, A. Ebrahimi, T. Hochrainer, H. Fabritius, S. Nikolov, M. Friák, N. Fujita, N. Grilli, K. Janssens, N. Jia, P. Kok, D. Ma, F. Meier, E. Werner, M. Stricker, D. Weygand, and D. Raabe, *DAMASK – The Düsseldorf Advanced Material Simulation Kit for modeling multi-physics crystal plasticity, thermal, and damage phenomena from the single crystal up to the component scale,* Computational Materials Science **158**, 420 (2019).

[55] K. Sedighiani, M. Diehl, K. Traka, F. Roters, J. Sietsma, and D. Raabe, *An efficient and robust approach to determine material parameters of crystal plasticity constitutive laws from macro-scale stress–strain curves,* International Journal of Plasticity **134**, 102779 (2020).

[56] K. Sedighiani, K. Traka, F. Roters, D. Raabe, J. Sietsma, and M. Diehl, *Determination and analysis of the constitutive parameters of temperature-dependent dislocation-density-based crystal plasticity models,* Mechanics of Materials (2021), 10.1016/j.mechmat.2021.104117.

[57] F. Massey, *The Kolmogorov-Smirnov Test for Goodness of Fit,* Journal of the American Statistical Association **46** (1951), 10.1080/01621459.1951.10500769.

[58] S. Maneewongvatana and D. Mount, *On the efficiency of nearest neighbor searching with data clustered in lower dimensions,* in *Lecture Notes in Computer Science (including subseries Lecture Notes in Artificial Intelligence and Lecture Notes in Bioinformatics)*, Vol. 2073 (2001).

[59] J. Segurado, R. A. Lebensohn, J. Llorca, and C. N. Tomé, *Multiscale modeling of plasticity based on embedding the viscoplastic self-consistent formulation in implicit finite elements,* International Journal of Plasticity **28** (2012), 10.1016/j.ijplas.2011.07.002.

[60] X. Ren, Y. Huang, X. Zhang, H. Li, and Y. Zhao, *Influence of shear deformation during asymmetric rolling on the microstructure, texture, and mechanical properties of the AZ31B magnesium alloy sheet,* Materials Science and Engineering A **800** (2021), 10.1016/j.msea.2020.140306.

[61] F. Pérocheau and J. H. Driver, *Texture gradient simulations for extrusion and reversible rolling of FCC metals,* International journal of plasticity **16** (2000), 10.1016/S0749-6419(99)00048-0.

[62] B. Hutchinson, *Deformation microstructures and textures in steels,* Philosophical Transactions of the Royal Society A: Mathematical, Physical and Engineering Sciences **357**, 1471 (1999).

[63] L. A. I. Kestens and H. Pirgazi, *Texture formation in metal alloys with cubic crystal structures,* Materials Science and Technology **32**, 1303 (2016).

6

IN-GRAIN TEXTURE EVOLUTION

Abstract

High-resolution three-dimensional crystal plasticity simulations are used to investigate deformation heterogeneity and microstructure evolution during cold rolling of interstitial free (IF-) steel. A Fast Fourier Transform (FFT)-based spectral solver is used to conduct crystal plasticity simulations using a dislocation-density-based crystal plasticity model. The in-grain texture evolution and misorientation spread are consistent with experimental results obtained using electron backscatter diffraction (EBSD) experiments. Crystal plasticity simulation shows that two types of strain localization develop during the large deformation of IF-steel. The first type forms band-like areas with large strain accumulation that sheared severely and appear as river patterns extending across the specimen. In addition to these river-like patterns, a second type of strain localization with rather sharp and highly localized in-grain deformation bands is identified. These localized features are dependent on the crystallographic orientation of the grain and extend within a single grain. In addition to the strain localization, the evolution of in-grain orientation gradients, dislocation density, kernel average misorientation, and stress in major texture components are discussed.

Parts of this chapter have been published in Sedighiani *et al.* [1].

6.1. Introduction

Plastic deformation of polycrystalline metallic materials is significantly heterogeneous in terms of strain, stress, and crystal reorientation. Characterization and understanding of these deformation heterogeneities and microstructural evolution during plastic deformation play a critical role in identifying the underlying mechanisms behind many physical phenomena. For instance, a thorough physical understanding of the mechanisms behind the phase-transformation or recrystallization behavior is not feasible without properly characterizing microstructural evolution during plastic deformation [2–7]. Underlying mechanisms behind damage formation, fracture, and failure in metals have also often been related to deformation localization and microstructures formed during the deformation [8–11]. Besides, the material properties of crystalline materials depend on the microstructures developing during the deformation including crystallographic texture [12, 13]. As a result, over the past years, a considerable amount of attention has been devoted to understand and characterize the intragranular deformation heterogeneity and microstructural evolution during plastic deformation [14–21].

Deformation microstructures are mainly quantified using experimental techniques such as electron backscatter diffraction (EBSD) [22–25] and transmission electron microscopy (TEM) [26, 27]. Choi and Jin [22], Choi and Cho [23] used EBSD analysis to examine the orientation dependency of the stored energy of deformed grains in cold-rolled low carbon steels. Allain-Bonasso *et al.* [24] studied the effect of orientation distributions and grain size on the development of deformation heterogeneities during tensile deformation of interstitial free (IF) steel by EBSD. Wang *et al.* [25] investigated shear band formation in cold-rolled Ta-2.5W alloy at various thickness reduction levels using EBSD analysis. Li *et al.* [26] investigated the microstructural evolution during cold rolling of IF-steel at different thickness reductions using scanning and transmission electron microscope techniques.

Despite the extensive knowledge that can be gained from experimental studies, experimental techniques suffer from several drawbacks. As the first drawback, the microtexture can be characterized solely based on the specimen surface, and determining the variation of microstructure through the thickness is only possible using destructive approaches. As a result, the actual neighboring and boundary conditions of the material points cannot be precisely determined. Another drawback of experimental techniques is the difficulties in tracking the material points, especially during large deformation. Uncertainty due to random errors (e.g. errors due to ill-defined boundary conditions), sensitivity to sample contamination, and economically expensive and time-consuming processes are a few more drawbacks of experimental procedures.

Crystal plasticity simulations [28] are an established and powerful alternative to model and quantify deformation processes at the microstructural level and the associated complex mechanical fields [29–36]. These models are developed based on physical mechanisms such as glide of dislocations on preferred slip systems and the interaction of dislocations with various defects. Crystal plasticity simulations have been compared with experimental data in several works. For instance, Raabe *et al.* [37] compared the spatial distribution of the plastic strain from channel-die experiments with crystal plasticity simulations for a sample of pure aluminum with 18 grains after an

8% sample thickness reduction. However, comparisons between simulations and experiments are mostly limited to small/moderate strains (strains less than 0.4) [37, 38] or simple microstructures (e.g. bicrystals) [39–42].

Conducting large-deformation crystal plasticity with high resolution is extremely challenging. Problems involving the deformation of solid materials are usually formulated in a Lagrangian context, in which the mesh is attached to the deformable body and deforms with a change in the material's shape. As a result, the mesh gets distorted due to the heterogeneity of the deformation [43, 44]. When the mesh distortion becomes too large, the simulation fails to converge. At the same time, modeling of in-grain localized deformation features requires a high-resolution crystal plasticity simulation, even up to hundreds of thousands of elements per crystal [43, 45]. A higher simulation resolution allows capturing more detailed localized deformation features, which results in earlier convergence issues. In addition, typical meshing approaches are computationally extremely expensive to be used for high-resolution crystal plasticity problems subjected to large deformation, see Chapter 5.

This chapter presents a combined computational/experimental study to investigate the evolution of in-grain deformation heterogeneity during cold rolling of IF-steel over a wide range of strains up to 77% thickness reduction. The large-deformation crystal plasticity simulations are conducted using the mesh replacement remeshing technique proposed in Chapter 5. This approach enables conducting high-resolution large-deformation crystal plasticity simulations and overcoming the associated mesh distortion problem due to the strain localization. The in-grain orientation spreads obtained using simulation are compared with two EBSD measurements performed on a cold-rolled IF steel sample after 77% thickness reduction. In addition, the orientation dependency of deformation heterogeneity, strain localization, and dislocation evolution are numerically investigated over a wide range of strains.

6.2. Experimental method

The material used in the present study is an IF-steel with chemical composition as given in Table 6.1. The initial microstructure and crystallographic texture of the material before cold rolling were measured on the RD-ND (rolling direction-normal direction) plane perpendicular to the transverse direction (TD) using electron backscatter diffraction (EBSD). The grain structure is almost completely equiaxed, and the material exhibits a mild texture, see Fig. 4.1.

Table 6.1: The chemical composition of the IF-steel considered in this study.

element	C	Mn	S	Ti	N	Al	Cr	Fe
wt. (%)	0.002	0.095	0.006	0.045	0.002	0.05	0.02	balance

We performed two EBSD measurements on two nearby areas of the cold-rolled IF-steel sample subjected to 77% thickness reduction ($\varepsilon = 1.47$). The two scanning areas are located at the mid-thickness of the rolling plane (ND-RD plane). Therefore, these areas experience a near plane-strain compression deformation mode, i.e. shear deformation modes are negligible. The first EBSD map of a scan area of 600 μm × 600 μm was measured with a step size of 0.3 μm. The second EBSD map of a

scan area of 594 μm × 438 μm was measured with a step size of 0.6 μm. Standard metallographic techniques were used to prepare the specimens for characterization. Analysis of the EBSD data was performed using the TSL OIM software. A more detailed description of the EBSD data analysis is presented in [46].

6.3. Crystal plasticity simulations

This study investigates the microstructure and texture evolution using two crystal plasticity simulations. The first example concerns the macroscopic texture evolution in a low-resolution RVE with 40000 grains (Section 6.4.1), while the second example investigates in-grain microstructure evolution using a high-resolution RVE with only 36 grains (Section 6.4.2). For both cases, the crystallographic orientations of the grains were sampled from the EBSD map of the undeformed hot-rolled sample (see Fig. 4.1). These RVEs are subjected to a plane-strain compression with a strain rate of 100 s^{-1}.

We use a Fast Fourier Transform (FFT) based spectral method [47, 48] implemented in DAMASK [49] to conduct the crystal plasticity simulations using the dislocation-density-based constitutive law [50, 51] outlined in Section 2.4. The material parameters used in this study are based on the parameters identified in Chapter 4 for IF-steel using the approach presented in Chapter 3. However, the hardening-related parameters are adjusted for large deformation use, see Table 6.2.

Table 6.2: Model parameters of IF-steel used for crystal plasticity simulations.

variable	description	units	value
ρ_0^α	initial mobile dislocation density	m/m^3	1.0×10^{12}
ρ_{d0}^α	initial dipole dislocation density	m/m^3	1.5×10^{12}
v_0	dislocation glide velocity pre-factor	m/s	1.4×10^3
ΔF	activation energy for dislocation glide	J	1.57×10^{-19}
p	p-exponent in glide velocity	–	0.325
q	q-exponent in glide velocity	–	1.55
τ_0^*	short-range barriers strength at 0 K	MPa	454
C_λ	parameter controlling dislocation mean free path	–	50
C_{anni}	coefficient for dislocation annihilation	–	2

6.3.1. Remeshing procedure

We use the remeshing technique (i.e. the mesh replacement method) presented in Chapter 5 to overcome the mesh distortion problem in high-resolution crystal plasticity simulations. This remeshing method is based on replacing the distorted mesh with a new undistorted mesh. The variables from the deformed stage are mapped onto the newly created mesh using a nearest-neighbor mapping algorithm. Finally, the

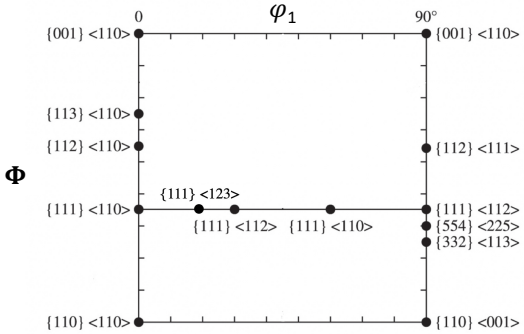

Fig. 6.1: $\varphi_2 = 45°$ section of the ODF showing the main rolling texture components in bcc metals.

simulation is restarted as a new simulation in which the initial state is set based on the last deformation state that had been reached.

During large deformation, the elements' aspect ratio, i.e. the ratio of the element size in the stretching direction to the element size in the compression direction, can become very large. Extensively elongated elements introduce errors in the simulation and, more importantly, can prevent strain localization. A multi-step mesh refinement method is used for updating the mesh density during the deformation at each remeshing step (see Chapter 5). The idea behind this approach is to keep the number of elements in the compression direction constant and adjust the number of elements in the stretching direction accordingly to keep the elements close to cube-shaped. The multi-step mesh refinement approach leads to a gradual rise in the number of elements and the simulation resolution during the deformation. Keeping the number of elements in the most compressed direction constant ensures a minimum information loss during mapping with a minimal increase in the simulation points [43].

6.4. Results and discussion

6.4.1. Macroscopic texture evolution

In bcc metals, the slip occurs in the well-established slip direction of $\langle 1\,1\,1\rangle$. However, the slip plane can be $\{1\,1\,0\}$, $\{1\,1\,2\}$, and at higher temperatures also $\{1\,2\,3\}$. The lattice rotates due to the shear strain and reaches a preferred orientation based on the loading conditions and the initial orientation of the lattice. There are numerous works devoted to studying the evolution of texture in bcc metals and especially steel [26, 44, 52–58]. In general, the rolling texture developed in bcc metals is not very sensitive to the type of material. However, the degree of deformation noticeably influences the deformation texture. The rolling texture in bcc metals belongs mainly to two families of α (RD$\|\langle 1\,1\,0\rangle$) and γ (ND$\|\langle 1\,1\,1\rangle$) fibers. Fig. 6.1 shows the $\varphi_2 = 45°$ section of the orientation distribution function (ODF). This section includes the most important components of the rolling texture in bcc metals.

6.4.1.1. Comparing simulation and experiments

We here compare the crystallographic texture obtained using the crystal plasticity simulation with the experimental data presented in [54, 59]. The RVE used for the simulation consists of 40000 grains, and the crystallographic orientations of the grains are assigned according to the EBSD map of the undeformed hot-rolled sample. A mesh with $20 \times 20 \times 100$ elements is used, i.e. each grain is represented by a single element. The RVE is subjected to a plane-strain compression up to 99% thickness reduction ($\varepsilon = 4.61$).

Fig. 6.2 shows the $\varphi_2 = 45°$ section of the ODF obtained using crystal plasticity simulation at different reductions, namely 0%, 50%, 75%, 85%, 95%, and 99%. The results show that after 75% thickness reduction, the two fibers α and γ are developed almost equally. At higher thickness reductions, the main features of the texture remain similar. However, the α-fiber becomes stronger and more prominent at the expense of weakening the γ-fiber. This is in agreement with experimentally observed behavior reported for low carbon steels, see Fig. 6.3 on low carbon steels [54].

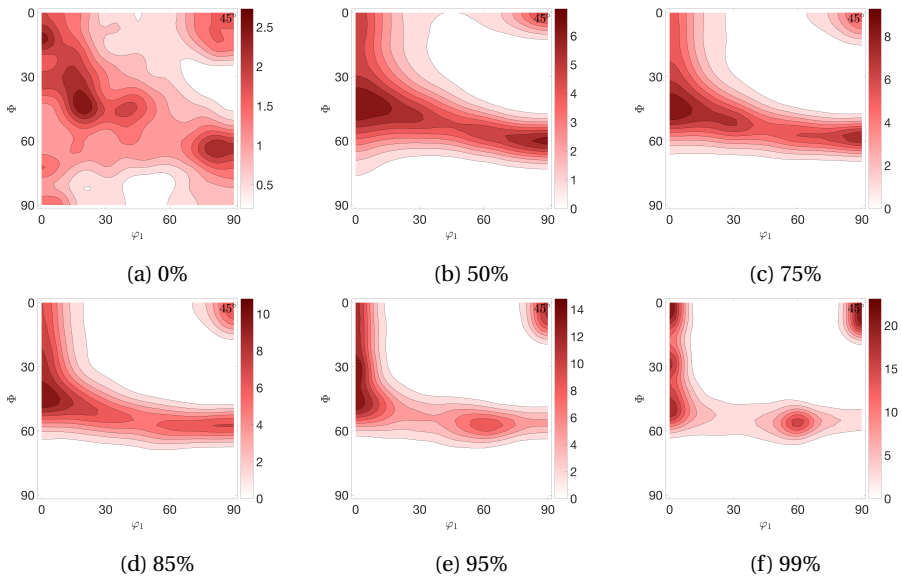

Fig. 6.2: Orientation density f(g) maps ($\varphi_2 = 45°$) at different thickness reductions obtained for IF-steel using crystal plasticity simulation.

The volume fractions of the main texture components obtained at different thickness reduction levels using the crystal plasticity simulation are shown in Fig. 6.4a. The volume fraction is calculated based on the number of material points with disorientation less than 10 degrees from the exact orientation of the texture component. It can be seen that the components belonging to the α-fiber strengthen continuously with increasing deformation. Although the γ-fiber components are initially strengthened with increasing applied strain, these texture components weaken at larger thickness reductions, i.e. after about 70–80% thickness reduction.

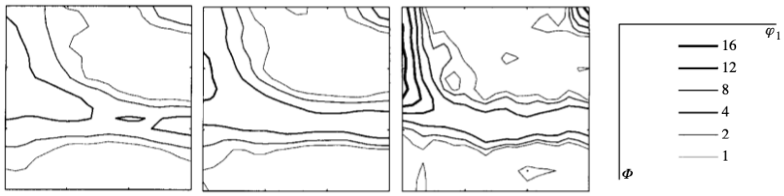

(a) 50% (b) 74% (c) 95%

Fig. 6.3: Orientation density f(g) maps ($\varphi_2 = 45°$) at different thickness reductions obtained for cold rolled low-carbon steel [54].

The volume fractions obtained from the experimental data for the same texture components are presented in Fig. 6.4b. The volume fractions and the evolution trends from the simulation are in excellent agreement with these experimental data. The only notable difference between the simulation and the experimental results is for texture components $\{114\}\langle011\rangle$ and $\{112\}\langle011\rangle$. Although both approaches show a steady increase in the volume fractions, the simulations slightly underestimate the intensity of these two components.

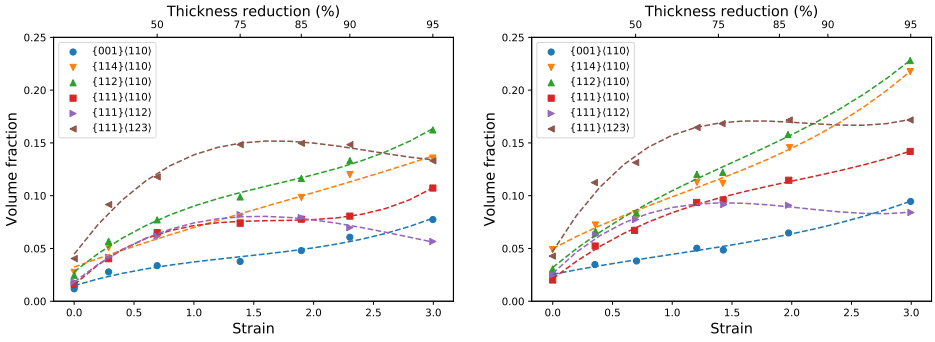

(a) (b)

Fig. 6.4: Volume fraction of the main texture components (a) obtained using the dislocation-density-based crystal plasticity model, (b) based on data from [54].

6.4.2. Microstructural evolution

The evolution of in-grain microstructure and microtexture in bcc metals has been the topic of interest for many experimental works [24, 26, 53, 60]. In the next step, we use a combined simulation and experimental study to investigate the deformation heterogeneity developed within grains at large strains. For this purpose, we conduct a large-deformation crystal plasticity simulation with high resolution using the approach presented in Chapter 5, and compare the results with two EBSD measurements performed on cold-rolled IF-steel (see Section 6.2).

The simulation is carried out using a 3D polycrystal RVE of 36 grains. The crystallographic orientations of the grains are assigned according to the EBSD map of the hot-rolled sample (see Fig. 4.1). The RVE is subjected to plane-strain compression up to a thickness reduction of 77%. The initial number of elements at the beginning of the deformation is $80 \times 48 \times 320$. The number of elements is gradually increased to $1280 \times 48 \times 320$ during the deformation using the multi-step mesh refinement method as described in Section 6.3.1.

Figure 6.5a shows the inverse pole figure (IPF) color maps parallel to the loading (vertical) directions in the mid-surface of the 3D simulation for different thickness reductions. The 3D IPF color maps for the same RVE after 77% thickness reduction is shown in Figure 6.5b. The $\varphi_2 = 45°$ section of the orientation distribution function for the 3D simulation is shown in Figure 6.5c. Plastic deformation leads to changes in the grains' orientation and the development of deformation textures. The simulation results show that a strong α-fiber and a slightly weaker γ-fiber are developed after a 77% thickness reduction. Figure 6.8a and Figure 6.9a show the IPF color map parallel to the loading (vertical) direction for the two EBSD measurements on two nearby areas of the industrially cold-rolled IF-steel sample subjected to 77% thickness reduction (see Section 6.2). The corresponding $\varphi_2 = 45°$ section of the orientation distribution function for these two EBSD maps are shown in Figure 6.8d and Figure 6.9d, respectively.

The orientation density maps at constant angles φ_2 for the simulation and the two EBSD maps are shown in Fig. 6.6. Despite some differences in the predicted texture, there is a good agreement between the three sets of results. The simulation results show that a strong α-fiber and a slightly weaker γ-fiber are developed after a 77% thickness reduction. The first EBSD measurement shows almost the same strength for the two fibers, while the second EBSD data shows a strong α-fiber and a much weaker γ-fiber. The main reason for the different observations is that neither of the data sets is statistically fully representative of the material microstructure. It is challenging to conduct simulations and experiments at such resolutions that full statistical representation of the material microstructure is obtained. Therefore, statistical differences are expected between the three sets of results, i.e. the two EBSD measurements and the simulation result. Low-resolution crystal plasticity simulations like the one presented in the previous section can be utilized to predict macroscopic texture evolution.

6.4.2.1. Misorientation spread

This section investigates the deformation heterogeneity in terms of misorientation spread developed within the RVE after 77% thickness reduction. For this purpose, the data is divided into low KAM (kernel average misorientation) regions, i.e. points whose KAM value belongs to the lower 20% of the data distribution, and high KAM regions, points whose KAM value belongs to the higher half of the data distribution. For calculating the KAM of a point, first the disorientations, i.e. the misorientations considering the cubic symmetry of the material, between the point and all neighboring points are calculated. Then, the average value is calculated. Fig. 6.7a shows the IPF color map parallel to the loading (vertical) direction for the mid-surface of the simulation. The low KAM and high KAM regions are shown respectively in Figs. 6.7b and 6.7c, and the corresponding orientation density maps are shown respectively in Figs. 6.7e and 6.7f.

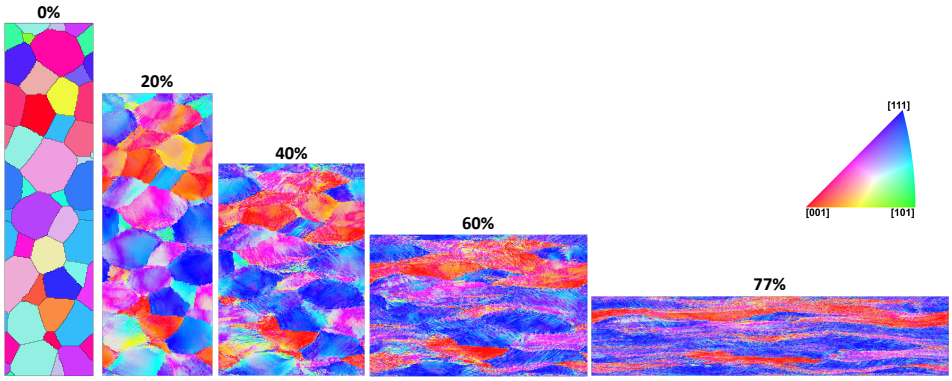

(a)

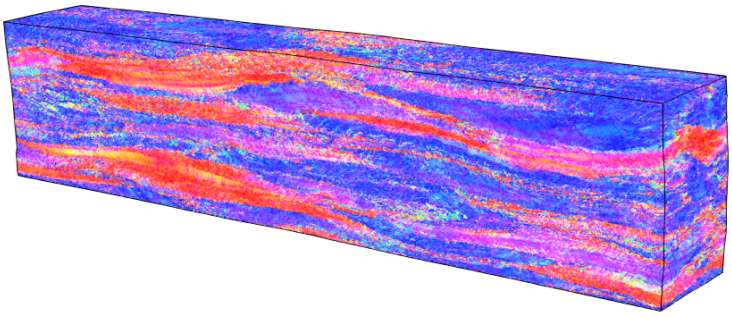

(b)

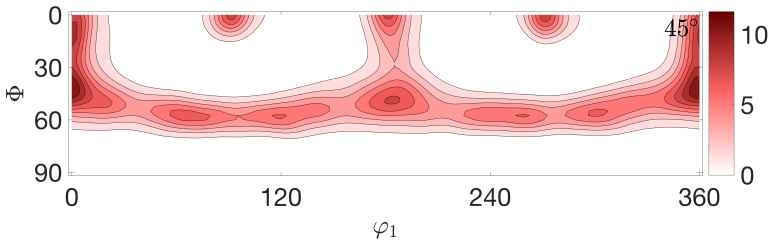

(c)

Fig. 6.5: (a) IPF color maps parallel to the loading (vertical) direction in the mid-surface of the 3D simulation at different thickness reductions. (b) The 3D IPF color maps and (c) Orientation density f(g) maps ($\varphi_2 = 45°$) for the same RVE after 77% thickness reduction.

The tendency to form in-grain misorientation spread is smaller in crystals belonging to the α-fiber. Specifically, grains close to the rotated cube orientation, $\{0\,0\,1\}\langle 1\,1\,0\rangle$, show minimal deformation heterogeneity, i.e. a very small misorientation spread. This is in accordance with the experimental observations (e.g. [54, 55]) that, for this texture component, the orientation does not change noticeably during the rolling deformation, and a uniform microstructure without significant orientation gradients is

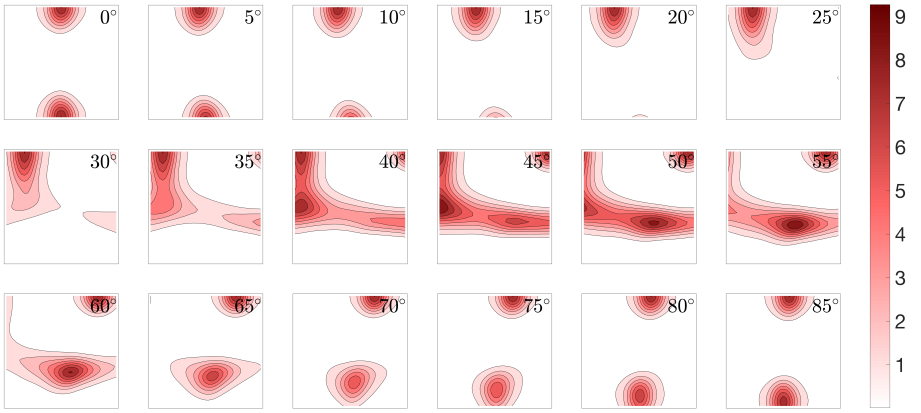

(a) crystal plasticity simulation

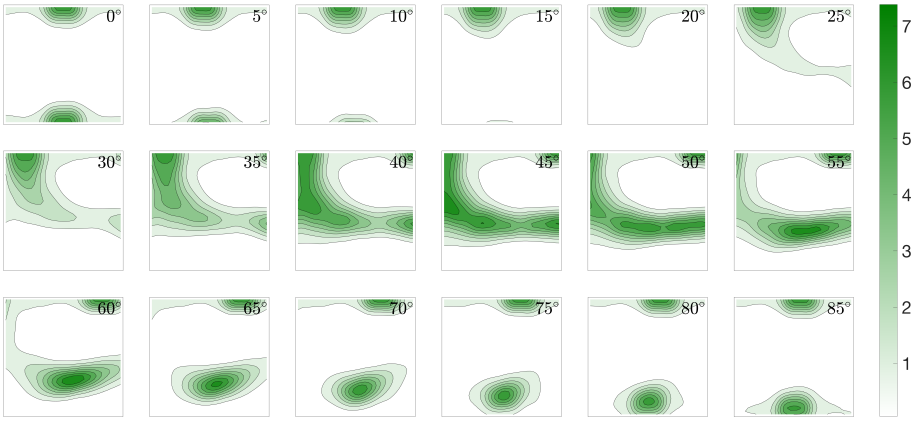

(b) EBSD measurement 1

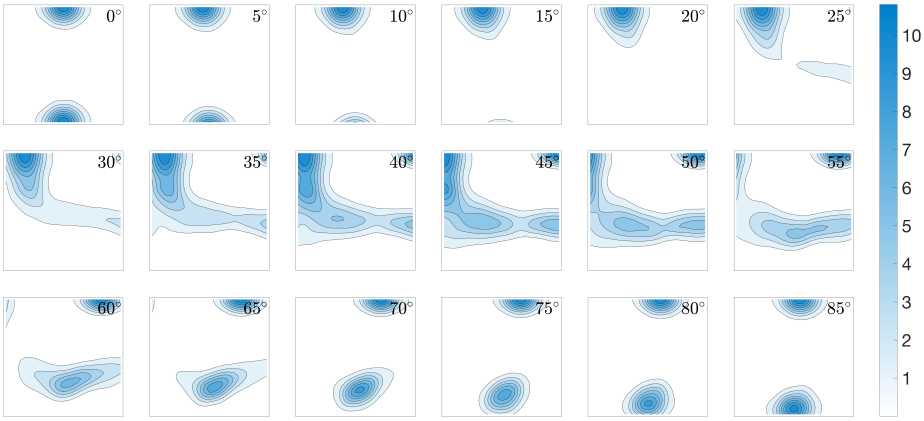

(c) EBSD measurement 2

Fig. 6.6: Orientation density f(g) maps obtained from the ODF sections at constant angles of φ_2 after 77% thickness reduction.

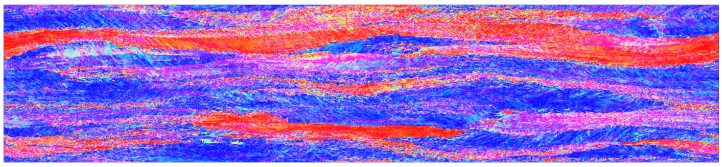

(a) full section

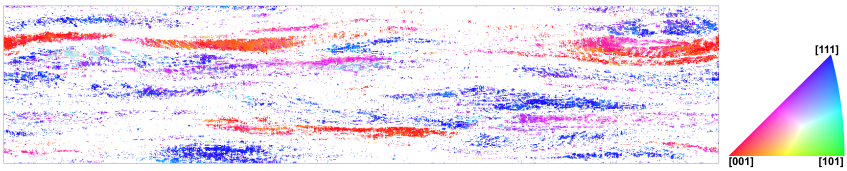

(b) low KAM region

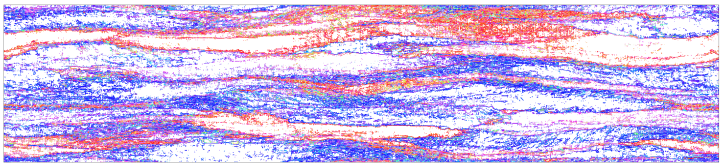

(c) high KAM region

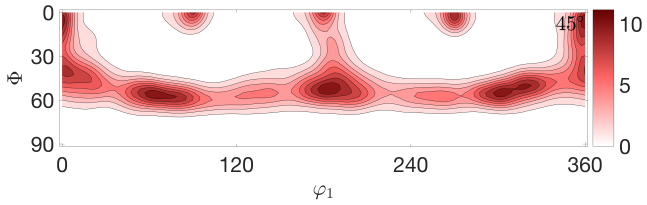

(d) full section

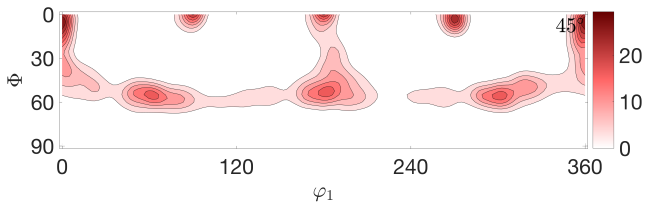

(e) low KAM region

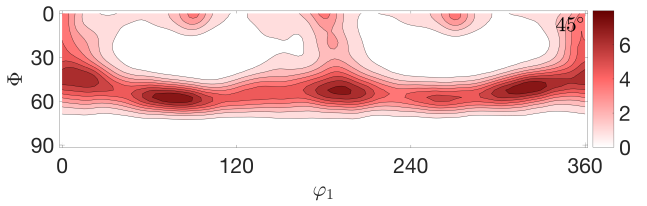

(f) high KAM region

Fig. 6.7: Simulation results showing the low and high KAM regions in the mid-surface of the 3D simulation. (a–c) IPF color maps parallel to the loading (vertical) direction, (d–f) orientation density f(g) maps obtained from the ODF section $\varphi_2 = 45°$.

formed during deformation, i.e. the in-grain orientation remains below 15° misorientation. The inverse Brass orientation, {1 1 2}⟨1 1 0⟩, shows similar behavior, and grains close to this crystallographic orientation show generally small misorientation spread. However, the in-grain misorientation spread is slightly larger compared to that of the rotated cube component. In general, the deformation heterogeneity increases for orientations further along the α-fiber, such as {1 1 2}⟨1 1 0⟩ and {1 1 1}⟨1 1 0⟩. The crystal plasticity simulation shows a stronger tendency to form in-grain misorientation spread in the γ-fiber compared to the α-fiber. The results from the two EBSD measurements confirm similar behavior, as shown in Figs. 6.8 and 6.9. Regions with small deformation heterogeneity and misorientation spread belong mainly to the α-fiber, while the components belonging to the γ-fiber show the strongest misorientation spread. These observations show significant similarities with experimentally reported results in the literature for bcc metals and IF-steel, e.g. [52, 54, 55, 57].

6.4.3. In-grain orientation gradients

In this section, we investigate the deformation heterogeneity in terms of in-grain orientation gradients (orientation variations within a grain). We quantify the in-grain deformation heterogeneity using grain orientation spread (GOS) and grain average misorientation (GAM). The GOS is the average of disorientation angles of all points within a grain to the grain mean orientation:

$$\mathrm{GOS_i} = \frac{1}{N_i}\sum_{j=1}^{N_i} \omega_{ij}, \tag{6.1}$$

where N_i stands for the number of points belonging to grain i, and ω_{ij} is the disorientation angle between point j and grain i's mean orientation considering the cubic symmetry of the material. The GAM is the average of KAM for all points within a grain:

$$\mathrm{GAM_i} = \frac{1}{N_i}\sum_{j=1}^{N_i} \mathrm{KAM}_j, \tag{6.2}$$

GAM can be seen as a local measure for the orientation variation inside the grains. Larger GOS and GAM reflect a higher degree of plastic deformation heterogeneity.

Fig. 6.10 shows the inverse pole figure distribution maps with respect to the loading direction (z) and stretching direction (x) for all grains. The grains are defined based on the initial microstructure before deformation (see Fig. 6.11b), and their GOS and GAM are shown in Fig. 6.11a. The large reorientation spread for the grains reveals that in addition to the initial orientation, other factors like spatial constraints of neighboring points also play a crucial role. This is because the resolved shear stresses on various slip planes are determined by the compression load combined with the spatial constraints applied by the neighboring material. In general, the GOS and the GAM values are noticeably smaller in grains belonging to the α-fiber (e.g. grains 18, 29, 31, and 32) than in grains belonging to the γ-fiber (e.g. grains 3, 4, 13, and 35). The smallest values of GOS and GAM belong to grains with orientations close to the rotated cube orientation.

Fig. 6.12 shows the correlation between the GOS and the GAM with volume fraction of various texture components. There is a strong negative correlation between the

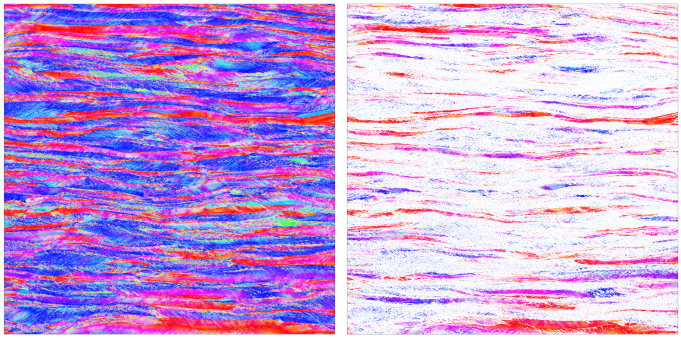

(a) full section (b) low KAM region

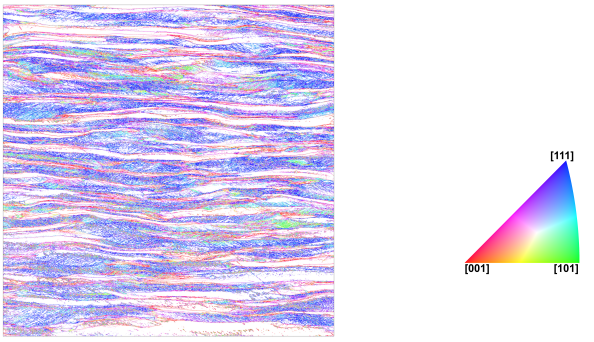

(c) high KAM region

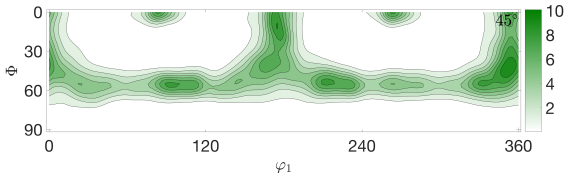

(d) full section

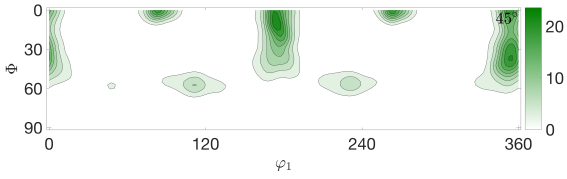

(e) low KAM region

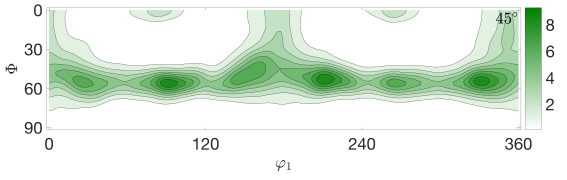

(f) high KAM region

Fig. 6.8: Results showing low and high KAM regions of EBSD measurement 1 for a 600 $\mu m \times 600\ \mu m$ scan area. (a–c) IPF color maps parallel to the loading (vertical) direction, (d–f) orientation density f(g) maps obtained from the ODF section $\varphi_2 = 45°$.

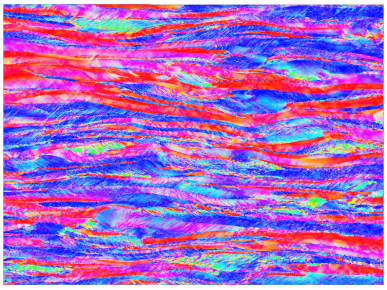

(a) full section

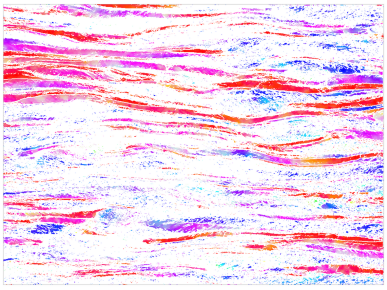

(b) low KAM region

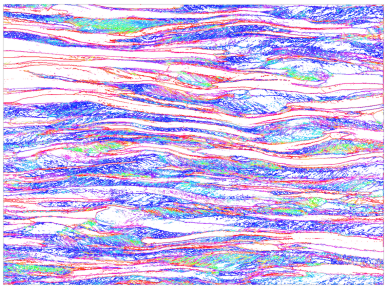

(c) high KAM region

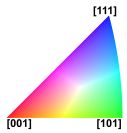

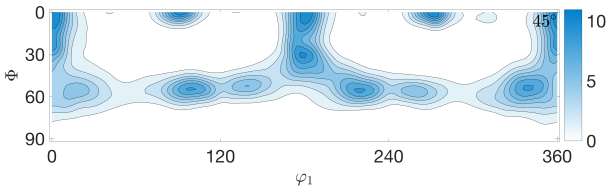

(d) full section

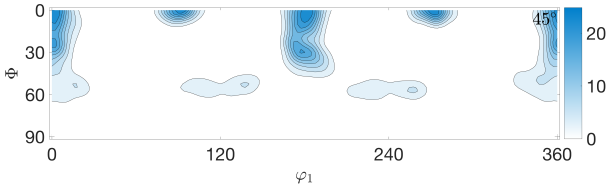

(e) low KAM region

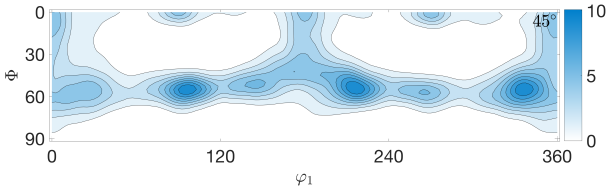

(f) high KAM region

Fig. 6.9: Results showing low and high KAM regions of EBSD measurement 2 for a 594 $\mu m \times 438\ \mu m$ scan area. (a–c) IPF color maps parallel to the loading (vertical) direction, (d–f) orientation density f(g) maps obtained from the ODF section $\varphi_2 = 45°$.

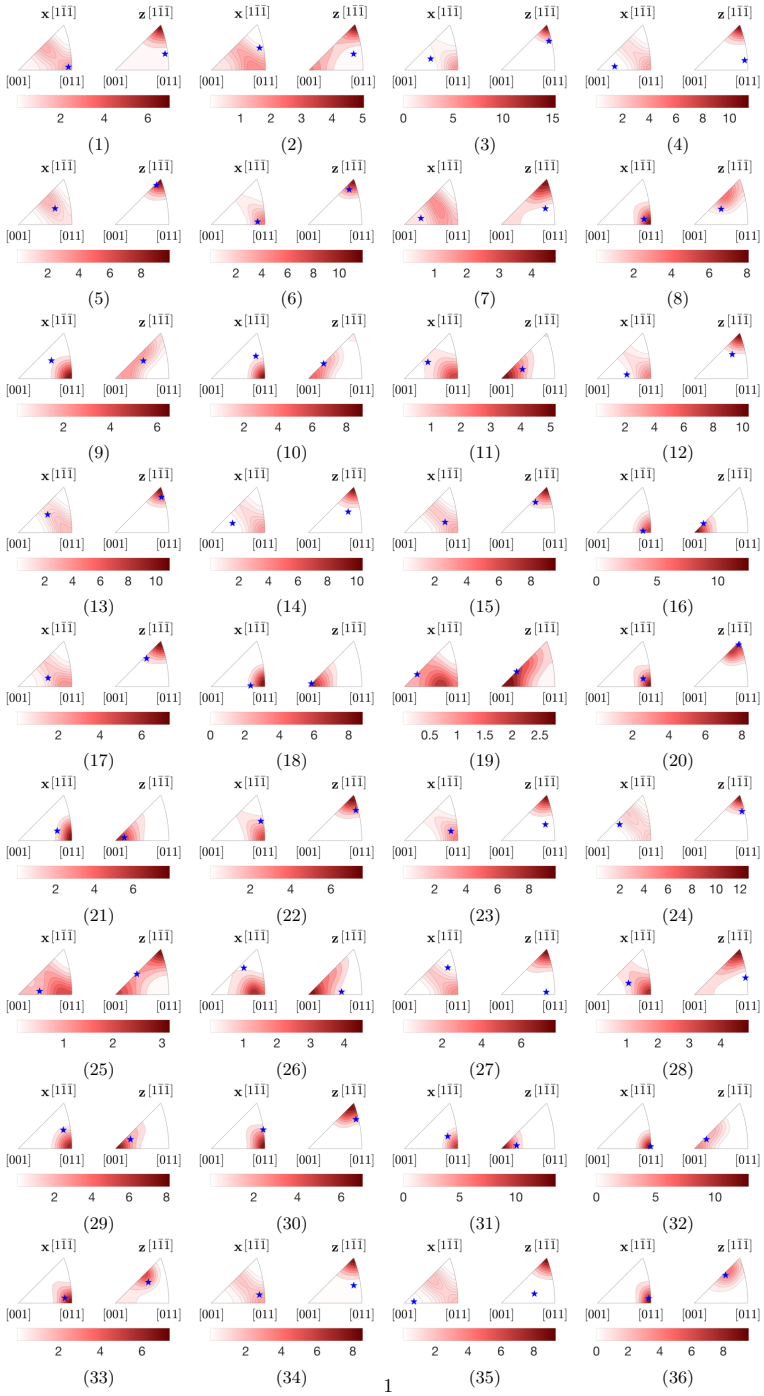

Fig. 6.10: Inverse pole figure distribution map with respect to the loading direction (z) and stretching direction (x) for all individual grains. The blue stars show the initial orientations.

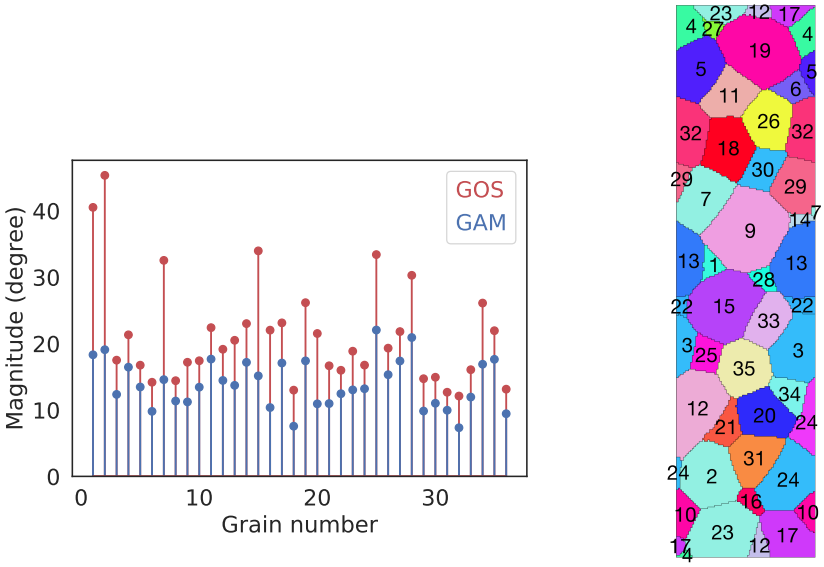

(a) (b)

Fig. 6.11: (a) GOS and GAM for all individual grains. (b) Grains are defined and numbered based on the initial microstructure before deformation.

volume fraction of the points belonging to the α-fiber with GOS and GAM, which means that a more uniform microstructure without significant orientation gradients is formed in grains with a larger volume fraction of α-fiber orientations. On the other hand, there is a weak positive correlation between the volume fraction of the γ-fiber with GOS and GAM, which implies noticeable variations in the orientation spread for grains with a similar fraction of orientations belonging to the γ-fiber. For example, the GOS & GAM values for grains 6 and 15 are respectively 14.2 & 9.8 and 34.0 & 15.1. This result indicates that local effects and the local stress field considerably affect the reorientation of crystal points rotating towards the γ-fiber. Therefore, altering the grain shape or orientation of a neighboring grain can suppress or promote grain fragmentation in these crystals more strongly than in the α-fiber grains. Between the γ-fiber components, we observed that the volume fraction of $\{554\}\langle225\rangle$ component has the strongest correlation with the GOS and GAM. On the other hand, the volume fraction of $\{111\}\langle110\rangle$ has the weakest correlation with the GOS and GAM. These outputs indicate that the in-grain orientation spread is orientation-dependent. The analysis presented here is based on how the initially uniform grains reorient during plastic deformation and form in-grain orientation gradients. It is one of the main advantages of simulations to allow simple tracking of the reorientation history for all points, while such an analysis for experimental methods is extremely complicated or sometimes impossible.

There is a significant difference between the GOS and the GAM for some grains, e.g. grain 2. A 2D section of grain 2 at the mid-surface is shown in Fig. 6.13. As can be seen, this grain has been fragmented into two regions of distinctly different orientations. As

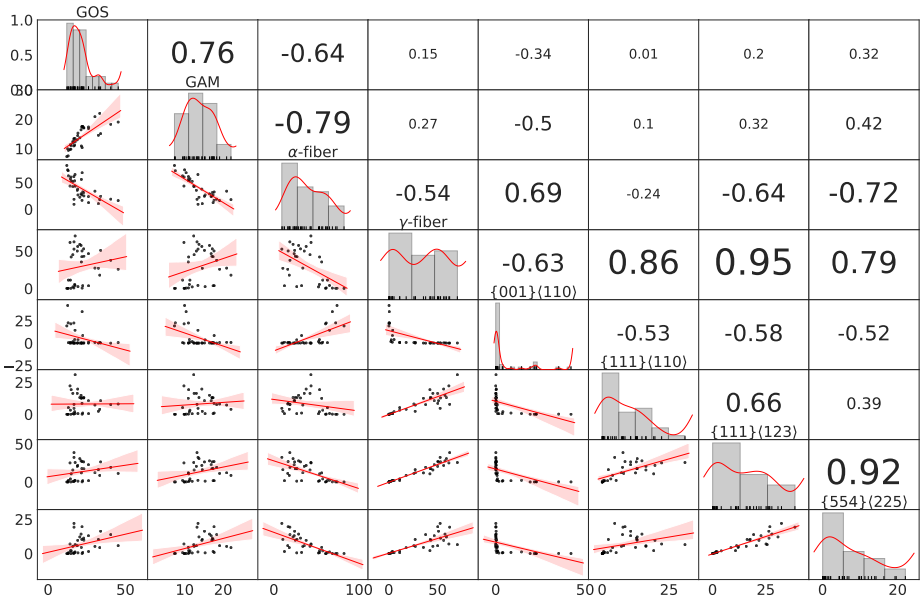

Fig. 6.12: Correlation between the GOS and GAM with volume fraction of various texture components.

a result, the misorientation angle to the grain mean orientation is noticeably large for most points within the grain. However, since the GAM measures local variation in the orientation, it captures the bifurcation. For such cases, looking at the GOS alone may be misleading.

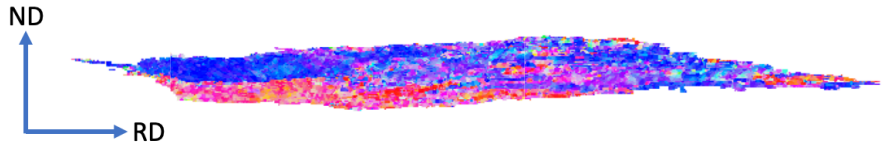

Fig. 6.13: A 2D section showing the IPF color maps parallel to the loading (ND) direction at the mid-surface of grain 2.

6.4.4. Shear localization

This section investigates the evolution of intergranular and intragranular shear localization during the deformation of the IF-steel over a wide strain range. Figure 6.14 shows the development of different variables (i.e. equivalent von Mises strain, equivalent von Mises stress, dislocation density, KAM, and Taylor factor) at the mid-surface of the RVE after a 20% thickness reduction ($\varepsilon = 0.22$). Non-crystallographic band-like deformation regions with large strain accumulation that appear as river-like

patterns are formed during the deformation, which pass through several grains and extend across the specimen (see Figure 6.14a). The local strain in these regions is, on average, around two times greater than the applied strain. These macroscopic bands are initially formed at an approximate angle of $\pm 40^\circ \sim 45^\circ$ with the rolling direction. The accumulation of the plastic strain in these macroscopic river-like patterns results in a significantly lower plastic strain in the neighboring regions.

One of the factors that promote such macroscopic strain localization is the contrast in the plastic behavior of neighboring grains (e.g. yield stress). Strain localization typically initiates near the grain boundaries of soft grains with lower strain hardening rates. The formation of an area plastically deformed decreases the effective load capacity of the sheared section and results in local mechanical instability. Consequently, the strain localization propagates through the specimen and creates the river-like patterns. The sharpness of the river-like patterns is higher when the contrast between the deformation behavior of the grains is greater (see region A1). However, a cluster of soft grains close to the areas of strain localization results in the broadening and homogenizing of the river-like patterns (see region A2). The high deformation concentration at these bands leads to a significantly lower strain in the surrounding regions. For example, for the grain shown in region A1, the strain in the rest of the soft grain is notably small.

In addition to the macroscopic river-like patterns which pass through several grains, a small number of rather sharp and highly localized in-grain deformation bands can also be observed. These bands extend inside a single grain, and it seems that they are originated at the grain boundaries (see region B1). They exist only in a very limited number of grains at this strain level and have developed mainly in hard grains interrupting the macroscopic river-like patterns. They are formed at an angle of approximately $\pm 30^\circ \sim 35^\circ$ with the rolling direction.

The stress values are generally higher in harder grains, i.e. orientations with larger Taylor factor. However, the macroscopic river-like patterns affect the stress distribution inside soft and hard grains considerably. The regions with high stress are mainly located inside hard grains next to the river-like patterns. The in-grain deformation also influences the stress distribution inside the grain. In general, the average stress inside grains with such features is notably larger than the total average stress.

With an increase of thickness reduction to 40% ($\varepsilon = 0.51$), the river-like patterns rotate down to inclination angles of $\pm 30^\circ \sim 35^\circ$ to the rolling direction (Fig. 6.15). In addition, the contrast between the strain in areas with large strain accumulation and the surrounding regions increases, which results in sharper river-like patterns. On the other hand, the in-grain deformation bands are more clearly visible, and they develop in a larger number of grains. These deformation bands still have an angle of around $\pm 30^\circ \sim 35^\circ$ with the rolling direction, so unlike the river-like patterns, they do not rotate notably toward the rolling direction. The grains that contain such microstructure features belong mostly to the γ-fiber.

After 60% thickness reduction ($\varepsilon = 0.92$), the river-like patterns rotate significantly to inclination angles of $\pm 15^\circ \sim 20^\circ$ to the rolling direction (Fig. 6.16). On the other hand, the angle for the deformation bands is still around $\pm 30^\circ \sim 35^\circ$, revealing that the inclination of deformation bands is not noticeably dependent on the applied strain.

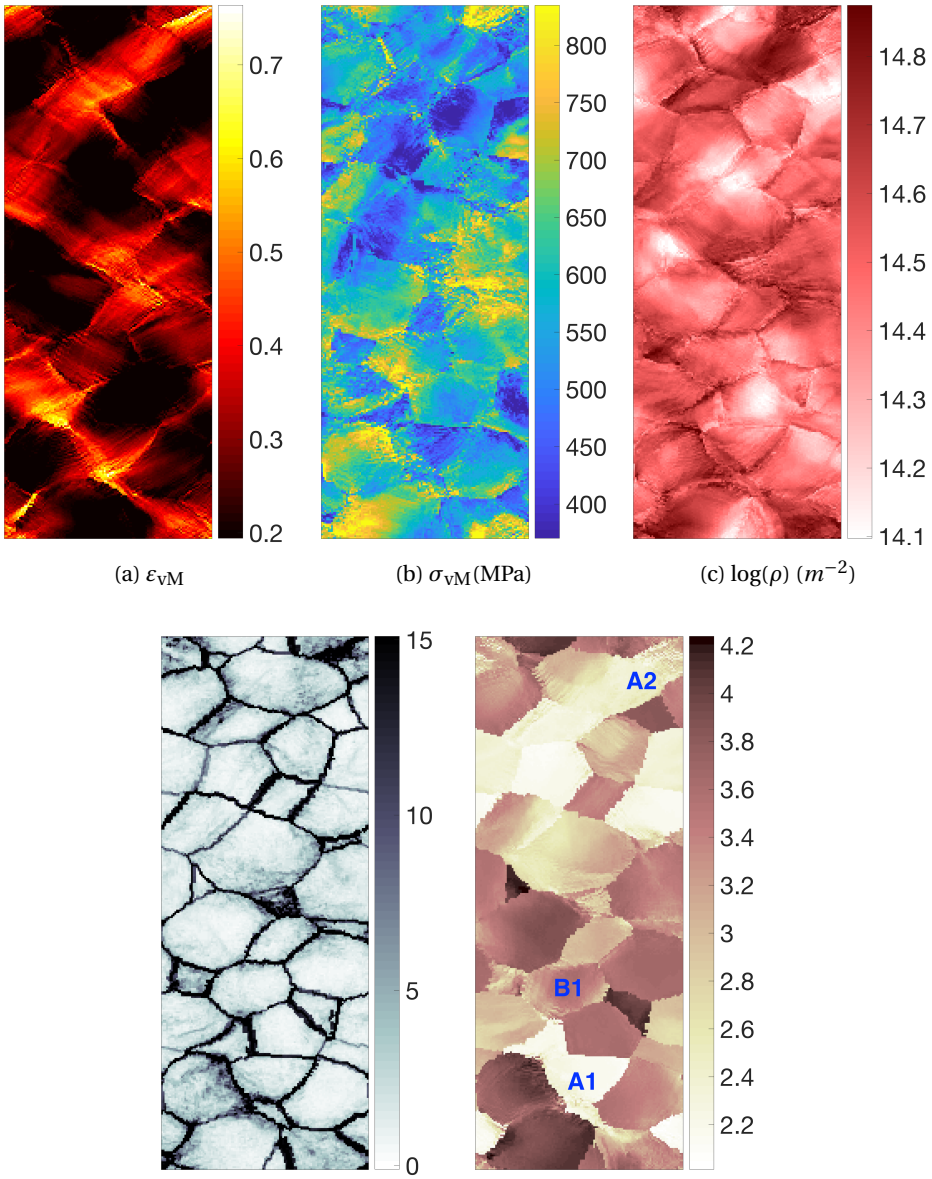

(a) $\varepsilon_{\mathrm{vM}}$ (b) σ_{vM}(MPa) (c) $\log(\rho)$ (m^{-2})

(d) KAM (degree) (e) Taylor factor

Fig. 6.14: Simulation results at the mid-surface after a 20% thickness reduction; (a) equivalent strain $\varepsilon_{\mathrm{vM}}$, (b) equivalent stress σ_{vM}(MPa), (c) $\log(\rho)$ (m^{-2}), (d) KAM (degree), (e) Taylor factor with respect to the loading (vertical) direction.

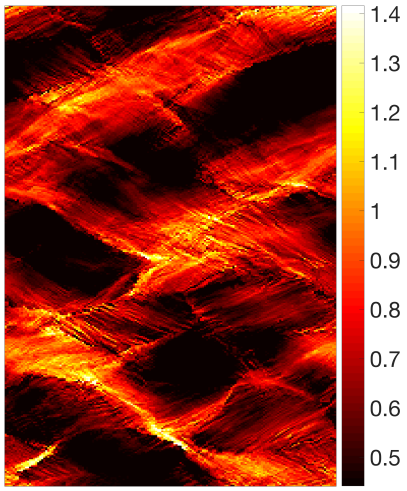

(a) $\varepsilon_{\mathrm{vM}}$

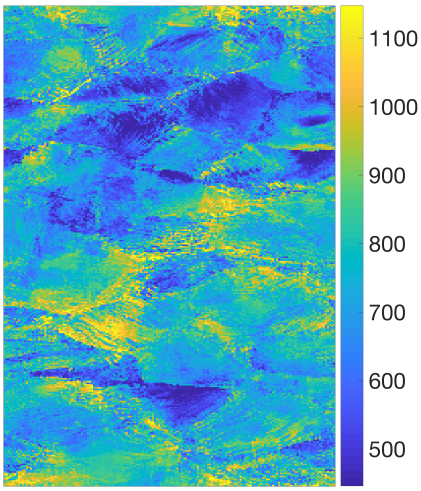

(b) σ_{vM}(MPa)

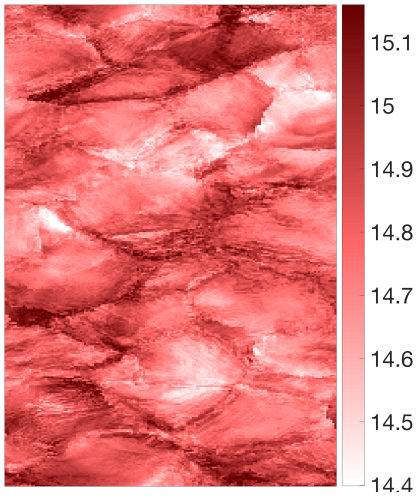

(c) $\log(\rho)$ (m^{-2})

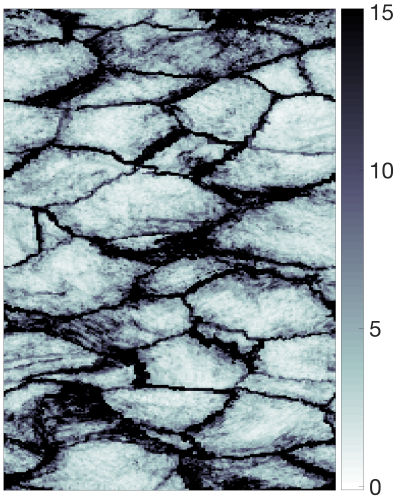

(d) KAM (degree)

Fig. 6.15: Simulation results at the mid-surface after a 40% thickness reduction; (a) equivalent strain $\varepsilon_{\mathrm{vM}}$, (b) equivalent stress σ_{vM}(MPa), (c) $\log(\rho)$ (m^{-2}), (d) KAM (degree).

After 60% thickness reduction, the in-grain deformation bands are well developed and established in some grains that mainly belong to the γ-fiber.

After 77% thickness reduction (ε = 1.47), the whole microstructure is severely deformed, and it is difficult to trace the original grain boundaries (Fig. 6.17). However, it is still possible to identify and trace some of the features previously observed at lower strains. The river-like patterns rotate further towards the rolling direction. In some places, they rotate to inclination angles of $\pm 5^\circ \sim 10^\circ$ to the rolling direction, while in some other places, they are almost parallel to the rolling direction. The localized strain in the river-like patterns can reach 4.0, around three times higher than the applied strain.

The in-grain deformation bands also rotate slightly, and their inclination angle with the rolling direction rotates to around $\pm 25^\circ \sim 30^\circ$. However, bands with an angle of around $\pm 15^\circ$ are also observed. The highly rotated deformation bands are mainly those developed at the early stages of deformation, i.e. those already visible at 20% thickness reduction. Moreover, the fraction of in-grain deformation bands has increased notably with increasing deformation. The in-grain deformation bands are orientation-dependent, i.e. they form preferentially in γ-fiber (high Taylor factor) grains. However, not all grains belonging to the γ-fiber contain such features. Similar experimental observations for steels have been reported [53, 58, 61].

A 3D view of the river-like patterns after 60% and 77% thickness reductions is shown in Figure 6.18a and Figure 6.18a, respectively. These patterns are aligned parallel to the transverse direction and extended through the depth of the RVE. Since these macroscopic band-like areas pass through several grains and extend across the specimen, they are comprised of regions belonging to both α-fiber and γ-fiber. The regions belonging to the γ-fiber are areas with relatively high local misorientations and stress. On the contrary, regions belonging to the α-fiber deform relatively homogeneous, and their stress value is relatively low. Therefore, the orientations belonging to the γ-fiber have significantly higher stored energy and misorientation than the α-fiber orientations. This facilitates the growth of recrystallized volumes of γ-fiber orientations, i.e. act as successful nucleation sites for recrystallization. This leads to the well-known γ-fiber recrystallization texture appearing after annealing of the cold-rolled IF-steel sheet [7, 54, 57].

Fig. 6.19 shows the deformation bands developed in a selected grain, i.e. grain number 24 (see Figure 6.11b). It can be seen that the orientation inside the in-grain shear bands is displaced from the matrix orientation of $\{111\}\langle 112\rangle$ toward the orientation of $\{554\}\langle 225\rangle$. This supports the role of in-grain shear bands in the nucleation of $\{554\}\langle 225\rangle$ recrystallization texture appearing after annealing of the cold-rolled IF-steel sheet.

Fig. 6.20a shows the evolution of the average equivalent strain with deformation in major texture components. The mean equivalent strain is larger in grains with smaller Taylor factors, i.e. orientations close to the rotated cube component. The mean equivalent strain decreases in orientations belonging to the γ-fiber, i.e. orientations with larger Taylor factors.

Fig. 6.20b compares the distribution of equivalent strain in major texture components as a boxplot. The figure illustrates the data for all elements after 77%

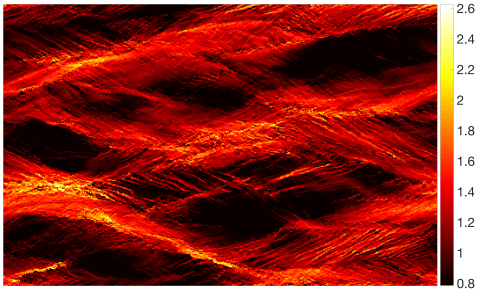

(a) $\varepsilon_{\mathrm{vM}}$

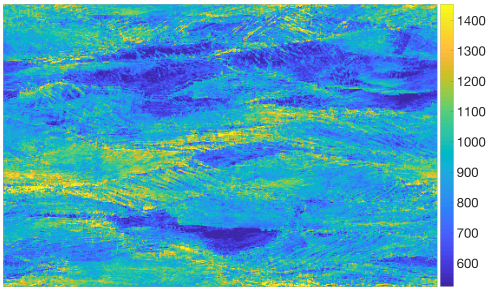

(b) σ_{vM}(MPa)

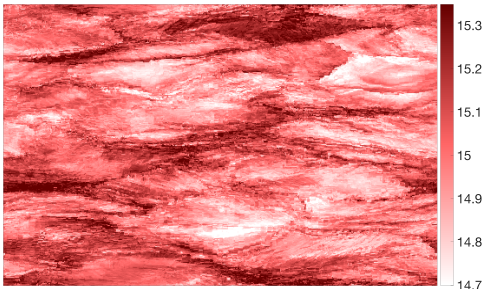

(c) log(ρ) (m^{-2})

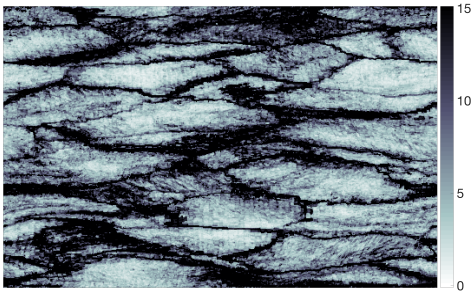

(d) KAM (degree)

Fig. 6.16: Simulation results at the mid-surface after a 60% thickness reduction; (a) equivalent strain $\varepsilon_{\mathrm{vM}}$, (b) equivalent stress σ_{vM}(MPa), (c) log(ρ) (m^{-2}), (d) KAM (degree).

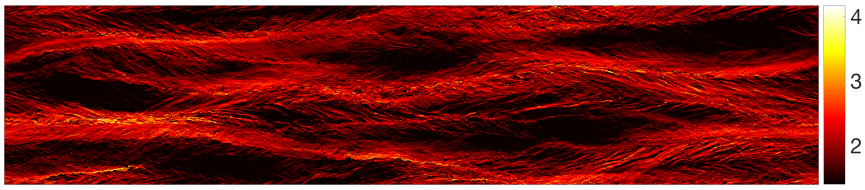

(a) $\varepsilon_{\mathrm{vM}}$

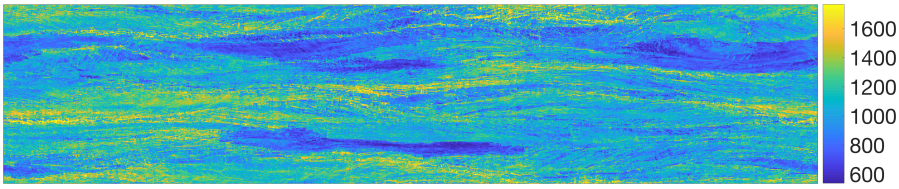

(b) σ_{vM}(MPa)

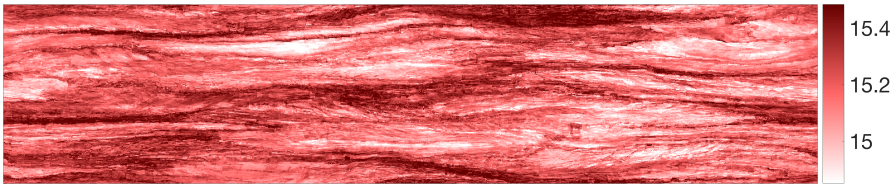

(c) $\log(\rho)$ (m^{-2})

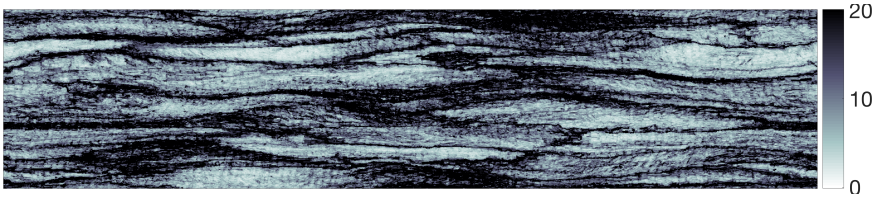

(d) KAM (degree)

Fig. 6.17: Simulation results at the mid-surface after a 77% thickness reduction; (a) equivalent strain $\varepsilon_{\mathrm{vM}}$, (b) equivalent stress σ_{vM}(MPa), (c) $\log(\rho)$ (m^{-2}), (d) KAM (degree).

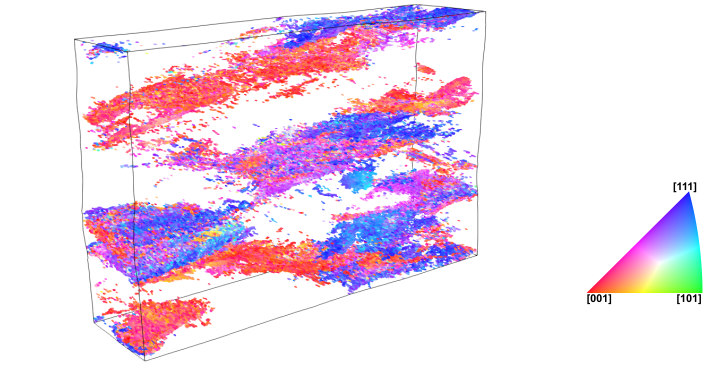

(a)

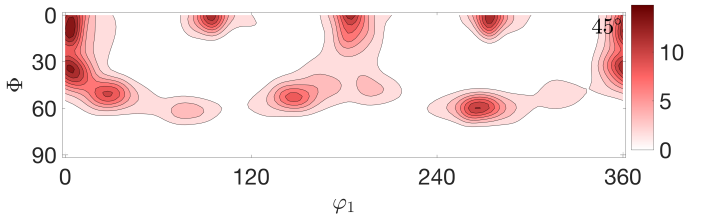

(b)

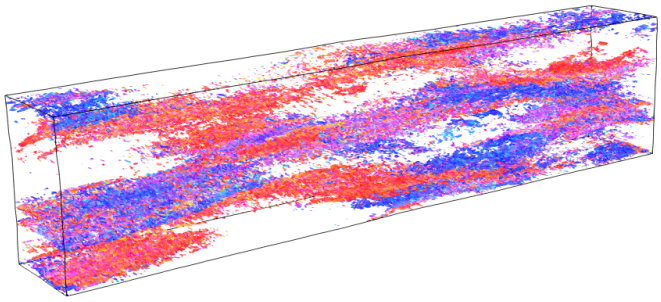

(c)

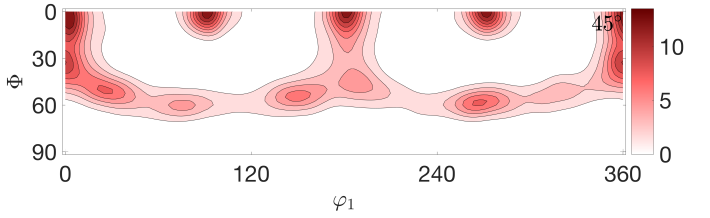

(d)

Fig. 6.18: 3D view of the river-like patterns shown in term of IPF color maps parallel to the loading (vertical) direction after (a) 60% thickness reduction and (c) 77% thickness reductions. The corresponding orientation density f(g) maps ($\varphi_2 = 45°$) after (b) 60% thickness reduction and (d) 77% thickness reductions.

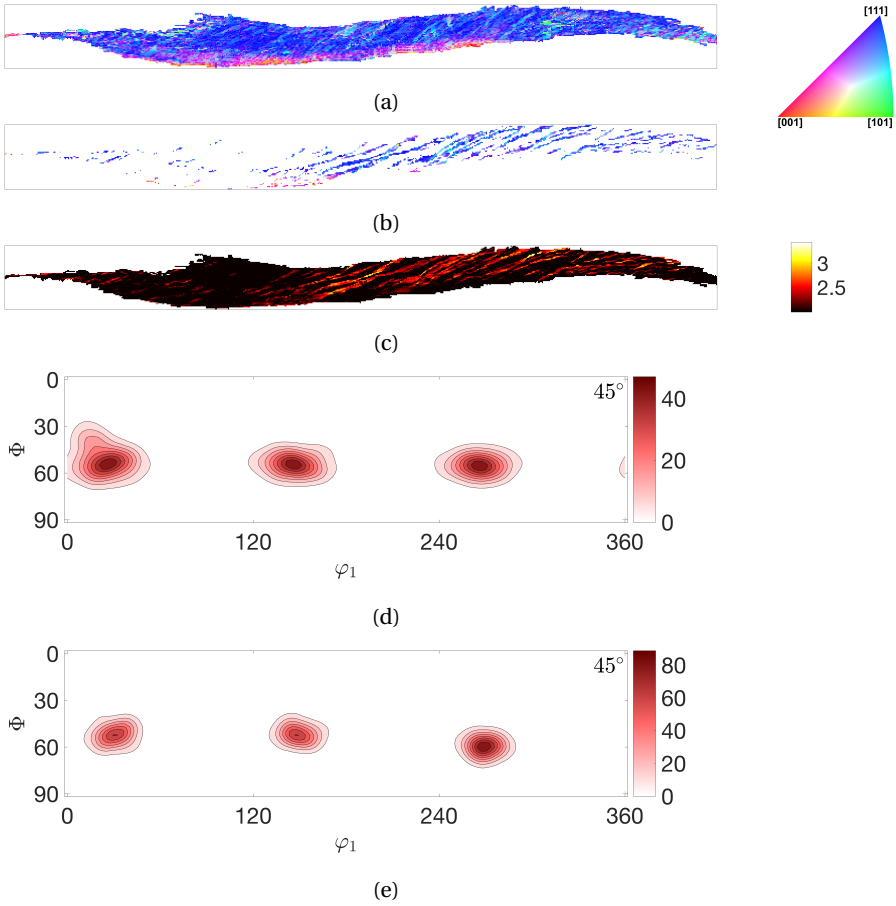

Fig. 6.19: A 2D section of grain 24 showing IPF color maps parallel to the loading (vertical) direction for (a) the full cross-section, (b) the highly sheared deformation bands. (c) Strain distribution at the deformation bands. Orientation density f(g) maps obtained from the ODF section $\varphi_2 = 45°$ for the (d) grain matrix and (e) deformation bands.

thickness reduction. The five horizontal lines of the boxplot represent the minimum, the maximum, the sample median, and the first and third quartiles. The outliers are not included in the figures. In addition to the notable difference in the median values, there is a significant difference between the range of the values for different texture components. The lower bound of the distributions follows almost the same trend as the median values, i.e. the lower bound decreases with an increase in the hardness of the orientation. However, the upper bounds are not orientation-dependent, it is almost the same for all orientations. This leads to a narrower distribution for the soft grains, i.e. orientations close to the rotated cube component. The distribution becomes wider for orientations further along the α-fiber, and it becomes noticeably wide for hard grains belonging to the γ-fiber. The widest distributions are for $\{111\}\langle 112\rangle$ and $\{111\}\langle 123\rangle$

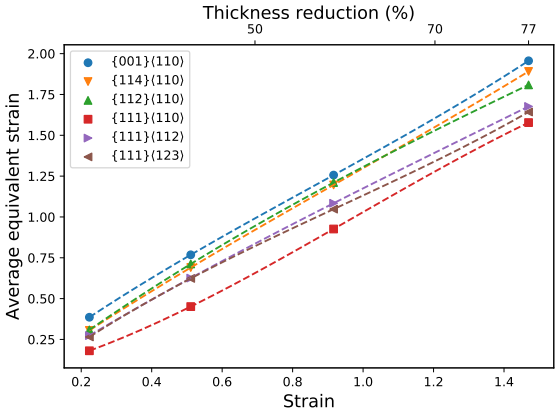

(a) $\varepsilon_{\mathrm{vM}}$

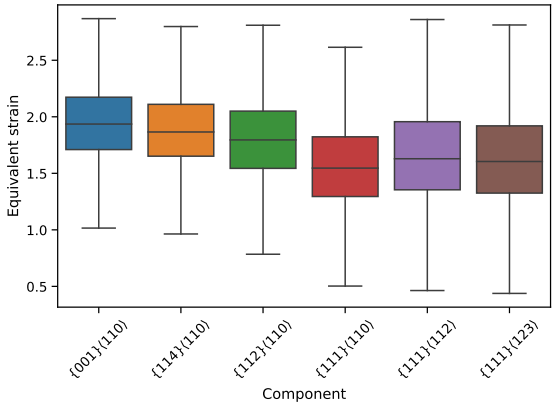

(b)

Fig. 6.20: (a) Evolution of the average equivalent strain with deformation in major texture components. (b) boxplots showing the distribution of equivalent strain in major texture components. The five horizontal lines of the boxplot represent the minimum, the maximum, the sample median, and the first and third quartiles.

components. This wide distribution is due to the formation of in-grain deformation bands in γ-fiber grains. The in-grain deformation bands are areas with large strain accumulation. The presence of these bands serves to redistribute plastic strain and significantly reduces the extent of the strain in regions next to these bands, resulting in a large contrast in the strain distribution in these grains.

6.4.4.1. Effect of multi-step mesh refinement method

This study uses a multi-step mesh refinement method to adjust the number of elements during the simulation. To further investigate the advantages of this meshing strategy, we have conducted a new simulation using the same RVE investigated in this section (see Figure 6.5a). However, the simulation is performed without using the multi-step

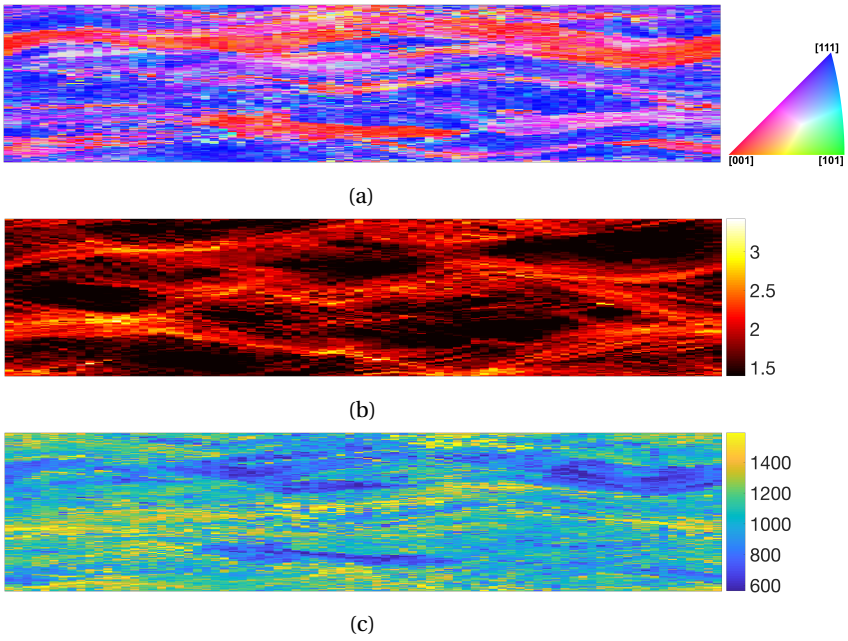

Fig. 6.21: Simulation results at the mid-surface after a 77% thickness reduction;(a) IPF color maps parallel to the loading (vertical) direction, (b) equivalent strain $\varepsilon_{\mathrm{vM}}$, and (c) equivalent stress σ_{vM}(MPa). The simulation is conducted without using the multi-step mesh refinement method and the mesh density is kept constant as $80 \times 48 \times 320$.

mesh refinement method, i.e. the mesh density is kept constant as $80 \times 48 \times 320$. Figure 6.21 shows the results after 77% thickness reduction. During the simulation, the element size in the loading direction decreases with increasing the deformation, while the element is elongated in the stretching direction. Therefore, the element becomes rectangular, and the element aspect ratio, the ratio of the element size in the stretching direction to the element size in the compression direction, considerably increases. For this example, the elements' aspect ratio reaches around 19 after 77% thickness reductions. These elongated elements prevent strain localization from occurring. An element represents the average response of a section in the discretized space. Therefore, when the element size is larger than the localized features, it will capture only the homogenized behavior and not the morphology of the localized deformation. This behavior can be seen clearly in Figure 6.21b, where these highly elongated elements substantially have reduced the level of strain localization. Although the simulation can still capture the global shape of the river-like patterns, it is no longer possible to recognize the detail inside and close to these patterns. In addition, it is no longer possible to identify the deformation bands inside the grains. One should note that the resolution of this simulation (i.e. approximately 3400 elements per grain) is still relatively high compared to the typical crystal plasticity simulations. Hence, the use of the multi-step mesh refinement approach is critical for capturing the in-grain microstructure evolution.

6.4.5. Evolution of dislocation density

6.4.5.1. Orientation dependency of dislocation density

Fig. 6.22 shows the IPF color map parallel to the loading (vertical) direction at the mid-surface. The data are divided to low dislocation density regions, i.e. points whose dislocation densities belong to the lower 20% of the data, and high dislocation density regions, points whose dislocation densities belong to the higher half of the data. Grains close to the rotated cube component generally have the lowest dislocation density. The dislocation density increases for orientations further along the α-fiber, similar to what was previously observed for KAM. On the other hand, regions that belong to the γ-fiber have the highest dislocation density.

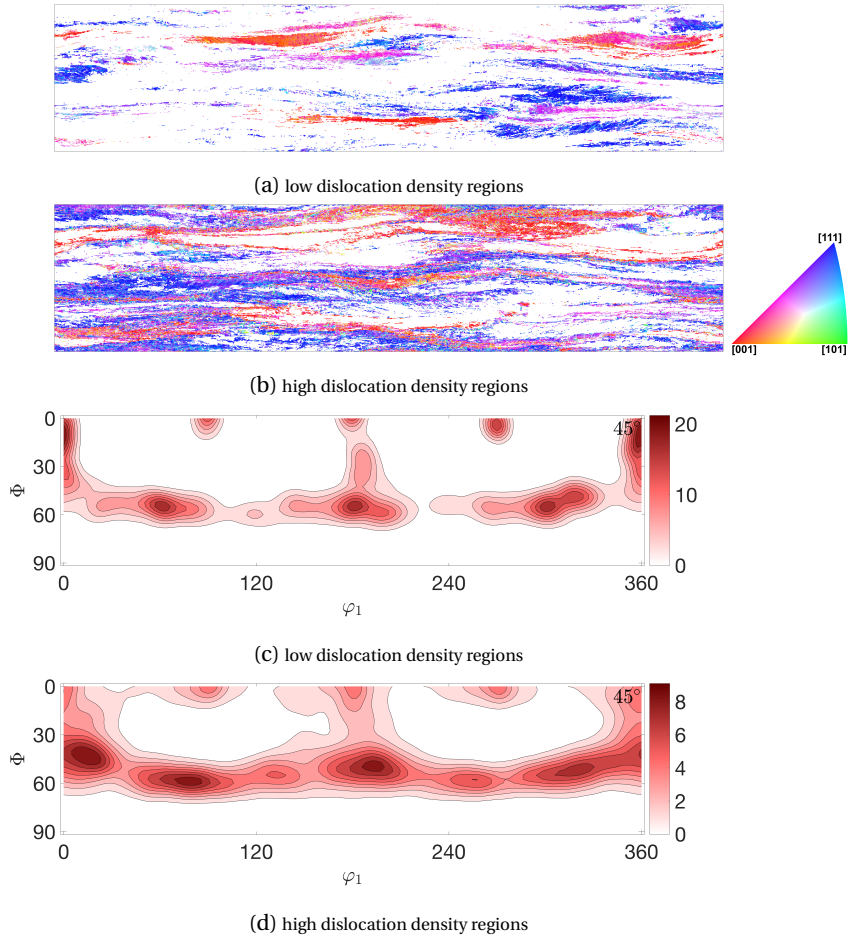

(a) low dislocation density regions

(b) high dislocation density regions

(c) low dislocation density regions

(d) high dislocation density regions

Fig. 6.22: Simulation results showing low and high dislocation density regions. (a,b) IPF color maps parallel to the loading (vertical) direction, (c,d) orientation density f(g) maps obtained from the ODF section $\varphi_2 = 45°$.

Fig. 6.23 shows the development of the dislocation density with deformation for major texture components. At 20% thickness reduction, the difference between the dislocation density of different orientations is relatively small. At larger strains, the difference between the dislocation density of γ-fiber and α-fiber components becomes more pronounced. After 77% thickness reduction, the average dislocation density of γ-fiber and α-fiber are 1.45×10^{15} and 1.6×10^{15} m^{-2}, respectively. It should be noted that $\{1\,1\,1\}\langle 1\,1\,0\rangle$ is a common component between γ-fiber and α-fiber. A similar trend for geometrically necessary dislocations (GND) has been reported experimentally, e.g. [58].

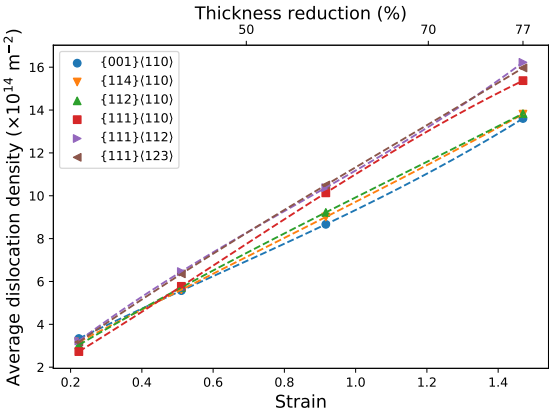

Fig. 6.23: Average dislocation density in major texture components.

6.4.5.2. Correlation between dislocation density and main variables

It is generally accepted that GNDs are related to the in-grain misorientation. Although the crystal plasticity model used here does not differentiate between the GNDs and SSDs (Statistically Stored Dislocations), it is still expected that the total dislocation density correlates with the local misorientation and KAM. Fig. 6.24a shows the correlation between the dislocation density with other main variables at different strain levels. There is a small positive correlation between the dislocation density and KAM at small strains (0.21). The correlation coefficient increases rapidly, and it reaches a significant value of 0.60 after a 77% thickness reduction. The high correlation value indicates that the dislocation density and the KAM are strongly correlated at large deformation. Fig. 6.24b shows a 2D probability density plot of the dislocation density and the KAM after 77% thickness reduction.

The correlation between the dislocation density and the equivalent strain follows an opposite trend. There is a strong positive correlation between these two variables at small strains (0.66). However, the correlation coefficient substantially decreases with increasing deformation, and it reduces to 0.13 after 77% thickness reduction. There is a moderate correlation between the equivalent stress and the dislocation density at small strains (0.42). The correlation coefficient steadily increases to 0.58 at 77% thickness reduction.

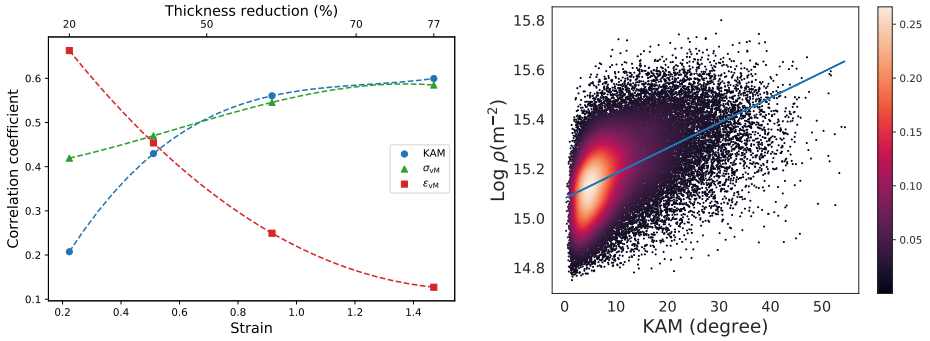

(a) (b)

Fig. 6.24: (a) Correlation between the dislocation density and main variables. (b) 2D probability density plot of the dislocation density and KAM. The blue line shows the linear regression line.

6.5. Conclusions

This study investigates the evolution of texture and deformation heterogeneity during large deformation of IF-steel using crystal plasticity simulation. In the first step, the texture evolution is investigated using an RVE consisting of 40000 grains in which each grain is represented by a single element. The RVE is subjected to a plane-strain compression up to 99% thickness reduction. The results show that the deformation texture obtained using the crystal plasticity simulation is in agreement with the typical rolling texture observed in BCC crystals, i.e. a strong α-fiber and γ-fiber. It is observed that the components belonging to the α-fiber strengthen continuously with increasing deformation. Although the γ-fiber components are initially strengthened with increasing the applied strain, these texture components weaken at larger thickness reductions, i.e. after about 70-80% thickness reduction.

However, discretization using only one element per grain does not allow strain gradient to develop within the grain, and the in-grain deformation heterogeneities cannot be described using such coarse discretization. Therefore, a high-resolution RVE consisting of 36 grains is used to investigate the in-grain microstructural evolution. The RVE is subjected to plane-strain compression up to a thickness reduction of 77%. At this deformation level, around 550000 elements on average are used for the discretization of each grain.

The results reveal that the crystallographic orientation of a grain is a critical factor in determining whether a grain deforms relatively homogeneously or heterogeneously. The orientations close to the rotated cube orientation show the minimal tendency to form orientation gradients. The deformation heterogeneity increases for orientations further along the α-fiber. On the other hand, the orientations belonging to the γ-fiber show the strongest misorientation spread. Meanwhile, band-like areas with sever strain localization extending across the specimen (which appear as river patterns) are formed during the deformation. These river-like patterns are initially formed at an approximate angle of $\pm 40^\circ \sim 45^\circ$ with the rolling direction. With increasing the thickness reduction,

the river-like patterns rotate significantly to inclination angles almost parallel to the rolling direction. The localized strain in the river-like patterns can reach a value that is three times the overall applied strain value. In addition to the macroscopic river-like patterns, several regions with rather sharp and highly localized in-grain deformation bands are identified. These deformation bands extend inside only one grain. These bands are formed at an angle of approximately $\pm 30° \sim 35°$ with the rolling direction, and their inclination angle is not noticeably dependent on the applied strain for a wide range of deformation. The in-grain deformation bands are orientation-dependent, and they form mainly in grains belonging to the γ-fiber. However, not all grains belonging to the γ-fiber contain such features.

The results reveal that the difference between the dislocation density of different orientations is relatively small at small strains. However, with increasing strain, the dislocation density in the γ-fiber becomes notably larger than in the α-fiber. Although dislocation density and KAM are weakly correlated at small strains, the correlation coefficient increases rapidly with increasing strain. The correlation between the dislocation density and the equivalent strain follows an opposite trend.

References

[1] K. Sedighiani, K. Traka, M. Diehl, F. Roters, J. Sietsma, and D. Raabe, *Crystal plasticity simulation of in-grain microstructural evolution during large deformation of IF-steel,* Submitted to Acta Materialia (2022).

[2] L. Chen, J. Chen, R. A. Lebensohn, Y. Z. Ji, T. W. Heo, S. Bhattacharyya, K. Chang, S. Mathaudhu, Z. K. Liu, and L. Q. Chen, *An integrated fast Fourier transform-based phase-field and crystal plasticity approach to model recrystallization of three dimensional polycrystals,* Computer Methods in Applied Mechanics and Engineering **285**, 829 (2015).

[3] P. Zhao, T. Song En Low, Y. Wang, and S. Niezgoda, *An integrated full-field model of concurrent plastic deformation and microstructure evolution: Application to 3D simulation of dynamic recrystallization in polycrystalline copper,* International Journal of Plasticity **80** (2016), 10.1016/j.ijplas.2015.12.010.

[4] D. Kim, W. Woo, W. Park, Y. Im, and A. Rollett, *Mesoscopic coupled modeling of texture formation during recrystallization considering stored energy decomposition,* Computational Materials Science **129** (2017), 10.1016/j.commatsci.2016.11.048.

[5] K. K. Alaneme and E. A. Okotete, *Recrystallization mechanisms and microstructure development in emerging metallic materials: A review,* (2019).

[6] M. Diehl and M. Kühbach, *Coupled experimental-computational analysis of primary static recrystallization in low carbon steel,* Modelling and Simulation in Materials Science and Engineering **28** (2020), 10.1088/1361-651X/ab51bd.

[7] K. Traka, K. Sedighiani, C. Bos, J. Galan Lopez, K. Angenendt, D. Raabe, and J. Sietsma, *Topological aspects responsible for recrystallization evolution in an IF-steel sheet – Investigation with cellular-automaton simulations,* Computational Materials Science **198**, 110643 (2021).

[8] C. C. Tasan, J. P. M. Hoefnagels, M. Diehl, D. Yan, F. Roters, and D. Raabe, *Strain localization and damage in dual phase steels investigated by coupled in-situ deformation experiments and crystal plasticity simulations,* International Journal of Plasticity **63**, 198 (2014).

[9] M. Diehl, M. Wicke, P. Shanthraj, F. Roters, A. Brueckner-Foit, and D. Raabe, *Coupled Crystal Plasticity–Phase Field Fracture Simulation Study on Damage Evolution Around a Void: Pore Shape Versus Crystallographic Orientation,* Jom **69**, 872 (2017).

[10] H. Hallberg, S. K. Ås, and B. Skallerud, *Crystal plasticity modeling of microstructure influence on fatigue crack initiation in extruded Al6082-T6 with surface irregularities,* International Journal of Fatigue **111** (2018), 10.1016/j.ijfatigue.2018.01.025.

[11] H. S. Oh, K. Biggs, O. Güvenç, H. Ghassemi-Armaki, N. Pottore, and C. C. Tasan, *In-situ investigation of strain partitioning and microstructural strain path development up to and beyond necking,* Acta Materialia **215** (2021), 10.1016/j.actamat.2021.117023.

[12] E. K. Cerreta, I. J. Frank, G. T. Gray, C. P. Trujillo, D. A. Korzekwa, and L. M. Dougherty, *The influence of microstructure on the mechanical response of copper in shear,* Materials Science and Engineering A **501** (2009), 10.1016/j.msea.2008.10.029.

[13] G. Zhou, M. K. Jain, P. Wu, Y. Shao, D. Li, and Y. Peng, *Experiment and crystal plasticity analysis on plastic deformation of AZ31B Mg alloy sheet under intermediate temperatures: How deformation mechanisms evolve,* International Journal of Plasticity **79** (2016), 10.1016/j.ijplas.2015.12.006.

[14] A. J. Beaudoin, H. Mecking, and U. F. Kocks, *Development of localized orientation gradients in fcc polycrystals,* Philosophical Magazine A: Physics of Condensed Matter, Structure, Defects and Mechanical Properties **73** (1996), 10.1080/01418619608242998.

[15] M. Sachtleber, Z. Zhao, and D. Raabe, *Experimental investigation of plastic grain interaction,* Materials Science and Engineering A **336**, 81 (2002).

[16] D. Raabe, Z. Zhao, and F. Roters, *Study on the orientational stability of cube-oriented FCC crystals under plane strain by use of a texture component crystal plasticity finite element method,* Scripta Materialia **50** (2004), 10.1016/j.scriptamat.2003.11.061.

[17] K. S. Cheong and E. P. Busso, *Effects of lattice misorientations on strain heterogeneities in FCC polycrystals,* Journal of the Mechanics and Physics of Solids **54** (2006), 10.1016/j.jmps.2005.11.003.

[18] C. Zhang, H. Li, P. Eisenlohr, W. Liu, C. J. Boehlert, M. A. Crimp, and T. R. Bieler, *Effect of realistic 3D microstructure in crystal plasticity finite element analysis of polycrystalline Ti-5Al-2.5Sn,* International Journal of Plasticity **69** (2015), 10.1016/j.ijplas.2015.01.003.

[19] J. Oddershede, J. P. Wright, A. Beaudoin, and G. Winther, *Deformation-induced orientation spread in individual bulk grains of an interstitial-free steel,* Acta Materialia **85** (2015), 10.1016/j.actamat.2014.11.038.

[20] D. Wang, M. Diehl, F. Roters, and D. Raabe, *On the role of the collinear dislocation interaction in deformation patterning and laminate formation in single crystal plasticity,* Mechanics of Materials **125** (2018), 10.1016/j.mechmat.2018.06.007.

[21] J. Cappola, J. C. Stinville, M. Charpagne, P. G. Callahan, M. P. Echlin, T. M. Pollock, A. Pilchak, and M. Kasemer, *On the Localization of Plastic Strain in Microtextured Regions of Ti-6Al-4V,* Acta Materialia **204**, 116492 (2021).

[22] S. H. Choi and Y. S. Jin, *Evaluation of stored energy in cold-rolled steels from EBSD data,* Materials Science and Engineering A **371** (2004), 10.1016/j.msea.2003.11.034.

[23] S. H. Choi and J. H. Cho, *Primary recrystallization modelling for interstitial free steels,* Materials Science and Engineering A **405** (2005), 10.1016/j.msea.2005.05.093.

[24] N. Allain-Bonasso, F. Wagner, S. Berbenni, and D. P. Field, *A study of the heterogeneity of plastic deformation in IF steel by EBSD,* Materials Science and Engineering A **548** (2012), 10.1016/j.msea.2012.03.068.

[25] S. Wang, Z. H. Wu, C. Chen, S. K. Feng, R. Liu, B. Liao, Z. H. Zhong, P. Lu, M. P. Wang, P. Li, J. W. Coenen, L. F. Cao, and Y. C. Wu, *The evolution of shear bands in Ta-2.5W alloy during cold rolling,* Materials Science and Engineering A **726** (2018), 10.1016/j.msea.2018.04.059.

[26] B. L. Li, A. Godfrey, Q. C. Meng, Q. Liu, and N. Hansen, *Microstructural evolution of IF-steel during cold rolling,* Acta Materialia **52**, 1069 (2004).

[27] D. A. Hughes and N. Hansen, *The microstructural origin of work hardening stages,* Acta Materialia **148** (2018), 10.1016/j.actamat.2018.02.002.

[28] F. Roters, P. Eisenlohr, L. Hantcherli, D. D. Tjahjanto, T. R. Bieler, and D. Raabe, *Overview of constitutive laws, kinematics, homogenization and multiscale methods in crystal plasticity finite-element modeling: Theory, experiments, applications,* Acta Materialia **58**, 1152 (2010).

[29] C. Reuber, P. Eisenlohr, F. Roters, and D. Raabe, *Dislocation density distribution around an indent in single-crystalline nickel : Comparing nonlocal crystal plasticity finite-element predictions with experiments,* Acta Materialia **71**, 333 (2014).

[30] M. Khadyko, S. Dumoulin, and O. S. Hopperstad, *Texture gradients and strain localisation in extruded aluminium profile,* International Journal of Solids and Structures **97_98**, 239 (2016).

[31] M. Diehl, D. An, P. Shanthraj, S. Zaefferer, F. Roters, and D. Raabe, *Crystal plasticity study on stress and strain partitioning in a measured 3D dual phase steel microstructure,* Physical Mesomechanics **20** (2017), 10.1134/S1029959917030079.

[32] M. Diehl, M. Groeber, C. Haase, D. A. Molodov, F. Roters, and D. Raabe, *Identifying Structure–Property Relationships Through DREAM.3D Representative Volume Elements and DAMASK Crystal Plasticity Simulations: An Integrated Computational Materials Engineering Approach,* JOM **69** (2017), 10.1007/s11837-017-2303-0.

[33] H. Zhang, J. Liu, D. Sui, Z. Cui, and M. W. Fu, *Study of microstructural grain and geometric size effects on plastic heterogeneities at grain-level by using crystal plasticity modeling with high-fidelity representative microstructures,* International Journal of Plasticity **100** (2018), 10.1016/j.ijplas.2017.09.011.

[34] M. Diehl, J. Niehuesbernd, and E. Bruder, *Quantifying the contribution of crystallographic texture and grain morphology on the elastic and plastic anisotropy of bcc steel,* Metals **9** (2019), 10.3390/met9121252.

[35] T. F. van Nuland, J. A. van Dommelen, and M. G. Geers, *Microstructural modeling of anisotropic plasticity in large scale additively manufactured 316L stainless steel,* Mechanics of Materials **153** (2021), 10.1016/j.mechmat.2020.103664.

[36] J. L. Dequiedt and C. Denoual, *Localization of plastic deformation in stretching sheets with a crystal plasticity approach: Competition between weakest link and instable mode controlled process,* International Journal of Solids and Structures **210-211** (2021), 10.1016/j.ijsolstr.2020.11.021.

[37] D. Raabe, M. Sachtleber, Z. Zhao, F. Roters, and S. Zaefferer, *Micromechanical and macromechanical effects in grain scale polycrystal plasticity experimentation and simulation,* Acta Materialia **49**, 3433 (2001).

[38] K. Thool, A. Patra, D. Fullwood, K. Krishna, D. Srivastava, and I. Samajdar, *The role of crystallographic orientations on heterogeneous deformation in a zirconium alloy: A combined experimental and modeling study,* International Journal of Plasticity **133** (2020), 10.1016/j.ijplas.2020.102785.

[39] S. Zaefferer, J. C. Kuo, Z. Zhao, M. Winning, and D. Raabe, *On the influence of the grain boundary misorientation on the plastic deformation of aluminum bicrystals,* Acta Materialia **51** (2003), 10.1016/S1359-6454(03)00259-3.

[40] A. Ma, F. Roters, and D. Raabe, *A dislocation density based constitutive model for crystal plasticity FEM including geometrically necessary dislocations,* Acta Materialia **54**, 2169 (2006).

[41] A. Ma, F. Roters, and D. Raabe, *On the consideration of interactions between dislocations and grain boundaries in crystal plasticity finite element modeling – Theory, experiments, and simulations,* Acta Materialia **54**, 2181 (2006).

[42] C. Rehrl, B. Völker, S. Kleber, T. Antretter, and R. Pippan, *Crystal orientation changes: A comparison between a crystal plasticity finite element study and experimental results,* Acta Materialia **60** (2012), 10.1016/j.actamat.2011.12.052.

[43] K. Sedighiani, V. Shah, K. Traka, M. Diehl, F. Roters, J. Sietsma, and D. Raabe, *Large-deformation crystal plasticity simulation of microstructure and microtexture evolution through adaptive remeshing,* International Journal of Plasticity **146**, 103078 (2021).

[44] D. K. Kim, J. M. Kim, W. W. Park, H. Lee, Y. T. Im, and Y. S. Lee, *Three-dimensional crystal plasticity finite element analysis of microstructure and texture evolution during channel die compression of if steel,* Computational Materials Science **100**, 52 (2015).

[45] H. Lim, C. C. Battaile, J. E. Bishop, and J. W. Foulk, *Investigating mesh sensitivity and polycrystalline RVEs in crystal plasticity finite element simulations,* International Journal of Plasticity **121**, 101 (2019).

[46] K. Traka, *Investigations on the early stages of recrystallization in low-carbon and interstitial-free steel sheets*, Ph.D. thesis, TU Delft (2022).

[47] P. Eisenlohr, M. Diehl, R. Lebensohn, and F. Roters, *A spectral method solution to crystal elasto-viscoplasticity at finite strains,* International Journal of Plasticity **46**, 37 (2013).

[48] P. Shanthraj, P. Eisenlohr, M. Diehl, and F. Roters, *Numerically robust spectral methods for crystal plasticity simulations of heterogeneous materials,* International Journal of Plasticity **66**, 31 (2015).

[49] F. Roters, M. Diehl, P. Shanthraj, P. Eisenlohr, C. Reuber, S. Wong, T. Maiti, A. Ebrahimi, T. Hochrainer, H. Fabritius, S. Nikolov, M. Friák, N. Fujita, N. Grilli, K. Janssens, N. Jia, P. Kok, D. Ma, F. Meier, E. Werner, M. Stricker, D. Weygand, and D. Raabe, *DAMASK – The Düsseldorf Advanced Material Simulation Kit for modeling multi-physics crystal plasticity, thermal, and damage phenomena from the single crystal up to the component scale,* Computational Materials Science **158**, 420 (2019).

[50] A. Ma and F. Roters, *A constitutive model for fcc single crystals based on dislocation densities and its application to uniaxial compression of aluminium single crystals,* Acta Materialia **52**, 3603 (2004).

[51] K. Sedighiani, K. Traka, F. Roters, D. Raabe, J. Sietsma, and M. Diehl, *Determination and analysis of the constitutive parameters of temperature-dependent dislocation-density-based crystal plasticity models,* Mechanics of Materials (2021), 10.1016/j.mechmat.2021.104117.

[52] D. Raabe and K. Luecke, *Rolling and annealing textures of bcc metals,* Materials Science Forum **157-6** (1994), 10.4028/www.scientific.net/msf.157-162.597.

[53] M. R. Barnett and J. J. Jonas, *Influence of ferrite rolling temperature on microstructure and texture in deformed low C and IF steels,* ISIJ International **37** (1997), 10.2355/isijinternational.37.697.

[54] B. Hutchinson, *Deformation microstructures and textures in steels,* Philosophical Transactions of the Royal Society A: Mathematical, Physical and Engineering Sciences **357**, 1471 (1999).

[55] D. Raabe, Z. Zhao, S. J. Park, and F. Roters, *Theory of orientation gradients in plastically strained crystals,* Acta Materialia **50** (2002), 10.1016/S1359-6454(01)00323-8.

[56] P. Van Houtte, S. Li, M. Seefeldt, and L. Delannay, *Deformation texture prediction: From the Taylor model to the advanced Lamel model,* International Journal of Plasticity **21**, 589 (2005).

[57] L. A. I. Kestens and H. Pirgazi, *Texture formation in metal alloys with cubic crystal structures,* Materials Science and Technology **32**, 1303 (2016).

[58] N. Deeparekha, A. Gupta, M. Demiral, and R. K. Khatirkar, *Cold rolling of an interstitial free (IF) steel—Experiments and simulations,* Mechanics of Materials **148** (2020), 10.1016/j.mechmat.2020.103420.

[59] D. Schlaefer and H. J. Bunge, *Development of the rolling texture of iron determined by neutron-diffraction.* Texture **1**, 157 (1974).

[60] Q. Z. Chen and B. J. Duggan, *On cells and microbands formed in an interstitial-free steel during cold rolling at low to medium reductions,* Metallurgical and Materials Transactions A: Physical Metallurgy and Materials Science **35 A** (2004), 10.1007/s11661-004-0178-5.

[61] M. Calcagnotto, D. Ponge, E. Demir, and D. Raabe, *Orientation gradients and geometrically necessary dislocations in ultrafine grained dual-phase steels studied by 2D and 3D EBSD,* Materials Science and Engineering A **527** (2010), 10.1016/j.msea.2010.01.004.

7

OUTLOOK AND FUTURE APPLICATIONS

Abstract

This chapter presents a further investigation of some recommendations presented in the previous chapters. First, incorporating cross-slip annihilation into the hardening model of the dislocation-density-based model is examined. Then, two sequentially coupled models are investigated for modeling static recrystallization and meta-dynamic recrystallization. The results of this section are mainly achieved in collaboration with other researchers. Moreover, the results should be seen as an introductory guideline for future work.

7.1. Incorporating cross-slip annihilation into crystal plasticity model

The hardening formulation of the dislocation-density-based constitutive law lacks cross-slip recovery and cannot describe the recovery process accurately. Due to the availability of many secondary slip systems in bcc materials, cross-slip of screw dislocations is a key mechanism in the evolution of the dislocation structures. The optimization methodology is used for developing and analyzing a stochastic formulation for cross-slip annihilation. The next section presents some ideas how including cross-slip annihilation can improve the hardening formulation.

7.1.1. Dislocation annihilation by cross-slip

The cross-slip annihilation takes place as follows: for a mobile dislocation moving on a slip system, if there is a mobile/immobile dislocation of the opposite sign in the immediate distance around the dislocation, the two dislocations create a temporary dipole (an annihilation pair) due to the attractive force between them. Three scenarios for the dipole can be imagined. First, the attractive force is large enough for the blocked dislocation (mobile dislocation) to change plane, and the annihilation occurs by cross-slip of the blocked dislocation. Second, the stress acting on the dipole is sufficiently large for the dipole to break up, and the two dislocations escape each other. Third, the balance of the forces results in a stable dipole. However, screw dipoles are stable only for a small interval of resolved shear stress and annihilation distance [1]. Therefore, only the first two scenarios are considered as feasible scenarios.

The cross-slip annihilation process implies that two conditions are required: (i) annihilation occurs only if a dislocation of the opposite sign exists within a critical distance for annihilation to create a temporary dipole, (ii) annihilation occurs only if the blocked dislocation cross-slips. In the following, these two necessary conditions for cross-slip are elaborated, and a stochastic formulation for cross-slip annihilation is suggested.

7.1.1.1. Annihilation pair formation

Let us assume a positive straight dislocation segment of length l moving with an average velocity v^α. During time $\mathrm{d}t$, the dislocation segment travels a distance $v^\alpha \mathrm{d}t$, and the annihilation volume will be:

$$V_{\text{an}} = (2d_{\text{an}}^{\alpha})(\zeta v^{\alpha} \mathrm{d}t)\, l \tag{7.1}$$

where $2d_{\text{an}}^{\alpha}$ is the annihilation distance. ζ is 2 for the annihilation of two mobile dislocations and 1 for the annihilation of a mobile and an immobile dislocation. The formation rate of a potential annihilation pair for positive screw dislocations per unit volume V is:

$$\dot{p}_{\text{cs}(i)}^{\alpha+} = \frac{N_{\text{m}}^{\alpha+}}{V} V_{\text{an}} \frac{N_i^{\alpha-} l}{V} = 2\zeta d_{\text{an}}^{\alpha} v^{\alpha} \rho^{\alpha+} \rho_i^{\alpha-}, \qquad i = \text{m}, \text{im} \tag{7.2}$$

where subscripts m and im stand for mobile and immobile dislocations, respectively. The total annihilation pair formation rate for two mobile dislocations is:

$$\dot{p}^{\alpha}_{\mathrm{cs}(m)} = \dot{p}^{\alpha+}_{\mathrm{cs}(m)} + \dot{p}^{\alpha-}_{\mathrm{cs}(m)} = 2d^{\alpha}_{\mathrm{an}}\, v^{\alpha} (\rho^{\alpha}_{\mathrm{m}})^2 = 2d^{\alpha}_{\mathrm{an}} \rho^{\alpha}_{\mathrm{m}} \frac{|\dot{\gamma}^{\alpha}|}{b}, \tag{7.3}$$

and the total annihilation pair formation rate for a mobile dislocation and an immobile dislocation is:

$$\dot{p}^{\alpha}_{cs(im)} = \dot{p}^{\alpha+}_{cs(im)} + \dot{p}^{\alpha-}_{cs(im)} = d^{\alpha}_{\mathrm{an}} \rho^{\alpha}_{\mathrm{im}} \frac{|\dot{\gamma}^{\alpha}|}{b} \tag{7.4}$$

Here, it is assumed to have the same number of positive and negative dislocations.

7.1.1.2. Cross-slip mechanism

Cross-slip of screw dislocations is an important mechanism in the evolution of dislocations and recovery processes of bcc materials due to the availability of a large number of secondary slip systems [2]. For example, considering $\langle 1\,1\,1\rangle\{1\,1\,0\}$ and $\langle 1\,1\,1\rangle\{1\,1\,2\}$ slip systems, a $\langle 1\,1\,1\rangle$ screw dislocation has six common different slip planes. This leads to wavy glide, which is observed in bcc materials [3].

Rhee *et al.* [2] suggested that for cross-slip of a screw dislocation segment to take place, the screw dislocation segment needs to bow out and form a 'super-kink' configuration. Therefore, cross-slip is a probabilistic thermally activated process [2]:

$$P_{\mathrm{cs}} \propto \exp\left(V_{\mathrm{cs}} \frac{\tau^* - |\tau^{\beta}|}{k_{\mathrm{B}} T}\right) \tag{7.5}$$

where P_{cs} is the probability of cross-slip, V_{cs} is the activation volume for cross-slip, τ^* is the critical activation stress for the formation of super-kink configuration, and τ^{β} is the resolved shear stress in the cross-slip plane.

Patra and McDowell [4] proposed a stochastic model for cross-slip based on this probabilistic technique where the screw dislocations cross-slip to the plane with the highest probability. This process decreases the dislocation evolution rate on the primary slip system and increases the dislocation evolution rate on the cross-slip plane. Alankar *et al.* [5] used the same kind of probabilistic technique for determining the redistribution of dislocation density for each slip system and calculating the new dislocation density evolution rates.

7.1.1.3. Cross-slip annihilation

Most crystal plasticity models consider cross-slip annihilation to be a deterministic, mechanically activated process governed by the applied stress and an annihilation distance (see Eq. (7.4)). However, cross-slip and, consequently, cross-slip annihilation are stochastic processes. Here, a stochastic formulation is proposed for the cross-slip annihilation by considering the probabilistic nature of the cross-slip process as elaborated above. The annihilation rate of screw dislocations for two mobile dislocations can be written as:

$$\dot{\rho}^{\alpha}_{\mathrm{an}(1)} = \dot{p}_{\mathrm{cs}(m)} P_{\mathrm{cs}} = 2d^{\alpha}_{\mathrm{an}} \rho^{\alpha}_{\mathrm{m}} \frac{|\dot{\gamma}^{\alpha}|}{b} A_0 \exp\left(V_{\mathrm{cs}} \frac{\tau^* - |\tau^{\beta}|}{k_{\mathrm{B}} T}\right) = 2C^{\alpha}_{\mathrm{cs}} \rho^{\alpha}_{\mathrm{m}} \frac{|\dot{\gamma}^{\alpha}|}{b} \exp\left(V_{\mathrm{cs}} \frac{\tau^* - |\tau^{\beta}|}{k_{\mathrm{B}} T}\right) \tag{7.6}$$

and for a mobile and an immobile dislocation as:

$$\dot{\rho}^{\alpha}_{\mathrm{an}(2)} = \dot{p}_{\mathrm{cs}(im)} P_{\mathrm{cs}} = d^{\alpha}_{\mathrm{an}} \rho^{\alpha}_{\mathrm{im}} \frac{|\dot{\gamma}^{\alpha}|}{b} A_0 \exp\left(V_{\mathrm{cs}} \frac{\tau^* - |\tau^{\beta}|}{k_{\mathrm{B}} T} \right) = C^{\alpha}_{\mathrm{cs}} \rho^{\alpha}_{\mathrm{im}} \frac{|\dot{\gamma}^{\alpha}|}{b} \exp\left(V_{\mathrm{cs}} \frac{\tau^* - |\tau^{\beta}|}{k_{\mathrm{B}} T} \right) \tag{7.7}$$

where $C^{\alpha}_{\mathrm{cs}} = A_0 d^{\alpha}_{\mathrm{an}}$, and A_0 is a normalization factor used in P_{cs}.

This formulation implies that cross-slip annihilation of two screw dislocations occurs only if a dislocation of the opposite sign exists within a critical distance and at the same time only if the mobile dislocation cross-slips.

7.1.2. Dislocation evolution rates

In addition to introducing the cross-slip annihilation into the formulation, the evolution rates of the mobile dislocation density, $\dot{\rho}^{\alpha}_{\mathrm{m}}$, is modified as:

$$\dot{\rho}^{\alpha}_{\mathrm{m}} = \dot{\rho}^{\alpha}_{\mathrm{multi}} - \dot{\rho}^{\alpha}_{\mathrm{tr}} - \dot{\rho}^{\alpha}_{\mathrm{an}(1)} - \frac{1}{2} \dot{\rho}^{\alpha}_{\mathrm{an}(2)}, \tag{7.8}$$

and the immobile dislocation density, $\dot{\rho}^{\alpha}_{\mathrm{im}}$, as:

$$\dot{\rho}^{\alpha}_{\mathrm{im}} = \dot{\rho}^{\alpha}_{\mathrm{tr}} - \frac{1}{2} \dot{\rho}^{\alpha}_{\mathrm{an}(2)}. \tag{7.9}$$

7.1.2.0.1 Dislocation generation ($\dot{\rho}^{\alpha}_{\mathrm{multi}}$): It is assumed that the multiplication of dislocations takes place in the sense of generation of Frank–Read dislocation loops and line length increase by the loop expansion. A pinned dislocation bows out and expands under a critical shear stress, and dislocation loops are repeatedly generated from the source. The generated loops migrate under the subjected load until they are being immobilized after a mean free path, Λ^{α}, due to their interaction with obstacles. Assuming that the expansion velocity is constant and similar for all dislocation loops, the total evolution rate of mobile dislocation density is:

$$\dot{\rho}^{\alpha}_{\mathrm{multi}} = \frac{2|\dot{\gamma}^{\alpha}|}{b \Lambda^{\alpha}} \tag{7.10}$$

7.1.2.0.2 Dislocation immobilization ($\dot{\rho}^{\alpha}_{\mathrm{tr}}$): A dislocation loop is trapped and immobilized after migrating a mean free path of Λ^{α}, which results in an immobilization rate of:

$$\dot{\rho}^{\alpha}_{\mathrm{tr}} = \frac{|\dot{\gamma}^{\alpha}|}{b \Lambda^{\alpha}} \tag{7.11}$$

7.1.3. Results

Fig. 7.1 shows the stress-strain curves for different loading conditions. It can be seen that the new formulation is capable of predicting the hardening behavior over a wide range of temperatures and strain rates. Moreover, the model is able to capture the rate sensitivity at different temperatures and vice versa. The results show a substantial

improvement in comparison with the results presented in Fig. 4.6. However, the model accuracy deteriorates at higher temperatures and lower strain rates. This difference is likely due to neglecting climb-based dynamic recovery, which can significantly affect the strain hardening response at high temperatures.

7.2. Coupled modeling of recrystallization

Recrystallization texture depends strongly on the deformation heterogeneity and microstructural evolution during plastic deformation. This subsection presents two sequentially coupled microstructure-based simulation methods for modeling static recrystallization and meta-dynamic recrystallization. The deformation heterogeneity is quantified using high-resolution crystal plasticity simulations performed using the dislocation-density-based crystal plasticity model. Meanwhile, recrystallization and grain growth simulations are conducted using a Cellular Automata model named CASIPT (Cellular Automata Sharp Interface Phase Transformation). More detail on formulations and assumptions used in the static and meta-dynamic recrystallization models are presented respectively in [6, 7] and [8].

The Cellular automata model uses a three-dimensional grid regularly spaced in x, y, and z directions, i.e. for a cell of dimension δ, there are 26 neighboring cells at distances of δ, $\sqrt{2}\delta$, and $\sqrt{3}\delta$. Transferring the output variables between the crystal plasticity model with deformed mesh and the Cellular Automata, which uses a regular mesh, is performed using the remeshing approaches presented in Chapter 5. The results of the two models are presented in the following subsections.

7.2.1. Static recrystallization[1]

A framework is developed to couple the high-resolution crystal plasticity simulations with a recrystallization model presented in [6, 7]. The recrystallization process is defined as a mechanism driven by the subgrains/grains boundary curvature. This allows all stages of recrystallization (i.e. nucleation, primary recrystallization, secondary recrystallization, grain growth) to occur simultaneously during the simulation. According to this approach, nucleation is not imposed but naturally occurs throughout the evolving substructure. As a result, many important and unresolved phenomena can be investigated at the nucleation stage. Coupling this recrystallization model with the dislocation-density-based crystal plasticity model allows systematically investigating many local processes, such as the onset of recrystallization at the shear bands.

As an example, a sequentially coupled simulation is conducted using the bicrystal example presented in Fig. 5.23b. The annealing step is performed at 800°. Fig. 7.2 illustrates the temporal microstructural evolution in the mid-section of the RVE. It can be seen that subgrain growth is favored within the γ-fiber grain. Fig. 7.3 shows the $\varphi_2 = 45°$ section of the orientation distribution function for the deformed and annealed states. The microtexture evolution during recrystallization changes the maximum from $\{1\,1\,2\}\langle 1\,1\,0\rangle$ deformation texture component to orientation components within the γ-fiber ($\{1\,1\,1\} \parallel$ ND fiber).

[1] The section is a joint result with the Ph.D. thesis of Konstantina Traka.

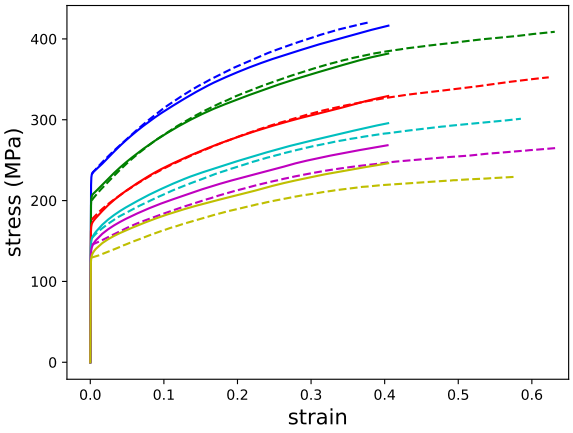

(a) $\dot{\varepsilon} = 0.1s^{-1}$

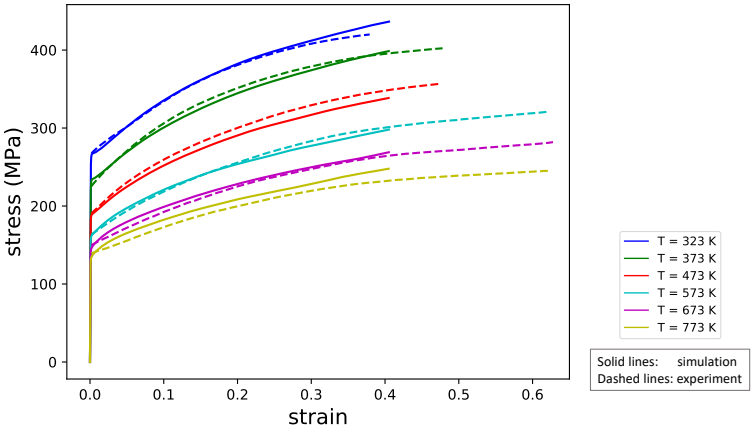

(b) $\dot{\varepsilon} = 1.0s^{-1}$

Fig. 7.1: Comparison between the model prediction and the experimental data for equivalent true stress-logarithmic strain curves deformed at various temperatures and at strain rates of (a) $0.1s^{-1}$ and (b) $1.0s^{-1}$. The solid lines show the model prediction, and the dashed lines show the experimental data.

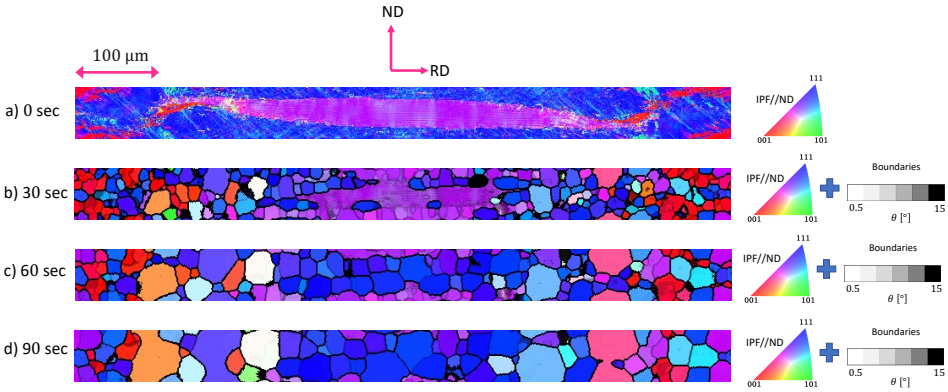

Fig. 7.2: IPF color maps parallel to the normal direction (ND) showing microstructural evolution in the mid-section along the transverse direction after (a) 0s (b) 30s (c) 60s (d) 90s.

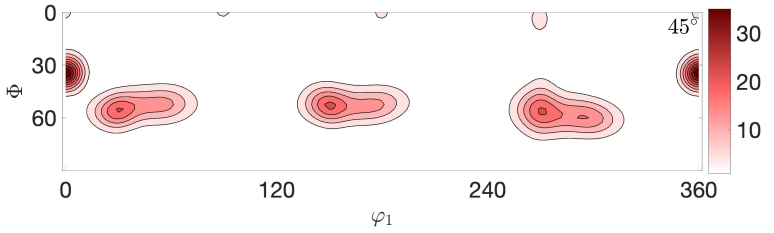

(a) 0s

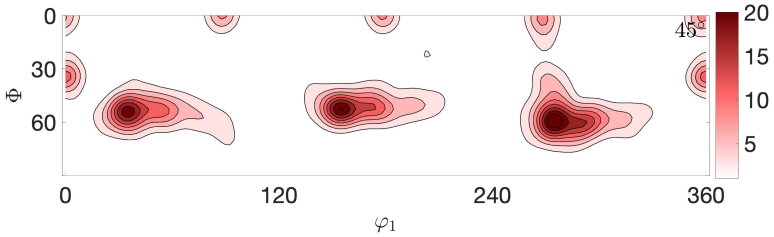

(b) 90s

Fig. 7.3: Orientation density f(g) maps ($\varphi_2 = 45°$) for (a) the deformed and (b) the recrystallized states.

This simple example confirms two important and well-known phenomena for IF-steel. Firstly, recrystallization occurs heterogeneously, and some regions recrystallize faster, while others resist and get consumed later by large recrystallized grains. Secondly, recrystallization results in changing the distribution of crystal orientations. Particularly components within the γ-fiber intensify at the expense of the α-fiber components.

7.2.2. Meta-dynamic recrystallization[2]

The sequentially coupled model developed for modeling meta-dynamic recrystallization [8] is used to simulate a multi-stand hot-rolling process. First, a 3D synthetic RVE with 846 initial grains is created, i.e. approximately 28 grains in the normal direction, 10 grains in the rolling direction, 3 grains in the transverse direction. This RVE is subjected to a plane-strain compression up to a total thickness reduction of 51% in three steps as:

- up to 30% thickness reduction with a strain rate of $15s^{-1}$ and an interpass annealing time of 5s
- up to 44% thickness reduction with a strain rate of $20s^{-1}$ and an interpass annealing time of 1s
- up to 51% thickness reduction with a strain rate of $25s^{-1}$ and an annealing time of 1s.

The IPF color maps parallel to the rolling (horizontal) direction and the rotation angle maps are shown respectively in Figs. 7.4 and 7.5 for different processing stages. After the first deformation step, a significant variation in the reorientation of different elements is evident. However, the level of deformation heterogeneity depends considerably on the grain orientation. During the interpass annealing step, the deformed grains with larger orientation scatter are recrystallized and replaced with almost uniform grains, i.e. grains with minimal orientation spread. After the second deformation step, orientation scatter is developed in the partially recrystallized microstructures. Again during the interpass annealing step, the grains with notable orientation scatter are recrystallized and replaced by uniform grains.

[2] The section is a joint result with the Ph.D. thesis of Vitesh Shah.

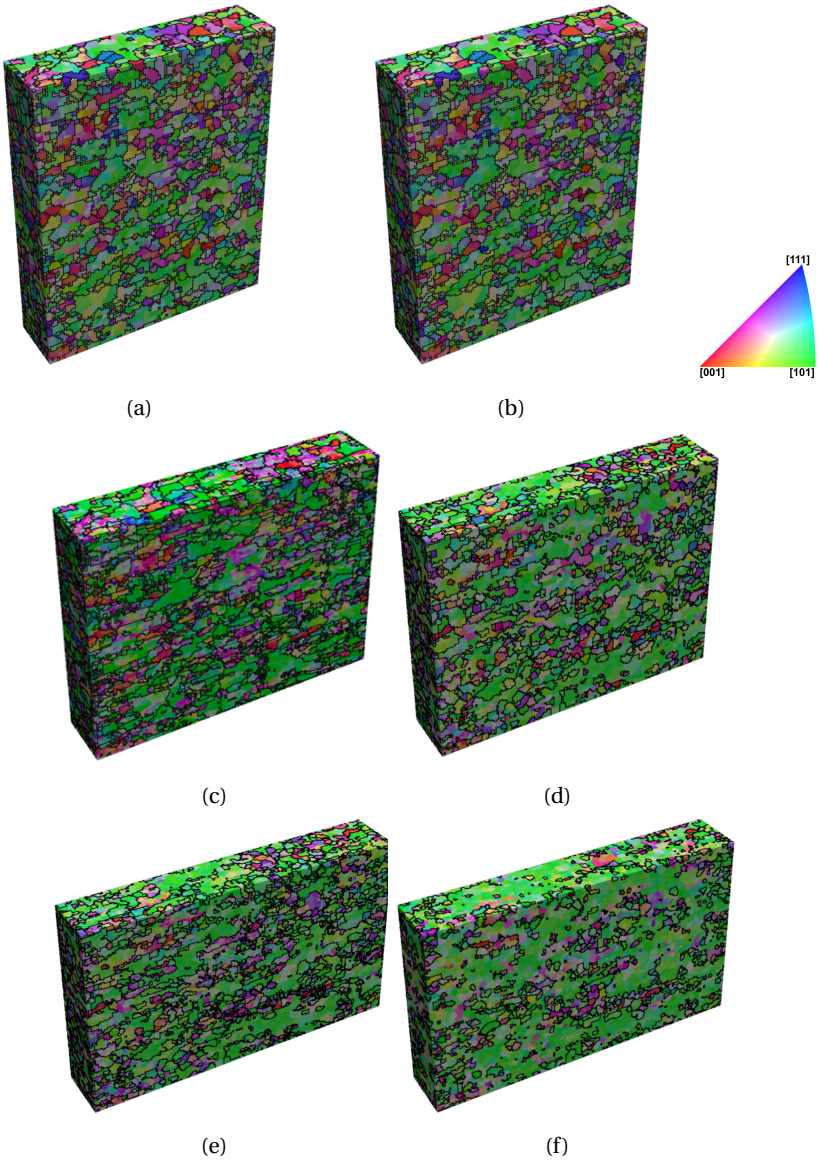

Fig. 7.4: IPF color maps parallel to the stretching (horizontal) direction after (a) 30% thickness reduction, (b) interpass annealing time of 5 s, (c) 44% thickness reduction, (d) interpass annealing time of 1 s, (e) 51% thickness reduction, (f) interpass annealing time of 1 s.

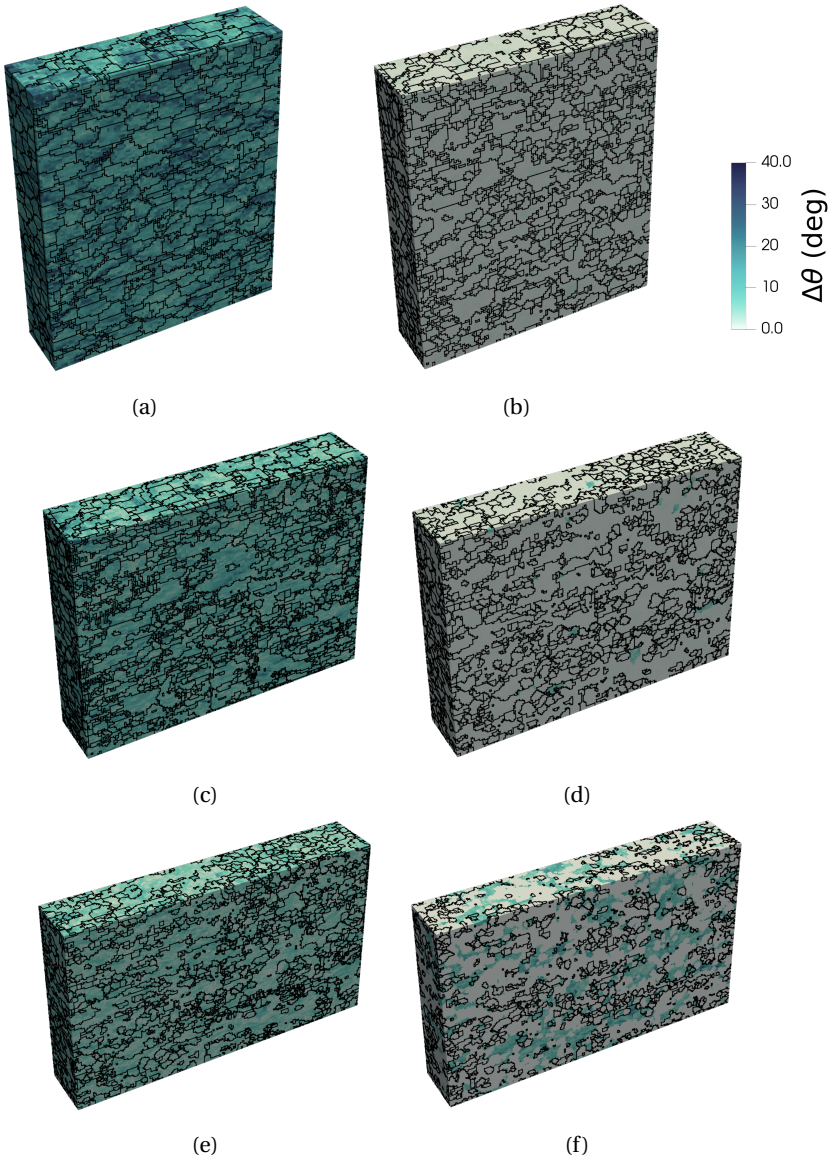

Fig. 7.5: Evolution of the dislocation density after (a) 30% thickness reduction, (b) interpass annealing time of 5 s, (c) 44% thickness reduction, (d) interpass annealing time of 1 s, (e) 51% thickness reduction, (f) interpass annealing time of 1 s.

References

[1] P. Pauš, J. Kratochvíl, and M. Beneš, *A dislocation dynamics analysis of the critical cross-slip annihilation distance and the cyclic saturation stress in fcc single crystals at different temperatures,* Acta Materialia **61** (2013), 10.1016/j.actamat.2013.09.032.

[2] M. Rhee, H. M. Zbib, J. P. Hirth, H. Huang, and T. De La Rubia, *Models for long-/short-range interactions and cross slip in 3D dislocation simulation of BCC single crystals,* Modelling and Simulation in Materials Science and Engineering **6** (1998), 10.1088/0965-0393/6/4/012.

[3] T. E. Mitchell and W. A. Spitzig, *Three-stage hardening in tantalum single crystals,* Acta Metallurgica **13** (1965), 10.1016/0001-6160(65)90054-4.

[4] A. Patra and D. McDowell, *Crystal plasticity-based constitutive modelling of irradiated bcc structures,* Philosophical Magazine **92**, 861 (2012).

[5] A. Alankar, D. P. Field, and H. M. Zbib, *Explicit incorporation of cross-slip in a dislocation density-based crystal plasticity model,* Philosophical Magazine **92** (2012), 10.1080/14786435.2012.685964.

[6] K. Traka, K. Sedighiani, C. Bos, J. Galan Lopez, K. Angenendt, D. Raabe, and J. Sietsma, *Topological aspects responsible for recrystallization evolution in an IF-steel sheet – Investigation with cellular-automaton simulations,* Computational Materials Science **198**, 110643 (2021).

[7] K. Traka, K. Sedighiani, M. Diehl, C. Bos, F. Roters, D. Raabe, and J. Sietsma, *Coupled modeling of texture formation during recrystallization,* To be submitted (2022).

[8] V. Shah, K. Sedighiani, J. van Dokkum, C. Bos, M. Diehl, F. Roters, and D. Raabe, *Coupling crystal plasticity and cellular-automata to model meta-dynamic recrystallization during hot-rolling at higher strain rates,* To be submitted (2022).

8

CONCLUSION

Abstract

This work first introduces a novel, computationally efficient, and fully automated approach to identify constitutive parameters of crystal plasticity models from macroscopic tests. In the next step, this approach is employed to examine the ability of a widely used temperature-dependent dislocation-density-based crystal plasticity formulation. After that, two adaptive remeshing approaches are introduced to overcome the mesh distortion problem and simulate large deformation of three-dimensional polycrystals. Finally, high-resolution three-dimensional crystal plasticity simulations are used to investigate deformation heterogeneity and microstructural evolution during large deformation of interstitial free (IF) steel. This chapter summarizes the main ideas, innovations, and conclusions of this work. Applications and recommendations for future studies are also provided.

8.1. Conclusions and recommendations

Plastic deformation of polycrystalline materials is significantly heterogeneous due to the complexity of the underlying microstructure, phases, composition, processing boundary conditions, leading to corresponding heterogeneity in strain, stress, crystal orientation. Characterization and understanding of the deformation heterogeneities and microstructural evolution during plastic deformation are critical from many aspects. (i) Prediction of the material properties is not possible without understanding the behavior, evolution, and mechanical response of microstructural features. (ii) The underlying mechanisms behind localization phenomena such as fracture and damage are related to the strain localization and microstructural evolution during deformation. (iii) Understanding the physics governing many multi-disciplinary fields is incomplete without adequately understanding the internal stresses developing in these heterogeneous microstructures.

Crystal plasticity simulations are a powerful tool for modeling and quantifying the deformation heterogeneities and the associated complex mechanical fields. These models are developed based on physical mechanisms such as glide of dislocations on preferred slip systems and the interaction of dislocations with various defects. The first step for the routine use of a crystal plasticity model is to identify a complete and accurate set of constitutive parameters. In this study, a novel and computationally efficient approach is developed for identifying constitutive parameters from macroscopic stress-strain data. The power of this methodology is demonstrated on the examples of a phenomenological crystal plasticity model, a dislocation-density-based crystal plasticity model, and a phenomenological crystal plasticity model incorporating deformation twinning. It is shown that the methodology reliably reproduces the known parameters of simulated reference compression/tension tests.

> **Recommendation 1:** *The optimization method (presented in Chapter 3) can be used to identify the material parameters of various materials. A systematic analysis of the barrier parameters (the parameters that define the barrier shape, i.e. ΔF, τ_0^*, p, and q) for different materials with similar lattice structures is needed to better understand the role of barrier interaction energy on the velocity of mobile dislocations in the dislocation-density-based crystal plasticity models. In addition, different researchers have used different values for the same material parameters. Such a systematic identification of material parameters and creating a library of material parameters will be an invaluable step towards consolidating the parameters used in the literature.*

Moreover, the optimization methodology is employed to quantitatively and systematically examine the role of the model parameters in the mechanical response of the dislocation-density-based model. For this purpose, the material parameters are first identified using macroscopic stress–strain curve data experimentally obtained for Interstitial Free (IF)-steel. It is observed that the dislocation-density-based constitutive law is capable of predicting the polycrystal yield stress over a wide range of temperatures and strain rates with a single set of material parameters. However, it fails to predict the material response at very high temperatures correctly. In addition, the temperature-dependent crystal plasticity model is not numerically stable at

temperatures close to and above the critical temperature if only the waiting time to overcome barriers is considered in the formulation of the dislocation velocity. The formulation has been modified and stabilized at high temperatures by adding the running time into the formulations.

An in-depth analysis of the parameters reveals that due to this distinct role of initial dislocation density, ρ_0^α, and dislocation glide velocity pre-factor, v_0, in determining the ration of temperature- over strain rate-sensitivity, it is possible to determine ρ_0^α and v_0 uniquely. However, the system is underdetermined for the barrier parameters. Therefore, it is impossible to determine these parameters uniquely without prior knowledge about the barrier strength and the critical temperature. Since the temperature-dependent motion of dislocations in the constitutive law used in this study has the same basis as the one proposed by Kocks *et al.* [1], most of the conclusions made in this study are expandable to many other models that use the same concept.

Recommendation 2: *The two phenomenological parameters p and q define the curvature in the relation between the activation energy for dislocation glide and the thermal stress. The main reason for introducing p and q in the way outlined in Chapter 4 is the simplicity of the equations. An alternative approach to fundamentally overcome the non-uniqueness issue is by using a mathematically reasonable profile for the barrier, such as a sinusoidal profile. In this case, activation energy for dislocation glide, ΔG, can be estimated directly from the barrier's profile by calculating the activation volume for dislocation glide. This overcomes the need to introduce the curvature in thermal stress by phenomenological parameters like p and q. Although such a barrier profile results in more complex equations for the constitutive law, it reduces the number of* phenomenological *material parameters. This can be a significant advantage for physics-based models, which generally have a large number of material parameters.*

Recommendation 3: *The hardening formulation of the dislocation-density-based constitutive law is not able to describe the dynamic recovery process accurately. In addition to the problems regarding the climb-based formulation, the model lacks cross-slip recovery. Due to the availability of many secondary slip systems in bcc materials, cross-slip of screw dislocations is a key mechanism in the evolution of the dislocation structures. Therefore, developing a physics-based hardening model that includes adequate formulations for climb-based and cross-slip-based recovery is invaluable (see Section 7.1). One can use the optimization method to examine and analyze the significance and outcome of different formulations efficiently.*

Problems involving the deformation of solid materials are usually formulated in a way (a Lagrangian context) that the mesh is attached to the deformable body and deforms with a change in the shape of the material. This means that the mesh becomes distorted due to the heterogeneity of the deformation. The mesh distortion initially introduces errors in the solution and delays convergence. Ultimately, the distortion becomes too large, and the simulation fails to converge. Therefore, overcoming mesh distortion is the next challenging step in modeling the deformation heterogeneity and

microstructural evolution during the large deformation of polycrystals. In this work, two approaches were proposed to overcome the mesh distortion problem at large strains, i.e. the mesh replacement method and the mesh distortion control method. The accuracy of the two methods was examined using different test cases designed to evaluate the various steps involved. It was shown that both approaches enable conducting accurate high-resolution large-deformation crystal plasticity simulations and overcoming the associated mesh distortion problem due to the strain localization.

In the mesh replacement method, the configuration with the distorted mesh is replaced by a new configuration with an undistorted mesh. Therefore, it can be stated that the mesh replacement method is like starting a new analysis in which the initial state of the model is obtained from a different analysis. In the mesh distortion control method, the undistorted mesh is achieved by removing the fluctuating part of the deformation and keeping the homogeneous part of the deformation. Hence, this approach requires finding a new equilibrium state for the smoothed mesh, contrary to the mesh replacement method. This leads to a higher computational cost for the mesh distortion control method, especially at large strain. Since no significant difference between the results from the two remeshing approaches was observed, a substantial amount of computational cost can be saved using the mesh replacement method. However, in the case of using periodic boundary conditions, it is challenging to preserve the periodicity requirements for some loading conditions, e.g. loading involving shear. For such complex loading conditions, the mesh distortion control method was proposed. Since the homogeneous part of the deformation is retained during the undistorted mesh generation for the mesh distortion control method, the periodicity requirements are always conserved regardless of the loading condition. Therefore, the mesh distortion control method's main advantage is that it enables remeshing in situations where the periodicity of the geometry would be broken by the mesh replacement method.

A global adaptive scheme is implemented for both remeshing approaches, allowing to update the number of elements in the three coordinate directions at any remeshing step. This adaptive scheme is important to prevent the elements' aspect ratio from becoming too large. Besides, a multi-step mesh refinement approach was suggested for efficient simulation of large-deformation high-resolution crystal plasticity problems. It was shown that this adaptive meshing strategy can be used, for example, to capture the effect of grain shape on the plastic deformation heterogeneity.

Recommendation 4: *Many microstructural processes (e.g. static recrystallization, dynamic recrystallization, or phase transformation) depend on the deformation heterogeneity and microstructural evolution during plastic deformation. However, most approaches for solving such problems are typically defined based on a regular undeformed mesh, and adjusting the formulations for a deformed mesh can be complicated. For instance, cellular automata models work with a regular mesh, and incorporating a deformed mesh makes it computationally inefficient to calculate the transformation rules. As a result, coupling cellular automata with crystal plasticity models becomes challenging. One can use the remeshing approaches to develop a sequentially coupled model to simulate problems like static or dynamic recrystallization.*

Recommendation 5: *Damage and fracture of materials are typically related to deformation localization. When there is a big contrast between the stiffness and yielding behavior of the material phases around the damage site, the localized strain can be a few times larger than the macroscopically applied strain. As a result, locations close to the damage sites are susceptible to mesh distortion, and this local distortion in the mesh can hinder simulating damage developed after the damage nucleation. One can explore the capabilities of the remeshing approaches to investigate the damage evolution for such cases.*

Recommendation 6: *In typical finite element simulations, mesh-convergence studies are usually performed by comparing the load-displacement (or stress-strain) behavior. In crystal plasticity simulation, mesh-convergence studies are more complicated. A low-resolution simulation is usually sufficient to predict stress-strain response or even global crystallographic texture. However, the detail of in-grain microstructural evolution that can be predicted depends significantly on the simulation's resolution. For instance, although the high-resolution simulation used in Chapter 6 can capture many details, the mesh density is not sufficient to observe the full detail of the river-like pattern shear bands. One may investigate how an increase in the mesh density per grain can improve the prediction of in-grain microstructural features. In addition, since a higher resolution allows capturing processes such as fragmentation, investigating the effect of the simulation's resolution on the local change in texture evolution can be valuable.*

Recommendation 7: *One of the challenges faced in this study was to perform a systematic comparison of two configurations. For this purpose, a statistical comparison using the Kolmogorov-Smirnov test was used. However, statistical analyses are not able to capture the local variations that are developing during plastic deformation. For instance, comparing the low-resolution and high-resolution examples in Chapter 5 showed a good statistical agreement between the two cases, while the observed in-grain patterns were different. Developing a robust methodology for conducting one-to-one comparisons can help to capture similarities and differences between local variations in microstructural features.*

Finally, large-deformation high-resolution three-dimensional crystal plasticity simulation and electron backscatter diffraction (EBSD) analysis were used to investigate deformation heterogeneity and microstructure evolution during cold rolling of IF-steel. It was observed that the in-grain texture evolution and misorientation spread are consistent for simulation and experimental results. The deformation texture obtained using simulation is according to the typical rolling texture observed in BCC crystals, i.e. a strong α-fiber and γ-fiber. It was observed that the components belonging to the α-fiber strengthen continuously with increasing deformation. Although the γ-fiber components are initially strengthened with increasing the applied strain, these texture components weaken at larger thickness reductions, i.e. after about 70-80% thickness reduction.

A significant level of deformation heterogeneity was observed during the plastic deformation. The crystallographic orientation of a grain is a critical factor in determining the degree in which a grain deforms heterogeneously. The orientations close to the rotated cube orientation show the minimal tendency to form orientation gradients. The deformation heterogeneity increases for orientations further along the α-fiber. On the other hand, the orientations belonging to the γ-fiber show the strongest misorientation spread.

During deformation, some non-crystallographic macroscopic shear bands that extend across the specimen (which appear as river patterns) are formed. These macroscopic bands are initially formed at an approximate angle of $\pm 40^\circ \sim 45^\circ$ with the rolling direction. With increasing the thickness reduction, the river-like patterns rotate significantly to directions almost parallel to the rolling direction. In addition to the macroscopic river-like patterns, several regions with rather sharp and highly localized in-grain deformation bounds were identified. These deformation bands extend inside only one grain, and they are formed at an angle of approximately $\pm 30^\circ \sim 35^\circ$ with the rolling direction. The inclination angle of in-grain deformation bands is not notably dependent on the applied strain for a wide deformation range. The in-grain deformation bands are orientation-dependent, and they form mainly in grains belonging to the γ-fiber. However, not all grains belonging to the γ-fiber contain such features.

It was observed that at small strains the difference between the dislocation density of different orientations is relatively small. However, with increasing strain, the average dislocation density becomes notably larger in the γ-fiber compared to the α-fiber. Moreover, although there is only a weak correlation between KAM and dislocation density at small strains, the correlation coefficient increases rapidly with increasing strain, reaching a significant value of 0.60 after a 77% thickness reduction. The correlation between the dislocation density and the equivalent strain follows an opposite trend.

Recommendation 8: *Mixed deformation mode occurs in many industrial processes, e.g. during rolling near the surface, asymmetric rolling, or extrusion. The mesh distortion control method can be used to model specimens under such complex boundary conditions. A systematic study of the effect of shear strain on microstructural evolution can be a useful contribution to the community.*

Recommendation 9: *Due to the strain localization at grain boundaries, they are one of the most critical microstructural features. Fig. 8.1 shows a high-resolution example after 50% thickness reduction. The evolution of the dislocation density and KAM is evidently affected by grain boundaries. Fig. 8.2 shows a selected grain and the dislocation density along a line. The dislocation density is minimum at the center of the grain, and it increases towards the grain boundaries. The deformation behavior at grain boundaries (or phase boundaries) is an important and exciting topic to investigate further. One may note that better results can be achieved using a non-local crystal plasticity model that explicitly accounts for the spatial redistribution of dislocations. The remeshing methods are not model-dependent and can be employed with such constitutive laws.*

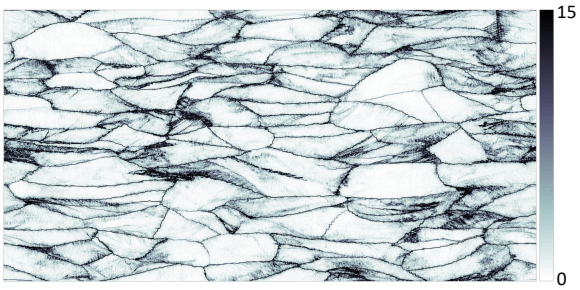

(a) KAM (degree)

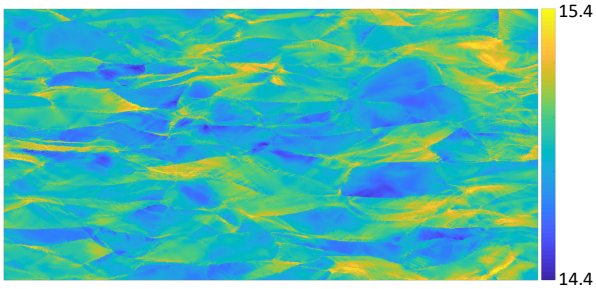

(b) Log dislocation density (m^{-2})

Fig. 8.1: A high-resolution simulation example showing the distribution of the KAM and dislocation density.

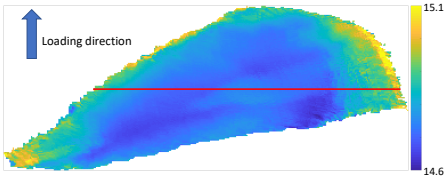

(a) Log dislocation density (m^{-2}) in a selected grain.

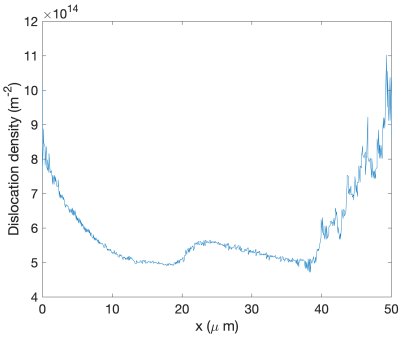

(b) Dislocation density along the red line.

Fig. 8.2: Distribution of the dislocation density for a selected grain.

Recommendation 10: *In general, the macroscopic texture developed in bcc materials is not significantly sensitive to the hardening model. On the contrary, our investigation shows that changing the hardening parameters (or hardening model) can significantly affect the in-grain microstructural evolution, e.g. the KAM distribution and the in-grain deformation band patterns. Further investigation of the effect of hardening behavior on the in-grain microstructural and texture evolution is needed.*

References

[1] U. Kocks, A. Argon, and M. Ashby, *Thermodynamics and kinetics of slip* (Pergamon Press, 1975).

[2] P. Pauš, J. Kratochvíl, and M. Beneš, *A dislocation dynamics analysis of the critical cross-slip annihilation distance and the cyclic saturation stress in fcc single crystals at different temperatures,* Acta Materialia **61** (2013), 10.1016/j.actamat.2013.09.032.

[3] M. Rhee, H. M. Zbib, J. P. Hirth, H. Huang, and T. De La Rubia, *Models for long-/short-range interactions and cross slip in 3D dislocation simulation of BCC single crystals,* Modelling and Simulation in Materials Science and Engineering **6** (1998), 10.1088/0965-0393/6/4/012.

[4] T. E. Mitchell and W. A. Spitzig, *Three-stage hardening in tantalum single crystals,* Acta Metallurgica **13** (1965), 10.1016/0001-6160(65)90054-4.

[5] A. Patra and D. McDowell, *Crystal plasticity-based constitutive modelling of irradiated bcc structures,* Philosophical Magazine **92**, 861 (2012).

[6] A. Alankar, D. P. Field, and H. M. Zbib, *Explicit incorporation of cross-slip in a dislocation density-based crystal plasticity model,* Philosophical Magazine **92** (2012), 10.1080/14786435.2012.685964.

[7] K. Traka, K. Sedighiani, C. Bos, J. Galan Lopez, K. Angenendt, D. Raabe, and J. Sietsma, *Topological aspects responsible for recrystallization evolution in an IF-steel sheet – Investigation with cellular-automaton simulations,* Computational Materials Science **198**, 110643 (2021).

[8] K. Traka, K. Sedighiani, M. Diehl, C. Bos, F. Roters, D. Raabe, and J. Sietsma, *Coupled modeling of texture formation during recrystallization,* To be submitted (2022).

[9] V. Shah, K. Sedighiani, J. van Dokkum, C. Bos, M. Diehl, F. Roters, and D. Raabe, *Coupling crystal plasticity and cellular-automata to model meta-dynamic recrystallization during hot-rolling at higher strain rates,* To be submitted (2022).

ACKNOWLEDGEMENTS

Many people have positively influenced me throughout my PhD project, and this project would not have been possible without their support. I strive to thank most of them, and I apologize to colleagues and friends that I neglected to mention.

Above all, I would like to thank my supervisors, Dierk Raabe, Jilt Sietsma, Martin Diehl, and Franz Roters, for their patience, guidance, and support. I am thankful for the extraordinary experiences you arranged for me and for providing opportunities to grow professionally. I have significantly benefited from your wealth of knowledge and our discussions. Martin, you have been an ideal mentor and friend, offering advice and encouragement throughout the project. Our conversations always inspired me to go further. The goal of this project would not have been realized without your persistent help. Franz, your insightful feedback pushed me to sharpen my thinking and brought my work to a higher level. Dierk, I'll forever be grateful for the encouragement you gave me when I needed it. Jilt, without your help and emotional support, I wouldn't have made it. It is an honor to be your student.

I would like to extend my sincere thanks to all my committee members, Leo Kestens, Ron Peerlings, Philip Eisenlohr, Stephen Niezgoda, and Maria Santofimia Navarro. I was delighted when you agreed to be on my thesis committee. Your encouraging words and thoughtful feedback have been very important to me. Leo, I've always loved our talks about science, mechanics, politics, history, etc. You have always made me think deeply, and I have learned a lot from you. Ron, thanks for all your help and support since my first days in the Netherlands. Your insightful questions and comments have always challenged me to think deeply and made my research so much richer. Philip, thank you for your encouraging and kind words and for your valuable comments. Steve, thank you for our conversation at the International Conference of Plasticity in Panama, which motivated me to look deeper at my work.

I am also indebted to several colleagues. First, I wish to thank my dearest friend Konstantina. Konstantina, my thesis builds on our strong collaboration, and many of its ideas were developed during our conversations. Thanks for all the discussions, conversations, arguments, agreements, disagreements, kind support, and the enjoyable time we have had. You are an inspiring colleague and a caring friend. David, thank you for all our conversations and for making my time in Düsseldorf so joyful. Vitesh, Sharan, Jesus, Markus, Pratheek, and Jaber, I greatly appreciate all of our discussions and conversations during my PhD years.

I would like to extend my sincere thanks to Kees Bos. Without your scientific contributions and help, I could not have accomplished this work. Michael Adamek, thanks for the help with the experiments and our table tennis games. Achim and Berthold, thanks for your help and assistance. Thank you to Viktoria Savran for coordinating my PhD project. I am also grateful to Prisca Koelman for all of the kindness and assistance you have provided.

I want to thank my dear friends and colleagues from the Materials Science and Engineering department at TU Delft. Rouman, Richard, Eric, Saskia, Behnam, Viviam, Jhon, Arthur, Vibhor, Chrysa, Carola, Reina, Hussein, Martina, Javi, Jan, Konstantine, Ankit, Edwin, Soroush, thank you for all your help and being so welcoming whenever I was at Delft. I would like also to thank my new colleagues from Tata Steel, Hans, Wil, Pascal, and Eisso.

Table tennis has been my escape from work whenever my mind needs a break. Thanks to all my friends and teammates from my table tennis club TAVERES. Special thanks to Hans for making training so enjoyable that I couldn't miss it even if I had deadlines. A special thanks to Ketemaw, my friend and my training partner. Training is not the same without you! Dion, Yiyu, Gilbert, Lukas, and Pranav, thanks for all the enjoyable games and training. I also wish to thank my teammates and friends Yohan, Marco, Milan, Wouter, Stef, Guus, Xaveria, Arjab, Nhan, Robin, Antoine, Debbie, Zelin, Sen, Janathon, Yasamin, Joel, Vincent, Mart, Paul, and Sven.

I have had the privilege of developing and maintaining several friendships outside of the office. A very special thanks to my dearest friends Sahar and Behrouz, with whom we have had an incredible journey in the Netherlands. Kamlesh, Foad, Fariba, Maysam, Susan, Kambiz, Alvi, Willem, Susanne, Zamid, and Hussein, thank you for all the happy moments together.

I also wish to thank my amazing friends outside the Netherlands. My dearest friend Aso, you are physically my most distant friend, but you are so close to my heart. Thanks for all the late-night, very, very long talks! Salar, thanks for all the motivation you gave me and for all the time we spent in the library. You deserve all the successes in the world, not the unjust stars! Hajir, you have been my wonderful, lifelong friend. Shahryar, Chiya, Behrouz, Saro, Xalid, Ako, and Mehdi, I am grateful to have you in my life. Soran, Hadi, and Thomas, thank you for the fantastic time at the conferences. Very special thanks to dear Ayat, Saiedian, Farahmandi, and Moradian for all the motivation and inspiration you gave me.

Finally, I owe my deepest gratitude to my family. I am forever thankful for your unconditional love and support. My deepest thanks to my wife, Leila, for your love, for constantly listening to me rant and talk things out, for the sacrifices you have made in order for me to pursue PhD degree, for reminding me of what is important in life, and for always being supportive of my adventures. I am also thankful to my brother, Kavan, for always motivating me to go further. Thank you for helping me with programming, genetic algorithm, and many other things. Thank you to my sister, Shima, for always being there for me and for telling me that I am awesome even when I didn't feel that way. Thanks to my uncle, Najma, my aunt, Rubaba, and my cousins Irien and Rojin, for your love and for giving us a second home in the Netherlands. I would like to express my deepest appreciation to my parents, Fatm and Mahya, for their endless support. You sacrificed everything and stood behind me when I was deprived of my right to education in Iran. Mom, your constant love and support keep me motivated and confident. Thank you for the numerous phone calls, for calming me down, and for having time for me anytime, anywhere. Dad, thank you for all of your love and for constantly reminding me of the end goal. Daya (grandma), I will be ever grateful to you, and I am sorry that you have not lived to see me graduate.

CURRICULUM VITÆ

Karo Sedighiani was born on the 21st of September 1983 in Saqqez, Kurdistan, where he finished primary and secondary school. He received a BSc in Mechanical Engineering with an emphasis in solid mechanics from Razi University in 2006. He was selected to study for a Master's degree in Mechanical Engineering at Iran's University of Science & Technology (IUST). In 2008, he was one of the students in Iran who were banned from continuing their education due to their human rights activity. Karo couldn't receive his degree while he successfully finished his master's and had only one course left to graduate. During the period he was pursuing his case, he continued working as a researcher in the Fracture and Fatigue Laboratory at IUST. In 2012, he moved to the Netherlands to start a new master's program at Eindhoven University of Technology. He received his MSc degree with great appreciation in 2014 in mechanical engineering with an emphasis on the mechanics of materials. After that, he worked as a senior scientist at Medtronic for four years, researching the fracture behavior of thin-film materials. In 2017, he joined Delft University of Technology and Max-Planck Institut für Eisenforschung to continue his education as a PhD researcher. Since February 2022, he has joined the research and development department at Tata Steel Netherlands as a principal researcher, supporting their program to develop new steel grades.

LIST OF PUBLICATIONS

8. **K. Sedighiani, V. Shah, K. Traka, M. Diehl, F. Roters, J. Sietsma, D. Raabe**, *Large-deformation crystal plasticity simulation of microstructure and microtexture evolution through adaptive remeshing*, International Journal of Plasticity **146**, (2021).

7. **K. Sedighiani, K. Traka, F. Roters, J. Sietsma, D. Raabe, and M. Diehl**, *Determination and analysis of the constitutive parameters of temperature-dependent dislocation-density-based crystal plasticity models*, Mechanics of Materials, (2021).

6. **K. Traka, K. Sedighiani, C. Bos, J.G. Lopez, K. Angenendt, D. Raabe, J. Sietsma**, *Topological aspects responsible for recrystallization evolution in an IF-steel sheet – Investigation with cellular-automaton simulations*, Computational Materials Science **198**, (2021).

5. **K. Sedighiani, M. Diehl, K. Traka, F. Roters, J. Sietsma, D. Raabe**, *An efficient and robust approach to determine material parameters of crystal plasticity constitutive laws from macro-scale stress–strain curves*, International Journal of Plasticity **134**, (2020).

4. **D. Raabe, B. Sun, A. K. Da Silva, B. Gault, H. Yen, K. Sedighiani, and et al.**, *Current challenges and opportunities in microstructure-related properties of advanced high-strength steels*, Metallurgical and Materials Transactions A **51**, (2020).

3. **K. Sedighiani, K. Traka, F. Roters, J. Sietsma, and D. Raabe, M. Diehl**, *Crystal plasticity simulation of in-grain microstructural evolution during large deformation of IF-steel, Submitted to Acta Materialia*, (2022).

2. **V. Shah, K. Sedighiani, J. van Dokkum, C. Bos, M. Diehl, F. Roters, D. Raabe**, *Coupling crystal plasticity and cellular automaton models to study meta-dynamic recrystallization during hot rolling at high strain rates, Submitted to Materials Science & Engineering A*, (2022).

1. **K. Traka, K. Sedighiani, M. Diehl, C. Bos, F. Roters, D. Raabe, J. Sietsma**, *Coupled modeling of texture formation during recrystallization, To be submitted*, (2022).